EVALUATION OF METAL-ORGANIC FRAMEWORKS, EGGSHELL-DERIVED HYDROXYAPATITE AND LAYERED DOUBLE HYDROXIDES IN ADSORPTION AND PHOTOCATALYTIC PROCESSES

by

Duygu Tuncel

B.S., Chemistry, Yıldız Technical University, 2012

M.S., Chemistry, Boğaziçi University, 2014

Submitted to the Institute for Graduate Studies in

Science and Engineering in partial fulfillment of

the requirements for the degree of

Doctor of Philosophy

Graduate Program in Chemistry

Boğaziçi University 2023

ACKNOWLEDGEMENTS

First and foremost, I would like to express my sincere gratitude to my supervisor Prof. Ayşe Neren Ökte for her attention, motivation, and patience in every stage of my graduate studies. It was a great pleasure and honor to be her student and to do academic research under her guidance. She has guided and encouraged me throughout my graduate years both academically and socially. She will always have a special place in my life

I would like to extend my appreciation to my committee members Prof. Naz Zeynep Atay Gök, Prof. Duygu Avcı Semiz, Prof. Nurcan Tüzün and Prof. Tarık Eren for taking their valuable time for reviewing this thesis and for their insightful comments.

I acknowledge to Boğaziçi University Research Foundation (Project No. 14B05P11/8820 and 17B05D5/13141 and 22BD8/19362) and the Joint Research and Technology Programs in years of 2011–2013 and 2013-2015 between Turkey (TUBITAK, 209T109-113Z448) and Greece (General Secretariat for Research and Technology and European Regional Development Fund, GSRT 10 TUR/1-25-1 and 14TUR SOL-NANO) for financial support.

I would like to thank all faculty members in the Boğaziçi University Chemistry Department for their altruism and kindness during my graduate years. I wish to thank Dr. Bilge Gedik Uluocak for SEM analysis and Ali Uzun for XRD analysis and Dr. Burcu Selen Çağlayan for XPS analysis.

I would also like to thank Prof. Dimitris Karamanis from the University of Patras, Department of Environmental Engineering (Greece) for his collaboration.

I would like to thank to my friends, colleagues and former labmates for moral support and friendship.

My deepest thanks to my dear mother, Feride Sunar Tuncel, my dear father, Mehmet Hasan Tuncel, and my dear brother, Baki Saim Tuncel for their unlimited love and support

throughout my entire life. Without their belief in me, I would not be where I am. I also express my sweetest thanks to my niece Azra Tuncel as being my little sunshine and her sweet mother Tutku Tuncel. I would also like to thank my beloved grandmother, whom I lost during my PhD years, for her warm and unconditional love. And a special thank is for my closest friend, my love, my husband Ahmet Melih Turan for his endless love, patience and encouragement. He has made everything easier ever since the day he came into my life.

ABSTRACT

EVALUATION OF METAL-ORGANIC FRAMEWORKS, EGGSHELL-DERIVED HYDROXYAPATITE AND LAYERED DOUBLE HYDROXIDES IN ADSORPTION AND PHOTOCATALYTIC PROCESSES

This dissertation aims to synthesize novel catalysts, examine their structural features and ultimately evaluate their performances in adsorption and photocatalytic degradation processes. In this respect, the dissertation has three chapters.

The first chapter reports TiO_2 and ZnO loaded metal-organic frameworks (MOFs). Cu-BTC and ZIF-8 are selected as hydrophilic and hydrophobic MOFs, respectively. The second chapter investigates two supported catalyst systems; ZnO and La-ZnO loaded eggshell and ZnO and La-ZnO loaded eggshell derived hydroxyapatite (HAP). The third chapter examines binary layered double hydroxides (LDHs), fly ash, zeolite and ZIF-8 supported LDHs and ternary LDHs. The crystal structure, surface morphology and functional properties of the as-prepared catalysts are determined using an X-ray diffractometer (XRD), nitrogen adsorption-desorption isotherms (BET), UV-Vis diffuse reflectance spectroscopy (UV-Vis DRS), scanning electron microscopy (SEM) with energy dispersive X-ray analysis (EDX) and X-ray photoelectron spectroscopy (XPS). Dark adsorption capacities and photocatalytic performances of the catalysts are controlled in the presence of methyl orange (MO) anionic dye, methylene blue (MB) cationic dye and salicylic acid (SA). The effect of relative humidity (RH) is also studied for the catalysts prepared in the first and second chapters. Dark kinetic analysis is followed via pseudo-first and pseudo-second order models. Langmuir, Freunlich and Temkin isotherms are employed to determine MO, MB and SA interactions with the catalysts. Pseudo-first order kinetic model and Langmuir-Hinshelwood kinetic analysis are studied for experiments under irradiation.

ÖZET

METAL-ORGANİK KAFES YAPILAR, YUMURTA KABUĞU TÜREVLİ HİDROKSİAPETİT VE ÇİFT KATMANLI HİDROKSİTLERİN ADSORPSİYON VE FOTOKATALİTİK PROSESLERDE DEĞERLENDİRİLMESİ

Bu çalışma, üç ana bölümden oluşmaktadır. Her bölümde, farklı bir katalist grubu sentezlenmiş, karakterizasyon çalışmaları yapılmış ve değerlendirilmiştir.

İlk bölümde TiO_2 ve ZnO eklenmiş metal-organik kafes yapıları (MOF) anlatılmaktadır. Cu-BTC-hidrofilik ve ZIF-8-hidrofobik MOF olarak seçilmiştir. İkinci bölüm, ZnO ve La-ZnO eklenmiş yumurta kabuğu ile ZnO ve La-ZnO eklenmiş yumurta kabuğu türevi hidroksiapatit yapılarından oluşan iki farklı katalist sistemini incelemektedir. Üçüncü kısım, ikili çift katmanlı hidroksitler (LDH), uçucu kül, zeolit ve ZIF-8 destekli LDH ile üçlü LDH yapılarını irdelemiştir. Hazırlanmış olan katalistlerin kristal yapıları, yüzey morfolojileri ve fonksiyonel özellikleri, X-ışını kırınım ölçeri (XRD), nitrojen adsorpsiyon-desorpsiyon izotermi (BET), dağınık yansıtımlı UV-görünür ışık spektroskopisi (UV-Vis DRS), enerji dağılımlı X-ışınları analizi ile taramalı elektron mikroskopu (SEM-EDX) ve X-ışını fotoelektron spektroskopisi kullanılarak belirlenmiştir. Katalistlerin karanlıktaki adsorpsiyon kapasiteleri ve ışık altındaki fotokatalitik performansları, anyonik boyar madde metil oranj (MO), katyonik boyar madde metilen mavisi (MB) ve salisilik asit (SA) varlığında kontrol edilmiştir. Birinci ve ikinci bölümlerde hazırlanmış olan katalistler için ayrıca bağıl nem (RH) etkisi de çalışılmıştır. Karanlıktaki kinetik analizleri, görünür-birinci derece ve görünür-ikinci derece modelleriyle takip edilmiştir. Langmuir, Freundlich ve Temkin izotermleri; MO, MB ve SA maddelerinin, katalistler ile olan etkileşimlerini belirlemek amacıyla tatbik edilmiştir. Işık altında çalışılan fotokatalitik deneyler için görünür-birinci derece kinetik modeli ve Langmuir-Hinshelwood kinetik analizi çalışılmıştır.

TABLE OF CONTENTS

LIST OF FIGURES

LIST OF TABLES

LIST OF SYMBOLS

B_T	Tempkin constant (kJ mol^{-1})
C_0	Initial concentration (mg L^{-1})
C_e	Equilibrium concentration (mg L^{-1})
D	Crystal size
e^-	Electron
E_{bg}	Band gap energy
h	Hour
h^+	Hole
k	Reaction rate constant
k_1	First-order reaction rate constant (min^{-1})
k_2	Second-order reaction rate constant (min^{-1})
K	Adsorption coefficient
K_F	Freundlich adsorption constant (L mg^{-1})
K_L	Langmuir adsorption constant (L mg^{-1})
K_T	Tempkin equilibrium binding constant (L mg^{-1})
M	Molarity
n	Heterogeneity factor
nm	nanometer
q_e	Adsorption capacity at equilibrium (mg g^{-1})
q_t	Adsorption capacity at time (mg g^{-1})
R	Rate
R^2	Linear regression coefficient
R_L	Separation Factor
r_{pore}	Pore radius
t	Reaction time
V_{pore}	Pore volume
wt	Weight
λ	Wavelength
θ	Angle between X-ray radiation

LIST OF ACRONYMS / ABBREVIATIONS

$Al_2O_3.2SiO_3$	Mullite
AOP	Advanced Oxidation Process
BET	Brunauer–Emmett–Teller method
BJH	Barrett, Joyner, and Halenda method
$CaCO_3$	Calcite
CaO	Lime
Cu-BTC	Copper benzene-1,3,5-tricarboxylate
CuO	Copper (II) Oxide
DRS	Diffuse Reflectance Spectroscopy
EDX	Energy Dispersive X-Ray
Fe_2O_3	Hematite
Fe_3O_4	Magnetite
FTIR	Fourier Transform Infrared Spectroscopy
FWHM	Full Width Half Maximum
HAP	Hydroxyapatite
La	Lanthanide
LDHs	Layered Double Hydroxides
LDOs	Layered Double Oxides
L-H	Langmuir Hinshelwood
MB	Methylene Blue
MO	Methyl Orange
MOF	Metal Organic Framework
PL	Photoluminescence Spectroscopy
PNC	Porous Nanocomposite
RH	Relative Humidity
SA	Salicylic Acid
SEM	Scanning Electron Microscopy
SiO_2	Silicon dioxide
TEM	Transmission Electron Microscopy
TiO_2	Titanium dioxide

UV-VIS	Ultra Violet-Visible light
XRD	X–Ray Diffraction
XPS	X-Ray Photoelectron Spectroscopy
ZIF-8	Zeolitic Imidazolate Framework
$Zn(OH)_2$	Zinc hydroxide
ZnO	Zinc oxide

1. INTRODUCTION

Advanced oxidation processes are widely employed as versatile methodologies for the destruction of pollutants. The superiority of AOPs over conventional technologies is the in-situ formation of highly reactive radicals to degrade recalcitrant components into harmless substances discarding a requirement for a secondary treatment stage [1-4].

Among AOPs, heterogeneous photocatalysis stands out as an efficient and promising tool for the degradation of organic contaminants in aqueous phase with key advantages of facile operation at ambient conditions, low-cost and environmentally benign [4]. Heterogeneous photocatalysis does not require any additional reagent beyond a photocatalyst which is defined as a substance activated upon absorbing a photon to accelerate reactions without being consumed. For this activation, the absorbed energy of light must be matched or exceeded the band gap energy (E_g) of the photocatalyst. E_g defines the energy between the highest occupied molecular orbital (HOMO) which is known as the valence band (VB) and the lowest unoccupied molecular orbital (LUMO) which is named as the conduction band (CB) of a photocatalyst [5]. Accordingly, upon irradiation of a photocatalyst by a photon with sufficient energy, an electron is promoted to the CB leaving behind an electronic vacancy, a positive hole in the VB as follows

$$\text{Photocatalyst} + h\nu \rightarrow e^- + h^+. \quad (1.1)$$

This photogenerated e^- and h^+ are prominently powerful to induce reduction and oxidation reactions by migrating to the surface of the photocatalyst [6]. The photogenerated h^+ is capable of direct oxidation of organics into CO_2 and H_2O as final products expressed as

$$h^+ + \text{organic compound} \rightarrow CO_2 + H_2O. \quad (1.2)$$

The alternative reactions of h^+ are with electron donors like water and/or hydroxyl ions to form hydroxyl radical OH as follows

$$h^+ + H_2O \rightarrow OH^\bullet + H^+ \quad (1.3)$$

$$h^+ + OH^- \rightarrow OH^\bullet. \quad (1.4)$$

$OH^\bullet$ radical is a powerful, non-selective oxidant that can oxidize all electron-rich molecules due to its electrophilic nature and high oxidation potential (2.8 eV) [7]. Thus, the produced $OH^\bullet$ radical can be directly responsible for the degradation of organic compounds

Simultaneously, the photoexcited e^- reacts with the surface oxygen (O_2) which is an efficient electron acceptor molecule to generate another strong oxidizing agent [8], superoxide radical ($O_2^{\bullet-}$) that can be written as

$$e^- + O_2 \rightarrow O_2^{\bullet-}. \quad (1.5)$$

The produced $O_2^{\bullet-}$ radical may protonate by forming hydroperoxyl radical ($HO_2^{\bullet}$)

$$O_2^{\bullet-} + H^+ \rightarrow HO_2^{\bullet} \quad (1.6)$$

which subsequently generates hydrogen peroxide (H_2O_2)

$$2HO_2^{\bullet} \rightarrow H_2O_2 + O_2. \quad (1.7)$$

The reaction of H_2O_2 with the $O_2^{\bullet-}$ leads to the formation of more $OH^{\bullet}$ radicals

$$H_2O_2 + O_2^{\bullet} \rightarrow OH^{\bullet} + O_2 + OH^-. \quad (1.8)$$

As an undesirable route, the produced e^- and h^+ can recombine and dissipate the absorbed light energy by releasing heat which is expressed as

$$e^- + h^+ \rightarrow \text{heat}. \quad (1.9)$$

Therefore, migration and trapping of e^- and h^+ by the surface H_2O, OH^- and O_2 is crucial to possess the oxidation-reduction reactions [8]

Among various types of photocatalysts, semiconductor metal oxides are considered the most appropriate materials with convenient electrical properties and band gap energies. TiO_2 and ZnO have received broad interest as semiconductor photocatalysts for the last decades due to their unique optical properties, long-term photostabilities, chemical durabilities, abundant availabilities and low-costs [9]. In the different crystal structures, anatase and wurtzite are regarded as the most photoactive phases of TiO_2 and ZnO, respectively, due to the great hole-trapping abilities and low exciton recombination rates. The band gap energies of both the anatase phase of TiO_2 and the wurtzite phase of ZnO are in between 3-3.3. eV [10]. In the overall structural features of anatase TiO_2 and wurtzite ZnO, the degree of crystallinity plays an important role in their photocatalytic efficiencies through crystalline purities and defects. Besides, crystal size affects the activity of a photocatalyst considering the excitation, trapping and recombination mechanisms of photogenerated species. Thus, the crystalline size determination of a photocatalyst is essential by using Scherrer's equation

$$D = \frac{A\lambda}{FWHM\ \cos\theta} \quad (1.10)$$

where D is the size of the crystal, A is Scherrer's constant, λ is the wavelength, FWHM is the full-width half maximum value of the corresponding diffraction peak and θ is the diffraction peak angle.

In the last decades, many attempts have been devoted to enhance the performance of photocatalysts. Among these, the insertion of additional energy levels into the band gap of a photocatalyst is proposed via the loading of metal ions. This leads to the suppression of the electron-hole recombination by the trapping act of loaded metal ions toward photogenerated electrons [6,11]. Recent studies report that the activities of the photocatalysts can be improved in the presence of rare-earth metals such as La, Gd, Eu, Ce, Dy [12-15]. The cationic rare-earth metals exist in the +3 oxidation state with empty d and f orbitals. The reduction to the +2 oxidation state of these cations is induced by the trapping of a photogenerated electron. If the stabilities of the cations are disturbed by this reduction, the cations tend to return their stable form (+3 oxidation state) by transferring the captured electron to the surface O_2. The reaction of the transferred electron with the O_2 results in the generation of superoxide radicals and hydroxyl radicals. Among the rare-earth metal cations, La^{3+} (with the electronic configuration of [Xe]), has the more vacant d and f orbitals for hosting photoelectrons and a higher tendency to transfer the trapped electron to O_2. Thus, the loading of La^{3+} can prolong the lifetime of charge carriers which eventually enhances the activities of photocatalysts [16-18].

Besides, since the photocatalytic reactions occur on the surface of the photocatalyst, the surface area is a key contributing factor to improve the efficiency of the photocatalyst. At the first stage of photocatalytic reactions, incident light-harvesting by a photocatalyst is a vital process. Then, the photogenerated electron-hole pair migrates to catalyst surface to react with water, oxygen and hydroxyl ions for the formation of active radicals. Thus, a large surface area provides more opportunity for a photocatalyst to contact light and activate the photoreactions. Apart from high photocatalytic activity, a large surface area promotes the adsorption of the target molecules on the photocatalyst surface and creates a synergistic effect for the removal of organic contaminants. Therefore, many strategies have focused to enhance the surface area of the photocatalysts by supporting them with various materials such as clays, activated carbon, zeolite, fly ash and metal-organic frameworks. In addition to the high surface area, the porous nature, inherit cavities and channels, and also layered

constructions of these support materials serve as active sites for the adsorption processes [19-21]. Moreover, the existence of several surface functional groups of these materials enables to the establishment of electrostatic attractions, Lewis acid-base interactions and H-bonding which eventually promotes the adsorption of target molecules under dark conditions.

2. OBJECTIVE AND SCOPE

This study consists of three chapters. In each chapter, a different catalyst group is synthesized, characterized and evaluated.

In the first chapter, hydrophilic-Cu-BTC and hydrophobic-ZIF-8 are selected as support materials from the metal-organic frameworks (MOFs). The effect of TiO_2 and ZnO loading on the Cu-BTC and ZIF-8 are examined in terms of morphological variations, dark adsorption capacities and photoactivity by means of several characterization techniques and kinetic analysis. Methyl orange (MO) and Methylene blue (MB) are used as model compounds. The effect of relative humidity (RH) on the stabilities and performances of the as-synthesized supported catalysts are controlled under different humid conditions.

In the second chapter, eggshell and eggshell-derived hydroxyapatite (HAP) are prepared as support materials. Their structural characterization, dark adsorption ability and photoactivity are investigated before and after ZnO and La-ZnO loading. Photocatalytic measurements and detailed kinetic evaluations are followed in the presence of MO and MB. 84% RH condition and stabilities are also controlled for all as-prepared catalysts.

In the third chapter, layered double hydroxides and oxides (LDHs, LDOs), and their fly ash, zeolite and ZIF-8-supported forms are synthesized, characterized and examined. This chapter has four sections. Binary, fly ash and zeolite-supported binary LDHs-LDOs are reported in the first, second and third sections, respectively. Ternary and ZIF-8-supported ternary LDHs-LDOs are reported in the fourth section. The binary LDHs are prepared from a combination of divalent and trivalent metal cations while the ternary forms include a mixture of co-existing divalent cations with trivalent cations. After structural determinations, the materials are studied in terms of dark adsorption capacities, photocatalytic performances, kinetic analysis and stabilities for MO, MB and salicylic acid (SA) degradations.

This study promises to pave new insights into the development of novel catalysts for adsorption and photocatalytic applications.

3. CU-BTC AND ZIF-8 SUPPORTED CATALYSTS

3.1. The Effect of ZnO or TiO_2 Loaded Nanoparticles on the Adsorption and Photocatalytic Performance of Cu-BTC and ZIF-8 MOFs

This section is published as: A.N. Ökte, D. Karamanis, E. Chalkia, D. Tuncel "The effect of ZnO or TiO_2 loaded nanoparticles on the adsorption and photocatalytic performance of Cu-BTC and ZIF-8 MOFs" *Materials Chemistry and Physics*, Vol. 187, pp 5-10, 2017. This copyrighted article is reproduced with permission from Elsevier (Figure B.1).

3.1.1. Introduction

Semiconductor photocatalysis is an important technique considering the degradation of organic pollutants. ZnO and TiO_2 are extensively used semiconductors in photocatalytic systems owing to their complementary physicochemical properties, low cost and non-toxicity [22, 23]. However, the tendency to agglomerate in suspension systems as a result of the small particle size and poor adsorption capacity by virtue of the non-porous structure makes their utilization difficult. To defeat these restrictions, much effort has been devoted to the treatment of the photocatalysts with porous supporting materials. Metal-organic frameworks (MOFs) and zeolitic imidazolate frameworks (ZIFs) are relatively new classes of porous materials formed by two major parts; the inorganic connectors and the organic linkers. The particular interest in MOFs is the easy tuning of their pore size from the micro to meso scale by changing the nature of the inorganic part and the organic linkers as well as the connectivity [24–26]. One of the most cited MOFs, Cu-BTC, is composed of metal coordination polymers having Cu acting as joints and benzene-1,3,5-tricarboxylate (BTC) ligand. The arrangement of Cu (II) ion with four oxygens from BTC linkers and water molecules promotes a vacancy in the framework [27]. Zeolitic imidazolate frameworks (ZIFs), a subfamily of MOFs, not only exhibit the chemical functionality of classical MOFs, but also represent zeolitic structural characteristics [28]. Among them, ZIF-8 with tetrahedrally coordinated Zn metal ion connected by organic imidazole ligands, shows high thermal and chemical stability in view of the angles between metal-imidazole-metal units

like Si-O-Si in zeolites [29]. These attractive features of Cu-BTC and ZIF-8 extended their application areas to hydrogen storage [30], CO_2 adsorption [31, 32], purification of harmful gases [33], liquid phase separation [34, 35] and dye adsorption processes [36]. Recent research has focused on semiconductor-MOFs heterostructures in photocatalytic degradation systems, but studies on the synergistic effect of TiO_2 and ZnO with Cu-BTC and ZIF-8 are still limited [37, 38].

Thus, the objective of the present work is to synthesize binary photocatalytic composites (ZnO-Cu-BTC, TiO_2-Cu-BTC, ZnO-ZIF-8 and TiO_2-ZIF-8) and examine their structures by means of X-ray diffraction technique (XRD) and scanning electron microscopy with energy dispersive analysis (SEM-EDX) and elemental mapping. Ultimately, the adsorption capacity and photocatalytic performance of the as-prepared composites are investigated during the decolorization processes of an anionic dye (methyl orange (MO)) and a cationic dye (methylene blue (MB)).

3.1.2. Experimental

3.1.2.1. Materials. Cu-BTC (Sigma-Aldrich) and ZIF-8 (Sigma-Aldrich) were used as support materials. Zinc nitrate hexahydrate ($Zn(NO_3)_2.6H_2O$) (99.0%, Merck), sodium carbonate (Na_2CO_3) (Merck), titanium tetraisopropoxide (98%, Aldrich), acetic acid (96%, Merck), methyl orange (Merck), methylene blue (Merck) were used as provided by the suppliers without further purification. Deionized water, purified with an Elga-Pure Water Purification (UHQ II) system, was used for preparing the solutions in the experiments.

3.1.2.2. Materials Synthesis. 0.25M ZnO was prepared by a coprecipitation method using 0.25M $Zn(NO_3)_2.6H_2O$ and 0.25M Na_2CO_3 precursors [39]. Briefly, 100 mL of $Zn(NO_3)_2.6H_2O$ were slowly added into vigorously stirred 100 mL of Na_2CO_3 solution. The resulting white suspension was agitated for 2 h at room temperature. The binary composites were prepared with the addition of 2 g Cu-BTC or ZIF-8 supports into the ZnO solutions. After stirring the mixed suspension for about 12h, several washings and centrifugations (at 4000 rpm) were applied. The resulting composites were dried at 100˚C for 12h, calcined in muffle furnace at 500˚C for 5h and named as 0.25M ZnO-Cu-BTC and 0.25M ZnO-ZIF-8.

25% TiO_2 was prepared by a sol-gel method using titanium tetraisopropoxide and acetic acid precursors [40]. Details of the methods explored in the previous studies [1,21]. Briefly, 20 mL of titanium tetraisopropoxide was gradually added to 80 wt % acetic acid solution under continuous stirring for 2 h at 50°C to produce a transparent sol. For the composites, requisite amount of titania-sol was added to the aqueous suspension of the Cu-BTC or ZIF-8. The resulting material was dried at 100°C for 12 h and then, calcined at 500°C for 5 h. Finally, the composites were ground into fine powder, stored in dark and named as 25% TiO_2-Cu-BTC and 25% TiO_2-ZIF-8.

3.1.2.3. Materials Characterization. The X-ray diffraction (XRD) patterns were recorded on a Rigaku-D/MAX-Ultima diffractometer using Cu-Kα radiation (λ=1.54°A) operating at 40 kV and 40 mA and a scanning rate of 2 min^{-1}. Scanning electron microscopy (SEM) in combination with energy dispersive X-ray analysis was done using an ESEM-FEG/EDAX Philips XL-30 instrument operating at 20 kV.

3.1.2.4. Photocatalytic Experiments. For the photocatalytic experiments, eight black-light-fluorescent lamps (Philips TL15W/5BLB) with an emission maximum of 365 nm were used in a laboratory-constructed box. Prior to illumination, 100 mL dye solutions (MO (3.27 mgL^{-1}) and MB (2.90 mgL^{-1})) were mixed with the composites (0.1 g) for 30 min to ensure the dark adsorption equilibrium. After irradiation, MO solutions were filtered via a Millipore filter and MB solutions were centrifuged before the analysis. UV-vis spectrophotometer (UV-2450, Shimadzu) was used to monitor the absorbance spectra of MO at 464 nm and MB at 664 nm as a function of irradiation time. All experiments were performed at room temperature and at pH=6.0 without concerning the degradation intermediates.

3.1.3. Results and Discussion

3.1.3.1. XRD Analysis. XRD patterns of ZIF8, Cu-BTC and the supported catalysts are shown at both low-angle ($2\theta < 10^o$) and high-angle ($20^o < 2\theta < 60^o$) ranges (Figure 3.1). ZIF-8 spectrum reveals the typical zeolite patterns with d 011, d 002, d 112, d 222 reflections at 7.5, 10.4, 12.7, 18.4°, respectively (Figure 3.1a) [41]. Intensities of these peaks decrease with calcination (ZIF-8 500°C) and diffraction peaks indexed to d 100, d 002, d 101, d 102, d 110,

d 103 and d 200 crystal planes of ZnO develop at 31.9, 34.6, 36.4, 47.7, 56.7, 63.1 and 66.6° (2θ), respectively. ZIF-8 peaks almost disappear with the addition of catalyst nanoparticles. The crystalline wurtzite ZnO structure appears in the pattern of 0.25M ZnO-ZIF-8, while 25% TiO_2-ZIF-8 shows anatase diffractions of d 101, d 200, d 105 and d 211 at 25.4, 48.2, 54.2 and 55.3° (2θ), respectively.

The Cu-BTC exhibits the characteristic diffraction peaks of d 200, d 222, d 400, d 440 at 6.7, 11.6, 13.5, 19.6^o (2θ), respectively (Figure 3.1b) [42]. CuO and Cu_2O peaks are not observed at 38.7 and 36.4^o. Similar to the ZIF-8 composites, 0.25M ZnO-Cu-BTC and 25% TiO_2-Cu-BTC reveal ZnO and anatase reflections. The representative ZnO and TiO_2 peaks are intensified within the Cu-BTC framework, indicating stronger interactions of catalyst nanoparticles with the Cu-BTC structure.

The crystalline sizes of ZnO and TiO_2 nanoparticles are calculated using Scherrer's equation for the broadening of (101) ZnO and (101) anatase peak reflections. The ZnO sizes are found as 16 nm (for 0.25 M ZnO), 23.8 nm (for 0.25M ZnO-Cu-BTC) and 26.6 nm (for 0.25M ZnO-ZIF-8). The TiO_2 sizes are evaluated as 18 nm (for 25% TiO_2), 21.1 nm (for 25% TiO_2-Cu-BTC) and 28.6 nm (for 25% TiO_2-ZIF-8). The increment in the sizes points out that support materials enhance the crystalline formation of ZnO and TiO_2 nanoparticles in the composite structures.

3.1.3.2. SEM-Mapping Analysis. SEM image of the Cu-BTC reveals truncated-octahedral-shaped particles with Cu (11.1%), C (65.7%) and O (23.3%) constituents (Figure 3.2a). The bean-shaped nanoparticles of the 0.25M ZnO-Cu-BTC involve Zn (36.1%) and C (28.4%) as major components, with well-dispersed ZnO nanoparticles (Figure 3.2b and c). The reduction in the carbon percentage indicates that ZnO nanoparticles mostly exist on the organic parts of Cu-BTC. 25% TiO_2-Cu-BTC exhibits irregularly distributed agglomerates with a high Ti percentage (65.5%) (Figure 3.2d and e). The ZIF-8 demonstrates rhombic-shaped particles as also noticed in the previous studies [43, 44] (Figure 2.2f). 0.25M ZnO-ZIF-8 morphology differs with the formation of spherical ZnO nanoparticles and their concentrated appearance in the mapping image (Figure 3.2g and h). The non-shaped domains are also detected in the image of 25% TiO_2-ZIF-8 with dominating Ti signals over the whole surface (Figure 3.2.i and j).

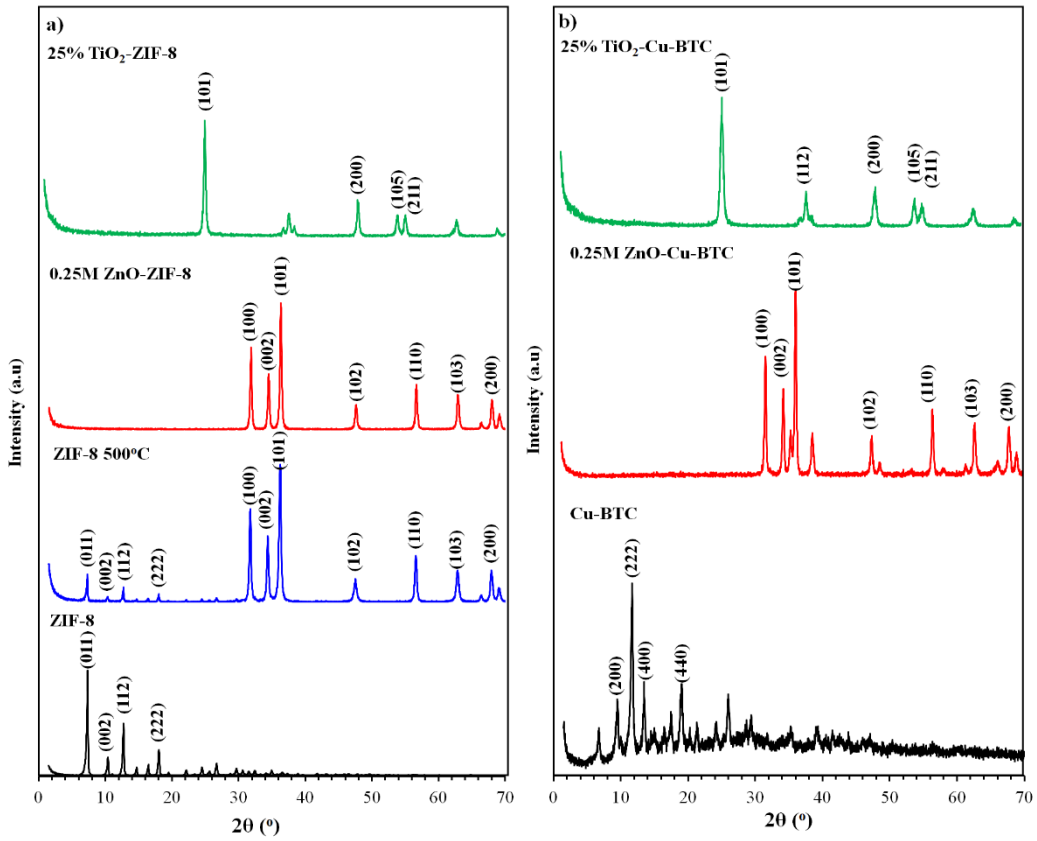

Figure 3.1. XRD patterns of (a) ZIF-8, ZIF-8 500ºC, 0.25M ZnO-ZIF-8, 25% TiO_2-ZIF-8, (b) Cu-BTC, 0.25M ZnO-Cu-BTC, 25% TiO_2-Cu-BTC.

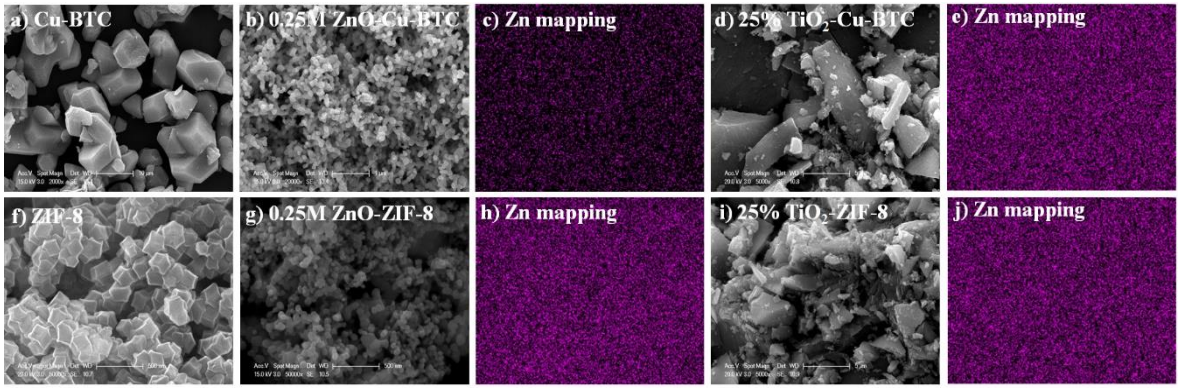

Figure 3.2. SEM images of (a) Cu-BTC, (b) 0.25M ZnO-Cu-BTC, (d) 25% TiO_2-Cu-BTC, (f) ZIF-8, (g) 0.25M ZnO-ZIF-8 and (i) 25% TiO_2-ZIF-8. Zn mapping of (c) 0.25M ZnO-Cu-BTC and (h) 0.25M ZnO-ZIF-8. Ti mapping of (e) TiO_2-Cu-BTC and (j) 25% TiO_2-ZIF-8.

3.1.3.3. Adsorption and Photocatalytic Tests. In the dark, the lowest MB remaining percentage (14.1%) is obtained in the presence of the Cu-BTC (Figure 3.3a). The dominance of negative charges through ligand groups in the Cu-BTC structure was theoretically proved [45]. Moreover, the surface charge of Cu-BTC was found to be more negative for pH values greater than 4.0 [36]. Thus, the interaction established between the Cu-BTC and MB can be through the ligands in the Cu-BTC structure and C–S+=C functional groups of MB. In addition, π–π interactions of the benzene rings and hydrogen bonding may promote the attractive forces between the Cu-BTC and MB [45, 46]. However, the existence of ZnO or TiO_2 nanoparticles on the surface of the Cu-BTC seems to limit these interactions and decrease MB adsorption. Contrarily, MO and Cu-BTC interaction is weaker due to the repulsive forces induced among the ligand-oxide groups of the Cu-BTC and the sulphonyl group of MO [36, 45]. Thus, Cu-BTC and its composites show a lower adsorption tendency to MO.

Photolysis of both MB and MO are weak and negligible (Figure 3.3b). Under irradiation, lower percentages of MO and MB are detected in the presence of Cu-BTC in comparison to that noticed during the photolysis reactions. The higher dark adsorption tendency of Cu-BTC for MB decreases its remaining percentage more than that for MO. Upon light excitation, organic linkers absorb light and then transfer the charge carriers to the central metal clusters, known as the antenna behavior of these linkers in several MOF structures [47]. Accordingly, the transfer of electrons to Cu clusters is expected via the excitation of Cu-BTC ligands for the reduction of Cu (II) into Cu (I) during the irradiation processes. Duke et al. followed the conversion of Cu (II) to Cu (I) by an XPS analysis in copper-based metal organic frameworks exposed to irradiation [48]. Such electron transfer restrains the recombination of electrons and holes and thereby initiates the degradation routes via holes with the generation of free radicals.

In the meantime, the strong interaction is restricted among the Cu-BTC moiety and MB under irradiation. The electron trade created between the linkers and the Cu clusters may disturb the conjugation within the linkers, damage the π-π interactions of the benzene rings and thus reduce the attractive forces between the Cu-BTC and MB under irradiation. This point out the difference between the dark adsorption capability and photodegradation performance of Cu-BTC through MB.

The Cu-BTC supported composites, however, reveal higher photocatalytic performances (Figure 3.3b). After 100 min irradiation, the remaining percentages of MB in solution are found as 6.9% (for 0.25 ZnO-Cu-BTC), 11.8% (for 25% TiO_2-Cu-BTC), whereas 14.1% MO and 36.4% MO are detected in the presence of 0.25 ZnO-Cu-BTC and 25% TiO_2-Cu-BTC, respectively.

In the dark, MO adsorption on the ZIF8 structure is much higher than that for MB (Figure 3.3c). The surface charge of ZIF-8 remains positive at pH values below 10 [49]. Since experiments in this study are carried out at pH around 6.0, a strong electrostatic interaction occurs between the positively charged ZIF-8 surface and negatively charged MO. The existence of Zn^{2+} ions within the ZIF-8 framework supports this attraction. However, a repulsive interaction is noticed between ZIF-8 and MB, which results in only 20% MB adsorptive removal in the dark after 100 min. A similar removal percentage (30%) for MB was obtained in the presence of ZIF-8 during the dark experiments in the study of Jing et al. [50]. In the ZIF-8 (500°C), the formation of ZnO (verified by the XRD analysis) increases the negative charges in the zeolitic frame. Surface oxygens in ZnO and TiO_2 structures were found to be responsible for these negative charges as also reported in the studies of Wang et al. and Houas et al., respectively [51, 52]. The C–S+=C functional groups of MB makes Lewis interactions with ZnO and improves the adsorption of MB in the presence of ZIF8 (500°C). Similarly, upon ZnO loading, the adsorption capacity of 0.25M ZnO-ZIF-8 decreases toward MO while that for MB increases. The 25% TiO_2-ZIF-8 does not reveal significant adsorption for both dyes due to the surface coverage of the composite with TiO_2 nanoparticles.

Under irradiation, ZIF-8 demonstrates a lower performance for MB and a higher decolorization percentage for MO, agreeing with its dark adsorption capacity towards MB and MO (Figure 3.3d). This result also signifies the photoactivity of ZIF-8 in the absence of catalysts, owing to the formation of charge carriers in the excited ZIF-8 [50]. On the other hand, ZIF8 (500°C) possesses lower activities for both dyes in comparison to ZIF-8. The calcination process may create defect sites, promote recombination of the charge carriers and decrease their individual contact with the MO and MB. ZnO loading accelerates the photocatalytic performance of ZIF-8. The best activity is obtained in the presence of 0.25M ZnO-ZIF-8 with MB (11.7%) and MO (3.3%) remaining percentages after 100 min

irradiation. This may be attributed to the enhancement in the crystalline formation of ZnO by the presence of Zn^{2+} metal ions in the ZIF-8 matrix. In the existence of 25% TiO_2-ZIF-8, the remaining MB and MO percentages in the solution are found as 16.6% and 29.1%, respectively. The difference in the dark adsorption capacities of ZIF-8 (not calcined) and of 25% TiO_2-ZIF-8 for MO explores the variations in their photoactivities. Under irradiation, the charge transfer reactions are accelerated via the enhanced electrostatic attraction between ZIF-8 and anionic MO. This creates a fast decrement in the remaining MO percentage within 20 min and thereafter no variation is noticed. However, TiO_2 loading decreases the availability of surface sites on the ZIF-8 through MO. This lowers the photocatalytic performance of 25% TiO_2-ZIF-8 in comparison to the activity of ZIF-8 alone.

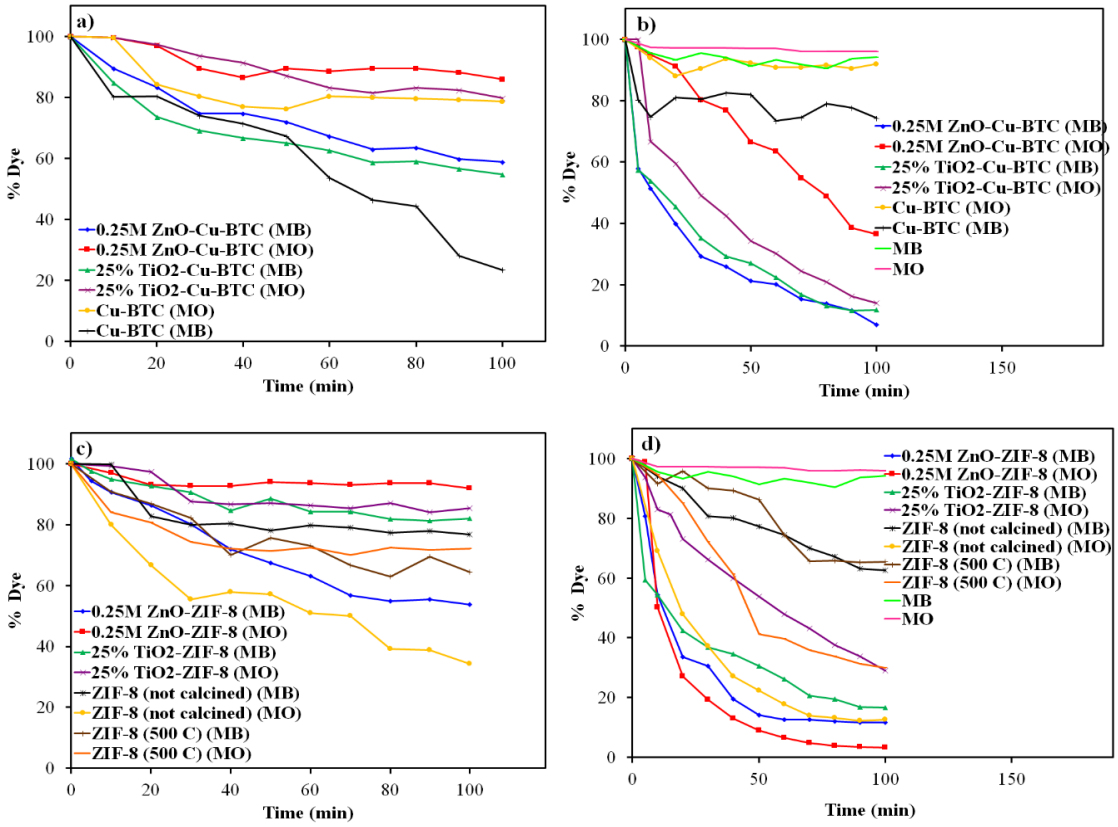

Figure 3.3. Cu-BTC and Cu-BTC supported composites (a) dark adsorption studies, (b) irradiation experiments, ZIF-8 (500^oC), ZIF-8 supported composites (c) dark adsorption studies, (d) irradiation experiments.

3.1.4. Conclusion

The supported nanocomposites have been synthesized by loading TiO_2 or ZnO photocatalysts on the surface of the Cu-BTC and ZIF-8. Characterization studies confirm the presence of well-distributed ZnO or TiO_2 nanoparticles on the composites. The electrostatic interactions and/or existence of functional groups within the supports and dye molecules induce differences in the dark adsorption capacities of the composites through MB and MO. Cu-BTC based composites show higher dark adsorption abilities and hence, higher degradation efficiencies toward MB. The already existing Zn^{2+} ions and ZnO addition enhance the photoactivity of 0.25M ZnO-ZIF-8 for both MB and MO. Thus, the promising performances of the composites may widen their potential applications via bifunctional properties with photocatalytic activity in addition to adsorption capability.

3.2. Efficient Photoactivity of TiO_2-Hybrid-Porous Nanocomposite: Effect of Humidity

This section is published as: D. Tuncel, A.N. Ökte, "Efficient Photoactivity of TiO_2-Hybrid-Porous Nanocomposite: Effect of Humidity", *Applied Surface Science*, Vol. 458, pp. 546-554, 2018. This copyrighted article is reproduced with permission from Elsevier (Figure B.2).

3.2.1. Introduction

Heterogeneous photocatalysis based on the usage of semiconductors is a significant route to degrade complex organic pollutants into non-toxic compounds (CO_2, H_2O etc.). In general, irradiation of a semiconductor with photons of energy higher than or equal to its band gap energy, excites the electron from the valence band to the conduction band of the semiconductor. The formation of the electron-hole pair is accomplished by leaving behind an empty hole of the photo-excited electron on the valence band. This photogenerated electron induces the reduction reactions by reducing the dye or reacting with electron acceptors such as ambient O_2 to give superoxide radical anion $O_2^{\bullet-}$. Besides, the

photogenerated hole (h^+) is directly able to oxidize the organic molecules or react with ambient OH^- or H_2O oxidizing them into $OH^\bullet$ radicals [53, 54]. The resulting $OH^\bullet$ radical as a very strong oxidizing agent can transform most toxic components into unhazardous end-products. In view of the mechanism, two main factors play a crucial role in the determination of the photocatalytic performance of the materials: separation of photogenerated carriers and adsorption of the target molecule. Hence, recent studies have focused on the usage of porous-high surface area support materials. The hybrid nanocomposites of TiO_2 supported systems are considered as novel heterostructures with varied surface properties. The synergy established in these structures combines the advantages of the components owing to the physical and chemical interactions.

Song et al. studied SiO_2/TiO_2 materials, prepared via a sol-gel method [55]. The resulting hybrid forms were characterized by several techniques and then evaluated under UV irradiation for the photocatalytic degradation of methylene blue. The XRD spectra of the samples were controlled at different temperatures. Before heat treatment, amorphous TiO_2 nanoparticles were noticed. Increment in calcination temperature to 550°C resulted in the formation of anatase crystals and disappreance of silica peaks. The photocatalytic activity of the hybrid materials was found to be higher than TiO_2 (P-25) for the degradation of methylene blue. Zhao et al. fabricated Ag modified hollow SiO_2/TiO_2 hybrid spheres via hydrothermal synthesis [56]. Only anatase-TiO_2 crystallized peaks were detected in SiO_2/TiO_2. Ag doped SiO_2/TiO_2 showed Ag diffractions in addition to the anatase peaks. Although crystalline form of SiO_2 was not observed in the XRD patterns of the hybrid materials, they possessed mesoporous structures. The lower BET surface areas in comparison to that of hallow SiO_2 spheres indicated occupation of the pores by TiO_2 and Ag species. Moreover, hybrid materials showed an enhanced photocatalytic performance for the degradation of RhB under UV and visible light irradiation. In the study of He et al., graphene was used as a platform for TiO_2 deposition due to its large surface area [57]. The mostly identified XRD peaks in graphene supported TiO_2 hybrid sheets indexed to anatase. The little shoulder to overlapping the anatase (200) peak contributed to stacked graphene sheets. Nitrogen isotherm adsorption-desorption measurements verified type IV isotherms of characteristic mesoporous materials. The dark adsorption capacity of the hybrid structure for 1.9-dimethyl MB was much higher than that of P-25 and the material prepared in the absence of graphene. The porous nature of the hybrid frame facilitated this adsorption and also

inhibited the aggregation of graphene. This further enhanced the degradation ability via electron-hole separation at TiO_2/graphene interface. TiO_2 nanoparticles supported on natural zeolite were characterized and then examined for adsorption and photocatalytic ability [58]. The characteristic stellerite and quartz peaks of the raw zeolite disappeared with increasing calcination temperature. High calcination up to 500°C was required for the crystallinity of TiO_2. Up to and above 500°C, no rutile or rutile/anatase mixed phase was noticed, suggesting stability of anatase TiO_2 particles on the zeolite surface. This was also evidenced by SEM and TEM images. Hysteresis loops detected in the presence of TiO_2 supported zeolites indicated formation of a mesoporous structure. Adsorption capacity of the as-prepared catalysts were examined for Cr (VI) adsorption. The supported catalyst at 500°C showed the highest adsorption capacity and the highest removal efficiency for the photocatalytic reduction of Cr (VI). This was attributed to the formation of better TiO_2 crystals and high surface area. In another TiO_2/zeolite study, loose of stellerite peaks was also observed, indicating destruction of the zeolitic framework [59]. The peaks in the XRD patterns were well indexed to anatase TiO_2. TiO_2/zeolite also possessed high surface area and pore volume in comparison to raw zeolite. SEM, TEM and XPS analysis confirmed formation of TiO_2 in the resultant composites. The enhanced adsorption capacities and photoactivities for the model compounds were attributed to high surface areas of TiO_2/zeolite structures.

Metal-organic frameworks (MOFs) are porous crystalline frameworks possessing high surface areas and well-ordered pore size. Notably, combination of MOF species and semiconductor nanoparticles could perform promising photocatalytic behavior by inhibiting recombination of photoexcited electron-hole pairs under light irradiation. A recent study used $ZnFe_2O_4$/ZIF-8 as precursor to fabricate mesoporous $ZnFe_2O_4$//ZnO nanocomposites [60]. After characterization details, the $ZnFe_2O_4$/ZnO hybrids possessed high surface area, high pore volume and showed an enhanced photoactivity for RhB degradation. The photogenerated electron-hole recombination was successfully inhibited by heterojunction structure between $ZnFe_2O_4$ and ZnO the pairs.

The hybrid frame facilitated adsorption of RhB and enhanced its photocatalytic degradation under UV illumination. Integration of TiO_2 on $Cu_3(BTC)_2$ was studied by Li et al [61]. XRD and EDS analysis confirmed formation of a hybrid structure between anatase TiO_2 and $Cu_3(BTC)_2$. The surface area of $Cu_3(BTC)_2$ was found to decrease after TiO_2

coating. Also, the hybrid structures inherited the octahedral profile from the $Cu_3(BTC)_2$ and had a relatively rough surface. The hybrid material was efficiently used for the photocatalytic conversion of CO_2 into CH_4 under UV illumination. The ultrafast transient analysis showed that the photoexcited electrons were transferred from TiO_2 to $Cu_3(BTC)_2$ and CO_2 can adsorb on the Cu sites during CO_2 uptake. They proposed that CO_2 reduction took place on the Cu sites of the $Cu_3(BTC)_2$ while the oxidation occurs on the TiO_2. HKUST-1@TiO_2 core-shell structure was investigated in terms of isopropanol oxidation [62]. Detection of anatase peaks in the XRD analysis signified growth of TiO_2 in the HKUST-1@TiO_2 composite. TiO_2 loaded on the surface of HKUST-1 resulted in reduced surface area of the composites. In SEM images, TiO_2 was uniformly distributed on the HKUST-1, enabling formation of a rough surface. It was found that complete degradation of isopropanol was possible in the presence of HKUST-1@TiO_2. Since photogenerated electrons can be effectively transferred from TiO_2 to HKUST-1, photogenerated holes accumulate on the TiO_2 surface and enhance the oxidation of isopropanol. In our previous work, the binary photocatalytic composites were synthesized by loading of TiO_2 and ZnO nanoparticles on the surface of Cu-BTC and ZIF-8 [63]. The XRD and SEM tests confirmed the distribution of the TiO_2 and ZnO photocatalysts on the support materials. The adsorption capacities and photocatalytic performances of the composites were examined for the degradation reactions of an anionic dye (methyl orange-MO) and cationic organic dye (methylene blue-MB). The results displayed that the electrostatic interactions played crucial role for the adsorption and photoactivity processes.

In this study, we extend our results to examine TiO_2-hybrid-porous nanocomposite (TiO_2-hybrid-PNC) in detail for both characterization and photoactivity measurements. TiO_2-hybrid-PNC is formed by using Cu-BTC as the supporting adsorptive porous material and TiO_2 as the photoactive material. The coupling of TiO_2 nanoparticles with Cu-BTC combining their advantages that are not readily achieved by the individual components. Although high temperature preparation conditions have an adverse effect on the ordered structure of the MOF based materials, the resultant hybrid structure serves a porous network to provide more space for TiO_2 nanoparticles, as also explored in previous hybrid composite studies [55–57]. This simultaneously improve the adsorption of probe molecule-methyl orange (MO) via electronic interactions. The structural features of the Cu-BTC and TiO_2-hybrid-PNC are followed by X-ray diffraction (XRD) analysis, scanning electron

microscopy (SEM) with energy dispersive X-ray (EDX and mapping) analysis, nitrogen adsorption-desorption isotherms (BET), X-ray photoelectron spectroscopy (XPS) and UV-Vis diffuse reflectance spectra (UV-Vis DRS). Photocatalytic degradation of MO is controlled in the existence of Cu-BTC and TiO_2-hybrid-PNC under UV irradiation.

Moreover, water vapor always exists in ambient conditions and hence, effect of water vapor on the photocatalytic performances of the as-prepared hybrid-porous-nanocomposite has been of much interest. It is well known that one of the most important paths for the photocatalytic degradation is production of OH radicals via interaction of water molecules with holes created in the photocatalyst upon light irradiation. Therefore, it can be suggested that humidity plays a positive role for the photocatalytic efficiency. Based on this consideration, dark adsorption capacities and photoactivities of Cu-BTC and TiO_2-hybrid-PNC are examined under different humidified values. To the best of our knowledge, this is the first-time demonstration of TiO_2-hybrid-PNC for simultaneous water adsorption and MO-photocatalytic degradation. It is highlighted that TiO_2-hybrid-PNC after exposure to high humid conditions improves its dark adsorption ability and photocatalytic activity. TiO_2-hybrid-PNC and TiO_2-hybrid-PNC (84% RH) are controlled at different initial MO concentrations following the pseudo-first order kinetics and Langmuir-Hinshelwood model. Stabilities of the TiO_2-hybrid-PNC and TiO_2-hybrid-PNC (84% RH) are maintained after 4-cycles.

3.2.2. Experimental

3.2.2.1. Materials. Cu-BTC (Sigma-Aldrich) is used as support material. It exhibits the truncated octahedral crystals with the Cu (11.1%), C (65.7%) and O (23.3%) constituents. Titanium tetraisopropoxide (98%, Aldrich), acetic acid (96%, Merck) and methyl orange (Merck) are used as provided by the suppliers without further purification.

3.2.2.2. Catalyst Preparation. The nanocrystalline TiO_2 powder is prepared from the precursors of titanium tetraisopropoxide ($Ti(OC_3H_7)_4$) and acetic acid (CH_3COOH) via sol-gel synthesis [64]. Briefly, a transparent sol of titania is obtained by gradual addition of 80 wt% acetic acid into 20 mL of titanium tetraisopropoxide at 50°C for 2 h. Requisite amount of titania-sol is then added to the aqueous suspension of the Cu-BTC. After agitation and

extensive washings, the precipitate is dried at 100^0C for 12 h and then calcined 500°C with a heating rate of 10^0 C min^{-1} for 6 h. The TiO_2 loading amount is 25% (the mass ratio of TiO_2 to Cu-BTC). The hybrid porous nanocatalyst obtained is named as TiO_2-hybrid-PNC. For comparison, TiO_2 is prepared following the above procedure in the absence of Cu-BTC.

3.2.2.3. Characterization Techniques. XRD patterns of the Cu-BTC and the TiO_2-hybrid-PNC are obtained with Rigaku-D/MAX Ultima diffractometer with Cu Kα radiation (λ =1.54 Å) operating at 40 kV and 40 mA and scanning rate 2 min^{-1}. The BET (Brunauner–Emmet–Teller) isotherms are obtained at liquid nitrogen temperature 77 K by using Quantachrome Nova 2200e automated gas adsorption system. The specific surface areas are determined using multi-point BET analysis and the pores sizes are measured by the BJH method of adsorption. The surface morphologies of the Cu-BTC and nanocomposite are determined using SEM in combination with EDX analysis on an ESEM-FEG/EDAX Philips XL-30 instrument operating at 20 kV using the catalyst powders supported on carbon tape. For the investigation of chemical states of the surface constituents, X-ray photoelectron spectroscopy (XPS) tests are carried out by using Thermo Scientific K-Alpha X-ray Photoelectron Spectrometer equipped with hemispherical electron analyzer and Al-K micro-focused monochrometer. The UV-Vis DRS of the materials are recorded on a Shimadzu UV-2450, equipped with an integrating sphere reflectance accessory. The baseline correction is done by $BaSO_4$. Efficiency of charge carrier trapping is examined with photoluminescence spectroscopy (PL) by using Cary eclipse fluorescence spectrophotometer equipped with a xenon discharge lamp as the excitation source.

3.2.2.4. Water Vapor Adsorption Measurements. Water vapor adsorption on the Cu-BTC and the TiO_2-hybrid-PNC is examined under 40%, 67% and 84% relative humidity (RH) values. Prior to the measurements, the samples are dried at 1000C. Then, 0.4 g of the samples are placed in desiccators. The required value of RH is achieved by balancing the varied saturated salt solutions at 250C via TFA Dostmann/Wertheim sensor housed inside the desiccators. Weight of samples are controlled for the uptake of water after 72 h. Humidified samples are named as Cu-BTC (40% RH), Cu-BTC (67% RH), Cu-BTC (84% RH), TiO2-hybrid-PNC (40% RH), TiO2-hybrid-PNC (67% RH) and TiO2-hybrid-PNC (84% RH). The amount of the adsorbed water is calculated by using the following equation:

$$W = \frac{m_h - m_d}{m_h} \quad (2.1)$$

where m_h is the weight of the humidified sample (g) and m_d is the weight of dry sample (g).

3.2.2.5. Photocatalytic Tests. Photocatalytic performances of the Cu-BTC, TiO_2-hybrid-PNC and humidified samples are examined in a laboratory constructed irradiation box. Eight black fluorescent lamps (Philips TL 15 W/5 BLB) of 320-440 nm are used as irradiation sources placed at two-sides of the box. The incident photon flux for all lamps is measured as 4.7 $x10^{15}$ photon/s using potassium ferrioxalate ectinometer in our previous experiments. A pyrex flask is used for 0.2 g of catalysts within 200 mL of MO solution. Prior to illumination, suspensions are magnetically stirred in the dark for 30 min. Aliquots (about 5 mL) are retrieved from the flask at certain time intervals and analyzed after filtering through Millipore filter (0.45 μm). UV-Vis Spectrophotometer (Shimadzu 2450) is used to monitor the absorbance spectra of MO as a function of irradiation time. Decolorization rate of MO is followed by the decrement in the absorbance peak at 464 nm.

3.2.3. Results and Discussion

3.2.3.1. XRD Analysis. XRD is used to determine crystal structures of Cu-BTC, TiO_2-hybrid-PNC and humidified samples (Figure 3.4). The typical pattern of Cu-BTC is composed of (200), (222), (400), (440) planes corresponding to 6.7, 11.6, 13.5, 19.6° (2θ) values, respectively, following MDI-JADE6 library (Figure 3.4a). TiO_2-hybrid-PNC contains a number of peaks that can be well indexed to anatase TiO_2 with planes of (101), (103), (200) and (105) at 25.4, 37.5, 48.6 and 54.75° (2θ), respectively. The anatase TiO_2 has sharp peaks, indicating high crystallinity. The rutile peak (2θ=27.4°) is not observed due to the ceasing of phase transition during formation of the hybrid structure. Diffraction peaks of Cu-BTC almost do not exist in the pattern of TiO_2-hybrid-PNC. This can be explained by the preparation procedure that destroys the crystalline framework of Cu-BTC, as observed in other hybrid composite studies [55–57]. Also, CuO (at 38.7°) and Cu_2O (at 36.4°) are not detected in the patterns of both Cu-BTC and TiO_2-hybrid-PNC.

Scherrer's equation is applied to calculate TiO_2 crystalline sizes through the reference of main (101) diffraction. TiO_2 nanoparticles are evaluated with 16.2 nm size. An enlargement in the size of TiO_2 nanoparticles (26.2 nm) is found in the presence of TiO_2-hybrid-PNC. Humidified Cu-BTC samples exist in a different environment which causes

reorganization of the frame and results in extra peaks at 8.2, 17.1 and 27.2° (2θ) (67% RH-Figure 3.4b). However, these peaks disappear under 84% RH, indicating completion of structural distortion upon extended exposure as also observed in the study of Al-Janabi et al. [65]. Humidified TiO_2-hybrid-PNC samples also reveal anatase signals, with similar crystalline sizes (21.8 nm for TiO_2-hybrid-PNC (40% RH), 21.4 nm for TiO_2-hybrid-PNC (67% RH) and 20.9 nm for TiO_2-hybrid-PNC (84% RH)) (Figure 3.4b). The slight reduction in the crystalline sizes in comparison to that calculated for TiO_2-hybrid-PNC can be due to the formation of a consolidated environment in the existence of water clusters.

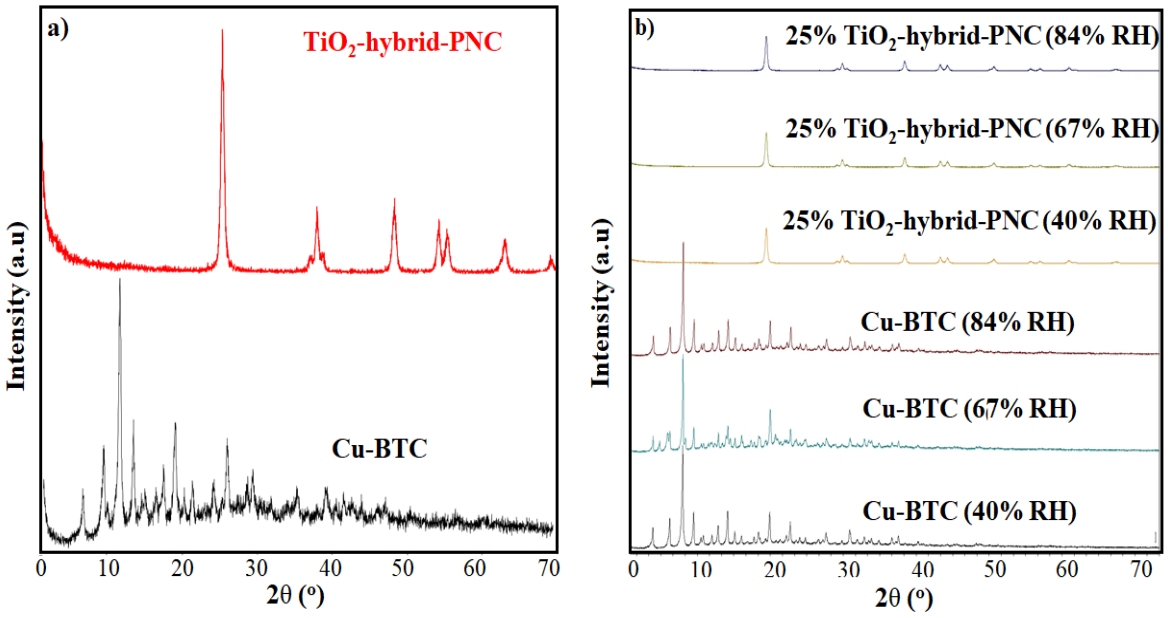

Figure 3.4. XRD patterns of the (a) Cu-BTC, TiO_2-hybrid-PNC, (b) Humidified Cu-BTC and TiO_2-hybrid-PNC.

3.2.3.2. Nitrogen Adsorption-Desorption Isotherms. Figure 3.5 shows nitrogen adsorption-desorption isotherms and the corresponding pore size distributions of the Cu-BTC, and TiO_2-hybrid-PNC. The Cu-BTC displays specific sorption behavior for the microporous materials classified as Type I isotherm (Figure 3.5a). The absence of the hysteresis implies that the Cu-BTC has no other pore network aside from the micropores. The loop noticed in TiO_2-hybrid-PNC curve ensures Type IV isotherm. This belongs to a characteristic mesoporous structure via capillary condensation in the partial pressure range from 0.4 to 1.0.

Accordingly, the pore size distribution curve of the TiO_2-hybrid-PNC is in the typical mesoporous region of 20-40 Å (Figure 3.5b). TiO_2-hybrid-PNC has a lower surface area (612 m^2 g^{-1}) in comparison to that of the Cu-BTC (1520 m^2 g^{-1}), as seen in other TiO_2 hybrid-MOF structures [60, 66].

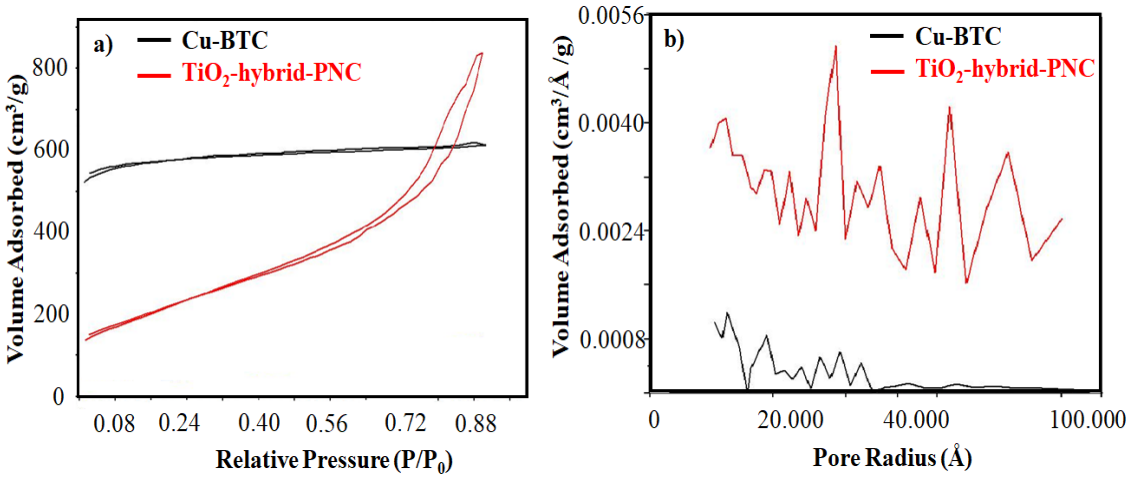

Figure 3.5. (a) BET surface area and (b) pore size distribution plots of Cu-BTC and TiO_2-hybrid-PNC.

3.2.3.3. SEM-Mapping Analysis. Morphologies of Cu-BTC, TiO_2-hybrid-PNC and humidified samples are examined by SEM (EDX-mapping) analysis (Figure 3.6). Sharp edged octahedrons are detected in the SEM image of Cu-BTC (Figure 3.6a). The characteristic octahedral structure of Cu-BTC is almost retained under humidified conditions (Figure 3.6b, and d). The surface appearance of Cu-BTC (67% RH) differs from Cu-BTC with observable cracks (Figure 3.6c). The extended water exposure in course of Cu-BTC (84% RH) creates more vacant sites with the approach of octahedrons (Figure 3.6). The typical morphology of Cu-BTC becomes uneven and rough upon TiO_2 stacking (Figure 3.6e). In humidified TiO_2-hybrid-PNC samples, surface appearances differ with heterogeneously distributed aggregates which may promote the adsorption of MO molecule (Figure 3.6f,g and h). TiO_2 nanoparticles within the hybrid structure are proved by the dense distribution of Ti signals in EDX-mapping analysis (Figure 3.6i).

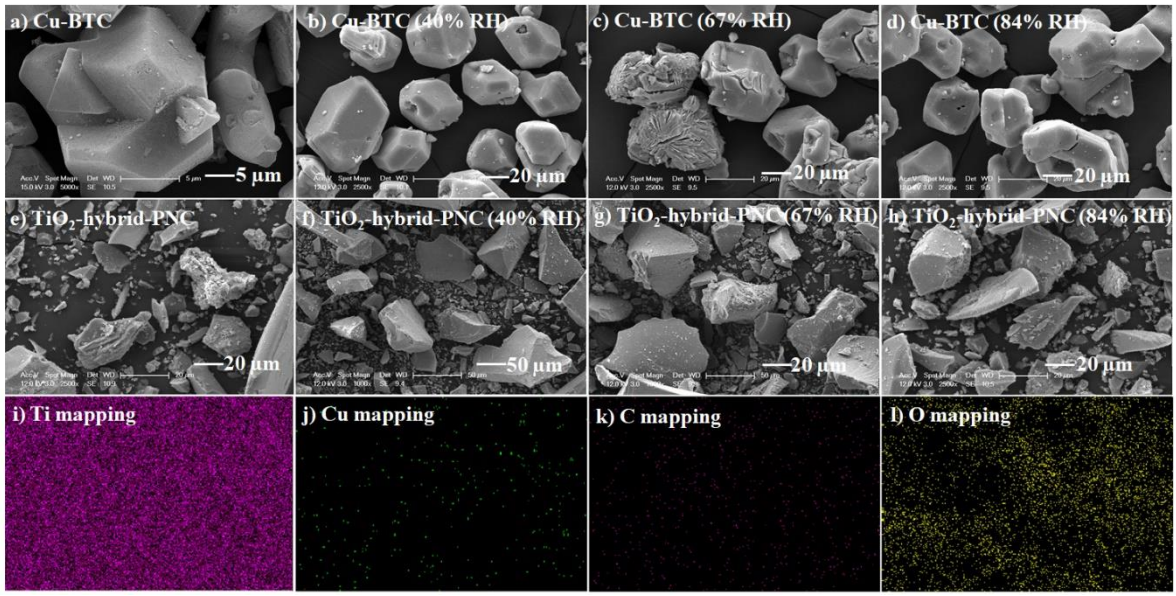

Figure 3.6. SEM images of (a) Cu-BTC, (b,c,d) Humidified Cu-BTC samples, (e) TiO_2-hybrid-PNC, (f,g,h) Humidified TiO_2-hybrid-PNC, Elemental analysis of TiO_2-hybrid-PNC (i) Ti mapping, (j) C mapping, (k) Cu mapping, (l) O mapping.

3.2.3.4. XPS Analysis. X-ray photoelectron spectroscopy (XPS) analysis is carried out to investigate surface composition and chemical states of constituents of Cu-BTC and TiO_2-hybrid-PNC. The survey spectrum of Cu-BTC contains Cu 2p, C 1s and O 1s peaks (Figure 3.7a). In addition to Cu 2p, C 1s and O 1s peaks, Ti 2p peak is observed in the spectrum of TiO_2-hybrid-PNC (Figure 3.7a). For Cu-BTC, two main signals of Cu $2p_{3/2}$ and Cu $2p_{1/2}$ with binding energies of 934.7eV and 954.6eV, respectively, are assigned to octahedrally coordinated Cu^{2+} (Figure 3.7b). The Cu doublets are separated by 20 eV and the well-known "shake-up satellite bands" appear at 938-948 eV and 961-965 eV regions as other indications of divalent state Cu content in Cu-BTC [67-69]. The Cu 2p spectrum of TiO_2-hybrid-PNC reveals the two doublets with the binding energies of 931.8eV and 951.3 eV. The slight shift in the binding energies points out an increment in the electron density around the Cu atom due the attractions between Cu^{2+} center and lone pair electrons of oxygens in TiO_2. For TiO_2-hybrid-PNC, two distinct peaks at 457.9 eV (for the Ti $2p_{1/2}$) and at 463.7 eV (for the Ti $2p_{3/2}$) are obtained due to Ti^{4+}, in good agreement with literature (Figure 3.7c) [70]. The O 1s spectra of the Cu-BTC appears with a wider peak at around 532.1 eV, deriving from O^{2+} ions in crystalline network of the Cu-BTC (Figure 3.7d). The peak at 529.1 eV in the

presence of TiO_2-hybrid-PNC represents the oxide (O^{2-}) peak of TiO_2. The C 1s doublet peaks at 284.4 eV and 288.1eV refer to the ligand groups of the Cu-BTC structure (Figure 3.7e). The characteristic peak at 284.4eV can attributed to the C–C bond and the one at 288.1 eV is ascribed to the C=O bond. The loose of the latter peak in the presence of TiO_2-hybrid-PNC, suggests the removal of most of the oxygen containing functional groups from the Cu-BTC.

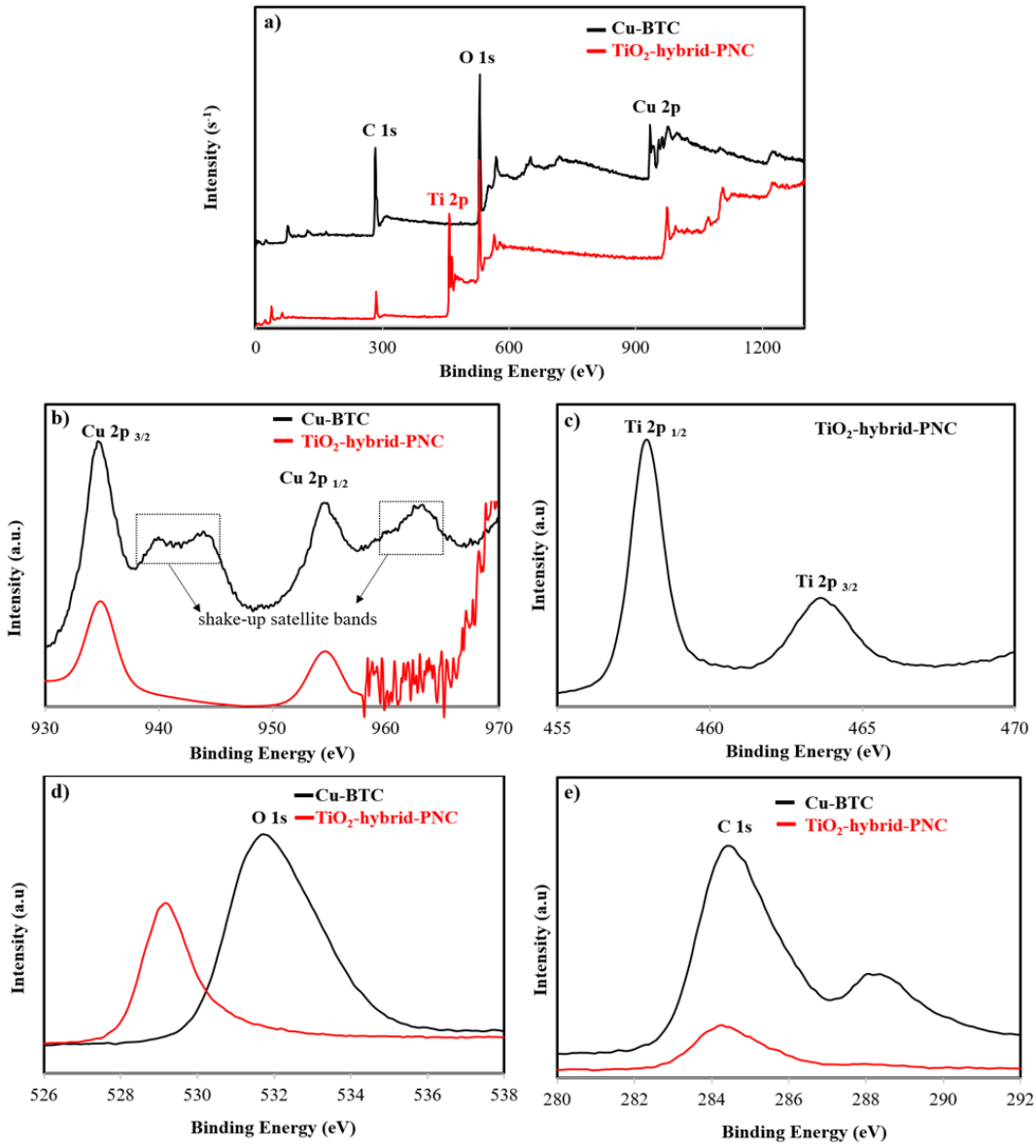

Figure 3.7. (a) XPS survey analysis of Cu-BTC and TiO_2-hybrid-PNC (b) Cu 2p spectra of Cu-BTC and TiO_2-hybrid-PNC (c) Ti 2p spectra of TiO_2-hybrid-PNC (d) O 1s spectra of Cu-BTC and TiO_2-hybrid-PNC (e) C 1s spectra of Cu-BTC and TiO_2-hybrid-PNC.

3.2.3.5. UV-Vis DRS Analysis. The optical absorption properties of TiO_2, Cu-BTC and TiO_2-hybrid-PNC are studied by DR-UV/Vis (Figure 3.8a). The converted UV–vis absorption spectra are used to estimate the band gap energies (E_g) of TiO_2 and TiO_2-hybrid-PNC (Figure 3.8b). TiO_2 nanoparticles show a flat band structure at 390 nm with a corresponding E_g of 3.18 eV. The profile of Cu-BTC is extending up to 600 nm with a slight edge around 380 nm. TiO_2-hybrid-PNC profile lies in between those of TiO_2 and Cu-BTC, suggesting impacts from both structures. The environment of TiO_2 nanoparticles varies in the presence of Cu-BTC and hence reduction in the E_g of TiO_2-hybrid-PNC (3.08 eV) is detected. Similar E_g decrements were also obtained upon TiO_2 loading on NH_2-UiO-66 and ZIF-8 MOF-structures [71].

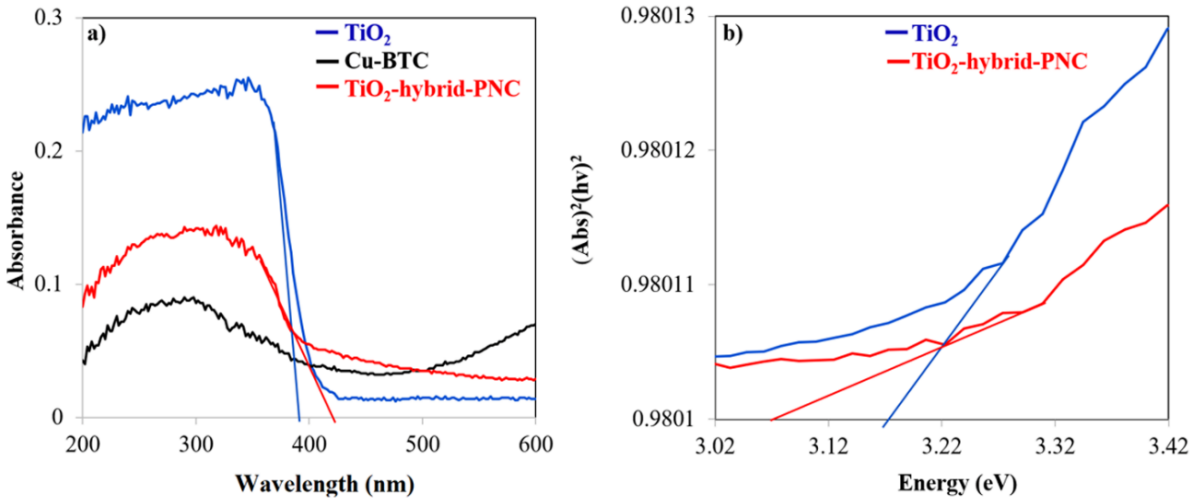

Figure 3.8. (a) UV-vis DRS spectra of TiO_2, Cu-BTC and TiO_2-hybrid-PNC (b) band gap absorption edges of TiO_2 and TiO_2-hybrid-PNC.

3.2.3.6. Photoluminescence Tests. Photoluminescence emission is originated from the radiative recombination of photogenerated electron-hole pair. The room temperature emission PL spectra of Cu-BTC and TiO_2-hybrid-PNC performed under an excitation wavelength of 270 nm are shown in Figure 3.9. The signal observed at 539 nm stems from the radiative recombination of free electrons in shallow traps and conductive bands with the free holes at the valence bands of both Cu-BTC and TiO_2-hybrid-PNC. The lower PL intensity of TiO_2-hybrid-PNC than that of Cu-BTC indicates that the heterostructure can effectively suppress the charge carrier recombination. This efficient separation of photoexcited electron-hole pair

occurs due to the fast electron transfer from TiO_2 nanoparticles to the Cu-BTC in the TiO_2-hybrid-PNC matrix. Thus, this charge separation and charge transfer can be considered as the main contribution to the promoted photocatalytic activity of TiO_2-hybrid-PNC.

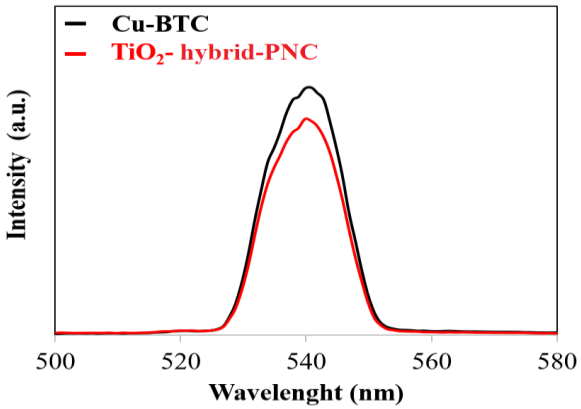

Figure 3.9. PL spectra of Cu-BTC and TiO_2-hybrid-PNC with an excitation wavelength of 270 nm.

3.2.3.7. Water Vapor Adsorption. The hydrophilicity of Cu-BTC and TiO_2-hybrid-PNC are controlled under 40, 67 and 84% RH conditions. In the presence of Cu-BTC, the amount of water vapor adsorption is found as 12%, 22% and 24% at 40%, %, 67% and 84% RH, respectively. Water vapor adsorption is expected through open metal sites in the Cu-BTC framework. The Cu atom in Cu-BTC has four coordination number with free sites facing the main pores of the structure [72]. Water molecules can accumulate on these sites, being responsible from the hydrophilic nature of Cu-BTC. Nevertheless, availability of vacant Cu sites and also pores decrease by the excess water molecules. Thus, while low dosage of water vapor molecules interacts with the Cu sites, exposure to higher dosages brings a saturation effect in the adsorption.

Contrarily, the water vapor adsorption capacity of TiO_2-hybrid-PNC is higher than that of Cu-BTC. 25%, 37%, 67% adsorptions are attained at 40%, 67%, 84% RH, respectively. Additional interactions appear among Ti^{4+} and lone pair electrons of oxygen in water molecules. Then, a multilayer coverage of water clusters may form through hydrogen bonding with the help of terminal and bridging oxygens of OH groups on TiO_2 nanoparticles. Hence, water vapor adsorption percentages increase as a function of RH values.

3.2.3.8. Dark Adsorption Capacities, Photocatalytic Activities and Kinetics. Dark adsorption tests are carried out in the presence of Cu-BTC, TiO_2-hybrid-PNC and the humidified samples. The remaining MO percentage in solution is found as the 78.2% at the end of the 100 min in the existence of the bare Cu-BTC (Figure 3.10a). Despite the repulsive interaction between the negatively charged ligand groups of Cu-BTC and the anionic dye MO, a certain extent of MO adsorption is observed. In addition to the attraction of the Cu-BTC's cationic metal sites towards MO, π-π interaction/stacking possibility among benzylic groups of Cu-BTC and MO structures can be responsible from this adsorption. Humidified Cu-BTC samples, however, show a lower tendency toward MO molecules in comparison to that of Cu-BTC (Figure 3.10a). The existence of water molecules restricts the availability of open-metal sites and leads a lower MO adsorption. Under irradiation, absorption of light by ligand groups is possible with a charge transfer to the metal sites [73]. The conversion of Cu (II) to Cu (I) was proved by an XPS analysis in copper-based metal organic frameworks under irradiation [74]. Although charge separation seems to be possible, destruction of conjugation among ligands decreases the π-π interaction between the Cu-BTC frame and MO. Therefore, Cu-BTC, Cu-BTC (40% RH) and Cu-BTC (67% RH) show a lower degradation rate under irradiation (Figure 3.10b). Among humidified Cu-BTC, the least remaining MO percentage (72.6%) is noticed with Cu-BTC (84% RH). Since the number of water molecules is high in Cu-BTC (84% RH), the probability of reaction with the holes (via charge separation) increases. This simultaneously generates more hydroxyl radicals and thus enhance the degradation route of MO.

Dark adsorption capacity of TiO_2-hybrid-PNC is found to be lower than that of Cu-BTC due to the repulsive interactions among the bridging oxygens of TiO_2 nanoparticles and the sulphonic group of MO (Figure 3.10c). However, humidified TiO_2-hybrid-PNC samples demonstrate a higher adsorption tendency toward MO as also suggested by the SEM images of these catalysts. The remaining MO concentration in humidified Cu-BTC (87.9% for Cu-BTC (40% RH), 85.3% (67% RH), and 80.1% (84% RH)) and humidified TiO_2-hybrid-PNC samples (77.2% for Cu-BTC (40% RH), 74.6% (67% RH)) and 70.1% (84% RH)) show a similar decreasing trend. The highest humidity condition (84% RH) supplies the highest MO adsorption via formation of more hydrogen bonds with excess water molecules in the matrix.

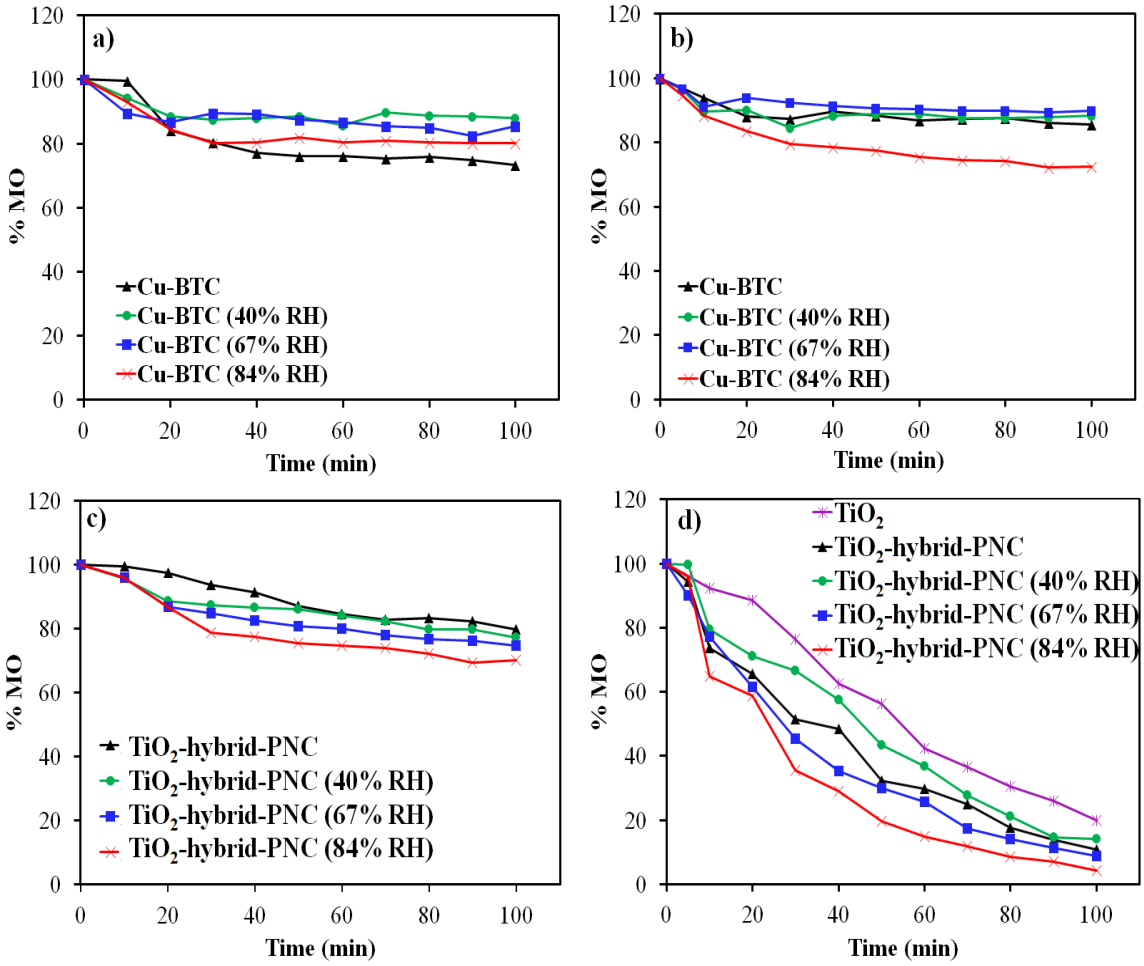

Figure 3.10. (a) Dark adsorption experiments in the presence of Cu-BTC and humidified Cu-BTC samples, (b) Photoactivities of Cu-BTC and humidified Cu-BTC samples, (c) Dark adsorption experiments in the presence of TiO_2-hybrid-PNC and humidified TiO_2-hybrid-PNC, (d) Photocatalytic activities of TiO_2-hybrid-PNC and humidified TiO_2-hybrid-PNC.

Photocatalytic performances of TiO_2-hybrid-PNC and humidified TiO_2-hybrid-PNC samples are compared with that of TiO_2 (Figure 3.10d). The remaining MO percentages are found as 19.1%, 11.3%, 14.1%, 8.7%, 4.1% for TiO_2, TiO_2-hybrid-PNC, TiO_2-hybrid-PNC (40% RH), TiO_2-hybrid-PNC (67%) and TiO_2-hybrid-PNC (84%), respectively. In the hybrid structures, photogenerated electrons from TiO_2 can be captured by the porous frame by inhibiting charge carrier recombination. Meanwhile, photogenerated holes can diffuse to the surface and initiate the degradation route of MO. Such electron transfer mechanism was also explored in the hybrid structure of HKUST-1@TiO_2 [62]. The better adsorption

capacity of humidified samples increases the MO level on the surface and facilitates the contact of MO with the photocatalytic sites. The excess water molecules in TiO_2-hybrid-PNC (67%) and TiO_2-hybrid-PNC (84%), enhance the reactions of holes with surface water molecules (interact via Ti^{4+}) and surface hydroxyl groups (form through bridging oxygens). This enables formation of more hydroxyl radicals and eventually accelerates the photocatalytic degradation by subsequent attacks of hydroxyl radicals to the MO moiety.

The influence of initial MO concentration on photocatalytic degradation is also investigated in the concentration range of 0.81-32.7 mg L^{-1} and in the presence of TiO_2-hybrid-PNC and TiO_2-hybrid-PNC (84% RH) (Figure 3.11a and b). The plot of ln ($[MO]_0/[MO]_t$) versus time shows a linear relation (Figure A.1), where $[MO]_0$ refers the initial concentration of MO after the dark adsorption (mg L^{-1}), $[MO]_t$ refers the concentration of MO in the remaining solution at time "t" (min) under irradiation. k is the rate constant (min^{-1}) and can be found from slopes of the lines. In the presence of TiO_2-hybrid-PNC (84% RH), higher k values are found owing to the formation of more hydroxyl radicals and enhanced photoactivity. As a general trend, an inverse relation between k and $[MO]_0$ is noticed for both supported catalysts (Table 3.1). In the case of TiO_2-hybrid-PNC, the increments in k values indicate validity of pseudo-first order kinetics for the MO concentrations varying from 0.81 mg L^{-1} to 8.17 mg L^{-1}. However, for the highest MO concentrations (from 16.3 mg L^{-1} to 32.7 mg L^{-1}), k values do not differ significantly. The surface coverage of the photocatalyst by more dye molecules brings a limiting effect to the interception of the direct contact between the photons and photocatalyst nanoparticles. This weak penetration of light limits the photocatalytic activity. Beyond 8.17 mg L^{-1}, the reaction rate reaches a saturation value, becomes independent of the high concentration of MO and follows zero order kinetics (Figure 3.11c). The plateau is also noticed in the presence of TiO_2-hybrid-PNC (84% RH), however, shifted to a higher concentration value (24.6 mg L^{-1}). This indicates that TiO_2-hybrid-PNC (84% RH) maintains its active surface sites even at high concentrations of MO and kinetics mostly follow pseudo first order.

Langmuir-Hinshelwood (L-H) model is also used to describe the relation between the degradation rate and initial MO concentration (Figure 3.11d). The model can be applied with the following linear form

$$\frac{1}{R} = \frac{1}{kK[MO]_0} + \frac{1}{k} \qquad (2.2)$$

where R is the rate of degradation, K is the adsorption coefficient of MO (L mg^{-1}) and k is the reaction rate constant (mg L^{-1} min^{-1}). The linearity in the plot of reciprocal of rate 1/R against the reciprocal of initial MO concentration confirms the application of L-H model to the supported catalyst system prepared in this study. The k values are calculated from the intercept (as 0.074 mg L^{-1} min^{-1} for TiO_2-hybrid-PNC and 0.337 mg L^{-1} min^{-1} for TiO_2-hybrid-PNC (84% RH)) and K values are evaluated from the slope of the straight line (as 0.478 L mg^{-1} for TiO_2-hybrid-PNC and 0.123 L mg^{-1} for TiO_2-hybrid-PNC (84% RH)).

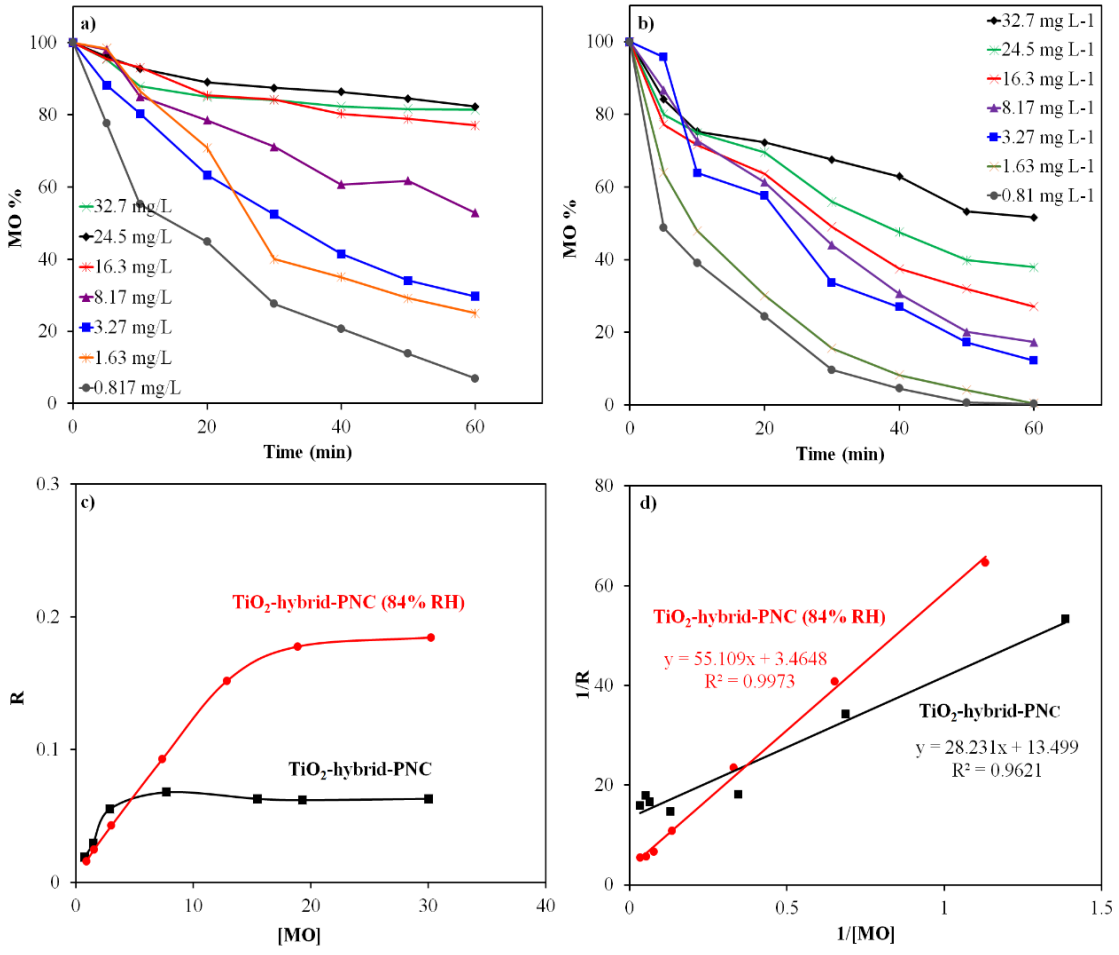

Figure 3.11. Effect of initial MO concentration in the presence of (a) TiO_2-hybrid-PNC and (b) TiO_2-hybrid-PNC (84% RH), (c) Kinetics of TiO_2-hybrid-PNC and TiO_2-hybrid-PNC (84% RH), (d) Langmuir-Hinshelwood analysis of TiO_2-hybrid-PNC and TiO_2-hybrid-PNC (84% RH).

Table 3.1. Effect of initial MO concentration on rate constants (k) and linear regression values (R) in the presence of TiO_2-hybrid PNC and TiO_2-hybrid PNC (84% RH).

	k (min^{-1})		**R**	
[MO]	TiO_2-hybrid PNC	TiO_2-hybrid PNC (84% RH)	TiO_2-hybrid PNC	TiO_2-hybrid PNC (84% RH)
32.7	0.0021	0.0061	0.9627	0.9701
24.5	0.0029	0.0094	0.9723	0.9721
16.3	0.0309	0.0248	0.9169	0.9791
8.17	0.0088	0.0271	0.9287	0.9955
3.27	0.0191	0.0364	0.9985	0.9987
1.63	0.0201	0.0411	0.9721	0.9952
0.81	0.0261	0.0475	0.9937	0.9938

3.2.3.9. Stability Tests. Figure 3.12 shows the stability of the TiO_2-hybrid PNC and TiO_2-hybrid PNC (84% RH) after being used 4 times under the same conditions. As the data shown, the degradation efficiency of MO decreased by 1.2% (TiO_2-hybrid PNC) and 0.9% (TiO_2-hybrid PNC (84% RH)) after the fourth application. Thus, the hybrid structures possess good stability and keep well photocatalytic activity in MO removal under the UV light.

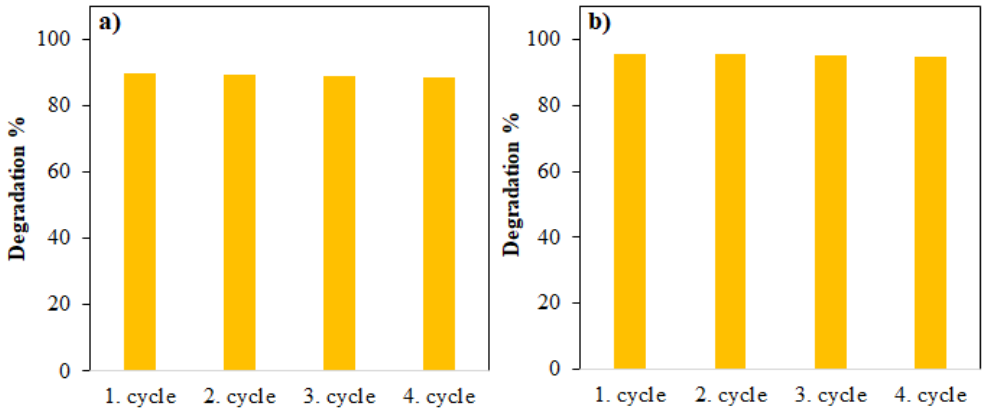

Figure 3.12. Recycling tests for (a) TiO_2-hybrid PNC and (b) TiO_2-hybrid PNC (84% RH).

3.2.4. Conclusion

In this study, a hybrid porous nanocomposite structure is prepared by using TiO_2 as photocatalyst and Cu-BTC as the porous support material. Hybrid structure has well developed TiO_2 crystals while Cu-BTC signals disappear. Formation of the mesoporous hybrid structure is confirmed by N_2 adsorption-desorption analysis. Homogeneous distribution of TiO_2 nanoparticles are evidenced by SEM-mapping images. Absorption profile of TiO_2-hybrid-PNC has impacts from both TiO_2 and Cu-BTC. According to PL spectra, reduction in charge carrier recombination is detected in the presence of the hybrid porous network. TiO_2-hybrid-PNC shows a higher water vapor adsorption capacity than Cu-BTC due to the additional interactions among Ti^{4+} and lone pair electrons of oxygen in water molecules. Dark adsorption capacity of TiO_2-hybrid-PNC are found to be lower in comparison to that of Cu-BTC toward MO. The reduction in surface area of Cu-BTC by TiO_2 loading restricts the number of available surface sites for the adsorption of MO. However, humidified TiO_2-hybrid-PNC catalysts can adsorb more MO molecules via formation of more hydrogen bonds. Simultaneously, the synergy established for the hybrid porous structures promotes the separation of the electron-hole pairs upon irradiation and leads to enhanced photocatalytic performance. The best photocatalytic efficiency is demonstrated by TiO_2-hybrid-PNC (84% RH). Pseudo first order kinetics is mainly followed and applicability of Langmuir-Hinshelwood model is observed for both TiO_2-hybrid-PNC and TiO_2-hybrid-PNC (84% RH). In the view of all results, combined with the water vapor adsorption capacities and photocatalytic activities such hybrid porous structures can be developed and applied to environmental systems.

3.3. ZnO@CuO Derived from Cu-BTC for Efficient UV-Induced Photocatalytic Applications

This section is published as: D. Tuncel, A.N. Ökte, "ZnO@CuO derived from Cu-BTC for efficient UV-induced photocatalytic applications", *Catalysis Today*, Vol. 328, pp. 149-156, 2019. This copyrighted article is reproduced with permission from Elsevier (Figure B.3).

3.3.1. Introduction

Zinc oxide (ZnO) is an active material and has been widely investigated because of its versatile physical and chemical properties [75-77]. In the field of photocatalytic processes, ZnO has emerged as leading candidate because of its unique characteristics, such as low cost, nontoxicity, and good thermal and chemical stability [75]. Nevertheless, two important drawbacks restrict the photocatalytic performance of ZnO. From the morphological aspect, low surface area and lack of porosity limit the adsorption of target molecules. As a second point, low light-harvesting efficiency and fast recombination of charge carriers hinder the photocatalytic efficiency [78]. These problems can be overcome either by using porous support materials to maximize the surface area via creating interior spaces to enable mass transfer or coupling of ZnO with other metal oxides to retard the recombination of photogenerated electrons and holes [79-82].

Cu-BTC, as a member of MOF family, is a porous material and constitutes benzene 1,3,5-tricarboxylate (BTC) ligands that bind to four coordination sites of each Cu (II) centers [83, 84]. The Cu-BTC structure has big cavities and octahedral cages. The unsaturated Cu sites act as strong adsorption parts for water vapor and/or various molecules via electronic interactions [85-87]. Alternatively, since Cu-BTC constitutes coordinated Cu- sites with BTC-ligands, it may be transformed into copper (II) oxide (CuO) form under different reaction conditions. In literature, Cu-BTC derived CuO catalysts have been rarely reported. Niu et al. reported Cu-BTC as both template and copper precursor to synthesize a hybrid catalyst consisting of porous carbon supported Cu/CuO nanoparticles [88]. The prepared composite demonstrated an excellent catalytic performance compared with other noble metal

catalysts. This was attributed to the obtained porous structure facilitating diffusion of reactants and products. In the study of Zheng et al, the Cu/ZnO catalyst was successfully achieved via the calcination and reduction processes of the Cu(Zn)-BTC precursor [89]. Characterization results confirmed that the Cu/ZnO catalyst derived from Cu-BTC was more active and stable than Cu/ZnO that prepared by other methods and the improved catalytic activity depended strongly on the interfacial area between Cu and ZnO. A comparative study between the CuO obtained via pyrolysis of Cu-BTC (CuO-p) and CuO prepared by co-precipitation method (CuO-c) was conducted by Peng et al [90]. The activity of CuO-p for the catalytic reduction of NO was found higher than that of CuO-c. Although CuO-p sample lost most of HKUST-1's surface area, the octahedral shape and particle size were well maintained.

In this study, ZnO@CuO nanocatalyst is prepared via CuO formation from Cu-BTC support and simultaneous in-situ buildup of ZnO nanoparticles. To the best of our knowledge, there are no reports available on such synthesis of ZnO@CuO nanocatalyst. ZnO@CuO heterojunction thermodynamically favors transfer of electrons and holes between ZnO and CuO due to their well-matched band positions [90]. Accordingly, suppression of charge carriers' recombination is satisfied by gathering electrons on ZnO sites and holes on CuO sites. This prolongs life time of the carriers and enables their mobilities toward surface adsorbed species. Therefore, ZnO@CuO shows a higher photocatalytic performance in comparison to the individual component ZnO. The crystal structure, surface morphology and functional properties of ZnO@CuO are characterized using X-ray diffractometer (XRD), raman spectroscopy, nitrogen adsorption-desorption isotherms (BET), UV-Vis diffuse reflectance spectroscopy (UV-Vis DRS), scanning electron microscopy (SEM) and X-ray photoelectron spectroscopy (XPS). Besides, possible effect of humidity on the structural properties of ZnO@CuO are examined at 40%, 67% and 84% relative humidity (RH) conditions. Dark adsorption abilities and UV irradiation-photoactivities of ZnO@CuO and humidified ZnO@CuO are evaluated in terms of methyl orange (MO) and methylene blue (MB) dyes as model pollutants. For MO, ZnO@CuO shows the highest dark adsorption capacity while for MB, ZnO@CuO (84%) has the strongest interaction. ZnO-CuO prepared by impregnation method reveals lower dark adsorption ability and photocatalytic performance than that of ZnO@CuO obtained from Cu-BTC.

3.3.2. Experimental

3.3.2.1. Materials. The Cu-BTC (Copper benzene-1,3,5-tricarboxylate, Aldrich), methyl orange (Merck), methylene blue (Merck), Zinc nitrate hexahydrate ($Zn(NO_3)_2 \cdot 6H_2O$) (99%, Merck), $Cu(NO_3)_2 \cdot 6H_2O$ (Merck), sodium carbonate (Na_2CO_3) (Merck) are provided by the suppliers. Deionized water is used for preparing solutions in the experiments purified with an Elga-Pure Water Purification (UHQ II) system.

3.3.2.2. Synthesis of Catalysts. The co-precipitation method is used to synthesize ZnO nanoparticles from the certain concentrations of precursors zinc nitrate hexahydrate ($Zn(NO_3)_2.6H_2O$) and sodium carbonate (Na_2CO_3).0.25M precursors are separately prepared and then mixed. The white suspension is agitated for 2 h at room temperature, then centrifuged and washed several times. Drying at 100°C for 12 h is followed by calcination at 300°C. The resulting material is 0.25M ZnO, referred as ZnO within the study.

The ZnO@CuO nanocatalyst is prepared by addition of 100 mL ZnO solution into the 2 gr of Cu-BTC. After agitation, extensive washings and centrifugation, the nanocomposite is dried at 100°C for 12 h, then calcined at 300°C for 5 h and named as ZnO@CuO. Dry humid conditions are about 30-35%. The humidified ZnO@CuO catalysts are prepared under 40%, 67% and 84% relative humidity (RH) conditions. After drying at 100^0C, ZnO@CuO is exposed to the certain RH percentages inside the climate chamber (KKS 115 TOP+INOX/G) for 72 h. The nanocatalysts are named as either humidified ZnO@CuO or ZnO@CuO (40% RH), ZnO@CuO (67% RH) and ZnO@CuO (84% RH).

$Zn(NO_3)_2.6H_2O$ and $Cu(NO_3)_2.6H_2O$ are also used to prepare ZnO-CuO nanocatalyst by impregnation method. Concentrations of the precursor solutions are regulated to 0.25M. Then, 100 mL of each solution is mixed. Further stirring is performed to obtain a homogeneous solution. After several centrifugation and washing steps, the nanocatalyst is dried at 100°C for 12 h and then, annealed at 300°C for 5 h.

3.3.2.3. Characterization Techniques. The crystal structures of the samples are identified by Rigaku-D/MAX Ultima X-ray diffractometer (XRD) with Cu Kα radiation (λ =1.54 Å) operating at 40 kV and 40 mA and scanning rate 2 min^{-1}. ZnO and ZnO@CuO are further

analyzed under atmospheric condition with the defocusing technique by Raman spectroscopy via a Renishaw inVia Raman microscope with the operation parameters: 532 nm 100 mW diode laser as the excitation source; laser intensity of ~5 mW; 10 s acquisition time; a total of 5 accumulations per spectrum. Before measurements, Raman spectrum is calibrated by using a silicon wafer peak at 520 cm^{-1}. The nitrogen adsorption-desorption isotherms are obtained under liquid nitrogen at 77 K with a Quantachrome Nova 2200e automated gas adsorption system. Multi point BET analysis and BJH method are used to measure the specific surface area and pore sizes of the materials. Absorption profiles of the catalysts are determined via UV-Vis diffuse reflectance spectroscopy by using Shimadzu UV-2450, equipped with an integrating sphere reflectance accessory. The baseline correction was done by $BaSO_4$. The analysis range was from 200 to 600 nm for all catalysts. The surface morphological analysis is done by using scanning electron microscopy in combination with EDX analysis on an ESEM-FEG/EDAX Philips XL-30 instrument operating at 20 kV using catalyst powders supported on carbon tape. For the investigation of chemical states of the surface constituents, X-ray photoelectron spectroscopy (XPS) tests are carried out by using Thermo Scientific K-Alpha X-ray Photoelectron Spectrometer equipped with hemispherical electron analyzer and Al-K micro-focused monochrometer.

3.3.2.4. Adsorption and Photocatalytic Tests. The adsorption capacity and photocatalytic performance tests of ZnO, ZnO@CuO and humidified ZnO@CuO are carried out in laboratory constructed box. Eight black fluorescent lamps (Philips TL 15 W/5 BLB) that supply light of wavelength 320-440 nm are used as irradiation sources within the box. The incident photon flux for all lamps is measured as $4.7x10^{15}$ photon/s using potassium ferrioxalate ectinometer in our previous studies [1]. A pyrex flask is used as a reactor for 0.2 gr catalyst in 200 mL MO or MB solution at continuous circulation mode at room temperature. Prior to illumination, to ensure the equilibrium of adsorption process, suspensions are magnetically stirred in the dark for 30 min. Aliquots (about 5 mL) are retrieved from the flask at certain time intervals. MO solutions are analyzed after filtering through Millipore filter (0.22 mm). MB solutions are controlled after centrifugation. The absorption spectra of MO or MB is monitored by UV-Vis Spectrophotometer. The decolorization of MO or MB is followed at 464 nm or 665 nm, respectively.

3.3.3. Results and Discussion

3.3.3.1. XRD Analysis. Figure 3.13a shows XRD patterns of Cu-BTC, ZnO@CuO and humidified ZnO@CuO catalysts. The characteristic diffraction peaks of Cu-BTC accumulate below 20° (2θ) as (200), (222), (400) and (440) reflections at 6.7, 11.6, 13.5 and 19.6° (2θ), respectively (MDI-JADE6). ZnO@CuO pattern includes ZnO reflections of (100), (002), (101), (102), (110) and (200) at 31.9, 34.6, 36.4, 47.7, 63.1 and 66.5° (2θ), respectively and also CuO reflection of (111) at 38.7° (2θ). Other CuO reflections at 35.5, 48.7, 58.3° (2θ) are not clearly observed since they may overlap with ZnO peaks. The absence of 42.1° and 42.5° (2θ) peaks indicate that Cu_2O and Cu do not form within the ZnO@CuO [91]. Low-angle Cu-BTC peaks are lost in the patterns of ZnO@CuO and humidified ZnO@CuO, indicating the transformation of Cu-BTC into CuO as also noticed in the study of Peng et al. [92]. The appearance of a small peak at around 12° (2θ) in humidified ZnO@CuO patterns may likely resemble water coordination to Cu as in the form of $Cu(OH)_2$ with (020) reflection. ZnO and CuO crystalline sizes are calculated from the line broadening of XRD peaks (101-for ZnO and 111-for CuO) by using Scherrer's formula. The ZnO sizes are found as 10.7, 12.5, 13.4, 24.8 nm for ZnO@CuO, ZnO@CuO (40% RH), ZnO@CuO (67% RH) and ZnO@CuO (84% RH), respectively. Similarly, CuO sizes are found to increase from 15.5 nm for ZnO@CuO to 19.6 nm for ZnO@CuO (84% RH).

3.3.3.2. Raman Analysis. For ZnO, Raman spectrum (Figure 3.13b) shows vibrational modes at 203, 329, 436, 579, 795, 908 and 1086 cm^{-1}. The peak at 329 cm^{-1} is assigned as E2 (high)–E2 (low) modes and the peak at 436 cm^{-1} is assigned to E2 (high) mode, these are the characteristic modes of ZnO [93, 94]. The peaks at 203, 579, 795 and 1086 cm^{-1} can be ascribed the order modes of ZnO [95]. Raman spectrum of the ZnO@CuO displays modes at 195, 314, 419, 629 and 1080 cm^{-1}. The peaks at 314 and 629 cm^{-1} correspond to the B1g and B2g modes of monoclinic CuO respectively, [96, 97] and the peaks at 195, 419 and 1080 cm^{-1} are assigned to other characteristics of ZnO [97]. In the spectrum of ZnO@CuO, the intensity of 436 cm^{-1} ZnO peak is diminished and shifted to 419 cm^{-1} owing to the coexistence of CuO. Raman modes in the ZnO@CuO is broadened and blue shifted due to the stress during the growth process of the composite. Similar shifts are also detected in the studies of Li et al. and Abraham et al. [93, 98]. Thus, the ZnO@CuO formation is further confirmed by the simultaneous existence of ZnO and CuO Raman modes, consistent with

the XRD results. Cu_2O phase does not form in the ZnO@CuO as indicated by the absence of representative Cu_2O signals at 146, 219 and 414 cm^{-1} [99].

3.3.3.3. Nitrogen Adsorption Isotherms. The specific surface area and pore structure of ZnO@CuO and ZnO are investigated by measuring the nitrogen adsorption-desorption isotherms (Figure 3.13c and d). ZnO exhibits type II isotherm, specific for nonporous materials. Its surface area and pore volume are found as 7.5 $m^2\ g^{-1}$ and 0.0012 $cm^3\ g^{-1}$, respectively (Figure 3.13c). For ZnO@CuO, increase in adsorbate volume at a low P/P_0 region indicates the presence of micropores due to the utilization of Cu-BTC during the synthesis. Additionally, the hysteresis loop at P/P_0= 0.4-0.64 implies the existence of mesopores. But the N_2 uptake in this region is very small, indicating formation of the small amount of mesopores in ZnO@CuO. The pore size distribution curve of ZnO@CuO displays that the pores are in a typical mesoporous region of 2-4 nm (Figure 3.13d). The surface area and pore volume of ZnO@CuO are determined as 45 $m^2\ g^{-1}$ and 0.039 $cm^3\ g^{-1}$, respectively. Recent studies reported surface areas of CuO/ZnO systems prepared by different precursors and methods as 11.2 $m^2\ g^{-1}$ for CuO/ZnO corn like architecture and 25 $m^2\ g^{-1}$ for p-CuO/n-ZnO nanoparticles [99]. Thus, ZnO@CuO stands out as a promising material with a higher surface area and porosity. With these circumstances, ZnO@CuO is expected to provide multiple accessible sites to contact with MO or MB.

3.3.3.4. UV-Vis DRS Analysis. UV-Vis DRS analysis and band gap energy plots of Cu-BTC, ZnO, ZnO@CuO and humidified ZnO@CuO are revealed in Figure 3.13e and f. Cu-BTC has an extended spectrum between 200-600 nm whereas ZnO exhibits a sharp absorption edge around 420 nm (Figure 3.13e) [100]. The characteristic edge of ZnO is observable in the profiles of ZnO@CuO and humidified ZnO@CuO. Humidified ZnO@CuO samples demonstrate higher absorption intensities than that of ZnO and ZnO@CuO which may be due to their rough surfaces, eventually being responsible for the enhanced photoactivities. The band gap energies are found as 3.18, 3.0, 2.81, 2.78 and 2.7 eV for ZnO, ZnO@CuO, ZnO@CuO (40% RH), ZnO@CuO (67% RH) and ZnO@CuO (84% RH), respectively (Figure 3.13f). Reductions in band gap energies were also found in Cu-doped ZnO nanostructures [101] and ZnO/CuO fibers [102] using the DFT method. Notably, ZnO@CuO and humidified ZnO@CuO greatly enhance the UV light absorbance and extend the light

utilization from UV to even visible range, similar to the CuO/ZnO ‘corn like’ architecture system [100].

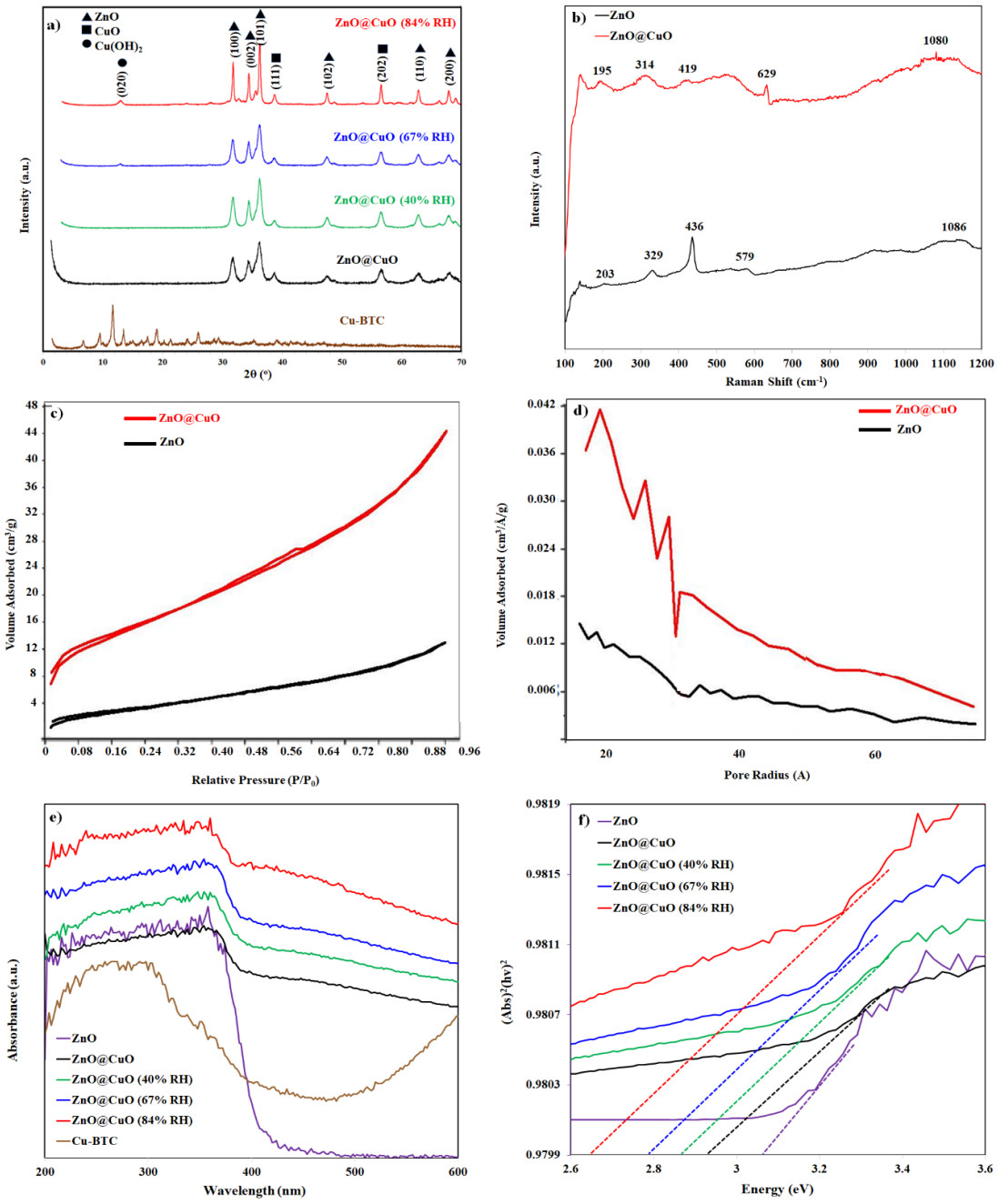

Figure 3.13. (a) XRD patterns of Cu-BTC, ZnO@CuO and humidified ZnO@CuO, (b) Raman spectrum of of ZnO and ZnO@CuO, (c and d) Nitrogen adsorption/desorption isotherms and pore size distribution plots of ZnO and ZnO@CuO, (e and f) UV-Vis DRS spectra and band gap absorption edges of Cu-BTC, ZnO, ZnO@CuO and humidified ZnO@CuO.

3.3.3.5. SEM-Mapping Analysis. Figure 3.14 depicts the SEM images of Cu-BTC, ZnO, ZnO@CuO and humidified ZnO@CuO. Cu-BTC has an octahedral structure as previously reported [103] (Figure 3.14a). Spherical nanoparticles of ZnO (Figure 3.14b) appear also in the image of ZnO@CuO (Figure 3.14c). The aggregates in ZnO@CuO morphology with octahedral shapes are inherited from Cu-BTC. The magnification of the aggregate labelled with red color in Figure 3.14c demonstrates the formation of closely attached and homogeneously distributed nanoparticles in ZnO@CuO (Figure 3.14d). The mapping images with EDX analysis of the whole surface verify the existence of Zn (49.5 wt%), Cu (20.6 wt%), O (12.2 wt%) and C (with 17.7 wt%) (Figure 3.14e-h). In humidified ZnO@CuO, surface roughness increases with respect to RH values (Figure 3.14i-k). A more compact and dense structure of ZnO@CuO (84%) may promote its dark adsorption capacity and degradation ability for MO or MB.

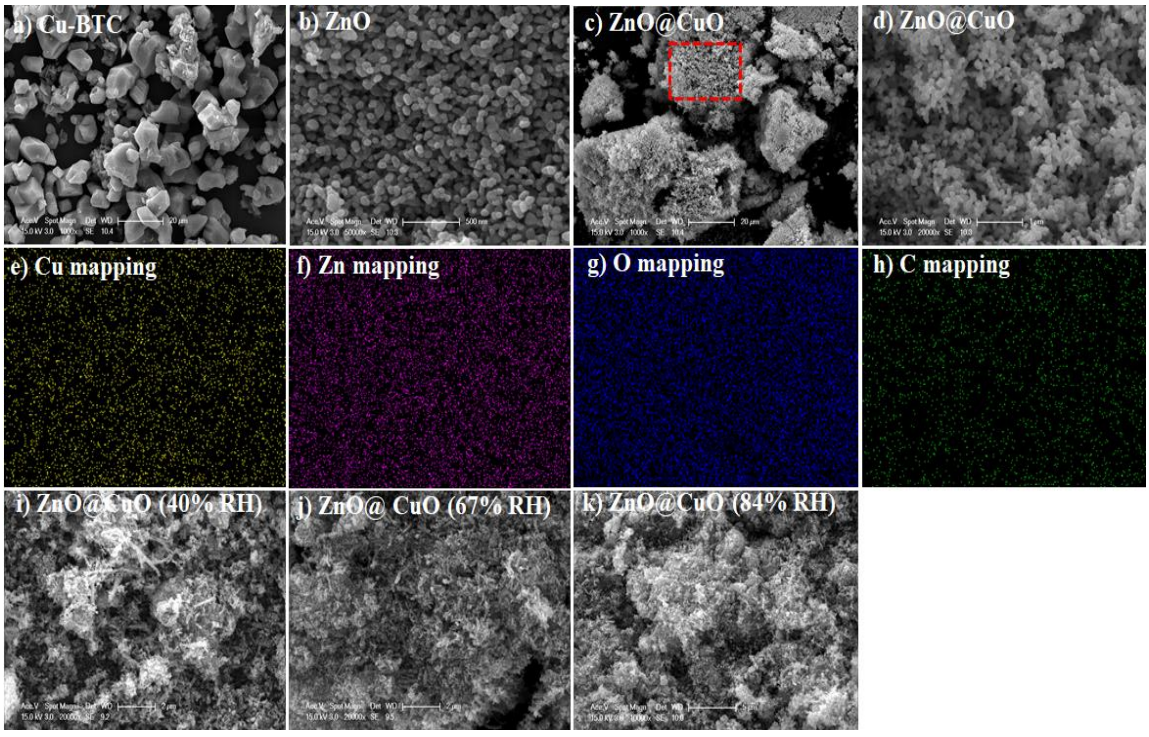

Figure 3.14. SEM images of (a) Cu-BTC, (b) ZnO, (c) ZnO@CuO (d) ZnO@CuO (magnified), (e-h) elemental mapping images of ZnO@CuO, (i-k) SEM images of humidified ZnO@CuO.

3.3.3.6. XPS Analysis. To further obtain evidence of the compositions and valence states of the nanocomposites, XPS measurement is carried out. The binding energy in the XPS spectra is calibrated using C 1s (286.6 eV). The survey spectrum of the ZnO@CuO in Figure 3.15a demonstrates Zn 2p and Zn Auger peaks in addition to the Cu 2p, C 1s and O 1s peak. Two major peaks at 933.3 and 953.5 eV are ascribed to Cu $2p_{3/2}$ and Cu $2p_{1/2}$ binding energy with spin-orbit splitting about 20.2 eV, respectively (Figure 3.15b). Moreover, the presence of two satellite peaks located at about 10 eV higher than those of the Cu $2p_{3/2}$ and Cu $2p_{1/2}$ indicates the existence of Cu^{2+} [104, 105]. The spectrum of Zn 2p has a doublet at 1021.65 eV and 1044.81 eV attributed to respective $Zn2p_{3/2}$ and $Zn2p_{1/2}$ peaks, indicating that the oxidation state of Zn in the ZnO@CuO is +2 (Figure 3.15c). The O 1s peak is deconvoluted into three subpeaks and assigned to 'O' in CuO (~529 eV), 'O' in ZnO (~530 eV) and 'O' in oxygen deficient regions (~531 eV) (Figure 2.15d) [106]. Evidently, the ZnO@CuO surface contains many oxygen vacancy defects. XPS results confirm the formation of ZnO and CuO in ZnO@CuO, corroborate the XRD results and in good agreement with the literature [107, 108].

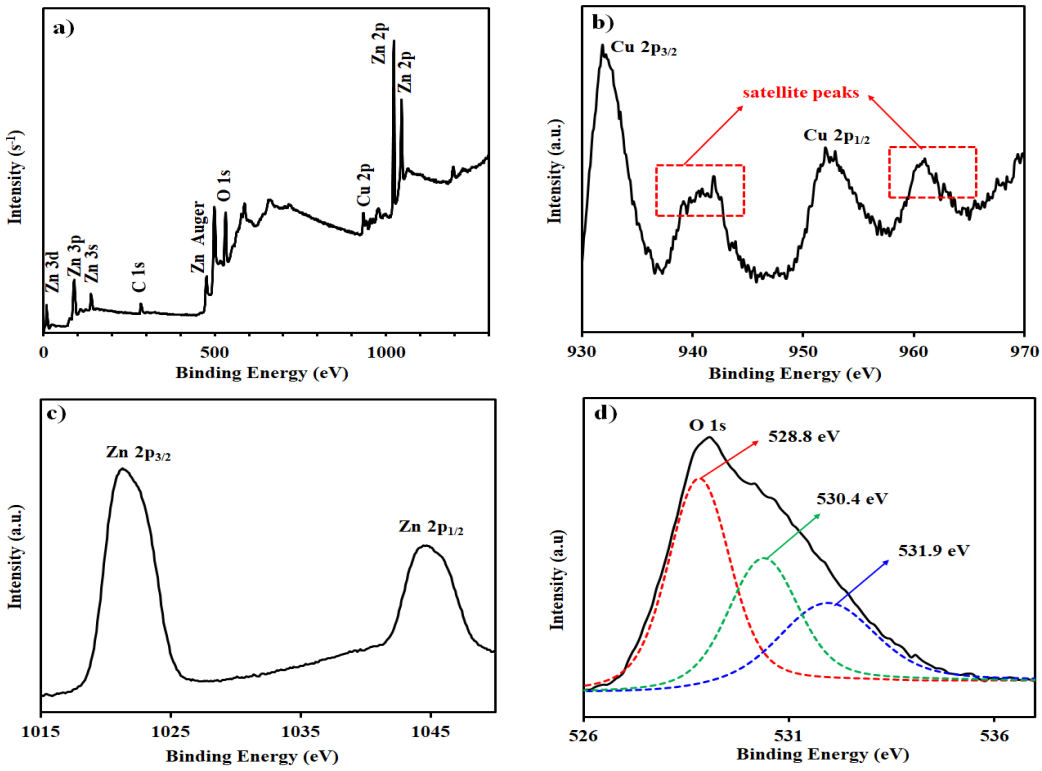

Figure 3.15. XPS survey scan of (a)ZnO@CuO, (b) XPS spectra of Cu 2p, (c) Zn 2p and (d) O 1s in ZnO@CuO.

3.3.3.7. Adsorption and Photocatalytic Tests. Figure 3.16 shows dark adsorption capacities and photocatalytic performances of ZnO, ZnO@CuO and humidified ZnO@CuO for MO and MB. In the presence of ZnO, the remaining percentages in solution are found as 95.6% for MO and 90.1% for MB (after dark adsorption) and 26.1% for MO and 21.2% for MB (after irradiation). It can be seen that the degree of dark adsorption and degradation is higher for both MO and MB in the presence of ZnO@CuO and humidified ZnO@CuO than that of ZnO. These improvements are due to the gradual formation of CuO from Cu-BTC precursor and its heterojunction with in-situ generated ZnO nanoparticles. The superior dark capacities can be explained by the increased surface area and pore volume of ZnO@CuO (45 m^2 g^{-1}, 0.039 cm^3 g^{-1}) in comparison to that of ZnO (7.5 m^2 g^{-1}, 0.012 cm^3 g^{-1}) and CuO (prepared by Cu-BTC 15.4 m^2g^{-1}, 0.14 cm^3g^{-1}). Under irradiation, the mechanism of enhanced photoactivities is explored based on electron transfer and energy band positions of ZnO and CuO (Figure 3.16a). Transfer of charge carriers is thermodynamically favored since both valence and conduction bands of CuO are above those of ZnO [109, 110]. Illumination excites the electrons in valence bands of CuO and ZnO to their conduction bands. Then, the photogenerated electrons of CuO is transferred to ZnO. Simultaneously, photogenerated holes of ZnO migrates to CuO. Eventually, more electrons can be on the conduction band of ZnO and more holes can accumulate on the valence band of CuO. Thus, life times of charge carriers are prolonged by suppressing their recombination as also postulated in the studies of Sriram et al. and Naseri et al. using DFT calculations [101, 102]. This eventually follows the promoted photoactivity of ZnO@CuO in comparison to that of ZnO. Separation and transfer of photogenerated electron-hole pairs for the improved photocatalytic performances are also confirmed for other heterostructures [111-113].

The remaining MO percentages in solution under dark conditions are found as 50.7%, 53.15%, 70.6% and 71.5% for ZnO@CuO, ZnO@CuO (40%), ZnO@CuO (67%) and ZnO@CuO (84%), respectively (Figure 3.16b). Under humid conditions, adsorption of water molecules on the whole frame of ZnO@CuO is expected. The predominant interaction of water molecules can be with Zn and Cu sites for low water content as also noticed in the studies of Gul-E-Noor et al. and Castillo et al. [114, 115]. When the amount of water increases, adsorption through the pores can be satisfied and the number of the surface OH groups increase around the ZnO@CuO. ZnO@CuO (40%) almost resembles dry humid conditions and shows a similar dark adsorption capacity with ZnO@CuO. However, the

higher number of OH groups in the presence of ZnO@CuO (67%) and ZnO@CuO (84%) decrease the available sites on the frames for the adsorption of negatively charged MO moiety. Contrarily, MB dark adsorption is enhanced by the increase in RH values of ZnO@CuO (Figure 3.16d). The negatively charged ZnO@CuO surface undergoes an electronic interaction with positively charged MB molecules.

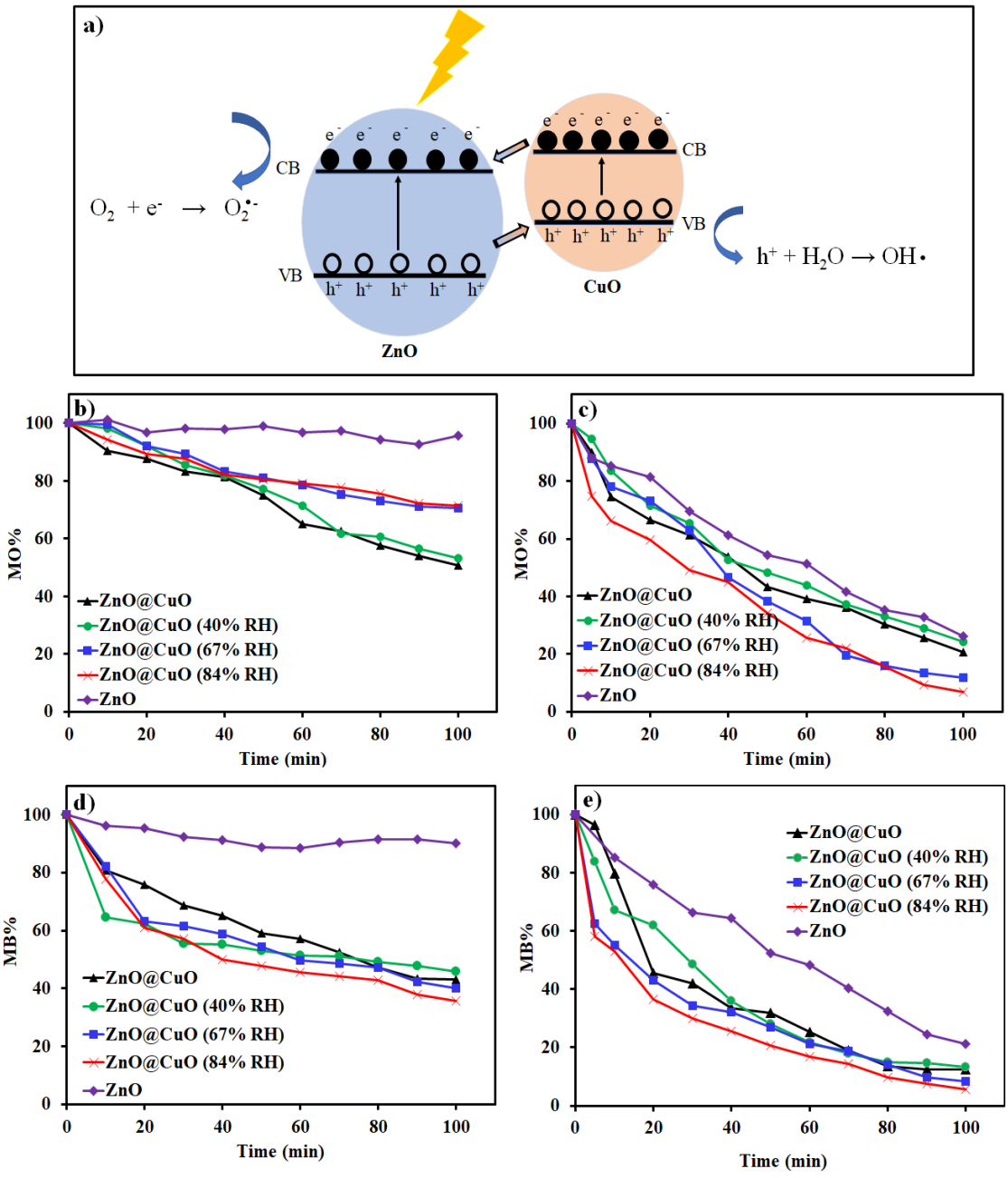

Figure 3.16. (a) Schematic presentation of charge carriers' transfer mechanism in ZnO@CuO under UV irradiation, (b-d) ZnO, ZnO@CuO and humidified ZnO@CuO; dark adsorption experiments for MO and MB, and (c-e) photoactivities for MO and MB.

Under irradiation, surface OH groups play major role in the photocatalytic processes for the production of hydroxyl radicals. Decolorization/degradation of azo dyes, gas/aqueous phase photocatalytic reactions and oxygen activation reactions by semiconductors occurs in the presence of highly reactive hydroxyl radicals [116, 117]. These radicals are generated via reactions of photogenerated holes with OH^- groups and/or H_2O molecules. ZnO@CuO under humid conditions is capable to produce more hydroxyl radicals. The successive attacks of these radicals are beneficial to obtain higher MO and MB decolorization percentages. Hence, the highest MO (93.3%) and MB (94.4%) decolorization percentages are detected in the presence of ZnO@CuO (84%) (Figure 3.16c and e). Moreover, the crystalline quality of ZnO and CuO nanoparticles has an effect in the photocatalytic performances of ZnO@CuO and humidified ZnO@CuO. The best photoactivity is achieved with highest crystallite sizes of both CuO and ZnO in the presence of ZnO@CuO (84%). Thus, it can be suggested that the migration of photogenerated electrons and holes to crystal surface is mostly favored under 84% RH to initiate redox reactions with the adsorbed MO and MB.

The catalyst ZnO-CuO prepared by the impregnation method show a lower dark adsorption capacity and photoactivity for both MO and MB in comparison to that of ZnO@CuO obtained from Cu-BTC (Figure 3.17). The larger surface area (45 $m^2\ g^{-1}$) and pore volume (0.039 $cm^3\ g^{-1}$) of ZnO@CuO enhance its adsorption ability and photocatalytic performance relative to the ZnO-CuO with 20.8 $m^2\ g^{-1}$ surface area and 0.029 $cm^3\ g^{-1}$ pore volume. The fabrication of ZnO and CuO simultaneously by impregnation method causes to loading of the photocatalysts on each other. Under irradiation, this leads to block the active sites of ZnO and CuO from absorbing the incoming photons, known as “shading effect” (or shielding effect). This effect is also explored in copper-doped titania catalysts prepared by the impregnation method for photocatalytic reduction of CO_2 and copper-modified titania in the oxidative reaction systems for enhanced photoactivities [118,119]. However, ZnO@CuO obtained from Cu-BTC provides distribution of ZnO and CuO nanoparticles in a larger area so that shielding effect can be inhibited and an effective photon utilization can be satisfied. This increases of efficiency of the catalytic process of ZnO@CuO.

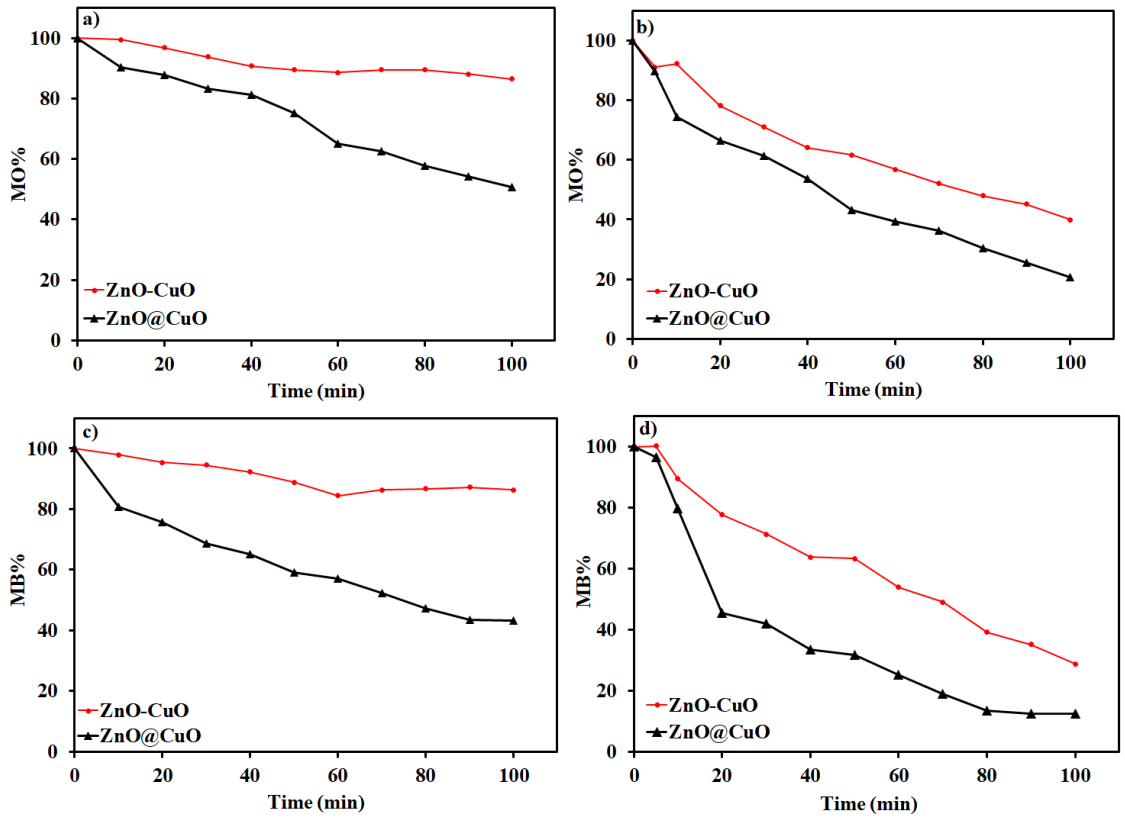

Figure 3.17. Dark adsorption (a-c) and photoactivity (b-d) comparison of ZnO-CuO and ZnO@CuO for MO and MB.

Kinetic analysis of ZnO@CuO and ZnO@CuO (84% RH) is performed in the concentration range of 0.81-32.7 mg L^{-1} for both MO and MB. Plots of ln $([MO]_0/[MO]_t)$ or $([MB]_0/[MB]_t)$ versus time show a linear relation, where $[MO]_0$ or $[MB]_0$ refers the initial concentration of MO or MB after the dark adsorption (mg L^{-1}), $[MO]_t$ or $[MB]_t$ refers the concentration of MO or MB at time "t" (min) under irradiation (not shown). Rate constant k (min^{-1}) can be found from the line-slopes. Pseudo-first order kinetics is followed by the inverse relation between k and $[MO]_0$ or $[MB]_0$ up to 8.17 mg L^{-1}. For the highest MO or MB concentrations (from 16.3 mg L^{-1} to 32.7 mg L^{-1}), k values do not differ significantly since path length of the photons entering the solution decreases. The weak penetration of the light limits the photocatalytic reaction at the junction of the catalyst surface. Therefore, beyond 8.17 mg L^{-1}, rates follow zero-order kinetics, being independent of high initial MO or MB concentrations (Figure 3.18a). As a general aspect, ZnO@CuO (84% RH) has higher k values owing to the formation of more $^{\bullet}OH$ radicals and promoted photoactivity.

Langmuir-Hinshelwood (L-H) model is also applicable to ZnO@CuO and ZnO@CuO (84% RH) (Figure 3.18b). Accordingly, the linearity in the plot of reciprocals of rates 1/R (R=rate of decolorization for MO or MB) versus the reciprocals of initial MO or MB concentrations gives the adsorption coefficient of MO or MB from the slopes (*K*, L mg^{-1}) and the reaction rate constant from the intercepts (k, mg L^{-1} min^{-1}). For ZnO@CuO, *k* values are found as 0.107 mg L^{-1} min^{-1} (for MO), 0.324 mg L^{-1} min^{-1} (for MB) and K values are calculated as 0.323 L mg^{-1} (for MO), 0.232 L mg^{-1} (for MB). For ZnO@CuO (84% RH), *k* values are found as 0.295 mg L^{-1} min^{-1} (for MO), 0.401 mg L^{-1} min^{-1} (for MB) and K values are calculated as 0.080 L mg^{-1} (for MO), 0.059 L mg^{-1} (for MB).

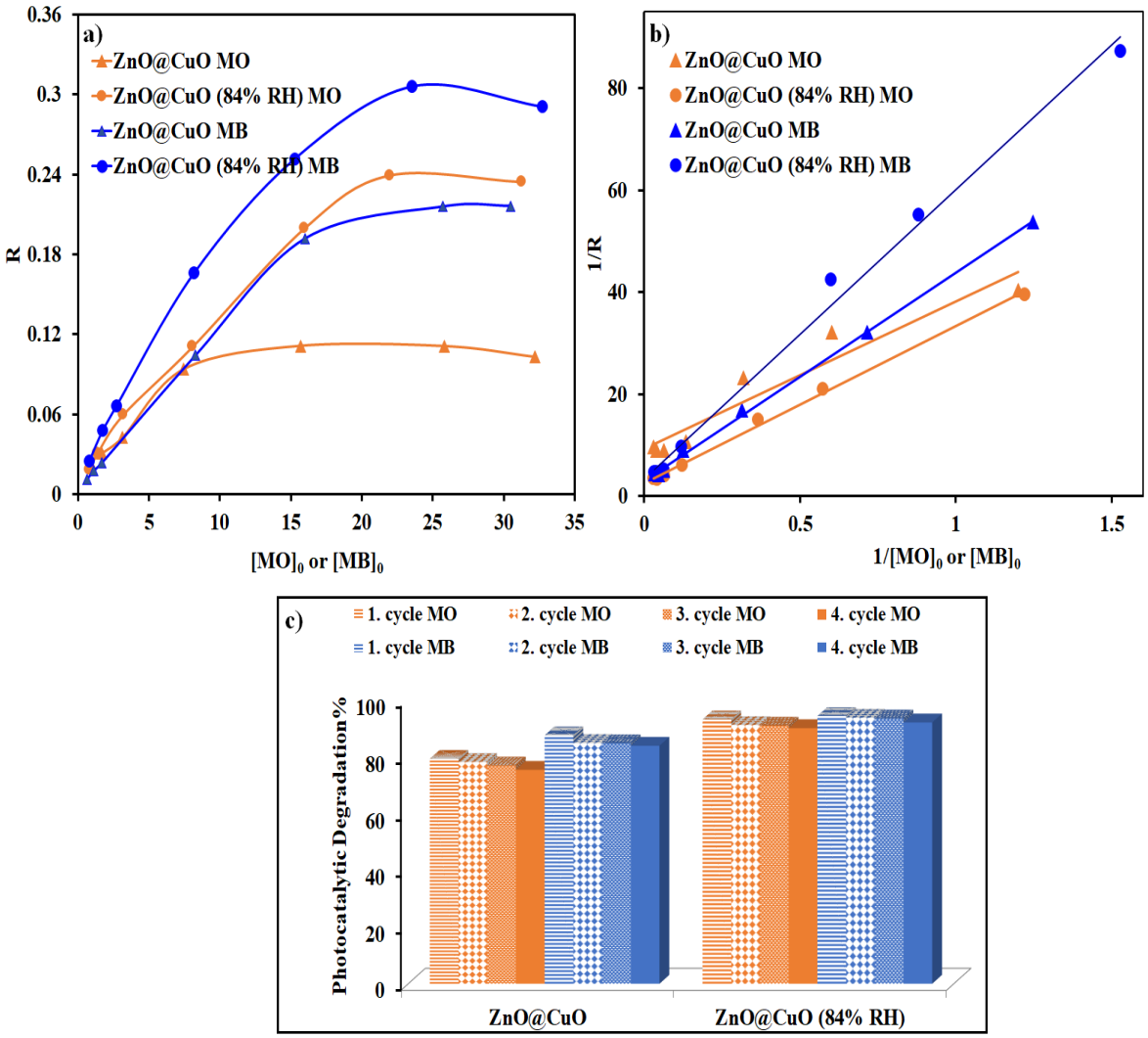

Figure 3.18. (a) Kinetic analysis, (b) Langmuir-Hinshelwood plots, (c) Reuse studies of ZnO@CuO and ZnO@CuO (84% RH) in the presence of MO and MB.

Figure 3.18c shows the reusability of ZnO@CuO and ZnO@CuO (84% RH) for the degradation of MO and MB over four cycles. After each cycle, the catalyst is separated from the reaction mixture, washed and then dried. Photoactivity reductions after the fourth cycle are found as 4.2% (for MO) and 5.1% (for MB) in the presence of ZnO@CuO and 2.1% (for MO) and 3.7% (for MB) in the existence of ZnO@CuO (84% RH). Since there is no significant decline in the performances, good stability and sustainability can be suggested for both ZnO@CuO and ZnO@CuO (84% RH). The slight decrements can be due to the passivation of the active surface sites in either CuO or ZnO and/or partial destruction of ZnO@CuO heterojunction via multiple washing.

3.3.4. Conclusion

ZnO@CuO is successfully synthesized by a simple and versatile procedure. CuO formation from Cu-BTC and simultaneous in-situ generation of ZnO nanoparticles are proved using XRD, Raman, BET, UV–Vis DRS, SEM-mapping (EDX) and XPS techniques. The high surface area and porosity of ZnO@CuO consolidate its adsorption capacity and photoactivity in comparison to ZnO. Moreover, the higher photocatalytic activity is mainly attributed to the improved charge separation in the ZnO@CuO heterojunction. Effect of humidity play an important role to both in the dark adsorption capabilities and photocatalytic performances. Increments in crystalline sizes of both ZnO and CuO are observed under highest RH values. Anionic (MO) or cationic (MB) character influence the electronic interactions with ZnO@CuO and humidified ZnO@CuO under dark conditions. The photocatalytic performances are enhanced by increments in humidity conditions for both MO and MB. As a concluding remark, ZnO@CuO can be suggested as cost-effective, highly efficient and eco-friendly reusable catalyst, having potential to expand the applications of ZnO combined MOF structures in environmental issues.

3.4. Improved Adsorption Capacity and Photoactivity of ZnO-ZIF-8 Nanocomposites

This section is published as: D. Tuncel, A.N. Ökte, "Improved Adsorption Capacity and Photoactivity of ZnO-ZIF-8 Nanocomposites", *Catalysis Today*, Vol. 361, pp. 191-197, 2021. This copyrighted article is reproduced with permission from Elsevier (Figure B.4).

3.4.1. Introduction

ZnO mediated photocatalysis is an impressive technique leading to degradation of toxic compounds. The surface morphology and crystallinity stand out crucial factors for determining photocatalytic efficacy of ZnO. Since, the high surface area and porosity bring out more active sites, highly active charge carriers can migrate the surface to react with the guest molecules [120]. Therefore, recent years much efforts are dedicated to enhance photocatalytic activity of ZnO by combining a wide range of porous materials. Zeolitic imidazolate framework-8 (ZIF-8), consisting of Zn^{2+} tetrahedrally coordinated with four 2-methylimidazole ligands, is a new type crystalline porous material in a subclass of metal organic frameworks. The similar topology of ZIF-8 arises from Im-Zn-Im bridge which is counterpart of the Si-O-Si bridge in zeolites and thus, provide high thermal stability to the framework [121, 122]. It can also maintain the ordered porosity and crystalline phase when it is immersed in organic solvents, water, and alkaline solution [123]. The water stability of ZIF-8 derived from the coordination of Zn metal with imidazole linkers that includes methyl groups and leads to hydrophobic structure [123]. Additionally, ZIF-8 can behave as an electron donor to provide electrons to Zn metal center, since 2-methylimidazole owns abundant delocalized electrons of π bond [124]. Despite these attractive features of ZIF-8, the ZIF-8 supported ZnO photocatalysts have been rarely reported in the literature. Wang et al synthesized ZnO@ZIF-8 heterostructure via in-situ growth strategy to test for the photocatalytic degradation of Cr(IV) and methylene blue [125]. The size selectivity was found as an important factor for higher degradation of Cr(IV). Yu et al. investigated degradation of methylene blue in the presence of core-shell ZnO@ZIF-8 [126]. They proposed a mechanism for the electron transfer from photoexcited organic ligands to metals, termed as ligand-to-metal-charge-transfer (LMCT). In the study of Du et al. the porous ZnO

photocatalyst was prepared by thermal treatment of ZIF-8 [127]. It was observed that high calcination temperature distort the porous structure of ZIF-8 and decrease the surface area.

The aim of this study is to synthesize ZnO-ZIF-8 300°C nanocomposite by combining attractive properties of ZnO photocatalyst and ZIF-8 support. The nanocomposite simultaneously possesses original ZIF-8 morphology-porous structure with adsorbed ZnO nanoparticles. Thus, our strategy includes two aspects: one is the utilization of high surface area and porous nature of ZIF-8, the other is the combination of ZIF-8 with ZnO to enhance both dark adsorption ability and photocatalytic efficiency. Apart from the literature, we focus on: (1) interaction of the nanocomposite with an anionic dye (MO) and a cationic dye (MB) under dark conditions, (2) photoactivity of the nanocomposite under UV irradiation, (3) comparative evaluations with ZnO, ZIF-8 and ZIF-8 300°C under dark and UV irradiation; (4) photoactivity and adsorption ability of the nanocomposite under humidity conditions; (5) reusability of the nanocomposite and its humidified form. To provide further investigation, crystalline structures and morphological features of ZIF-8, ZIF-8 300ºC and ZnO-ZIF-8 300ºC are followed by X-ray diffraction (XRD) analysis, fourier transform infrared (FTIR) spectroscopy and scanning electron microscopy (SEM) with energy dispersive X-ray (EDX and mapping) analysis. The surface area and porosity of the samples are determined by nitrogen adsorption-desorption isotherms (BET). Absorption profiles are examined by DRS UV-vis analysis. Variations on the structural features of ZIF-8 and the nanocomposite are controlled under different relative humidity (RH) values (40, 67, 84% RH). The examination of humidity effect on adsorption capacity and photocatalytic efficiency extend the application of ZnO-ZIF-8 300°C in real conditions. The photocatalytic performance of ZnO-ZIF-8 300°C is found to be higher than the two single components of the nanocomposite. This is attributed to efficient charge separation and active sites supplied by ZIF-8. ZnO-ZIF-8 300°C structure is maintained under humidity conditions. ZnO-ZIF-8 (84% RH) is found to exhibit the highest photoactivity for both MO and MB.

3.4.2. Experimental

3.4.2.1. Materials. The ZIF-8 (Aldrich), methyl orange (Merck), methylene blue (Merck), Zinc nitrate hexahydrate ($Zn(NO_3)_2 \cdot 6H_2O$) (Merck), sodium carbonate (Na_2CO_3) (Merck) are provided by the suppliers.

3.4.2.2. Synthesis of Catalysts. The ZnO-ZIF-8 300ºC is synthesized from zinc nitrate hexahydrate ($Zn(NO_3)_2 \cdot 6H_2O$) and sodium carbonate (Na_2CO_3) precursors via co-precipitation method [128]. Briefly, the dissolved ($Zn(NO_3)_2 \cdot 6H_2O$) in 100 mL deionized water is added slowly into a 100 mL (Na_2CO_3) solution and mixed for 2 h at room temperature. Requisite amount of ZnO solution is then mixed with the aqueous suspension of ZIF-8. After centrifugation and extensive washings, the precipitate is dried at 100ºC for 12 h and calcinated in a muffle furnace at 300ºC for 5 h. The resulting nanocomposite is labeled as ZnO-ZIF-8 300ºC. For comparison, the bare ZnO is prepared with the same procedure in the absence of ZIF-8. The ZIF-8 300ºC is obtained by the calcination of the raw ZIF-8 at 300ºC for 5 h under ambient air. The humidified ZnO-ZIF-8 300ºC nanocomposites are prepared inside the climate chamber (KKS 115 TOP+INOX/G) for 72 h, under 40%, 67% and 84% relative humidity (RH) values. The nanocomposites are named as ZnO-ZIF-8 300ºC (40% RH), ZnO-ZIF-8 300ºC (67% RH), ZnO-ZIF-8 300ºC (84% RH).

3.4.2.3. Characterization Techniques. The crystallinity of the samples are determined by Rigaku-D/MAX Ultima X-ray diffractometer (XRD) with Cu Kα radiation (λ =1.54 Å) operating at 40 kV and 40 mA and scanning rate 2 min^{-1}. The FTIR spectra are recorded on the Thermo Scientific Nicolet 6700 FTIR spectrometer in the range of 4000–400 cm^{-1}. Nitrogen adsorption-desorption tests are carried out under liquid nitrogen at 77 K with a Quantachrome Nova 2200e automated gas adsorption system. To measure the specific surface area and pore sizes of materials, multi point BET analysis and BJH method are used. Absorption spectrums are obtained via UV-Vis spectrophotometer (Shimadzu UV-2450) equipped with an integrating sphere reflectance accessory. The surface morphologies are examined by using scanning electron microscopy in combination with EDX analysis on an ESEM-FEG/EDAX Philips XL-30 instrument operating at 20 kV using catalyst powders supported on carbon tape. The chemical states of the surface constituents are confirmed by XPS by using Thermo Scientific K-Alpha X-ray Photoelectron Spectrometer equipped with hemispherical electron analyzer and Al-K micro-focused monochrometer.

3.4.2.4. Adsorption and Photocatalytic Tests. The adsorption capacities and photocatalytic performances are carried out in laboratory constructed box continuous circulation mode at room temperature. Adsorption capacity of the samples are examined under the dark

conditions. For photocatalytic tests, eight black fluorescent lamps (Philips TL 15 W/5 BLB) that supply light of wavelength 320-440 nm are used. The incident photon flux for all lamps is measured as 4.7 $x10^{15}$ photon/s using potassium ferrioxalate ectinometer in our previous experiments. A pyrex flask is used as a reactor for 0.2 gr catalyst in 200 mL MO or MB solution at continuous circulation mode at ambient conditions. This amount is regulated according to the general trends in similar reaction systems, since catalysts with concentrations higher than 1 g L^{-1} inhibit the light penetration and hence decrease the photoactivity [129]. The concentrations of 3.27 mg L^{-1} (for MO) and 3.19 mg L^{-1} (for MB) are used to simulate a medium loaded with such dye molecules [129]. To reach the adsorption equilibrium, suspensions are magnetically stirred in the dark for 30 min. During the irradiation process, aliquots (about 5 mL) are retrieved from the flask at certain time intervals and analyzed after filtering through Millipore filter (0.22 μm). The characteristic absorption intensity of MO at 464 nm and MB at 665 nm are measured by using Shimadzu UV-Vis (2450) Spectrophotometer to monitor the variation in concentration of MO and MB during the photocatalytic decolorization runs.

3.4.3. Results and Discussion

3.4.3.1. XRD Analysis. XRD analysis is used to assess the crystallinity of ZIF-8, ZIF-8 300ºC and ZnO-ZIF-8 300ºC and humidified samples (Figure 3.19a and Figure A.2). The ZIF-8 displays the diffraction peaks at 7.5, 10.4, 12.7, 18.4º (2θ), representing (011), (002), (112), (222) crystal planes of the zeolitic structure (MDI-JADE6) (Figure 3.19a). Despite the decrements in the peak intensities, all diffraction peaks of ZIF-8 300ºC are located in the same positions of ZIF-8 peaks. Thus, ZIF-8 structure is maintained after calcination as also detected in the studies of Wang et al. [130] and Pan et al. [131]. Additionally, peaks emerged at 31.9, 34.6, 36.4, 47.7, 56.7, 63.1 and 66.6º (2θ) are ascribable to (100), (002), (101), (102), (110), (103) and (200) reflections of ZnO hexagonal wurtzute structure, respectively. This indicates that ZIF-8 undergoes partial phase transformation and forms ZnO with ambient oxygen at 300ºC. Zhou et al. [132] also noticed such an alteration in the structure of ZIF-8 at high temperatures.

The sharp and intensified ZnO peaks in the ZnO-ZIF-8 300ºC pattern show the successful growth of ZnO nanoparticles within the matrix. Contrarily, ZIF-8 reflections are

suppressed due to the phase transformation of ZIF-8 and homogeneous dispersion of ZnO on the ZIF-8 surface. Under the humid conditions, ZIF-8 and ZIF-8 300ºC patterns do not show a significant variation (Figure A.2). In addition to intense ZnO peaks, ZIF-8 peaks are preserved in the patterns of humidified ZnO-ZIF-8 300ºC catalysts.

The crystalline sizes of materials are estimated according to the Scherrer equation based on the most intense peaks of ZIF-8 (011) and ZnO (101). The size of ZIF-8 crystallites are found as 27.8 nm and 23.3 nm for ZIF-8 and ZIF-8 300ºC, respectively. The decrement can be due to the partial disruption of ZIF-8 frame at 300ºC. The ZnO crystalline sizes are calculated as 10.7 nm (for the ZIF-8 300ºC) and 24.2 nm (for ZnO-ZIF-8 300ºC), indicating that ZIF-8 reinforces the formation of ZnO nanoparticles. Moreover, increase in humidity percentage enables interaction of ZnO nanoparticles with water vapor molecules. This leads to small variation in ZnO sizes as 24.9 nm, 25.3 nm and 25.9 nm for ZnO-ZIF-8 300ºC (40% RH), ZnO-ZIF-8 300ºC (67% RH) and ZnO-ZIF-8 300ºC (84% RH)), respectively.

3.4.3.2. FTIR Analysis. Figure 3.19b shows FTIR spectra of ZIF-8, ZIF-8 300ºC, ZnO-ZIF-8 300ºC, ZnO and 2-methylimidazole. ZIF-8 demonstrates peaks of aromatic C-H stretching in the imizadole rings at 3135 cm^{-1} and aliphatic C-H stretching in the methyl groups at 2929 cm^{-1} [133]. The signal at 1583 cm^{-1} is associated with C=N stretching modes whereas the peaks at 1422 cm^{-1} and 1383 cm^{-1} correspond to the entire ring stretching. The peak located at 1146 cm^{-1} is ascribed to aromatic C-N stretching mode. The in-plane bending mode of imidazole ring and the aromatic bending mode of sp^2 C-H are assigned to the signals at 994 and 760 cm^{-1}, respectively [133]. Similarly, the peak at 684 cm^{-1} is derived from out of plane bending of 2-methylimidazole ring. The Zn-N vibration is detected at 424 cm^{-1}, due to the coordination of zinc ions to the linkers via nitrogen atoms [134]. The shift in this peak to 433 cm^{-1} (in the presence of ZIF-8 300ºC) and 435 cm^{-1} (in the presence of ZnO-ZIF-8 300ºC) confirm formation of ZnO, being in good agreement with Zn-O stretching at 436 cm^{-1} in the pattern of ZnO. Meanwhile, ZnO-ZIF-8 300ºC shows characteristic peaks of ZIF-8, implying that ZIF-8 structure is preserved in the nanocomposite. This is also consistent with the XRD pattern of ZnO-ZIF-8 300ºC.

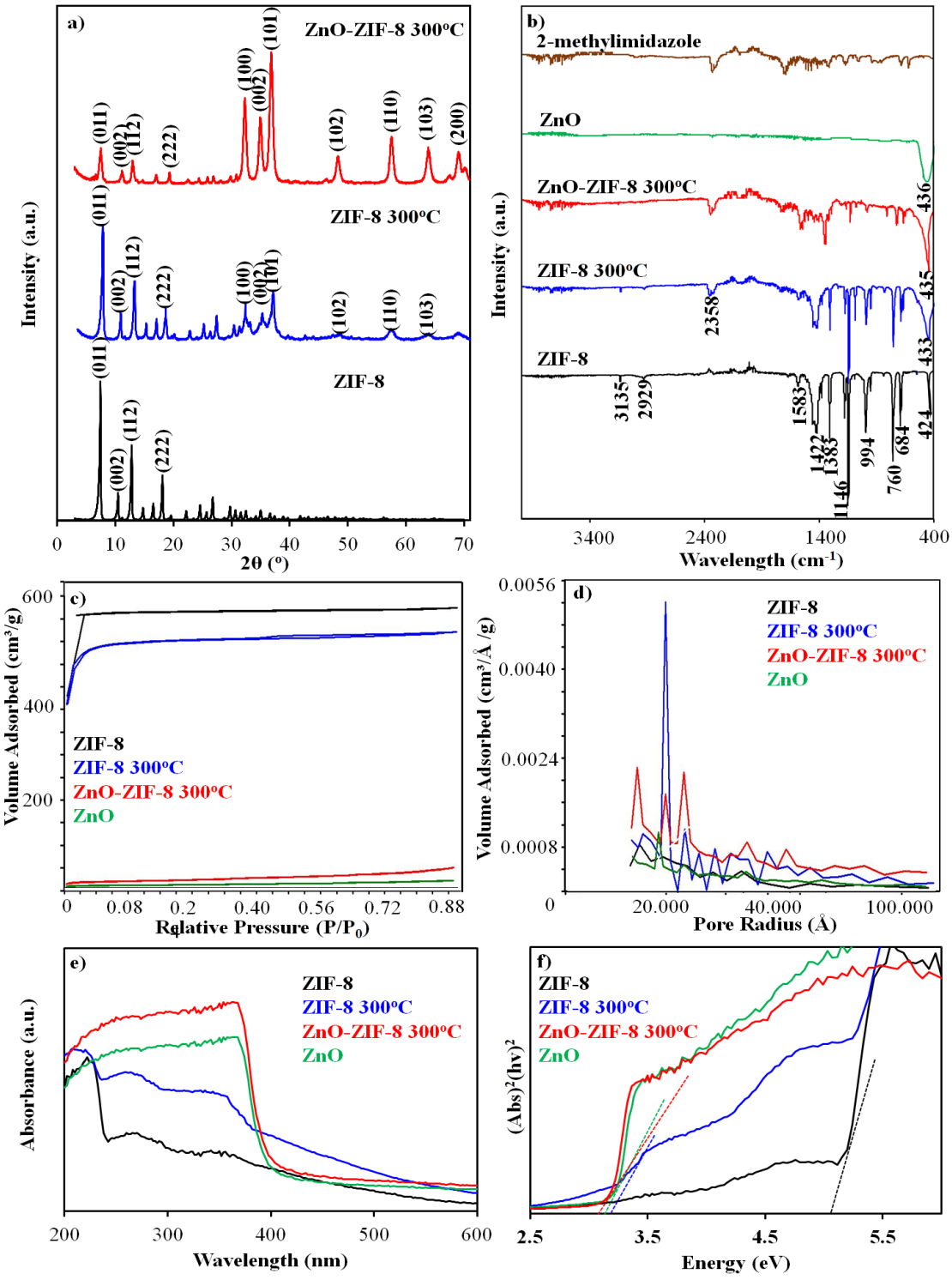

Figure 3.19. (a) XRD patterns of ZIF-8, ZIF-8 300ºC, ZnO-ZIF-8 300ºC, (b) FTIR spectra of ZIF-8, ZIF-8 300ºC, ZnO-ZIF-8 300ºC, ZnO, 2-metylimidazole (c) Nitrogen adsorption/desorption isotherms and (d) pore size distribution plots of ZIF-8, ZIF-8 300ºC, ZnO and ZnO- ZIF-8 300ºC (e) UV-Vis DRS spectra and (f) band gap absorption edges of ZIF-8, ZIF-8 300ºC, ZnO-ZIF-8 300ºC and ZnO.

3.4.3.3. Nitrogen Adsorption-Desorption Isotherms. Figure 3.19c and d show nitrogen adsorption-desorption isotherms and pore size distributions of ZIF-8, ZIF-8 300ºC, ZnO and ZnO-ZIF-8 300ºC, respectively. ZIF-8 curve fits well with a type I isotherm, which is typical for microporous structures. BET surface area and pore size of ZIF-8 are measured as 1218 $m^2\ g^{-1}$ and 0.011 $cm^3\ g^{-1}$, respectively. Calcination and introduction of ZnO nanoparticles reduce the area (357 $m^2\ g^{-1}$ for ZIF-8 300ºC and 206 $m^2\ g^{-1}$ for ZnO-ZIF-8 300ºC) and expand the pore volume (0.026 $cm^3\ g^{-1}$for ZIF-8 300ºC and 0.036 $cm^3\ g^{-1}$for ZnO-ZIF-8 300ºC). For ZIF-8 300ºC, an adsorption edge is detected at low relative pressures similar to that of ZIF-8, while the adsorbed amount is lower. ZIF-8 300ºC also exhibits a small capillary condensation at high pressures (0.4-0.6 P/P_0) due to the generation of mesopores during the calcination process. Similarly, Zhou et al. confirmed formation of mesopores under oxygen atmosphere for carbonized ZIF-8 [132]. ZnO-ZIF-8 300ºC reveals type IV isotherm typical for mesoporous structures with capillary condensation in the range of high P/P_0 (0.6-0.9). The increments in surface area and the pore volume of ZnO-ZIF-8 300ºC in comparison to the bare ZnO (7.5 $m^2\ g^{-1}$, 0.012 $cm^3\ g^{-1}$) signify the importance of ZIF-8 existence in the nanocomposite. Consequently, an extension in the adsorption ability and photocatalytic activity of ZnO-ZIF-8 300ºC is expected.

3.4.3.4. UV-Vis DRS Analysis. The optical property of the samples is investigated by UV–vis diffuse reflectance spectroscopy (DRS) (Figure 3.19e). ZIF-8 owns an absorption edge around 227 nm. This strong absorption has a similar origin with previously reported MOF-5 profile [135]. MOF-5 possessed a semiconductor behavior via its Zn_4O_{13} clusters and the organic ligand acting as an efficient energy transfer antenna [135]. Hence, ZnN_4 clusters might perform in the same way within the matrix of ZIF-8, induce a charge transfer mechanism from ligand to metal and create an excitonic absorption [136]. ZIF-8 300ºC profile differs from the ZIF-8 with a tailed absorption edge around 380-400, indicating formation of ZnO during the calcination process. Meanwhile, ZnO-ZIF-8 300ºC has an analogous profile to that of bare ZnO. The enhanced characteristic edge of ZnO confirms the successful growth of ZnO nanoparticles in the nanocomposite. In addition, the UV-vis absorption spectra of the samples are transformed to the band-gap values which are evaluated by measuring the x-axis intercept of an extrapolated tangential line from the linear region of the curves (Figure 3.19f). The band gaps of ZIF-8, ZIF-8 300ºC, ZnO-ZIF-8 300ºC and ZnO are estimated to be 4.9 eV, 3.2 eV, 3.0 eV and 3.1 eV, respectively. Accordingly, the

enhanced absorption of ZIF-8 300ºC and ZnO-ZIF-8 300ºC in the UV region inspire us to evaluate their photocatalytic activities under UV irradiation.

3.4.3.5. SEM-Mapping Analysis. The morphologies of the samples are examined by SEM (EDX-mapping) analysis (Figure 3.20). ZIF-8 has octahedral cubic particles with major constituents of C (73.8 at. %), N (17.6 at. %), Zn (6.7 at. %), and O (1.8 at. %) (Figure 3.20a-e). The micrograph of ZIF-8 300° (Figure 3.20f) demonstrates distorted particles on and around the ZIF-8 frame. Mapping images of ZIF-8 300° are shown in Figure 3.20g-j. Zn signals dominate on both distorted particles and ZIF-8 octahedrons (Figure 3.20g). The whole surface shows higher percentages of Zn (12.7 at. %) and O (15.7 at. %) in comparison to the percentages detected in the presence of ZIF-8. Additionally, two regions are labelled on the surface. The first one (labelled as I) is selected on a distorted particle which exhibits 15.4 at. % Zn and 10.7 at. % O (Figure 3.20k). The second labeled region is on an octahedron with 13.6 at. % Zn and 8.7 at. % O (Figure 3.20l). Thus, increments in Zn and O percentages indicate formation of ZnO particles and their random dispersion over the matrix.

In the image of ZnO-ZIF-8 300°C, cubic morphology of ZIF-8 is retained (Figure 3.20m). Besides, formation of agglomerated particles and their heterogeneous distribution are detected. Figure 3.20n-r display mapping images. Zn signals accumulate on the particles (Figure 3.20n). Three regions are labelled to examine the constituents (Figure 3.20s-u). The EDX analysis of the first (11.5 at. % Zn and 24.67 at. % O) and third regions (11.24 at. % Zn and 26.5 at. % O) show similar percentages of Zn and O. The second region has much higher percentages (25.7 at. % Zn and 35.3 at. % O). These corroborate the generation of ZnO nanoparticles for ZnO-ZIF-8 300°C. Under humid conditions, the morphologies of ZIF-8 and ZIF-8 300ºC do not differ upon increasing RH values (Figure 3.21).

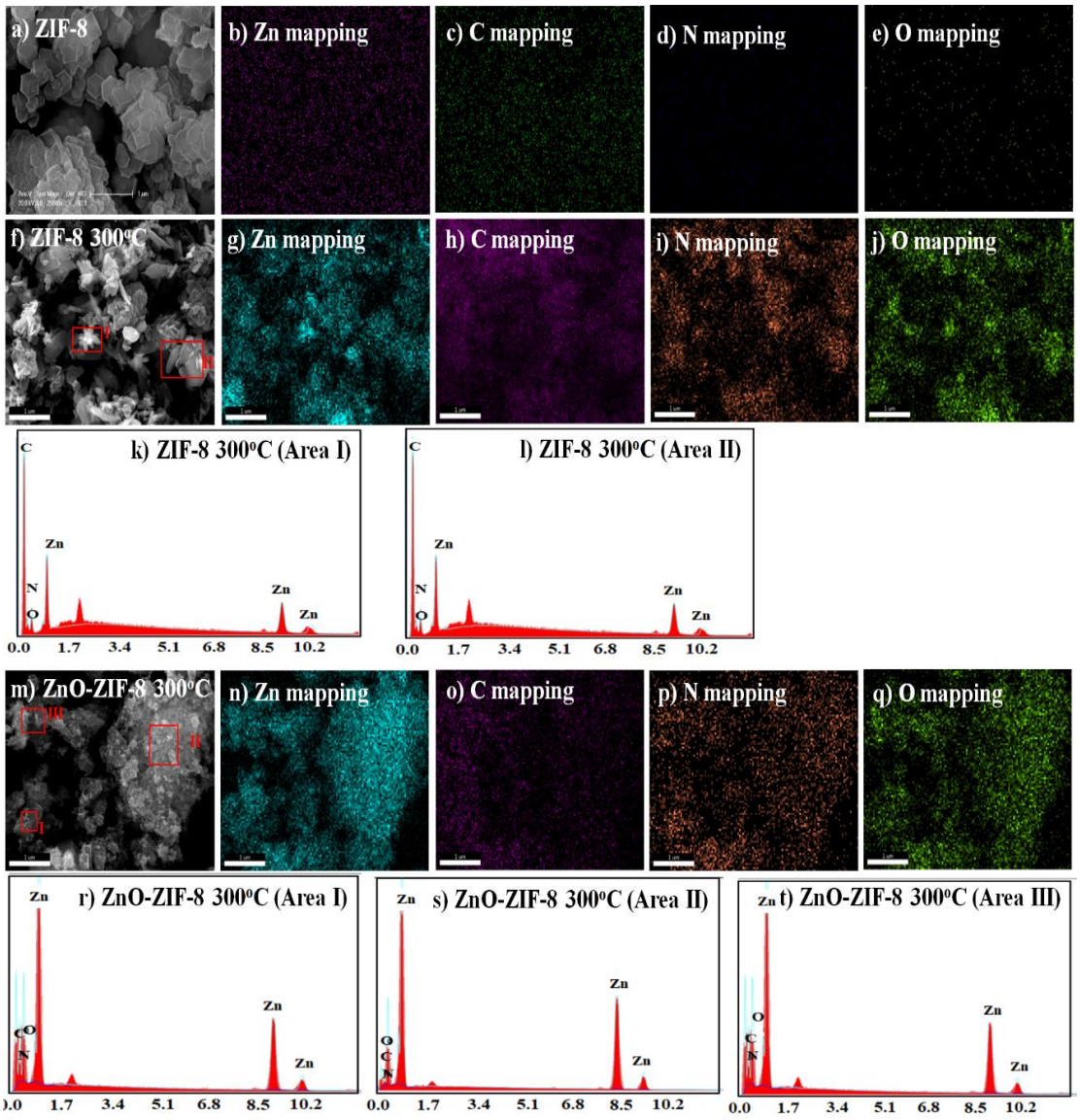

Figure 3.20. SEM images of ZIF-8 (a), ZIF-8 300ºC (f) and ZnO-ZIF-8 300ºC (m), Elemental mapping analysis of ZIF-8 (b-e), ZIF-8 300ºC (g-j) and ZnO-ZIF-8 300ºC (n-r), EDX analysis of ZIF-8 300ºC (k,l) and ZnO-ZIF-8 300ºC (s-u).

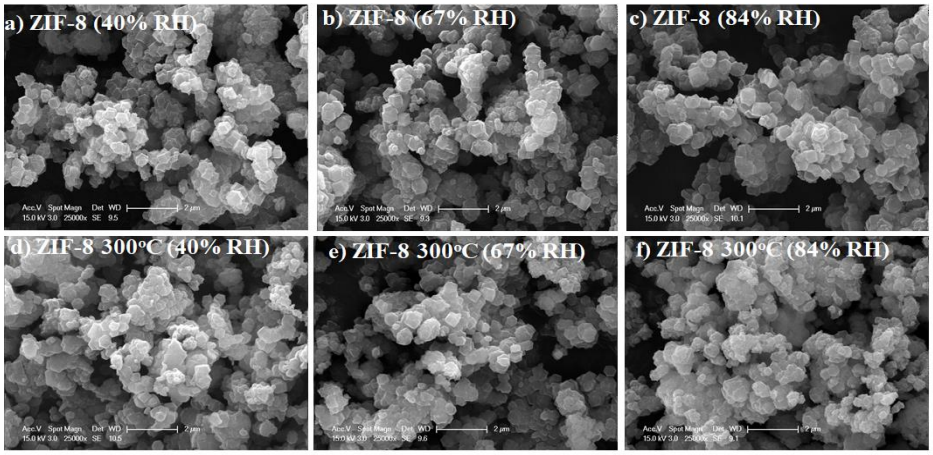

Figure 3.21. SEM images of ZIF-8 and ZIF-8 300°C under humidified conditions.

3.4.3.6. XPS Analysis. XPS measurement is conducted to determine chemical states of atoms in ZIF-8, ZIF-8 300°C and ZnO-ZIF-8 300°C. Survey scans of ZIF-8 and ZIF-8 300°C reveal sharp peaks of Zn 2p, C 1s, O 1s and N 1s, whereas only Zn 2p, O 1s and C 1s are observed in the spectrum of ZnO-ZIF-8 300°C (Figure 3.22a). For ZIF-8 300°C, the intensity of C and N peaks decrease due to the distortion of ligand groups during the calcination process. In the presence of ZnO-ZIF-8 300°C, formation of ZnO nanoparticles increase the intensity of O 1s peak.

For all samples, Zn 2p has a doublet at 1022 eV ($2p_{3/2}$) and at 1045 eV ($2p_{1/2}$) which are in accordance with the binding energy of Zn 2p in pure ZnO [137] (Figiure 3.22b). For ZIF-8, $2p_{3/2}$ state is deconvoluted into two peaks, which are assigned to Zn-N (1020.94 eV) and Zn-O (1021.48 eV) bonds, respectively [138]. ZIF-8 300°C exhibits slight shifts in these energies due to the variation in the environment of Zn atom during calcination. Besides, there is an increment in the intensity of Zn-O peak, being consistent with XRD, FTIR and UV-vis DRS results. ZnO-ZIF-8 300°C also shows an intensified Zn-O peak signal. The in-situ buildup of ZnO nanoparticles within ZIF-8 matrix weakens the interaction between Zn and N atoms of the ligands, while promoting Zn-O bond formation. Thereafter, electron density around Zn atoms decreases via electron withdrawing ability of O atoms. This is verified by the higher binding energy of Zn-O peak in the presence of ZnO-ZIF-8 300°C (1021.88 eV) in comparison to that of ZIF-8 (1021.48 eV) and ZIF-8 300°C (1021.66 eV). Zn $2p_{1/2}$ peak behave in a similar manner, Zn-O peak signal and also binding energies are

higher for both ZIF-8 300ºC (1045.48 eV) and ZnO-ZIF-8 300ºC (1045.58 eV) than ZIF-8 (1045.29 eV). Simultaneously, Zn-N peak intensity decreases for ZIF-8 300ºC and then disappears for ZnO-ZIF-8 300ºC.

In Figure 3.22c, ZIF-8 does not show a peak in O 1s region since it does not involve O in its structure. For ZIF-8 300ºC, a broad peak at around 530.8 eV is detected, which corresponds to carbonate species formed during the calcination [138, 139]. The O 1s spectrum of ZnO-ZIF-8 300ºC can be fitted into two peaks, centered at 529.75 and 531.27 eV, which are ascribed to lattice oxygen of Zn-O and oxygen in hydroxyl groups bound to Zn sites, respectively [140].

In the C 1s spectrum of ZIF-8, two deconvoluted peaks with binding energies of 284.11 and 285.03 eV are assigned to sp^2 hybridized C atoms in aromatic imidazole rings and sp^2 C bonded in the hetero-cycle N=C-N, respectively (Figure 3.22d). For ZIF-8 300ºC, these peaks shift to lower values due to the variation in the ligand groups during the calcination. An additional type of carbon is noticed at 286.53 eV (for ZIF-8 300ºC) and 288.71 eV (for ZnO-ZIF-8 300ºC), which belongs to surface loosely bound carbonate species (i.e., CO_3, C-O, C=O bonds) [131].

For ZIF-8, N 1s fitting has two peaks; the first one is assigned to N atom of imidazole linkers at 398.01 eV and the second belongs to nitrogen atom at Zn-N bond at 398.61 eV (Figure 3.22e). In ZIF-8 300ºC spectra, slight shifts of these peaks to higher binding energies and decrements in both peak intensities are detected. Such alterations are attributed to decrement in electron density around N atoms in Zn-N bond and replacement of N atoms with O atoms during the calcination process. For ZnO-ZIF-8 300ºC, N 1s peak is not observed.

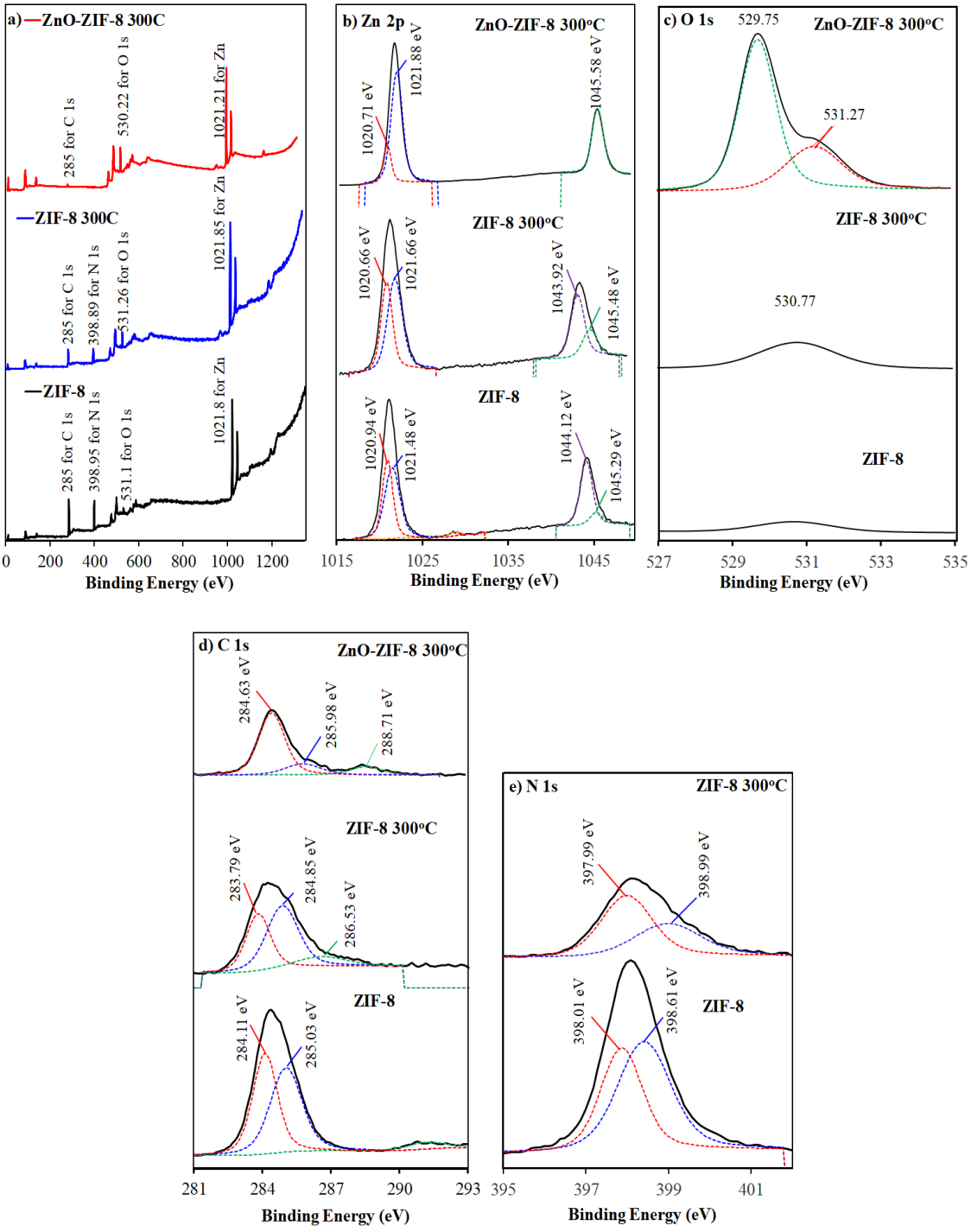

Figure 3.22. (a) XPS survey scan, XPS spectra of (b) Zn 2p, (c) O 1s, (d) C 1s and (e) N 1s in ZIF-8, ZIF-8 300°C and ZnO-ZIF-8 300°C.

3.4.3.7. Adsorption and Photocatalytic Tests. Figure 3.23 displays dark adsorption capacities and photocatalytic performances of ZIF-8, ZIF-8 300ºC, ZnO, ZnO-ZIF-8 300ºC and humidified ZnO-ZIF-8 300ºC catalysts. Under dark conditions, ZnO does not show significant adsorption for both MO and MB (Figure 3.23a and c). In the presence of ZIF-8, the remaining MO percentage is found as 33.4% after 100 min (Figure 3.23a). The surface of ZIF-8 is positively charged at pH values less than 10 [141]. This favors the adsorption of negatively charged MO moiety due to the interaction between the cationic metal center of ZIF-8 and the sulfonic group of MO. Contrarily, repulsive forces exist between ZIF-8 and positively charged MB, causes limited dark adsorption (about 20%) after 100 min (Figure 3.23c). In the presence of ZIF-8 300ºC, the formation of ZnO nanoparticles creates a negatively charged surface due to the lone pair electrons of oxygens in Zn-O bond, as previously reported [142]. Therefore, ZIF-8 300ºC dark adsorption capacity is higher for MB than that for MO (Figure 3.23a and c). Despite the repulsive interactions between ZnO nanoparticles and MO in ZnO-ZIF-8 300ºC, a significant extent of MO adsorption is observed relative to ZIF-8 300ºC and bare ZnO (Figure 3.23a). This can be elucidated by the change in the structure of ZnO-ZIF-8 300ºC from a non-porous form (in the presence of bare ZnO) and a microporous form (in the presence of ZIF-8 300ºC) to a mesoporous matrix. In the case of MB, Columbic interactions among C-S^{+}=C functional groups and ZnO nanoparticles improve the dark adsorption ability of ZnO-ZIF-8 300ºC in comparison to ZIF-8 300ºC, ZIF-8 and bare ZnO (Figure 3.23c). The adsorption capacity of ZnO-ZIF-8 300ºC is further examined under humidified conditions (Figure 3.23e and g). An increase in surface hydroxyl groups is expected from ZnO-ZIF-8 300ºC (40 %RH) to ZnO-ZIF-8 300ºC (84% RH). Accordingly, the affinity of ZnO-ZIF-8 300ºC toward MO gradually decreases with the increasing RH values, indicating a competition between surface hydroxyl groups and sulphonic groups of MO (Figure 3.23e). For MB, humidified nanocomposites show a better adsorption capacity (Figure 3.23g). The highest adsorption is achieved in the presence of ZnO-ZIF-8 300ºC (84%). ZnO-ZIF-8 300ºC (40%) and ZnO-ZIF-8 300ºC (67%) show a similar trend as that of ZnO-ZIF-8 300ºC.

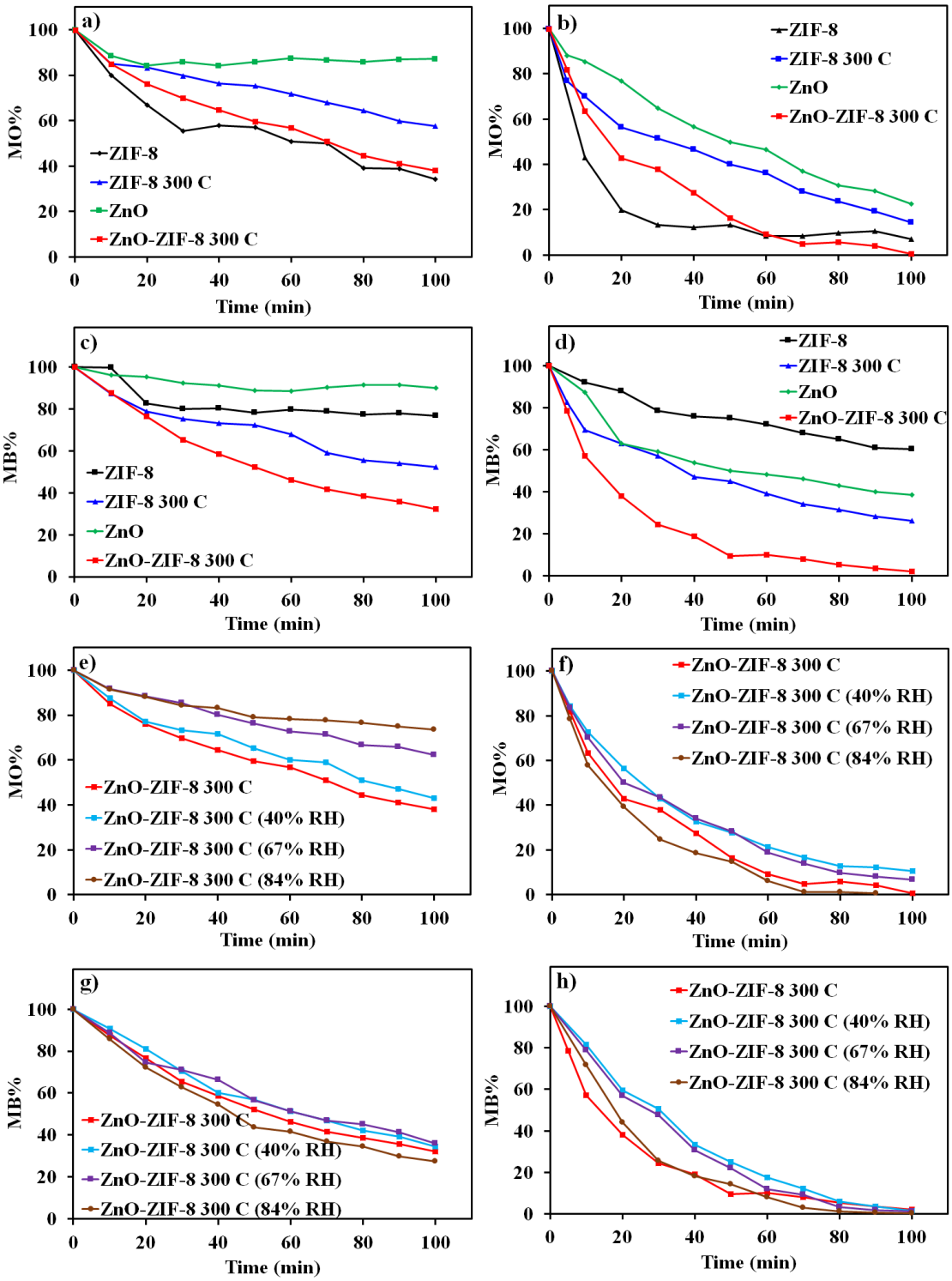

Figure 3.23. ZIF-8, ZIF-8 300ºC, ZnO and ZnO-ZIF-8 300ºC; (a and c) Dark adsorption experiments for MO and MB and (b and d) Photoactivities for MO and MB. ZnO-ZIF-8 300ºC and humidified ZnO-ZIF-8 300ºC; (e and g) Dark adsorption experiments for MO and MB and (f and h) photoactivities for MO and MB.

Under irradiation, ZIF-8 shows a higher photocatalytic performance for MO than that for MB, being consistent with its dark adsorption capacities (Figure 3.23 b and d). Its activity was deduced to ligand-to-metal charge transfer mechanism [136, 143, 144]. ZIF-8 300ºC reveals a better performance than bare ZnO (7.6 m^2 g^{-1}, 0.013 cm^3 g^{-1}) due to its higher surface area (357 m^2 g^{-1}) and pore size (0.026) (Figure 3.23b). The difference in the adsorption tendency of ZIF-8 toward MO and MB affect the variation in the photoactivity of ZIF-8 300ºC in comparison to the activity of ZIF-8. In this sense, ZIF-8 300ºC possesses a lower activity for MO relative to ZIF-8 whereas MB degradation is enhanced in the existence of ZIF-8 300ºC than that of ZIF-8 (Figure 3.23 b and d).

For ZnO-ZIF-8 300ºC, improved ZnO crystallinity detected in XRD analysis and enlarged pore size measured in BET analysis inevitably increases the photocatalytic efficiency (Figure 3.23b and d). The synergy established between ZnO and ZIF-8 is beneficial to interfacial charge transfer; electrons move from ZIF-8 to ZnO while holes migrate from ZnO to ZIF-8. A similar mechanism was postulated for TiO_2-ZIF-8 nanocomposite [143]. The photogenerated electrons can be captured by oxygen molecules and produce super oxide radicals. Simultaneously, photogenerated holes react with water molecules to generate hydroxyl radicals. Formation of these radicals enhance the degradation routes of MO and MB via subsequent attacks. ZnO-ZIF-8 300ºC also performs efficiently under humid conditions (Figure 3.23f and h). ZnO-ZIF-8 300ºC (84% RH) provides more hydroxyl radicals to photocatalytic reactions and hence, shows the highest activity.

3.4.3.8. Stability Tests. The reusability of ZnO-ZIF-8 300ºC and ZnO-ZIF-8 300ºC (84% RH) is also tested (Figure 3.24). For cyclic runs, catalysts are separated by centrifugation after photocatalytic degradation, washed with deionized water and dried for the subsequent experiment. As shown in Figure 3.24a and b, an excellent degradation performance is maintained even after four cycle. The activity loss of 1 or 2% between first and fourth runs can be attributed to the residual molecules and/or intermediates accumulated on the surface or pores of the nanocomposites. Thus, ZnO-ZIF-8 300ºC and ZnO-ZIF-8 300ºC (84% RH) can be suggested as potential catalysts for the photocatalytic degradation processes.

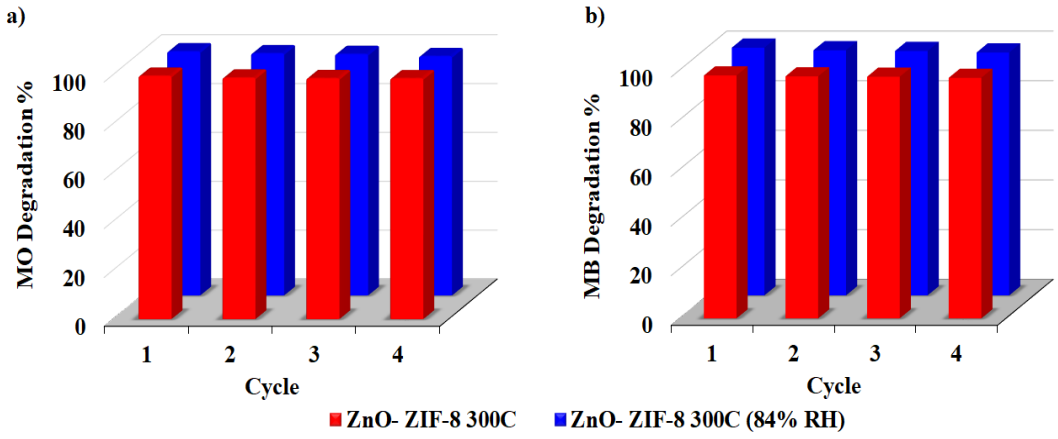

Figure 3.24. Stability tests of ZnO-ZIF-8 300ºC and ZnO-ZIF-8 300ºC (84% RH) for (a) MO and (b) MB.

3.4.4. Conclusion

ZnO-ZIF-8 300ºC is synthesized via a facile procedure by combining of ZnO with ZIF-8 at 300ºC. The successful growth of ZnO on the nanocomposite is confirmed by XRD, FTIR, BET, UV–Vis DRS, SEM-mapping (EDX) and XPS techniques. The higher surface area and porosity enhance adsorption ability and photocatalytic performance of ZnO-ZIF-8 300ºC in comparison to that of ZnO. The efficient charge separation in the matrix is also responsible for the high photoactivity toward both anionic dye MO and cationic dye MB. ZnO-ZIF-8 300ºC (84% RH) demonstrates the highest photocatalytic performance due to the formation of more hydroxyl radicals. After four cycles, ZnO-ZIF-8 300ºC and ZnO-ZIF-8 300ºC (84% RH) show good stabilities and imply favorable reusabilities. This study highlights a promising approach of synthesizing ZnO-ZIF-8 300ºC and its humidified form as effective and stable nanocomposites for environmental applications

4. EGGSHELL SUPPORTED AND EGGSHELL DERIVED HAP SUPPORTED CATALYSTS

4.1. Introduction

Eggshell is a waste material discarded in large quantities from food manufacturers and consumers. Recycling waste eggshell into a useful product can lead to economic benefits besides the environmental profit [145]. Since it can be easily adapted to the adsorption processes as a non-toxic, stable and effective adsorbent, utilization of the eggshell in water treatment has attracted much attention in the last decades [146–149]. Moreover, chemical composition of the eggshell (94% $CaCO_3$, 1% $MgCO_3$, 1% calcium phosphate and 4% organic matter) makes it a desirable biosource for the synthesis of calcium-based materials such as hydroxyapatite (HAP) [149, 150].

HAP mineral is a member of the apatite family with the chemical formula of $Ca_{10}(PO_4)_6(OH)_2$ and a Ca/P stochiometric ratio of 1.67 [151]. HAP structure is composed of a positively charged part of Ca^{2+} ion which is hexagonally coordinated with the negatively charged six O^{2-} sites, belonging to six PO_4^{3-} groups (Figure 4.1) construction [152].The surface of HAP possesses Brønsted acid sites from P-OH groups, Lewis acid sites from Ca^{2+} ions and the basic sites from OH^- and PO_4^{3-} groups construction [153]. HAP crystal arranged in a hexagonal lattice which can stabilize large amounts of substances in the active sites, vacancies and structural defects along with its flexible construction [154]. Therefore, it has also been identified as a good adsorbent material in adsorption applications due to its specific surface which provides affinity toward target molecules [152]. Recent studies focus on the adsorption properties and photoactivities of HAP and HAP-based materials under UV irradiation [151, 155–158]. The photoactivity of HAP is attributed to the change in the electronic state of PO_4^{3-} groups via superoxide radical formation [157, 159]. Meanwhile, the surface hydroxyl groups can react with the photogenerated holes to form the hydroxyl radicals. The oxygen vacancies in the HAP structure can act as electron receivers to inhibit the electron-hole recombination. Besides, the hexagonal structure of HAP enhances its

photoactivity due to the inherit ion channels which enable the charge carrier migration. The method of synthesis affects the adsorption performance and photoactivity of HAP.

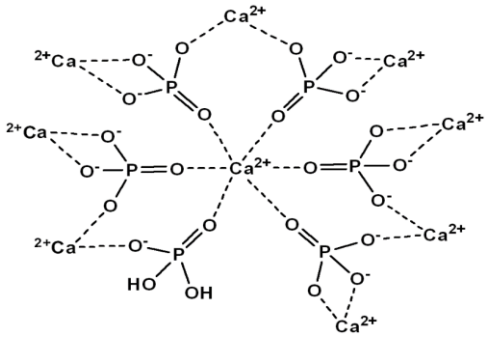

Figure 4.1.Structure of HAP.

The majority of HAP is produced by various synthetic routes using calcium-based ingredients such as $Ca(NO_3)_2$ [160, 161], $CaCl_2$ with $C_6H_5PO_4Na_2$ [162], $Ca_3(PO_4)_2$ with CaO and $CaCO_3$ [163]. However, recent studies are devoted to the development of alternative methods for the production of HAP by utilizing natural sources such as bovine bone [164], cuttle fish bone [165], mussel shell [157], clam shell [166], crab shell and eggshell [167]. Among these precursors, eggshell stands out as an ideal candidate to produce HAP since it has a calcium-rich nature (with 94% $CaCO_3$), being abundantly available and low-cost. Moreover, it is noticed that the eggshell-derived HAP displays higher thermal stability, higher surface area and photoactivity compared to the HAP materials which produced by synthetic precursors [168, 169].

This chapter consists of two parts; in the first part, eggshell, ZnO-eggshell 500°C, La-ZnO-eggshell 500°C, eggshell (RH), ZnO-Eggshell 500°C (RH), and La-ZnO-Eggshell 500°C (RH) are prepared, characterized and evaluated in terms of adsorption capacities and photoactivities. In the second part, HAP 100°C, HAP 500°C, ZnO-HAP 500°C, La-ZnO-HAP 500°C, HAP 100°C (RH), HAP 500°C (RH), ZnO-HAP 500°C (RH) and La-ZnO-HAP 500°C (RH) are prepared, characterized and examined for the adsorption properties and photocatalytic performances. HAP is synthesized at 100°C from the eggshell and its thermal stability is controlled at 500°C. ZnO and La-ZnO loading on both eggshell and HAP matrixes induce higher adsorption abilities and photoactivity for MO and MB. The structural characteristics of the eggshell and HAP, before and after ZnO and La-ZnO loading, are

examined by XRD, SEM-EDX, BET and UV-vis DRS analysis. Moreover, sensitivity to water vapor is considered as a weakness that can negate the potential applications of the as-prepared materials as adsorbents and photocatalysts. Thus, it is crucial to understand the behavior of the as-prepared materials under humid conditions. Since Cu-BTC and ZIF-8 systems demonstrate higher adsorption capacities and photoactivity at the relative humidity (RH) value of 84%, such characteristics of the eggshell and eggshell-derived HAP materials are also controlled at 84% RH. This detailed study is expected to pave new insights into the development of eggshell-supported nanocomposites and eggshell-derived HAP materials.

4.2. Experimental

4.2.1. Synthesis of Materials

4.2.1.1. Preparation of Eggshell. Eggs are supplied from the local markets. The eggshell separated from the inner layer, after washing several times, is dried at 100°C for 12 h and then, crushed and grounded to obtain the powder form. Thereafter, it is utilized as support material for ZnO nanoparticles.

4.2.1.2. Preparation of ZnO. The preparation of ZnO follows a co-precipitation method where $Zn(NO_3)_2 \cdot 6H_2O$ (Merck) and Na_2CO_3 (Merck) are used as precursors [128]. 0.25M solutions of each precursor are mixed and the resultant white solution is agitated for 2 h at room temperature. Then, the precipitate, after a number of centrifugations and washings, is dried at 100°C for 12 h, calcined at 500°C for 5 h in the muffle furnace, and stored in the dark and named as ZnO.

4.2.1.3. Preparation of La-ZnO. In order to prepare La-ZnO catalysts, $La(NO_3)_3.6H_2O$ (Merck) is used as a precursor. The concentration of La^{3+} ions is adjusted as 1% (wt) by dissolving the requisite amount of the precursor in deionized water. Then, 1 g of the as-prepared ZnO catalyst is added to this precursor solution. The mixture is stirred for 12 h at room temperature. Finally, the precipitate is centrifuged, washed several times, dried at 100°C for 12 h, then, calcined at 500°C for 5 h in the muffle furnace and named as La-ZnO.

4.2.1.4. Preparation of ZnO-Eggshell 500ºC. 1 gr of the eggshell is suspended in 100 mL of deionized water. The mixture of white ZnO solution and the eggshell suspension is stirred for 12 h. Then, the precipitate is separated by centrifugation, which also follows several washing steps. Finally, the precipitate is dried at 100ºC for 12 h, then calcined at 500ºC for 5 h in the muffle furnace, and named as ZnO-Eggshell 500ºC.

4.2.1.5. Preparation of La-ZnO-Eggshell 500ºC. The La-ZnO solution prepared in the Section 4.2.1.3 is mixed with the 1 gr of eggshell and magnetically stirred for 12 h at room temperature. Finally, the precipitate is centrifuged, washed several times, dried at 100ºC for 12 h, then calcined at 500ºC for 5 h in the muffle furnace and named as La-ZnO-Eggshell 500ºC.

4.2.1.6. Preparation of HAP. The eggshell is used as a calcium precursor for the synthesis of HAP, a co-precipitation method. In the first stage, CaO is obtained from the eggshell via calcination at 900ºC for 2 h in the muffle furnace with a heating rate of 10 °C/min. $CaCO_3$ as being the main constituent of the eggshell is transformed into CaO and CO_2 as follows

$$CaCO_3 \rightarrow CaO + CO_2. \quad (4.1)$$

The second stage involves the formation of $Ca(OH)_2$ and its reaction with H_3PO_4 (Merck). Briefly, 5.67 gr of CaO is hydrolyzed in 100 mL deionized water to yield $Ca(OH)_2$ which is expressed as

$$CaO + H_2O \rightarrow Ca(OH)_2. \quad (4.2)$$

Then, 3120 µL of H_3PO_4 is gradually added into $Ca(OH)_2$ solution. The continuous mixing of this solution for about 2 h at 100°C forms HAP with a molar Ca/P ratio of 1 as follows

$$10Ca(OH)_2 + 6H_3PO_4 \rightarrow Ca_{10}(PO_4)_6(OH)_2 + 18H_2O. \quad (4.3)$$

Finally, the solution is cooled down at room temperature. The obtained precipitate is separated by centrifugation and dried at 100°C. The final product is denoted as HAP 100°C. For further analysis, the as-prepared HAP is calcined at 500°C in the muffle furnace for 5 h and named as HAP 500°C.

4.2.1.7. Preparation of ZnO-HAP 500ºC. 1 gr HAP 100°C in deionized water is mixed with the white ZnO solution for 12 h at room temperature. The precipitate is centrifuged and washed several times. Then, it is dried at 100ºC for 12 h, calcined at 500ºC for 5 h in the muffle furnace and denoted as ZnO-HAP 500ºC.

4.2.1.8. Preparation of La-ZnO-HAP 500ºC. The La-ZnO solution prepared in the Section 4.2.1.3 is mixed with the 1 gr of HAP 100ºC and magnetically stirred for 12 h at room temperature. Finally, the precipitate is centrifuged, washed several times, dried at 100ºC for 12 h, then calcined at 500ºC for 5 h in the muffle furnace and named as La-ZnO-HAP 500ºC.

4.2.2. Preparation of Humidified Materials

The humidified samples are prepared by using the climate chamber (KKS 115 TOP+INOX/G) conducted with the relative humidity (RH) value of 84% for 72 h and named eggshell (RH), ZnO-Eggshell 500ºC (RH), La-ZnO-Eggshell 500ºC (RH), HAP 100°C (RH), HAP 500°C (RH), ZnO-HAP 500ºC (RH) and La-ZnO-HAP 500ºC (RH). Similar to the Cu-BTC and ZIF-8 materials, before the water vapor adsorption, the materials are dried 100°C for 6 h to remove adventitious water molecules. Then, the requisite amounts of dried samples are positioned in the chamber at constant temperature (24ºC) to ensure a stable baseline and the accurate delivery of the required delivery of water vapor. Gravimetric analysis is performed by measuring the weight of the samples after 72 h humidity exposure.

4.2.3. Characterization Techniques

X-ray diffraction (XRD) through Rigaku-D/MAX Ultima diffractometer with Cu Kα radiation (λ =1.54 Å) operating at 40 kV and 40 mA with the scanning rate 2 min^{-1}, Quantachrome Nova 2200e automated gas adsorption system at liquid nitrogen temperature (77 K), scanning electron microscopy (SEM) coupled to energy-dispersive X-ray analysis on an ESEM-FEG/EDAX Philips XL-30 instrument operating at 20 kV and UV–vis diffuse reflectance spectroscopy (UV-2450, Shimadzu) are used in the characterization studies of the as-prepared materials.

4.2.4. Adsorption and Photocatalytic Tests

The adsorption and photocatalytic performances of the as-prepared materials are explored in the presence of MO and MB. The experimental equipment, procedures followed and technical analysis are discussed in detail in Section 3.

4.3. Results and Discussion

4.3.1. XRD Results

Figure 4.2a exhibits XRD patterns of the eggshell, ZnO-Eggshell 500ºC and La-ZnO-Eggshell 500ºC. $CaCO_3$ (calcite) is confirmed as the major phase of the eggshell at 23.1°, 29.5°, 36.0°, 39.4°, 43.2°, 47.5°, 48.5°, 56.6°, 57.5°, 61.1° and 65.6° (2θ) peaks with corresponding indices of (012), (104), (110), (113), (202), (018), (116), (105), (211), (214) and (300), respectively, (MDI-JADE6). In the spectrum of ZnO-Eggshell 500°C, all characteristic peaks of the eggshell are preserved. Additionally, hexagonal ZnO wurtzite peaks are noticed at 32.1°, 34.5°, 36.3°, 56.7°, 62.9°, and 68.1° (2θ) and assigned to the (100), (002), (101), (110), (103) and (112) planes, respectively. The attenuation of the eggshell peaks implies the successful distribution of the in-situ formed ZnO crystallites on the eggshell surface. The La-ZnO-Eggshell 500ºC spectrum shows both eggshell and ZnO peaks. The dispersion of the La ions on the ZnO surface is suggested instead of their penetration into the ZnO crystallites due to the mismatch of La^{3+} (0.116 nm) and Zn^{2+} (0.079 nm) ionic radii. The lower intensities of eggshell and ZnO peaks in La-ZnO-Eggshell 500ºC with broadened shapes relative to that of ZnO-Eggshell 500°C indicate the distributed La ions on the nanocomposite surface. La crystallinity in the form of La_2O_3 is not detected, due to the low loading percentage of La (1%).

Crystalline sizes of $CaCO_3$ and ZnO are evaluated using Scherrer's equation (Table 4.1). $CaCO_3$ crystalline sizes, based on the most intense (104) plane, of eggshell, ZnO-Eggshell 500ºC and La-ZnO-Eggshell 500ºC are calculated as 46.6 nm, 44.4 nm and 43.6 nm, respectively. The introduction of ZnO or La-ZnO on the eggshell matrix induces 2-3 nm decrements in the $CaCO_3$ sizes. This may be explored by the attack of oxygen atoms of ZnO on the vacant oxygen sides of $CaCO_3$, which ultimately decreases the Ca-O bond length in the calcite structure. For ZnO-Eggshell 500ºC and La-ZnO-Eggshell 500ºC, ZnO crystalline sizes via (101) plane are calculated as 23.5 and 14.4 nm, respectively. An increment in the crystalline size of ZnO is noticed in ZnO-Eggshell 500ºC, in comparison to that of raw ZnO 500ºC (16.1 nm). The electron deficiency of Zn^{2+} ions can be supplied by the oxygen atoms of carbonate groups of $CaCO_3$. Thus, a longer Zn-O distance is expected, which may enlarge

the ZnO size. Although the ZnO crystalline size of La-ZnO-Eggshell 500ºC (14.4 nm) is quite similar to that of raw La-ZnO (15.1 nm), it decreases about 10 nm relative to that of ZnO-Eggshell 500ºC 1 [18]. Hence, the accumulation of La^{3+} on ZnO and their co-existence on the eggshell suppress the expansion of both ZnO and calcite grains.

The eggshell (RH), ZnO-Eggshell 500ºC (RH) and La-ZnO-Eggshell 500ºC (RH) reveal similar XRD patterns compared to that of unhumidified samples (Figure 4.2b). Significant variations in $CaCO_3$ crystallite sizes are not detected. However, hydrogen bonding through oxygen atoms in the carbonate groups of $CaCO_3$ is expected which reduces the surface relaxation of these groups and subsequently increases the stability of the structure. The highest increment noticed in $CaCO_3$ crystalline size is about 4 nm (from 44.4 nm-ZnO-Eggshell 500ºC to 48.2 nm-ZnO-Eggshell 500ºC (RH)). Thus, the possibility of more hydrogen bonding in the presence of ZnO nanoparticles and water molecules leads to the enhancement of $CaCO_3$ crystal growth in the ZnO-Eggshell 500ºC (RH). However, the existence of La^{3+} ions on the surface hinders the probable interaction of water molecules and limits the increment of $CaCO_3$ crystalline size in La-ZnO-Eggshell 500ºC (RH) (45.9 nm). In terms of ZnO crystalline sizes, almost similar values are calculated for both humidified and unhumidified samples (Table 4.1). Though the diffusion of the ZnO into the eggshell may support the generation of more hydrogen bonding, this may not improve the crystal growth of ZnO in ZnO-Eggshell 500ºC and La-ZnO-Eggshell 500ºC due to the crystalline boundaries in the restricted area.

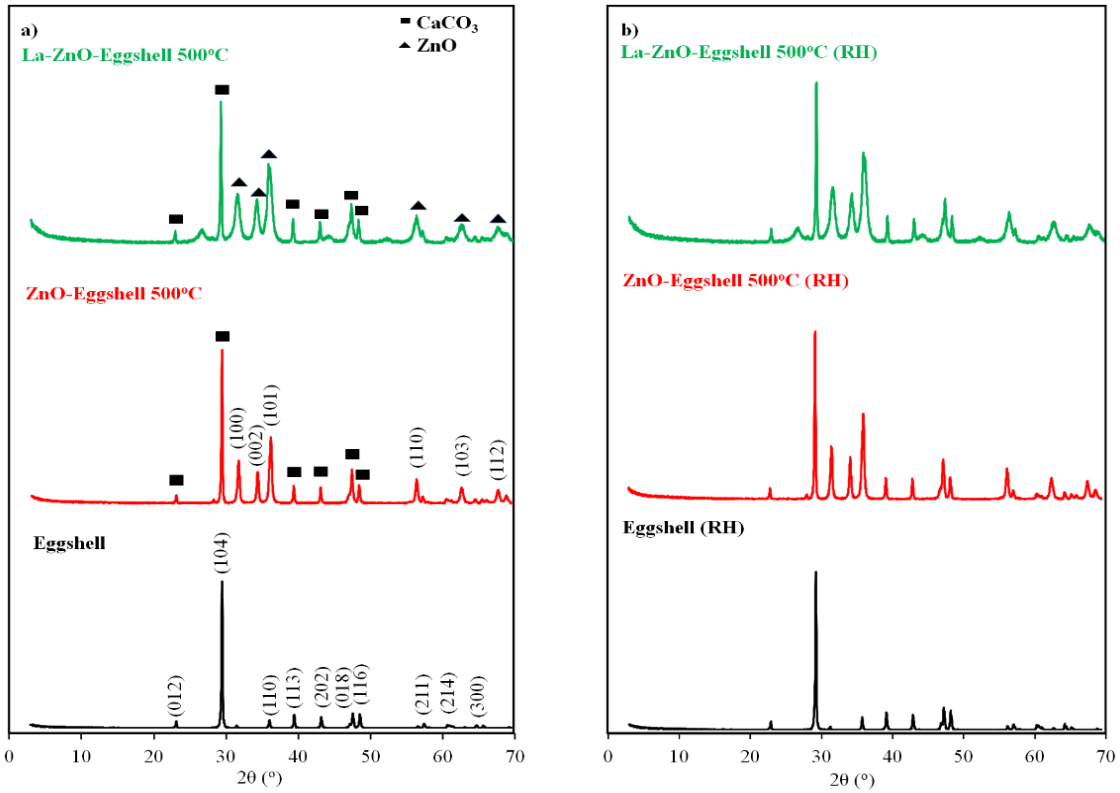

Figure 4.2. XRD patterns of (a) eggshell, ZnO-Eggshell 500ºC and La-ZnO-Eggshell 500ºC, (b) eggshell (RH), ZnO-Eggshell 500ºC (RH) and La-ZnO-Eggshell 500ºC (RH).

Table 4.1. Crystalline sizes, surface areas (BET), pore volumes (Vpore) and pore radius (r_{pore}) of the eggshell, ZnO-Eggshell 500ºC and La-ZnO-Eggshell 500ºC.

Materials	***D* (nm) $CaCO_3$**	***D* (nm) ZnO**	**BET (m^2g^{-1})**	**V_{pore} ($cm^3\ g^{-1}$)**	**r_{pore} (nm)**
Eggshell	46.6	-	1.30	0.0026	15.0
ZnO-Eggshell 500ºC	44.4	23.5	4.98	0.0083	15.3
La-ZnO-Eggshell 500ºC	43.6	14.4	13.9	0.0210	15.9
Eggshell (RH)	47.1	-	-	-	-
ZnO-Eggshell 500ºC (RH)	47.8	23.4	-	-	-
La-ZnO-Eggshell 500ºC (RH)	45.9	14.1	-	-	-
La-ZnO	-	15.1	18.1	0.028	18.4
ZnO	-	15.2	7.6	0.013	35.0

The XRD profiles of HAP 100ºC, HAP 500ºC, ZnO-HAP 500ºC and La-ZnO-HAP 500ºC are represented in Figure 4.3a. The diffraction peaks at 10.8, 21.8, 22.9, 25.8, 28.1, 29.9, 31.8, 32.9, 33.9, 35.9, 38.5, 39.8, 41.8, 43.9, 45.8, 46.7, 48.1, 49.4, 50.6, 53.1, 56.1, 59.9, 61.7, 64.1, 65.2º (2θ) are indexed to (100), (200), (111), (002), (102), (210), (211), (112), (300), (202), (301), (212), (310), (221), (311), (203), (222), (312), (213), (321), (004), (322), (420), (331), (214) and (502) crystal planes of HAP, respectively. Peaks of $Ca_3(PO)_4$ (26.4º (2θ)) and $Ca_2P_2O_7$ (30.9º (2θ)) impurities are also detected. After thermal treatment, the characteristic HAP peaks are retained and the intensity of impurity peaks decrease. This confirms the thermal stability of HAP at 500ºC, being in agreement with the study of Pattanayak et al. [170]. For ZnO-HAP 500ºC, in addition to the HAP peaks, ZnO peaks are noticed at 32.1°, 34.5°, 36.3°, 56.7°, 62.9°, and 68.1° (2θ), ascribable to (100), (002), (101), (110), (103) and (112) planes, respectively. A secondary phase such as zinc phosphate is not detected within ZnO-HAP 500ºC frame. ZnO incorporation broadens the HAP peaks and also decreases their intensities relative to HAP 500ºC. Besides, the intensity of the peak around 32° (2θ) is amplified owing to the overlap of HAP (211) peak at 31.8º (2θ) and ZnO (110) peak at 32.1º (2θ). In the pattern of La-ZnO-HAP 500ºC, typical HAP and ZnO peaks are observed. Similar to the La-ZnO-Eggshell 500ºC, characteristic diffraction peaks of La oxides crystallinities are not recorded. In the meantime, peak intensities of La-ZnO-HAP 500ºC become lower in comparison to those of ZnO-HAP 500ºC, pointing out the La^{3+} dispersion over the matrix.

The crystalline sizes of HAP and ZnO are displayed in Table 4.2. The HAP crystal size is calculated as 14.7 nm for HAP 100ºC according to the most prominent peak at 31.8° (2θ). Since the phase purity is improved during the heat treatment, crystal size increases to 22.6 nm in the presence of HAP 500ºC [171, 172]. For ZnO-HAP 500ºC, the HAP crystal size is found as 12.8 nm. The lower crystalline size of HAP in ZnO-HAP 500ºC than that of the HAP 500ºC (22.6 nm) can be explained by the existence of ZnO in the nanocomposite matrix. Zn^{2+} ions may be embedded into the HAP lattice via two routes: the first one is incorporation into the probable Ca defects since Ca and Zn ions have the same oxidation state and the second one is the substitution with the convenient Ca^{2+} ions due to the smaller ionic radius of Zn^{2+} (0.74 Å) than that of the Ca^{2+}(0.99 Å) [173, 174]. Subsequently, the Ca-O bond length (2.3 Å) decreases to 1.96 Å in the case of Zn-O bond. Thus, the incorporation and/or substitution of Zn in the lattice cause an inhibitory effect on the HAP crystalline

growth. Similar to ZnO-HAP 500ºC, HAP crystal size also decreases in the presence of La-ZnO-HAP 500ºC (14.6 nm) (Table 1). Although, La ions are firstly expected to disperse on ZnO surface according to the preparation procedure, some way freely stay in the solution phase and are in contact with the HAP surface. Thereafter, the substitution of La^{3+} ions in place of Ca^{2+} ions in the place of Ca^{2+} ions cannot be suggested due to the mismatch of ionic radius of La^{3+} (1.16 Å) and Ca^{2+} ions (0.99 Å). Thus, the heterogeneously existing La^{3+} ions on the HAP suppress the HAP crystal expansion. The ZnO crystalline sizes of ZnO-HAP 500ºC (11.9 nm) and La-ZnO-HAP 500ºC (11.8 nm) are compared to ZnO (15.1 nm) and La-ZnO (15.2 nm) via broadening of ZnO (101) peak reflection. The probable incorporation and/or substitution of Zn^{2+} ions within the HAP structure decreases Zn-O bond length from 1.96 Å (in the ZnO tetrahedral structure) to 1.72 Å (inside the HAP lattice). This leads to a reduction in ZnO crystalline size. An analogous decrement is also noticed in La-ZnO-HAP 500ºC.

The HAP 100ºC (RH), HAP 500ºC (RH), ZnO-HAP 500ºC (RH) and La-ZnO-HAP 500ºC (RH) exhibit similar XRD patterns compared to their corresponding unhumidified forms (Figure 4.3b, Table 4.2). Although HAP has hydrophilic nature, the interaction with water under humid conditions does not create a significant variation in HAP crystalline sizes. The probable hydrogen bonding established between phosphate groups of HAP and water molecules may be responsible for the minor increments in the crystalline sizes (less than 1 nm) of HAP in HAP 100ºC (RH) and HAP 500ºC (RH) [175]. In the case of ZnO-HAP 500ºC (84% RH), possibility of hydrogen bond formation increases owing to the existence of ZnO nanoparticles. This induces about a 2 nm increment in the HAP crystalline size. However, the increment in the size of HAP crystallites for La-ZnO-HAP 500ºC (RH) is lower than that of the ZnO-HAP 500ºC (RH) due to the restriction of hydrogen bonding via distribution of La^{3+} ions on the nanocomposite surface.

The new humid environment of ZnO-HAP 500ºC (RH) and La-ZnO-HAP 500ºC (RH) generates more steric boundaries on ZnO crystallites. Accordingly, ZnO crystalline sizes of ZnO-HAP 500ºC (RH) (10.8 nm) and La-ZnO-HAP 500ºC (RH) (10.4 nm) are found smaller (about 1-1.5 nm) than their unhumidified nanocomposites.

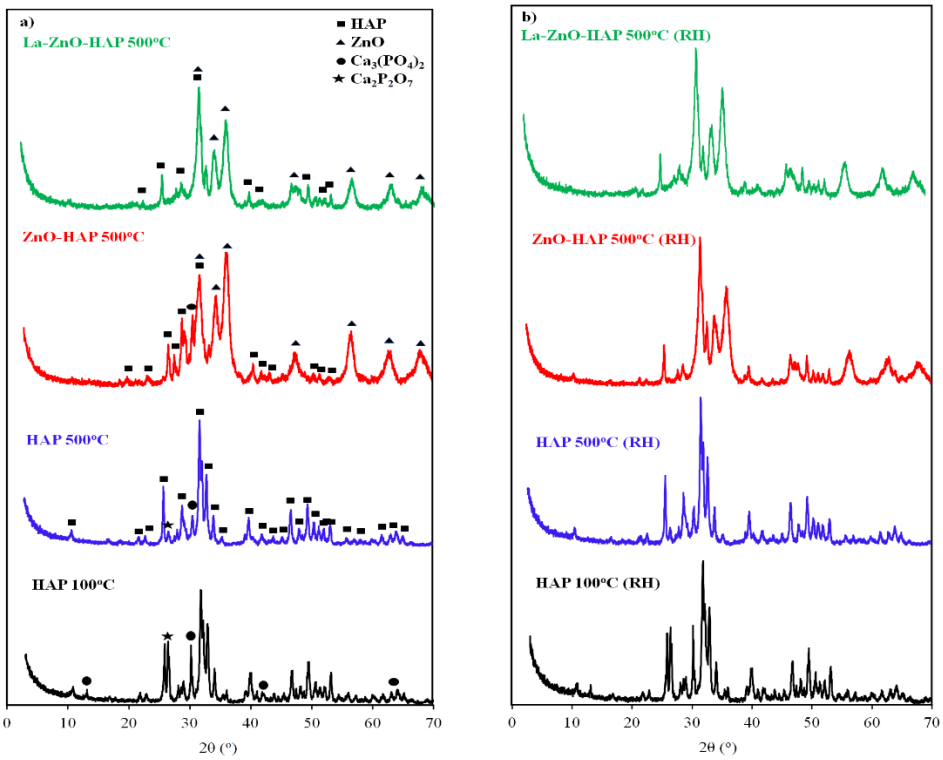

Figure 4.3. XRD patterns of (a) HAP 100ºC, HAP 500ºC, ZnO-HAP 500ºC and La-ZnO-HAP 500ºC, (b) HAP (RH), HAP 500ºC (RH), ZnO-HAP 500ºC (RH) and La-ZnO- HAP 500ºC (RH).

Table 4.2. Crystalline sizes, surface areas (BET), pore volumes (Vpore) and pore radius (r_{pore}) of the HAP 100ºC, HAP 500ºC, ZnO-HAP 500ºC, La-ZnO-HAP 500ºC.

Materials	***D* (nm) HAP**	***D* (nm) ZnO**	**BET (m^2g^{-1})**	**V_{pore} ($cm^3\ g^{-1}$)**	**r_{pore} (nm)**
HAP 100ºC	14.7	-	2.93	0.0042	15.0
HAP 500ºC	22.6	-	18.5	0.0315	15.8
ZnO-HAP 500ºC	12.8	11.9	21.4	0.0350	16.6
La-ZnO-HAP 500ºC	14.6	11.8	39.1	0.0603	17.8
HAP 100ºC (RH)	15.6	-	-	-	-
HAP 500ºC (RH)	23.2	-	-	-	-
ZnO-HAP 500ºC (RH)	14.6	10.8	-	-	-
La-ZnO-HAP 500ºC (RH)	15.1	10.4	-	-	-

4.3.2. Nitrogen Adsorption-Desorption Isotherms

The nitrogen adsorption/desorption isotherms and pore size distribution curves of the eggshell, ZnO-Eggshell 500ºC, and La-ZnO-Eggshell 500ºC are illustrated in Figure 4.4. The isotherm of the eggshell is identified as type II which is encountered in non-porous or microporous materials (Figure 4.4a). ZnO-Eggshell 500ºC and La-ZnO-Eggshell 500ºC curves fit well with the type IV isotherm accompanied by H3 hysteresis loop at a high relative pressure (P/P_0=0.48-0.96) which is characteristic for the mesoporous structures. The pore size distribution curve of the eggshell reveals low peak intensities indicating poor porous properties while ZnO-Eggshell 500ºC and La-ZnO-Eggshell 500ºC curves display pores in the typical mesoporous region of 20-40 Å (Figure 4.4b). The specific surface area and pore volume of ZnO-Eggshell 500ºC (4.98 m^2g^{-1} and 0.0083 cm^3 g^{-1}) are higher than those of the eggshell (1.30 m^2g^{-1} and 0.0026 cm^3 g^{-1}) due to the formation of interparticle voids among ZnO aggregates within the mesoporous frame (Table 4.1). In the case of La-ZnO-Eggshell 500ºC, La dispersion inhibits the formation of ZnO aggregates and hence increases the specific surface area (13.91 m^2g^{-1}) and pore volume (0.0210 cm^3 g^{-1}).

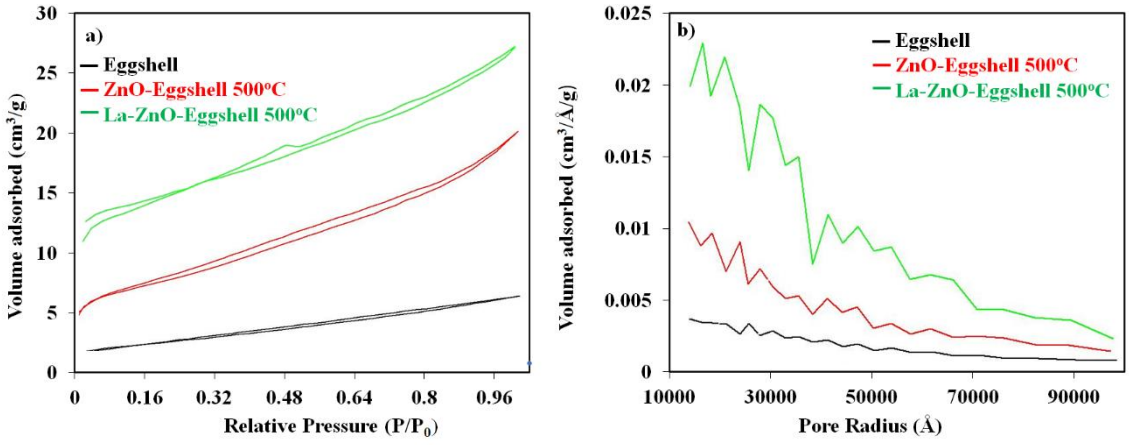

Figure 4 4. (a) Nitrogen adsorption-desorption isotherms and (b) pore size distribution curves of Eggshell, ZnO-Eggshell 500ºC and La-ZnO-Eggshell 500ºC.

The isotherms of HAP 100ºC, HAP 500ºC, ZnO-HAP 500ºC and La-ZnO-HAP 500ºC follow the type IV with H3 hysteresis loop associated with the N_2 capillary condensation of mesopores (Figure 4.5a). The peak positions on the pore size distribution

curves of HAP 100ºC, HAP 500ºC, ZnO-HAP 500ºC and La-ZnO-HAP 500ºC mainly lie in the range of mesoporous region (Figure 4.5b). Calcination of HAP increases the specific surface area (2.98 m^2g^{-1} for HAP 100ºC and 18.5 m^2g^{-1} for HAP 500ºC) and expands the pore volume (0.0042 cm^3g^{-1} for HAP 100ºC and 0.0315 cm^3g^{-1} for HAP 500ºC) due to the improvement of HAP crystallinity after thermal treatment (Table 4.2) [176]. Further increments in the surface area and pore volume are noticed in the presence of ZnO-HAP 500ºC (21.4 m^2g^{-1} and 0.0350 cm^3g^{-1}) and La-ZnO-HAP 500ºC (39.1 m^2g^{-1} and 0.0603 cm^3g^{-1}). Similar to the nanocomposites prepared with eggshell, void spaces among ZnO aggregates within the HAP frame point out such increments in the BET areas and pore volumes in comparison to that of HAP 500ºC. Thus, the generation of new mesoporous structures in the ZnO-Eggshell 500ºC, La-ZnO-Eggshell 500ºC, ZnO-HAP 500ºC and La-ZnO-HAP 500ºC are expected to facilitate the adsorption ability and photocatalytic activities of these nanocomposites.

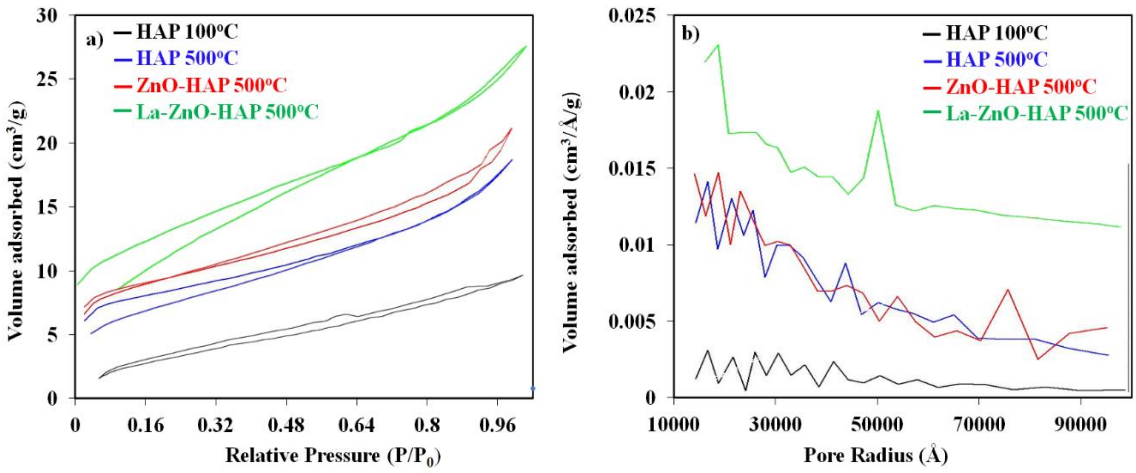

Figure 4.5. (a) Nitrogen adsorption-desorption isotherms and (b) pore size distribution curves of HAP 100ºC, HAP 500ºC, ZnO- HAP 500ºC and La-ZnO- HAP 500ºC.

4.3.3. SEM-EDX Analysis

The eggshell, ZnO-Eggshell 500ºC, La-ZnO-Eggshell 500ºC morphologies are examined by SEM-EDX analysis (Figure 4.6). Eggshell reveals irregularly shaped nanoparticles with different sizes and open voids (Figure 4.6a). Based on the EDX analysis of the selected area, the main components of the eggshell are detected as Ca (17.32%), C

(18.52%), and O (62.77%) in addition to the traces of Mg (0.71%) and Si (0.21%) (Figure 4.6b). Both ZnO-Eggshell 500ºC and La-ZnO-Eggshell 500ºC images differ from the image of the eggshell (Figure 4.6c and e). A rough surface with cauliflower-like particles is noticed in the image of ZnO-Eggshell 500ºC and cotton balls of different sizes are observed in the image of La-ZnO-Eggshell 500ºC. The existence of ZnO nanoparticles and also La ions on the corresponding nanocomposites are verified with the detection of Zn and La signals (Figure 4.6d and f). Meanwhile, the decrements in the other percentages relative to those of the eggshell also indicate the distribution of ZnO and La-ZnO nanoparticles on the eggshell.

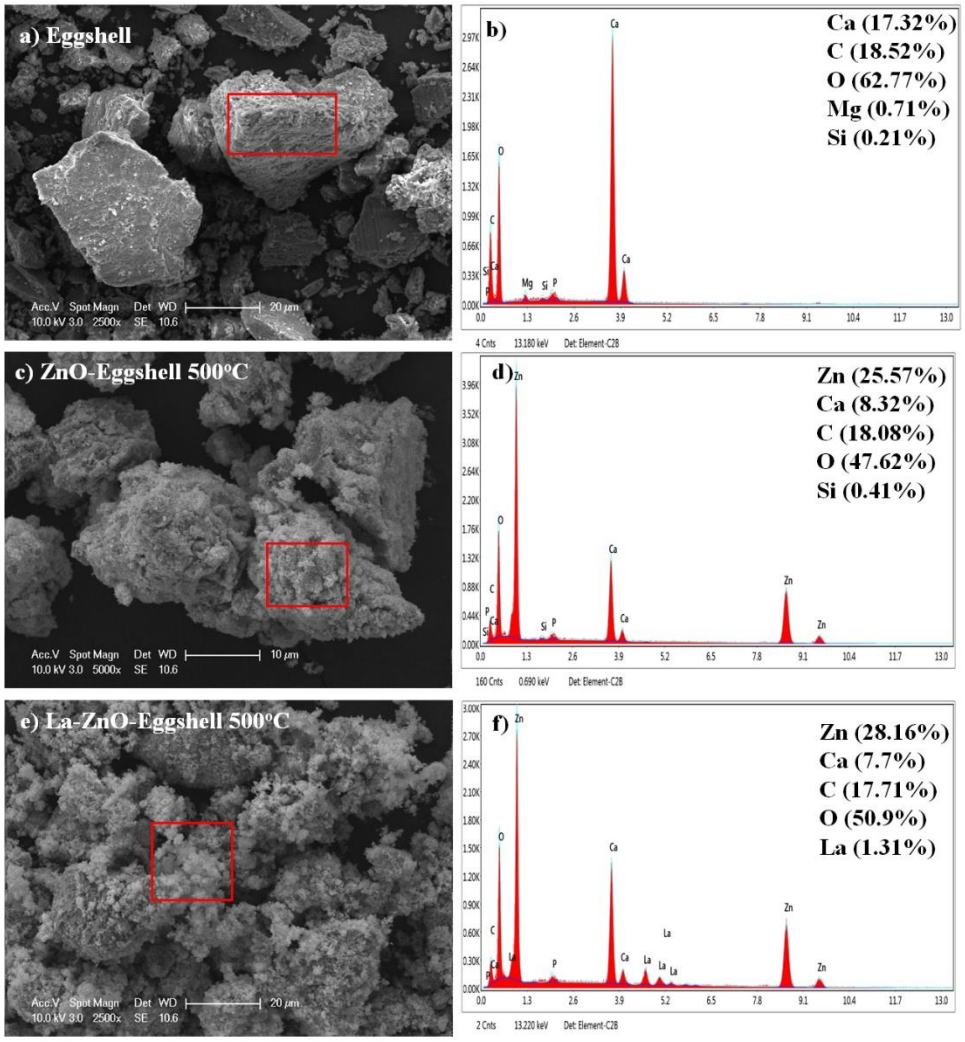

Figure 4.6. SEM images and EDX analysis of (a,b) the eggshell, c,d) ZnO-Eggshell 500ºC and (e,f) La-ZnO-Eggshell 500ºC.

Morphologies and elemental compositions of the HAP 100ºC, HAP 500ºC, ZnO-HAP 500ºC and La-ZnO-HAP 500ºC are depicted in Figure 4.7. The HAP 100ºC exhibits plate-like structures with Ca (19.81%) O (66.27%) and P (13.03%) constituents in the selected area (Figure 4.7a,b). Phase purity and high crystallinity of HAP structures synthesized via various precursors supplied 1.67 stoichiometric ratio for Ca/P [170]. The formation of defects and impurities during the preparation of HAP at 100ºC induces a deviation in this ratio is 1.52. Upon calcination, the morphology of the HAP differs and plate-like structures transform into irregularly distributed rough surface particles (Figure 4.7c). The EDX analysis of the labeled area in Figure 4.7d shows reductions in the phosphate P (11.2%) and oxygen O (61.07%) percentages, attributed to volatilization of phosphorous atoms as oxide forms through the heat treatment. Accordingly, phase purity and improved crystallinity of HAP 500ºC are confirmed by the Ca/P ratio of 1.68 being in agreement with the XRD results. The micrograph of ZnO-HAP 500ºC displays the heterogeneously distributed aggregates on HAP particles (Figure 4.7e). The Zn signals (17.41%) are detected for the selected area in Figure 6e, demonstrating in-situ-build up ZnO nanoparticles on the HAP. Moreover, the decrement of Ca percentage (12.35%) and Ca/P ratio (1.63) ZnO-HAP 500ºC verify the substitution of Zn ions into the HAP lattice (Figure 4.7f) [174]. In the image of La-ZnO-HAP 500ºC, agglomerates with grained particles become more prominent (Figure 4.7g). La-ZnO on the HAP is confirmed with the simultaneous notification of La (1.3%) and Zn (19.9%) in the EDX analysis of La-ZnO-HAP 500ºC (Figure 4.7h). Slight decrements in the other percentages and Ca/P ratio (1.61) may also suggest La-ZnO adsorption on the surface of HAP.

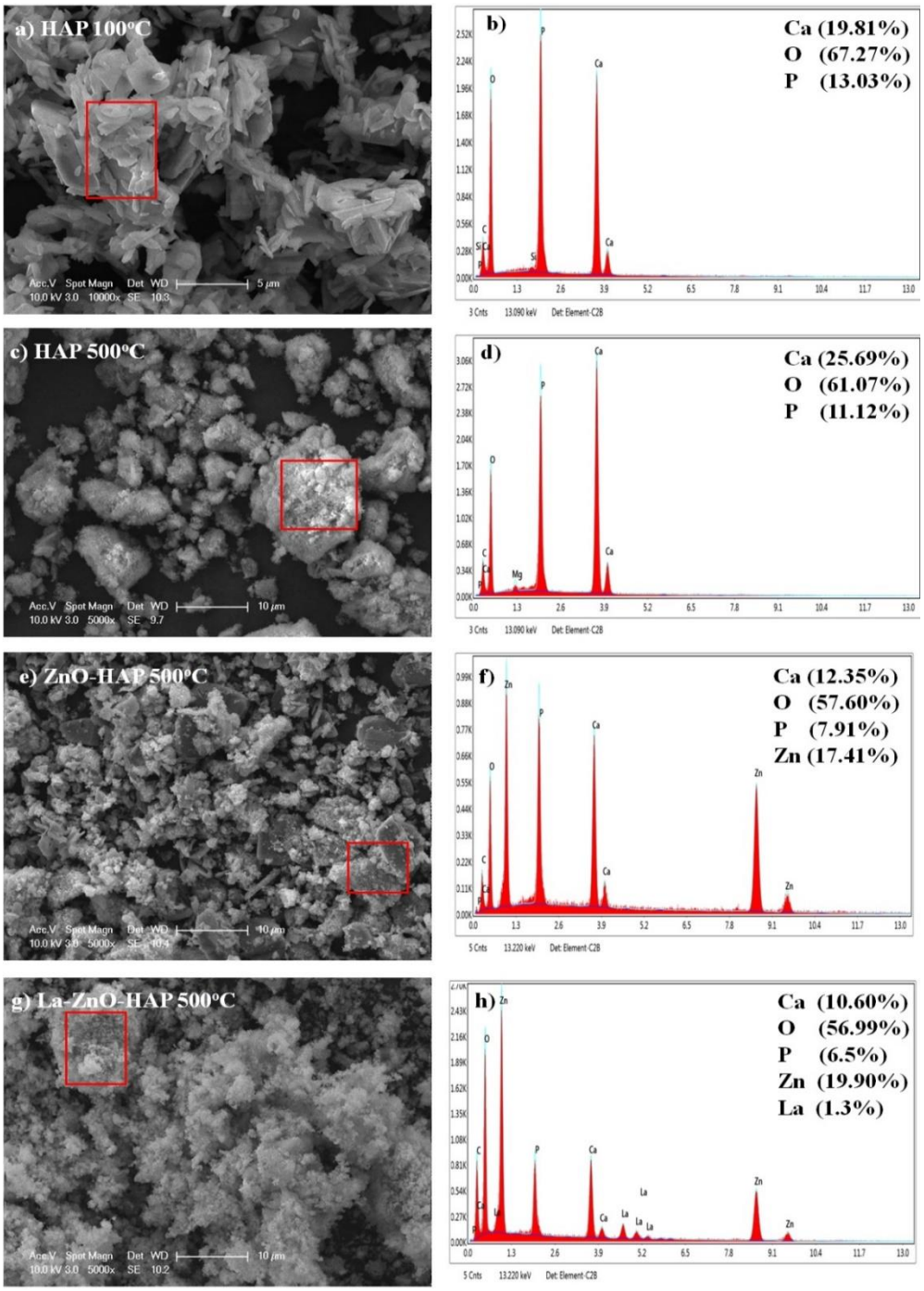

Figure 4.7. SEM images and EDX analysis of the (a,b) HAP 100°C, (c,d) HAP 500°C, (e,f) ZnO-HAP 500°C and (g,h) La-ZnO-HAP 500°C.

4.3.4. UV-Vis DRS Analysis

The eggshell does not show a significant absorption edge in the UV-vis region as also reported in the study of Huang et al. (Figure 4.8a) [177]**.** However, the profiles of ZnO and La-ZnO reveal a strong absorption edge at around 390 nm which is characteristic for ZnO. An analogous ZnO edge is also observed in the spectrums of ZnO-Eggshell 500ºC and La-ZnO-Eggshell 500ºC, confirming the successful generation of ZnO crystallites on the nanocomposites. The existence of the eggshell does not lead to a significant variation in the absorption profile of ZnO-Eggshell 500ºC in comparison to the ZnO. Meanwhile, the introduction of La ions to ZnO frame (La-ZnO 500ºC) and to eggshell as La-ZnO (La-ZnO-Eggshell 500ºC) increases the intensities relative to that of ZnO. Moreover, the highest absorption intensity achieved in the presence of La-ZnO-Eggshell 500ºC may suggest an enhancement in photoactivity. ZnO-Eggshell 500ºC (RH) and La-ZnO-Eggshell 500ºC (RH) exhibit similar profiles to those of corresponding unhumidified samples.

The band gap energies plotted as the tangents of $(Ahv)^2$ versus photon energy, are estimated as 3.19, 3.13, 3.22 and 3.10 eV for ZnO, La-ZnO, ZnO-Eggshell 500ºC and La-ZnO-Eggshell 500ºC, respectively (Figure 4.8b). The decrement in the band gap of La-ZnO compared to ZnO is attributed to the merging of the La impurity bands closer to the lower edge of the ZnO conduction band due to the spin-orbital coupling between La ions and O atoms of ZnO [178–180]. On the other hand, the higher band gap value of ZnO-Eggshell 500ºC than that of the ZnO may arise from the repulsion forces between the lowest conduction band of the ZnO that originated from 4s state of Zn atom and the highest valence band edge from the 2p state of O atom, with the increasing Zn and O distance in ZnO lattice. This is also verified by the increment of the ZnO crystalline size for ZnO-Eggshell 500ºC via XRD results [180]. In the case of La-ZnO-Eggshell 500ºC, La existence in the matrix induces the reduction in the band gap energy due to the above-mentioned interaction of La with ZnO. The La-ZnO (RH) (3.15 eV), ZnO-Eggshell 500ºC (RH) (3.20 eV) and La-ZnO-Eggshell (RH) (3.10 eV) have almost similar band gap energies with their unhumidified corresponding forms.

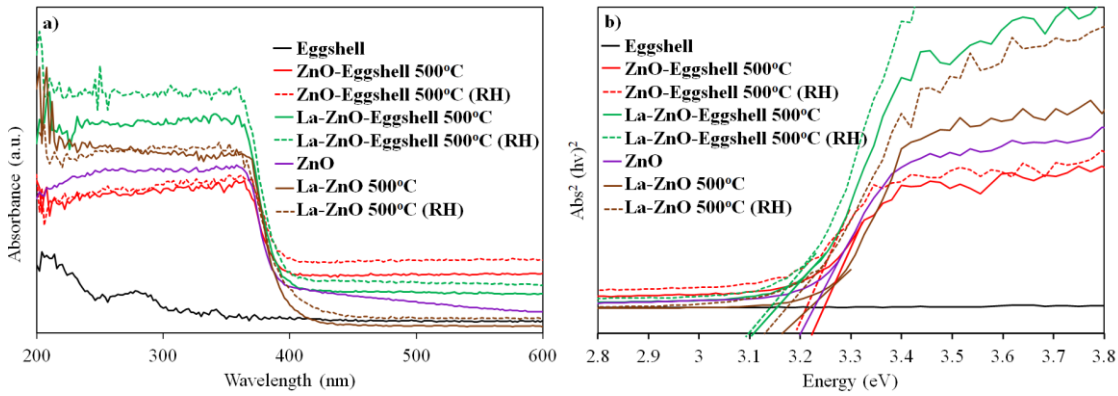

Figure 4.8. (a) UV–vis DRS spectra, (b) band gap absorption edges of eggshell, ZnO, La-ZnO 500°C, ZnO-Eggshell 500°C, La-ZnO-Eggshell 500°C and humidified samples.

The spectrums of HAP 100°C and HAP500°C show a low absorption edge at about 280 nm indicating the activity under UV light due to the oxygen vacancies in the HAP matrix (Figure 4.9a) [156]. The intensity of the HAP spectrum increases upon calcination at 500°C owing to its phase purity and high crystallinity as noticed in the XRD analysis [181]. The spectra of La-ZnO 500°C, ZnO-HAP 500°C and La-ZnO-HAP 500°C display an obvious ZnO edge at around 390 nm. The absorption edge of La-ZnO-HAP 500°C shifts to the longer wavelengths due to the improved electron transitions from the valence band of HAP oxygens to the conduction band of Zn atoms ($O_{2p} \rightarrow Zn_{3d}$). Moreover, the higher absorption intensity of the La-ZnO-HAP 500°C than those of the La-ZnO 500°C and ZnO-HAP 500°C implies the enhanced absorption ability of the nanocomposite owing to the synergy among La-ZnO and HAP. Analogous ZnO absorption edges are also detected in the profiles of humidified samples.

In the literature, HAP samples that are synthesized by using unnatural precursors reveal band gap values of about 5 eV in the UVC region [169, 182, 183]. However, utilization of natural sources with carbonate contents such as fish bone, mussel shell, or eggshell induce oxygen vacancies in the lattice and narrow the band gap energy to 3.4-3.8 eV [169, 184, 185]. Accordingly, the band gap energies of HAP 100°C and HAP 500°C are calculated as 3.61 eV and 3.40 eV, respectively (Figure 4.9b). The decrement in the band energy of HAP 500°C relative to the HAP 100°C is due to the formation of more oxygen deficiencies upon thermal treatment as also detected in the SEM-EDX analysis. The band

gap energy of HAP 500ºC (3.40 eV) decreases with the incorporation and/or substitution of the ZnO into the HAP lattice (for ZnO-HAP 500ºC (3.15 eV)) due to the formation of a hybrid orbital which combines 2p orbitals of oxygen atoms in HAP and 3d orbitals of Zn atoms in ZnO (Figure 4.9c) [183, 185]. In the case of La-ZnO-HAP 500ºC, the co-existence of La and ZnO induces additional electronic levels, which eventually reduces the band gap of the nanocomposite to 3.08 eV [186]. Band gap energies of the humidified samples (3.32 eV for HAP 100ºC (RH), 3.15 eV for HAP 500ºC (RH), 3.05 eV for ZnO-HAP 500ºC (RH) and 3.03 eV for La-ZnO-HAP 500ºC (RH)) decrease in comparison to the their unhumidified forms. Adsorption of the water molecules on the deficient sites are expected, which can promote electron accepting abilities via reducing the band gap values [182].

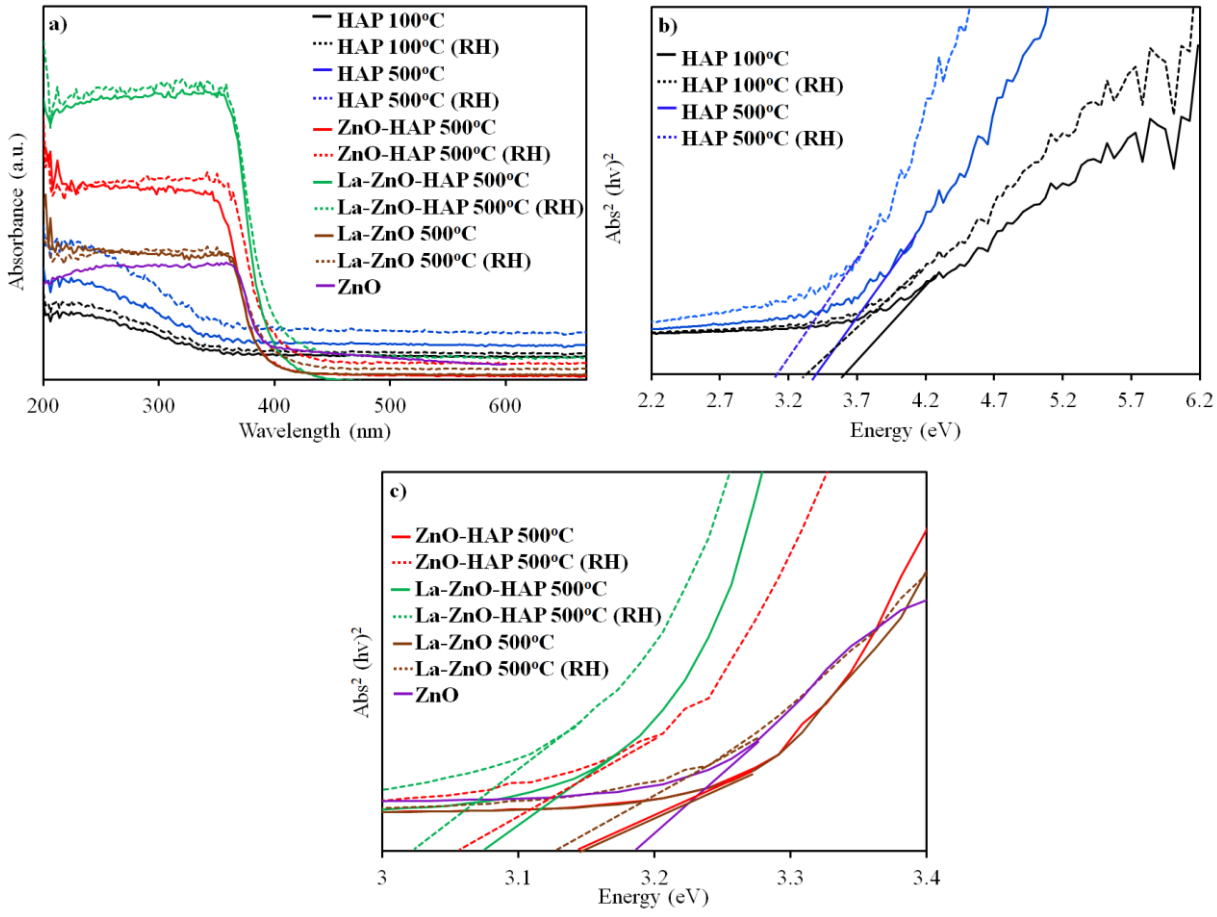

Figure 4.9. (a) UV-vis DRS spectra, band gap absorption edges of (b) HAP 100ºC, HAP 500ºC, HAP 100ºC (RH), HAP 500ºC (RH), (c) ZnO, La-ZnO 500ºC, ZnO-HAP 500ºC, La-ZnO-HAP 500ºC and humidified forms.

4.3.5. Adsorption and Photocatalytic Tests

The dark adsorption capacities and photocatalytic efficiencies of the ZnO, La-ZnO, eggshell, ZnO-Eggshell 500ºC, La-ZnO-Eggshell 500ºC and humidified samples are displayed in Figure 4.10. The results show that not only porosity but also electrostatic forces play a crucial role in the adsorption processes of MO and MB. Accordingly, the remaining percentages of MO and MB are found as 93.4% and 86% in the presence of ZnO (Figure 4.10a,c) due to the nonporous structure of ZnO. The relatively higher adsorption of MB on ZnO than that of the MO is related to the probable electrostatic attractions between the oxygen atoms of ZnO and C-S^+=C functional group of MB.

The existence of La^{3+} leads to a variation in the surface charge of La-ZnO and promotes the adsorption of MO (80.2% remaining percentage) providing Lewis interaction between the sulphonic groups of MO and La^{3+} ions. Contrarily, the La-ZnO and MB interaction is weaker due to the repulsive forces among the La cations and MB (90.6% remaining MB).

The residual percentages of the MO and MB in the presence of the eggshell are found as 73.1% and 79%, respectively. The eggshell surface is positively charged for pH values less than its point of zero charge (11.4) owing to the protonation of the surface carbonate groups [187]. Hence, favorable attraction is expected in between sulphonic groups of MO and Ca^{2+} of the eggshell since natural pH of MO solution is found as 5.85 (Figure 4.11a). Also, hydrogen bonding can be formed among the carbonate groups of the eggshell and nitrogen atom in MO. In the case of MB, repulsive forces are dominant in between MB (natural pH=7.88) and positively charged eggshell surface. However, there seems to be limited adsorption among nitrogen atoms of MB and protonated carbonate groups of the eggshell via hydrogen bonding (Figure 4.11b) [188, 189].

In ZnO-Eggshell 500ºC, binding of ZnO nanoparticles is suggested through carbonate groups and Ca^{2+} ions of the eggshell. The mesoporous structure and high surface area of ZnO-Eggshell 500ºC as confirmed by the BET analysis, enhance the adsorption of MO (63% remaining percentage) and MB (53% remaining percentage). In addition to the hydrogen bonding, the electrostatic attraction in between Zn^{2+} ions and sulphonic group of

MO, and also Lewis acid-base interaction between Zn^{2+} ions and nitrogen atoms enhance MO adsorption (Figure 4.11c). Similarly, MB adsorption follows hydrogen bonding and Lewis acid-base interactions (Figure 4.11d). But, presence of ZnO within the frame induces a negative charge dominance which ultimately increases the adsorption of MB than that of MO.

Although La-ZnO-Eggshell 500ºC reveals Lewis acid-base, hydrogen bonding and electrostatic attractions for both MO and MB, its adsorption tendency differs in the sense that MO remaining percentage (45%) in the solution is found to be lower than that for MB ((57%). Thus, while interactions of La^{3+} ions with sulphonic groups of MO increases the adsorption of MO, repulsions between La^{3+} ions and C-S^{+}=C functional groups of MB decreases the adsorption of MB (Figure 4.11e and f).

In the eggshell (RH), water vapor adsorption is calculated as 23% and the adsorption mechanism is proposed via two routes: the first one is the interaction between water molecules and the carbonate groups of the eggshell and the second one is the electrostatic attraction in between water molecules and Ca^{2+} ions of the eggshell (Figure 4.12). Accordingly, the number of hydrogen bonding interactions are expected to increase and the remaining percentages of MO (60%) and MB (76%) decrease in comparison to that of eggshell (Figure 4.12a and b).

Contrarily, ZnO-Eggshell 500ºC (RH) has a higher water vapor adsorption percentage (27.5%), contributed to the electrostatic attraction of the Zn^{2+} ions and water molecules, hydrogen bonding between water molecules and the oxygen atoms of ZnO and another hydrogen bonding between water molecules and oxygen atoms of the surface carbonate groups of the eggshell (Figure 4.12c and d). Hence, adsorption percentages of both MO (56% remaining percentage) and MB increases (40% remaining percentage) relative to the percentages obtained in the presence of ZnO-Eggshell 500ºC. The adsorption of MO is driven by the formation of hydrogen bonds between sulphonate oxygens and nitrogen atoms of MO and water molecules. For MB, in addition to hydrogen bonds between water molecules and nitrogen atoms of MB, electrostatic interaction between water molecules and C-S^{+}=C functional group participates in the adsorption process. The higher adsorption tendency of ZnO-Eggshell 500ºC (RH) for MB than that of the MO is attributed to the

increment of the partial negative charge on the nanocomposite surface due to the existence of water molecules.

Water vapor adsorption capacity of La-ZnO-Eggshell 500ºC (RH) (29%) does not significantly differ in comparison to that of ZnO-Eggshell 500ºC (RH) (27.5%). Although the electrostatic attractions are probable between water molecules and La^{3+} ions, saturation of the eggshell surface with La-ZnO nanoparticles limits the water adsorption on La-ZnO-Eggshell 500ºC (RH) (Figure 4.12e, and f). Meanwhile, Lewis acid-base interactions, hydrogen bonding and electrostatic attractions promote the adsorptions of MO and MB on the ZnO-Eggshell 500ºC (RH) surface. But, in contrast to ZnO-Eggshell 500ºC (RH), MO adsorption is found to be higher than that of MB in the existence of La-ZnO-Eggshell 500ºC (RH). Similar to the La-ZnO-Eggshell 500ºC, while interactions of sulphonic groups of MO and La^{3+} ions favors the MO adsorption, attractions of C-S^{+}=C functional groups of MB and La^{3+} ions reduces the MB adsorption.

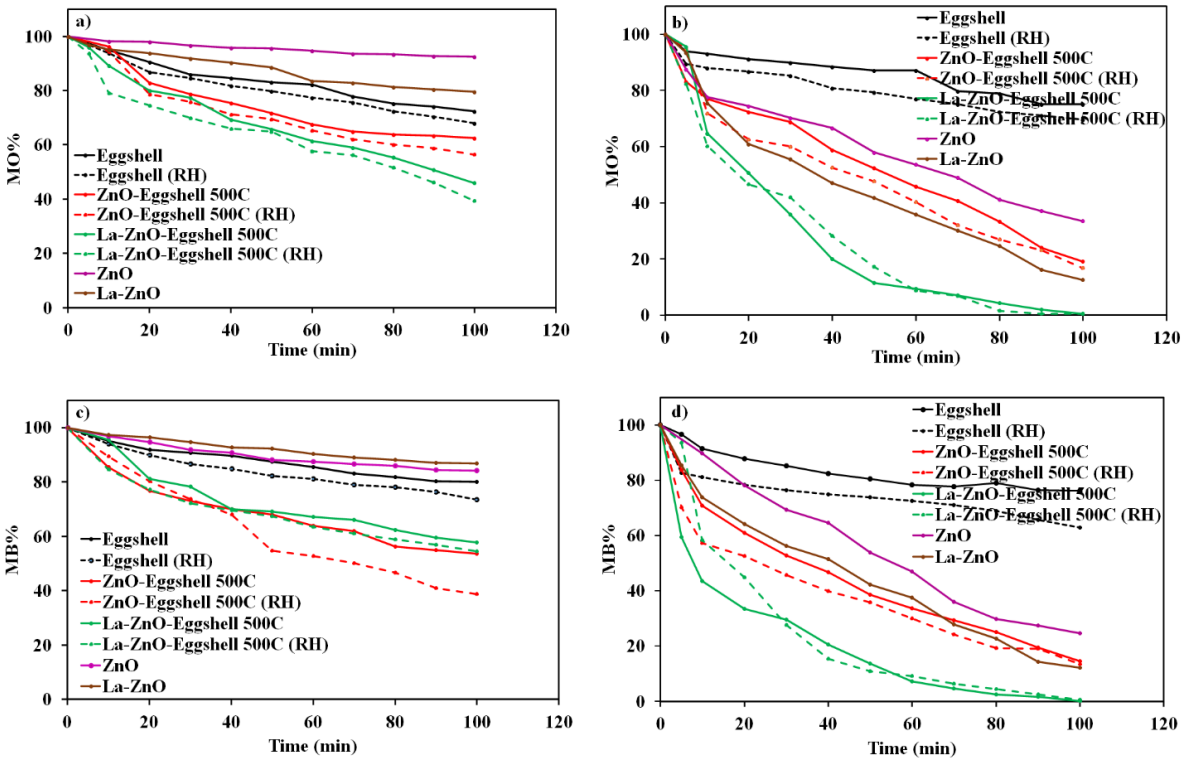

Figure 4.10. (a,c) Dark adsorption and (b,d) photocatalytic degradation of MO and MB in the presence of ZnO, La-ZnO, eggshell, ZnO-Eggshell 500ºC, La-ZnO-Eggshell 500ºC and humidified samples.

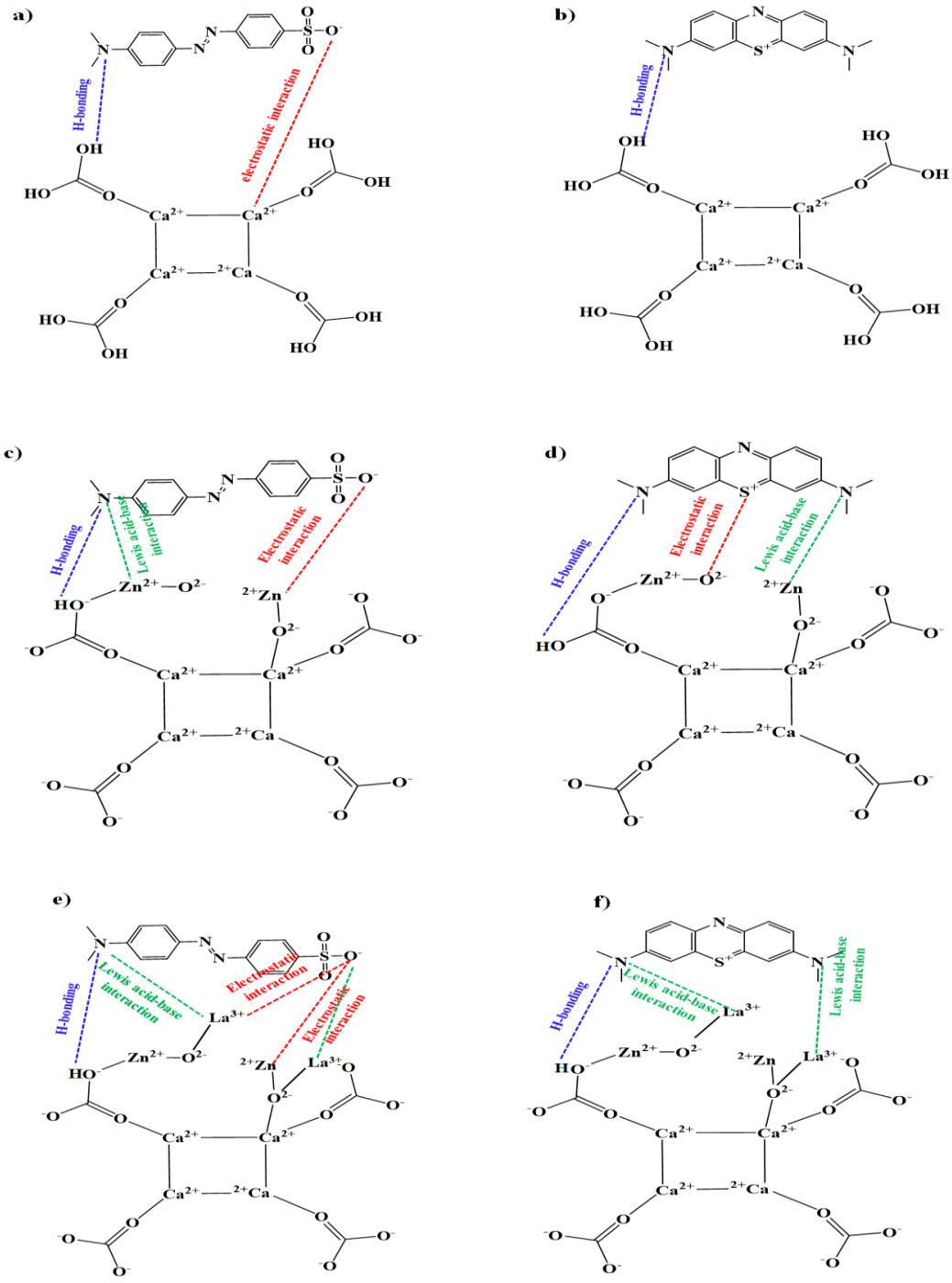

Figure 4.11. Postulated adsorption mechanisms of MO and MB on (a,b) eggshell, (c,d) ZnO-Eggshell 500°C and (e,f) La-ZnO-Eggshell 500°C.

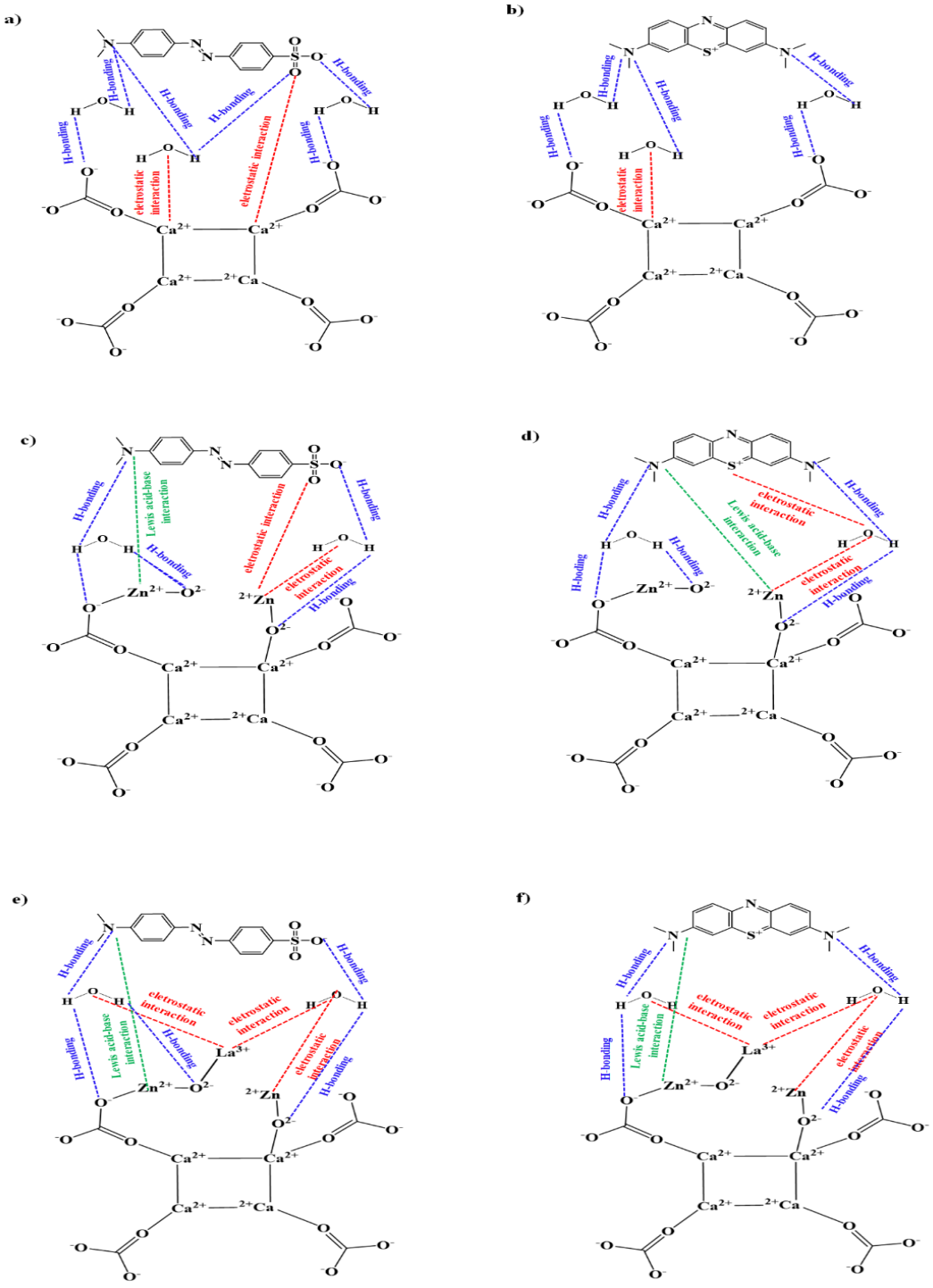

Figure 4.12. Postulated adsorption mechanisms of MO and MB on (a,b) eggshell (RH), (c,d) ZnO-Eggshell 500ºC (RH) and (e,f) La-ZnO-Eggshell 500ºC (RH).

The eggshell does not exhibit an activity under UV illumination since it cannot possess a band in its absorption profile as verified by the UV-vis DRS spectra (Figure 4.8). Thus, the remaining percentages of MO (75%) and MB (77%) under irradiation can be explored by the adsorption capability of the eggshell (Figure 4.10b and d).

The lower remaining percentages of MO (12%) and MB (13%) in the existence of La-ZnO than those detected in the presence of ZnO (MO (33%) and MB (24%)) point out a different path for the degradation processes (Figure 4.10b and d). The photogenerated electron-hole (e^--h^+) pairs upon illumination of ZnO may undergo recombination as an undesired route, instead of reacting with the surface oxygen and water. Hence, it is crucial to improve the photocatalytic activity of ZnO via inhibition and/or retardation of electron-hole recombination. The presence of La^{3+} ions on the ZnO matrix can effectively scavenge electrons due to their partially filled 5d orbitals and, hence prolong the life-time of electron-hole pairs as follow

$$La^{3+} + e^- \rightarrow La^{2+}. \quad (4.4)$$

Since the produced La^{2+} ions are unstable and tend to return to their stable +3 oxidation state, trapped electrons migrate to O_2 to form superoxide radicals ($O^{\bullet}_2^-$) as follow

$$La^{2+} + O_2 \rightarrow La^{3+} + O^{\bullet}_2^-. \quad (4.5)$$

This subsequently promotes formation of hydroxyl radicals ($OH^{\bullet}$) with the following rections

$$O^{\bullet}_2^- + H+ \rightarrow HO^{\bullet}_2 \quad (4.6)$$

$$2HO^{\bullet}_2 \rightarrow H_2O_2 + O_2 \quad (4.7)$$

$$H_2O_2 + e^- \rightarrow OH^- + OH^{\bullet}. \quad (4.8)$$

These radicals exhibit strong oxidizing properties and being responsible from the degradation routes of both MO and MB.

The higher photocatalytic performance of the ZnO-Eggshell 500ºC (%19 MO and %16 MB remaining percentages) than that of the ZnO can be ascribed to the dispersion of ZnO nanoparticles on the eggshell as evidenced by XRD, SEM (EDX), BET and UV-vis DRS analysis (Figure 4.10b and d). This eventually leads to an increment in the number of active sites of ZnO-Eggshell 500ºC for the adsorption of MO and MB. Moreover, the formation of an interface between ZnO and eggshell is probable, providing a new transport

channel for the photo-generated electrons and delaying the electron-hole recombination [190]. Contrarily, photoactivity of ZnO-Eggshell 500ºC is similar (for MB degradation) or a bit lower (for MO degradation) than that of La-ZnO. This may suggest a weaker charge separation efficiency in the ZnO-Eggshell 500ºC matrix in comparison to La-ZnO. In the presence of La-ZnO-Eggshell 500ºC, both MO and MB degradations are accomplished within about 80 min owing to the combined effects of electron trapping capability, enhanced radical formation facility, and the high porosity in the nanocomposite. The remaining percentages of MO and MB are found as 69% and 62% in the existence of eggshell (RH). The higher photodegradation efficiency of the eggshell (RH) compared to the unhumidified form is attributed to its enhanced adsorption ability due to the interactions of water molecules with MO and MB. For ZnO-Eggshell 500ºC (RH) and La–ZnO-Eggshell 500ºC (RH), adsorbed water molecules on the surfaces promote the generation of hydroxyl radicals and hence support the photocatalytic degradation of MO and MB.

For adsorption experiments, HAP 100ºC, HAP 500ºC, ZnO-HAP 500ºC, La-ZnO-HAP 500ºC and humidified samples are evaluated under dark conditions (Figure 4.13 a and c). The HAP structure provides a number of active sites to interact with the dye molecules depending on its pH_{pzc} value (reported in the range of 6.4- 7.2) [191]. Hence, at pH values below the pH_{pzc}, protonation of PO^- and $CaOH^0$ groups creates positively charged $CaOH_2^+$ and neutral POH^0 sites while at pH values above the pH_{pzc}, deprotonation generates $CaOH^0$ and PO^- species on the surface of HAP 100ºC (Figure 4.14a) [192]. Accordingly, electrostatic interactions are suggested among $CaOH_2^+$ of HAP 100ºC and negatively charged sulphonic groups of MO (with 65% of remaining MO) since natural MO solution has a pH value of 5.85. However, deprotonated species are expected in the presence of MB solution with a natural pH of 7.88 (Figure 4.14b). This promotes the electrostatic attraction between PO^- of HAP 100ºC and the positively charged sulfur groups of MB and also the Lewis acid-base interaction among the nitrogen atom of MB and Ca^{2+} in the HAP 100ºC, which eventually attributed to the adsorption of MB (with 54% of remaining MB) [193].

The thermal treatment promotes the adsorption percentages of both MO (55% remaining percentage) and MB (47% remaining percentage), which is corroborated by the higher surface area and porosity values of HAP 500ºC than that of HAP 100ºC. Moreover,

accessibility of Ca^{2+} sites in the HAP 500ºC structure owing to the oxygen deficiencies may improve the electrostatic interactions of MO and MB (Figure 4. 14c and d).

In the frame of ZnO-HAP 500ºC, ZnO can be bound to oxygens of phosphate groups and simultaneously, Zn^{2+} ions can be substituted in place of Ca^{2+} ions within the HAP lattice (Figure 4.14e and f). The substituted Zn ions in the HAP lattice enhance the MO adsorption due to the higher electronegativity of Zn^{2+} ions than that of the Ca^{2+} ions (with 44% of remaining MO). Contrarily, additional Lewis acid-base interaction between substituted Zn^{2+} ions and MB does not vary the adsorption percentage of MB significantly (with 45% of remaining MB), it almost stays similar that noticed in the presence of HAP 500ºC.

In La-ZnO-HAP 500ºC, similar routes are suggested for the adsorption of La-ZnO on the HAP frame. The decrements in the residual percentages of both MO (34%) and MB (37%) can be attributed to the high surface area and pore volume of La-ZnO-HAP 500ºC relative to that of ZnO-HAP 500ºC and HAP 500ºC. In the case of MO, in addition to the Lewis acid-base interaction between La^{3+} ions and nitrogen atoms of MO, electrostatic interactions can be established among La^{3+} ions and sulphonic group of MO (Figure 4.14g). Adsorption of MB is ascribed to the Lewis acid-base interaction between La^{3+} ions and nitrogen atoms of MB (Figure 4.14h).

For HAP 100ºC (RH) and HAP 500ºC (RH), two probable water adsorption paths are proposed; an electrostatic interaction between water molecules and Ca^{2+} of HAP and also hydrogen bonding between water molecules and phosphate groups of HAP (Figure 4.15a-d) [175]. These contacts lead to 38% of water vapor adsorption for HAP 500ºC (RH) and 31% of water vapor adsorption for HAP 100ºC (RH). Oxygen-deficient sites in the HAP 500ºC (RH) induce an increment in the water adsorption capacity via occupation by the oxygens of the water molecules. In comparison to HAP 100ºC and HAP 500ºC, MO and MB adsorption percentages increase in the presence of HAP 100ºC (RH) and HAP 500ºC (RH). Hydrogen bond formation between water molecules and MO or MB reduce their remaining percentages as 60% and 48% for MO in the presence of HAP 100ºC (RH) and HAP 500ºC (RH), respectively and 47% and 42% for MB in the presence of HAP 100ºC (RH) and HAP 500ºC (RH), respectively.

Water vapor adsorption percentages of ZnO-HAP 500ºC (RH) and La-ZnO-HAP 500ºC (RH) are found as 40% and 49%, respectively. The probable interaction of water molecules is assumed to be via distributed ZnO or La-ZnO nanoparticles and substituted Zn atoms on the HAP matrix (Figure 4.15e-h). Subsequently, hydrogen bonding formed between water molecules and sulphonic groups of MO and nitrogen atoms of MB, improves the adsorption of MO (with 34% of remaining MO) and MB (with 36% of remaining MB) in the presence of ZnO-HAP 500ºC (RH) (Figure 4.15e and f). For La-ZnO-HAP 500ºC (RH), an electrostatic attraction is expected between water molecules and La^{3+} ions which provides more hydrogen bonding and then promotes the adsorption of MO (with 24% of remaining MO) and MB (with 30% of remaining MB) (Figure 4.15g and h).

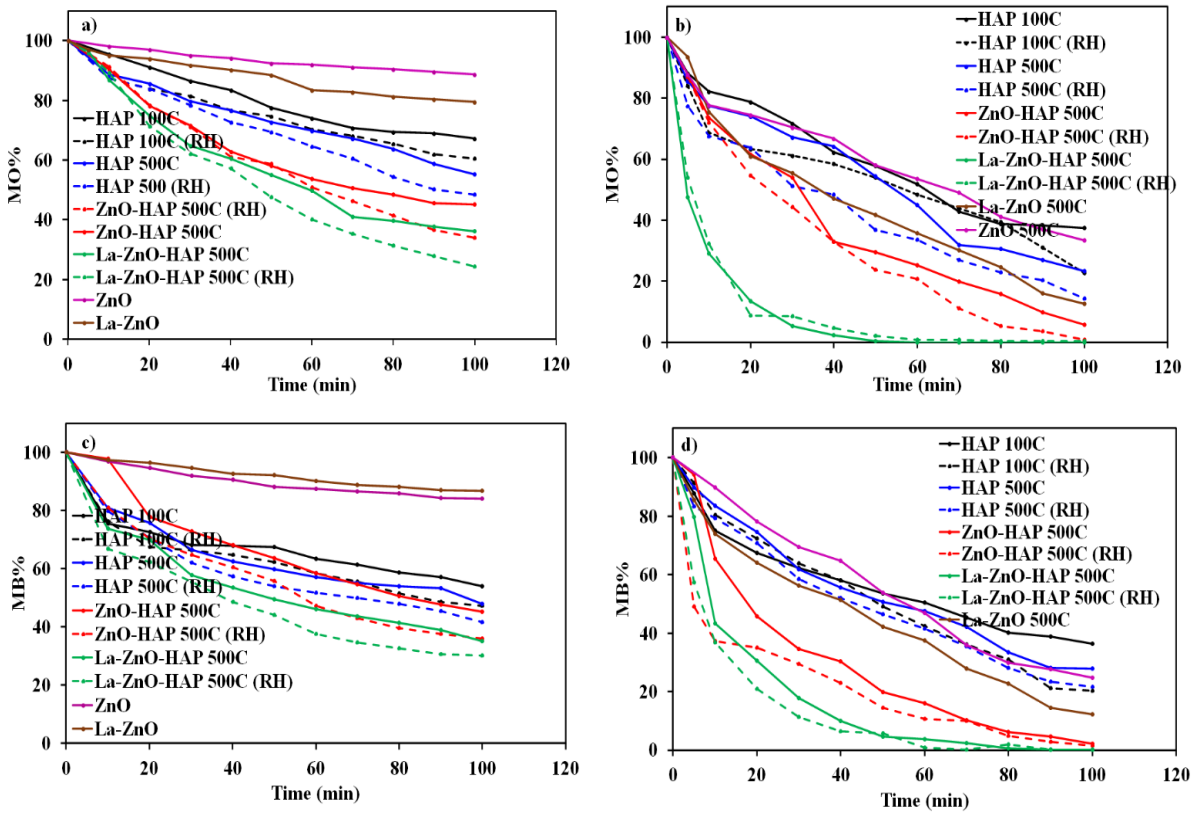

Figure 4.13. (a,c) Dark adsorption experiments and (b,d) Photocatalytic degradation of MO and MB in the presence of ZnO, La-ZnO, HAP 100ºC, HAP 500ºC, ZnO-HAP 500ºC, La-ZnO-HAP 500ºC and humidified samples.

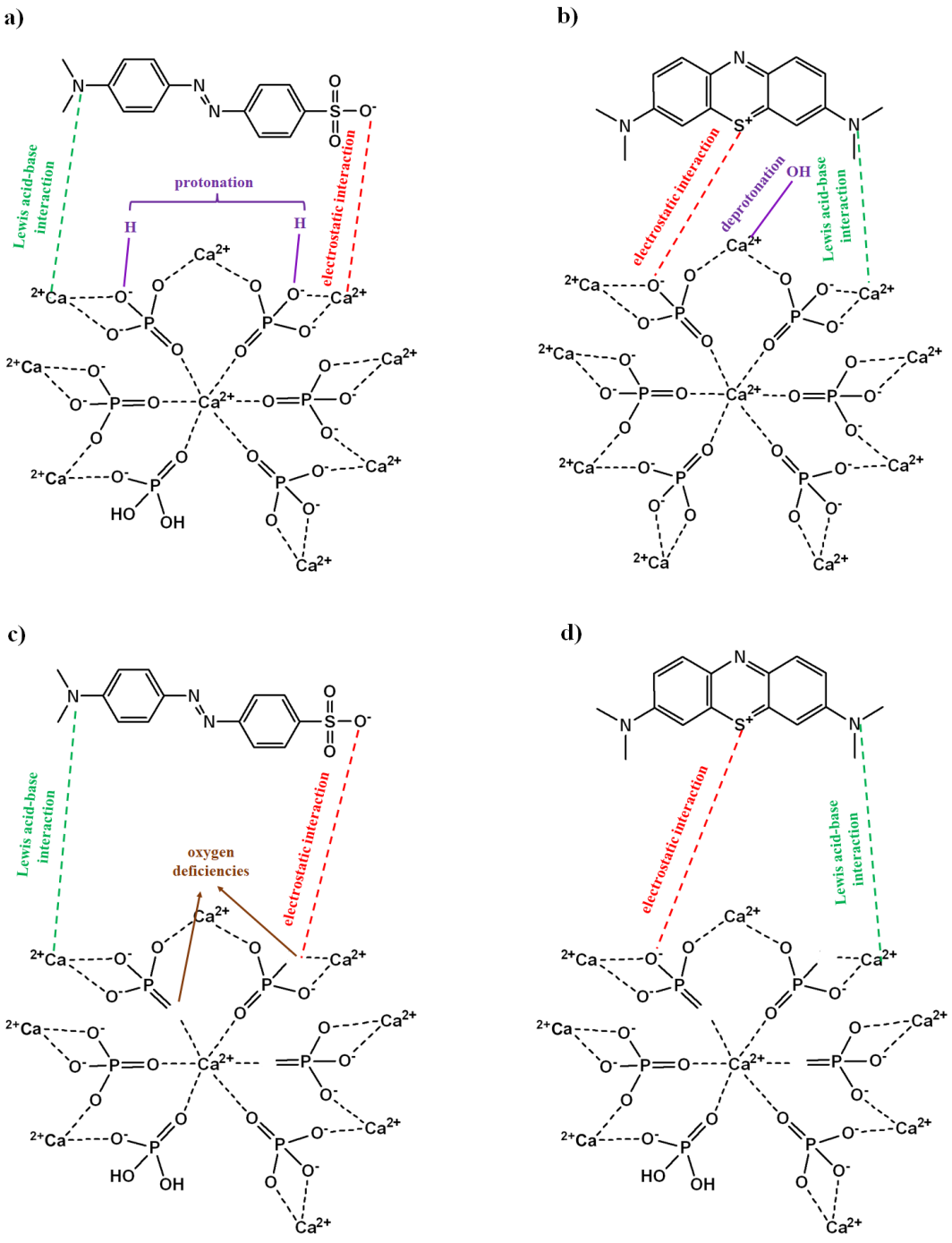

Figure 4.14. Postulated adsorption mechanism of MO and MB on (a,b) HAP 100°C, (c,d) HAP 500°C, (e,f) ZnO-HAP 500°C and (g,h) La-ZnO-HAP 500°C.

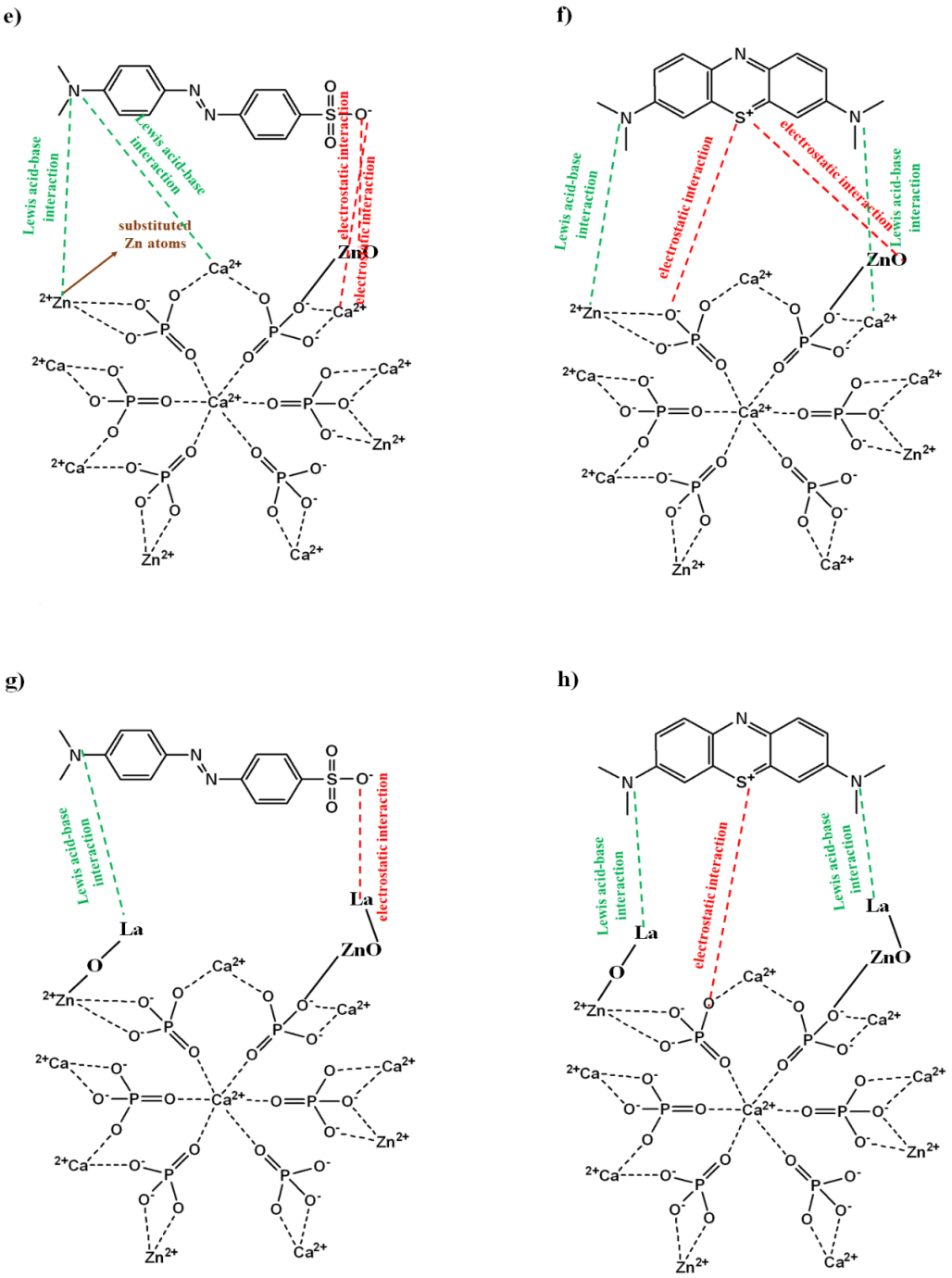

Figure 4.15. (cont) Postulated adsorption mechanism of MO and MB on (a,b) HAP 100ºC, (c,d) HAP 500ºC, (e,f) ZnO-HAP 500ºC and (g,h) La-ZnO-HAP 500ºC.

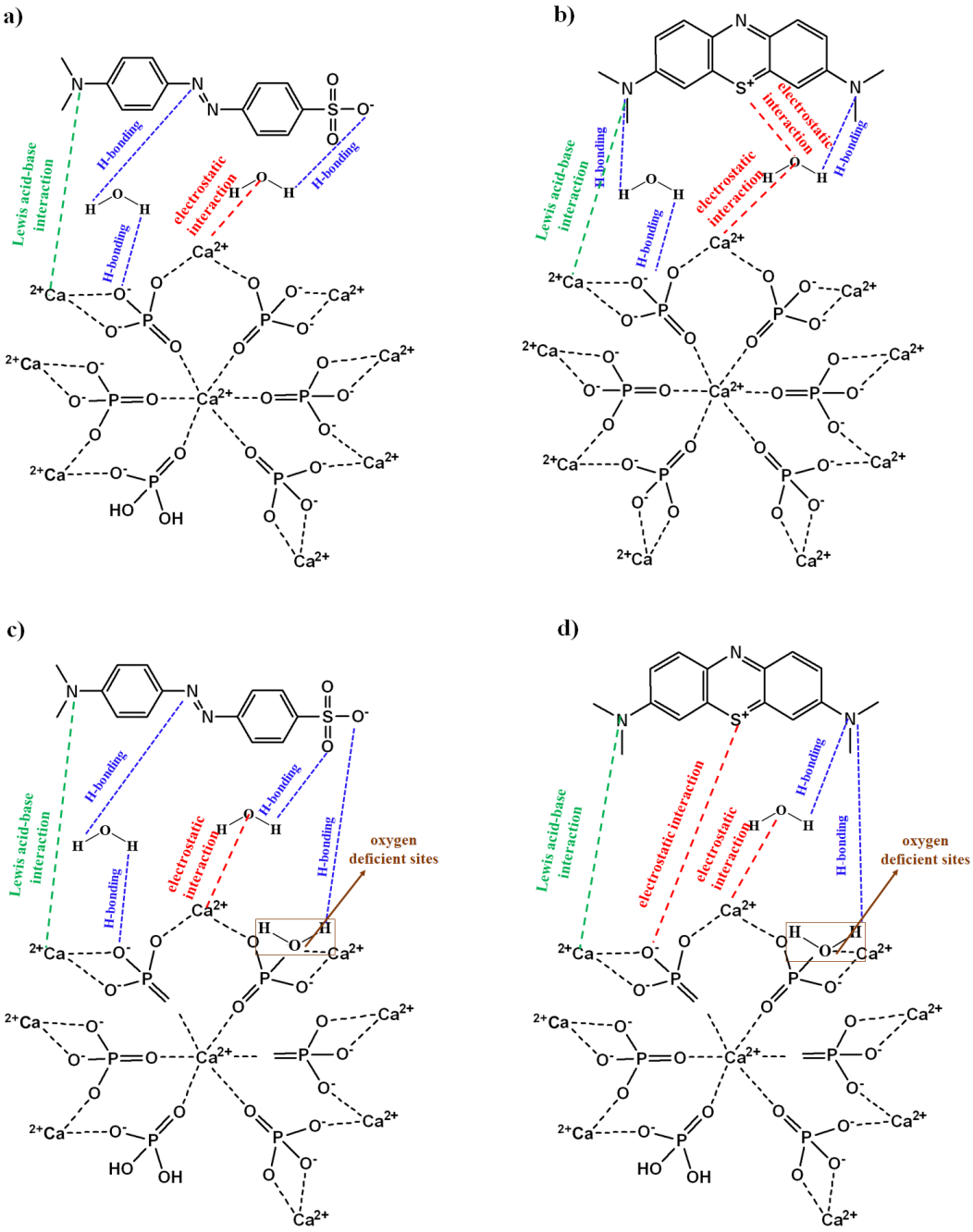

Figure 4.16. Postulated adsorption mechanism of MO and MB on (a,b) HAP 100ºC (RH), (c,d) HAP 500ºC (RH), (e,f) ZnO-HAP 500ºC (RH) and (g,h) La-ZnO-HAP 500ºC (RH).

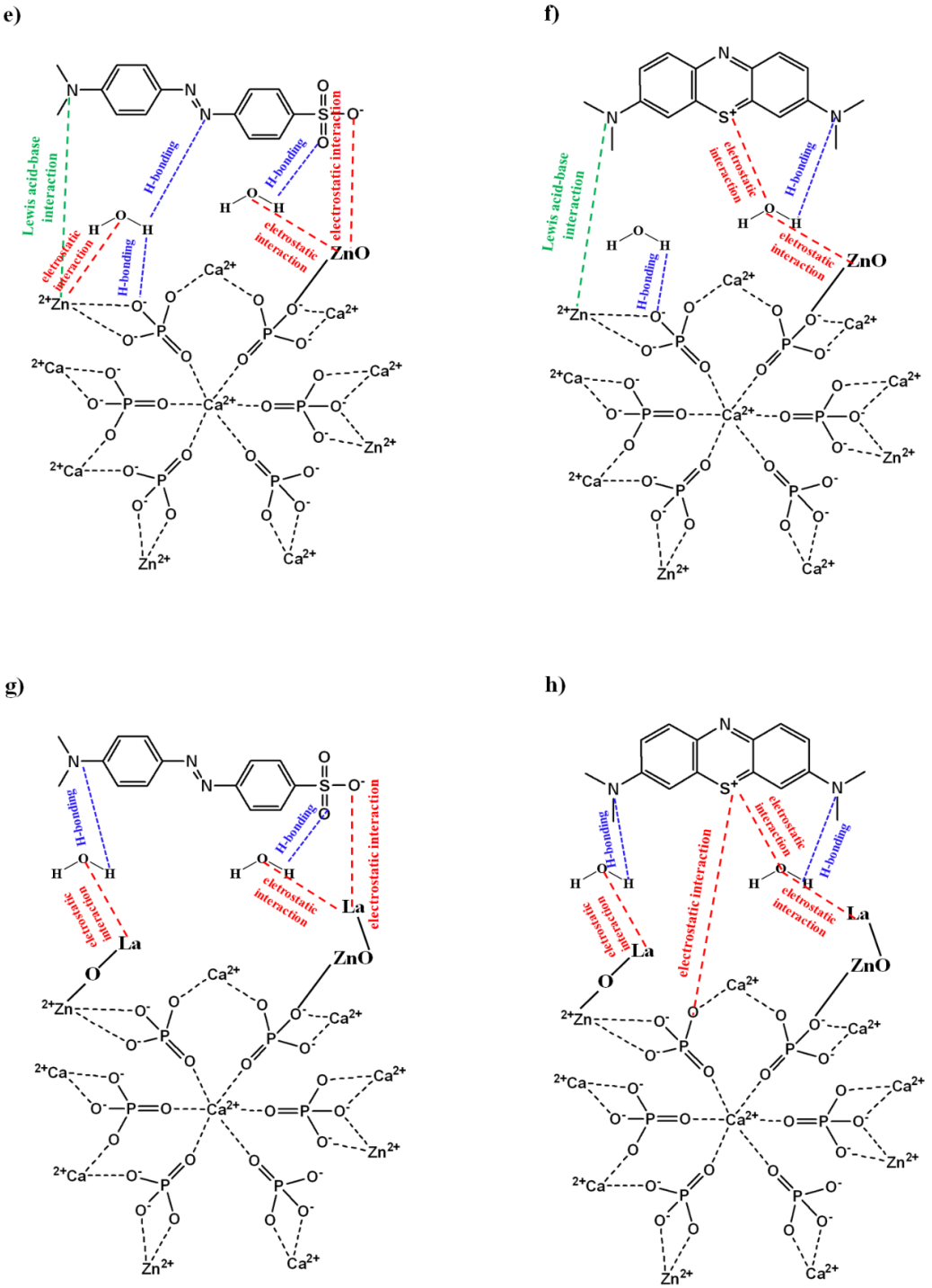

Figure 4.16. (cont) Postulated adsorption mechanism of MO and MB on (a,b) HAP 100ºC (RH), (c,d) HAP 500ºC (RH), (e,f) ZnO-HAP 500ºC (RH) and (g,h) La-ZnO-HAP 500ºC (RH).

Figure 4.13b and d show photoactivities of HAP 100ºC, HAP 500ºC, ZnO-HAP 500ºC, La-ZnO-HAP 500ºC and humidified samples. The photoactivity of HAP is derived from the oxygen vacancies at the PO_4^{3-} and HPO_4^{2-} groups formed during irradiation [194]. Consequently, electrons in HAP react with the neighboring oxygens on these vacancies to form superoxide radicals, which produce hydroxyl radicals via water molecules. Simultaneously, OH groups on the surface of HAP or adsorbed H_2O molecules can react with the photogenerated holes to generate hydroxyl radicals. These radicals actively take part in the degradation processes of MO and MB [194]. Accordingly, in the presence of HAP 100ºC, the residual percentages of MO and MB are found as 37% for MO and 36% for MB, respectively. For HAP 500ºC, lower percentages are detected (23% remaining MO percentage and 27% remaining MB percentage) owing to the increment in the oxygen deficiencies upon calcination. This results in the formation of more active centers and hence, higher photocatalytic activities.

In the case of ZnO-HAP 500ºC, incorporation and/or substitution of the ZnO into the HAP lattice leads to an enhanced photoactivity in comparison to the individual performances of ZnO, HAP 100ºC and HAP 500ºC. A similar trend is also noticed in the dark experiments of ZnO-HAP 500ºC. In this composite, both HAP and ZnO nanoparticles can initiate the generation of electrons, holes and their subsequent reactions with OH and water groups. Moreover, oxygen-deficient sites in HAP can accept photo-induced electrons of ZnO [195, 196]. Ultimately, the extended life-time of charge carriers results in the enhanced photoactivity with 5% residual MO and 2% residual MB. Promoted light absorption and reduced band gap energy of ZnO-HAP 500ºC relative to that of ZnO and HAP via UV-vis DRS analysis also support this improved photoactivity.

In the presence of La-ZnO-HAP, the photocatalytic degradations of MO and MB are almost completed within 60 min. The synergy established between La-ZnO and HAP serves as a greater reaction platform for the degradation of MO and MB via the high surface area and pore volume of La-ZnO-HAP. The existence of La ions in the matrix leads to the increased separation efficiency of the photogenerated charge carriers and induce the formation of more radicals participating in the photocatalytic reactions.

HAP 100^{o}C (RH), HAP 500^{o}C (RH), ZnO-HAP 500^{o}C (RH), and La-ZnO-HAP 500^{o}C (RH) behave similarly to their unhumidified forms and also follow the same trend of their dark adsorption capacities. The presence of adsorbed water molecules on each matrix increases the generation of hydroxyl radicals and their subsequent attacks to the MO and MB moieties.

4.3.6. Dark Adsorption Kinetics and Isotherms

The dark adsorption kinetics of eggshell, ZnO-Eggshell 500^{o}C, La-ZnO-Eggshell 500^{o}C and humidified samples are evaluated using pseudo-first order and pseudo-second order kinetic models (Figure A.3-A.6). The pseudo-first order rate constants, k_1 (min^{-1}), pseudo-second order rate constants, k_2 (g mg^{-1} min^{-1}), the adsorption capacities of MO and MB q_t (mg g^{-1}) at time t (min), equilibrium adsorption capacities, q_e (mg g^{-1}), and correlation coefficients (R^2) are listed in Table 4.3. In pseudo-first-order analysis, there exist significant differences between the calculated (q_c (calc)) and experimental equilibrium adsorption capacities (q_e (exp)). Contrarily, the fitting of the kinetic data in the pseudo-second order equation shows good linearity with higher correlation coefficients for both MO and MB. This confirms that adsorption processes of eggshell, ZnO-Eggshell 500^{o}C, La-ZnO-Eggshell 500^{o}C are driven by the chemical sorption through the electrostatic interaction formed with the functional groups of MO and MB. Similarly, Eggshell (RH), ZnO-Eggshell 500^{o}C (RH), and La-ZnO-Eggshell 500^{o}C (RH) follow pseudo-second order model with increased number of hydrogen bonding.

Dark adsorption kinetics of HAP 100^{o}C, HAP 500^{o}C, ZnO-HAP 500^{o}C, La-ZnO-HAP 500^{o}C and humidified samples are also explored by the pseudo-first order and pseudo-second order kinetic models. The validity of each model is controlled by the corresponding correlation coefficients (R^2) as well as the experimental and calculated data (Table 4.4). The fitted plots of these models are shown in Figure A.7-A.10. The linear fitting of the pseudo-second order model gives higher values of correlation coefficients (R^2) than those fitting to the pseudo-first order kinetic model. In addition, rather than the q_e (calc) values calculated by pseudo-first order kinetics, the q_e (calc) values of the pseudo-second-order model are closer to the experimental q_e (q_e (exp)) values Thus, the pseudo-second order model describes well the kinetic behavior of the samples, confirming that chemisorption is the main

adsorption mechanism. Similarly, the correlative parameters and linearized plots for the humidified samples suggest that pseudo-second order model is more appropriate to represent the adsorption routes of MO and MB. Besides, the highest k_2 values belong to the La-ZnO-HAP 500°C and La-ZnO-HAP 500°C (RH), verifying the highest rate of dark adsorption results of these catalysts due to the increased number of the functional groups and the mesoporous structure.

Table 4.3. Kinetic parameters of MO and MB adsorption on eggshell, ZnO-Eggshell 500°C, La-ZnO-Eggshell 500°C, eggshell (RH), ZnO-Eggshell 500°C (RH), La-ZnO-Eggshell 500°C (RH).

		Pseudo-first order $\ln(q_e - q_t) = \ln q_e - k_1 t$			**Pseudo-second order** $\frac{t}{q_t} = \left(\frac{1}{k_2 q_e^2}\right) + \frac{t}{q_e}$		
	q_e	**k_1**	**q_c**	**R^2**	**k_2**	**q_c**	**R^2**
MO							
Eggshell	1.88	0.029	0.412	0.9512	0.244	1.65	0.9927
ZnO-Eggshell 500°C	2.10	0.032	0.623	0.9518	0.605	2.32	0.9938
La-ZnO-Eggshell 500°C	2.84	0.063	1.029	0.9588	0.968	3.01	0.9958
Eggshell (RH)	2.08	0.030	0.523	0.9518	0.345	1.92	0.9931
ZnO-Eggshell 500°C (RH)	2.38	0.049	0.823	0.9525	0.762	2.73	0.9941
La-ZnO-Eggshell 500°C (RH)	2.93	0.073	1.231	0.9596	0.989	3.11	0.9968
MB							
Eggshell	1.57	0.028	0.392	0.9508	0.092	1.12	0.9905
ZnO-Eggshell 500°C	2.75	0.061	0.789	0.9534	0.909	2.98	0.9948
La-ZnO-Eggshell 500°C	2.27	0.036	0.809	0.9523	0.691	2.61	0.9941
Eggshell (RH)	1.73	0.022	0.401	0.9511	0.209	1.34	0.9922
ZnO-Eggshell 500°C (RH)	2.92	0.070	1.121	0.9544	0.976	3.07	0.9967
La-ZnO-Eggshell 500°C (RH)	2.52	0.054	0.989	0.9538	0.887	2.78	0.9942

Table 4.4. Kinetic parameters of MO and MB adsorption on HAP 100°C, HAP 500°C, ZnO-HAP 500°C, La-ZnO-HAP 500°C, HAP 100°C (RH), HAP 500°C (RH), ZnO-HAP 500°C (RH), La-ZnO-HAP 500°C (RH).

		Pseudo-first order $\ln (q_e - q_t) = \ln q_e - k_1 t$			**Pseudo-second order** $\frac{t}{q_t} = (\frac{1}{k_2 q^2_e}) + \frac{t}{q_e}$		
	q_e	**k_1**	**q_c**	**R^2**	**k_2**	**q_c**	**R^2**
MO							
HAP 100°C	2.17	0.007	0.31	0.9738	0.620	1.67	0.9922
HAP 500°C	2.62	0.011	0.56	0.9769	0.697	1.98	0.9946
ZnO-HAP 500°C	2.85	0.026	1.45	0.9917	0.856	2.76	0.9962
La-ZnO-HAP 500°C	3.09	0.037	1.60	0.9925	0.989	3.19	0.9978
HAP 100°C (RH)	2.32	0.009	0.34	0.9533	0.614	1.87	0.9937
HAP 500°C (RH)	2.75	0.014	0.78	0.9257	0.756	2.12	0.9948
ZnO-HAP 500°C (RH)	3.03	0.035	1.88	0.9626	0.975	3.10	0.9977
La-ZnO-HAP 500°C (RH)	3.21	0.047	2.04	0.9634	1.492	3.55	0.9981
MB							
HAP 100°C	2.65	0.011	0.89	0.9265	0.769	2.10	0.9944
HAP 500°C	2.76	0.016	0.98	0.9164	0.780	2.29	0.9955
ZnO-HAP 500°C	2.83	0.029	1.31	0.9436	0.809	2.42	0.9958
La-ZnO-HAP 500°C	2.94	0.031	1.61	0.9734	0.934	2.99	0.9974
HAP 100°C (RH)	2.80	0.019	1.12	0.9515	0.789	2.34	0.9953
HAP 500°C (RH)	2.88	0.024	1.43	0.9570	0.878	2.87	0.9963
ZnO-HAP 500°C (RH)	2.95	0.032	1.45	0.9513	0.945	3.03	0.9974
La-ZnO-HAP 500°C (RH)	3.18	0.042	1.67	0.9563	1.322	3.21	0.9979

Langmuir, Freundlich and Temkin adsorption isotherm models are employed to investigate the interactions of MO and MB with eggshell, ZnO-Eggshell 500°C, La-ZnO-Eggshell 500°C and humidified samples (Figure A.11-A.16). For all isotherms, the values of correlation coefficients (R^2), equilibrium concentrations C_e (mg L^{-1}), adsorption capacities at equilibrium points q_e (mg g^{-1}), maximum adsorption capacities q_L, (mg g^{-1}), Langmuir constants K_L (L mg^{-1}), Freundlich constants K_F (L mg^{-1}), heterogeneity factors 1/n, Tempkin

constants B_T (kJ mol^{-1}) and equilibrium binding constants K_T (L mg^{-1}) are depicted in Table 4.5. For the eggshell, ZnO-Eggshell 500ºC, La-ZnO-Eggshell 500ºC, higher R^2 values and maximum adsorption capacities, q_L (mg g^{-1}), are obtained with the application of the Langmuir model. Therefore, adsorptions of MO and MB are suggested with a monolayer coverage on a homogenous surface of equally available and energetically equivalent sites [197]. The decline in the energy of adsorbance values, K_L (L mg^{-1}), is obtained with the increasing monolayer adsorption capacities (q_L) as in the following order: La-ZnO-Eggshell 500ºC<ZnO-Eggshell 500ºC<eggshell. Moreover, the separation factor (R_L) determines the type of adsorption whether to be favorable ($0<R_L<1$) or unfavorable ($R_L>1$) in the Langmuir type of adsorption. Accordingly, R_L values for MO and MB adsorption are found to be in between 0 and 1, supporting the suitability of the Langmuir model for eggshell, ZnO-Eggshell 500ºC, La-ZnO-Eggshell 500ºC (Table 4.6). On the other hand, the adsorption data of the eggshell (RH), ZnO-Eggshell 500ºC (RH), La-ZnO-Eggshell 500ºC (RH) are well described by the Freundlich model. Thus, heterogeneous adsorption of MO and MB on humidified samples through the water molecules with additional hydrogen bonds verifies the results of dark adsorption tests. Besides, the surface heterogeneity and adsorption intensity are represented by the parameter 1/n from the slope of ln q_e versus ln C_e plot. The numerical values of 1/n vary in between 0 and 1. The favorable adsorption through surface heterogeneity of the eggshell (RH), ZnO-Eggshell 500ºC (RH), La-ZnO-Eggshell 500ºC (RH) is satisfied since their 1/n values approach to zero.

Although Temkin adsorption isotherms reveal lower correlation coefficients compared to Langmuir and Freundlich models, the increment in K_T and R^2 values shows similar trends. Hence, the highest (K_T) and R^2 values are obtained in the presence of La-ZnO-Eggshell 500ºC for MO adsorption (4.66 L mg^{-1} and 0.9799) and ZnO-Eggshell 500ºC for MB adsorption (4.06 L mg^{-1} and 0.9752) in accordance to the results of Langmuir model. Meanwhile, La-ZnO-Eggshell 500ºC (RH) for MO adsorption (5.16 L mg^{-1} and 0.9802) and ZnO-Eggshell 500ºC (RH) for MB adsorption (5.11 L mg^{-1} and 0.9802) correlate to the results of Freundlich model. The heat of adsorption (B_T) represents the heat release during the adsorption processes. B_T values higher than zero indicate the exothermic nature of the MO and MB adsorption processes [198].

Langmuir, Freundlich and Temkin isotherm models are also applied to the adsorption data of HAP 100ºC, HAP 500ºC, ZnO-HAP 500ºC, La-ZnO-HAP 500ºC and humidified samples (Figure A.17-A.24, Table 4.7). The Langmuir isotherm fits better to HAP 100ºC, HAP 500ºC, ZnO-HAP 500ºC and La-ZnO-HAP 500ºC rather than Freundlich and Temkin models. Accordingly, uniform distribution of MO and MB as a monolayer adsorption occurs on the surface active sites. The lowest adsorption energy of K_L and highest adsorption capacity are determined in the presence of La-ZnO-HAP 500ºC. Besides, the R_L values of HAP 100ºC, HAP 500ºC, ZnO-HAP 500ºC, La-ZnO-HAP 500ºC fall in between 0 and 1, supporting the favorable adsorption of MO and MB via Langmuir model (Table 4.8). Freundlich model better fits to the HAP 100ºC (RH), HAP 500ºC (RH), ZnO-HAP 500ºC (RH), and La-ZnO-HAP 500ºC (RH) with the highest correlation coefficients (R^2) and heterogeneity factor 1/n values (in the range of 0 to 1). This implies multilayer adsorption of MO and MB on the heterogeneous surfaces of humidified samples. Despite the lower values of the correlation coefficients of the Temkin isotherms than those of the Langmuir and Freundlich models, K_T binding constants are correlated with the adsorption abilities of the materials. The highest K_T and R^2 values are noticed for both MO (5.34 L mg^{-1} and 0.9816) and MB (5.18 L mg^{-1} and 0.9803) in the presence of La-ZnO-HAP 500ºC being consistent with the results of Langmuir model. In the meantime, La-ZnO-HAP 500ºC (RH) shows the highest values for MO adsorption (6.74 L mg^{-1} and 0.9905) and MB adsorption (6.72 L mg^{-1} and 0.9888) in accordance with the results of Freundlich model. Also, the positive values of adsorption energy, B_T, suggest that both MO and MB adsorptions proceed as exothermic processes.

Table 4.5. Adsorption isotherm models for MO and MB on eggshell, ZnO-Eggshell 500°C, La-ZnO-Eggshell 500°C, eggshell (RH), ZnO-Eggshell 500°C (RH), La-ZnO-Eggshell 500°C (RH).

	Langmuir $\frac{C_e}{q_e} = \frac{1}{K_L q_L} + \frac{C_e}{q_L}$			**Freundlich** $\ln q_e = \ln K_F + \frac{1}{n} \ln C_e$			**Tempkin** $q_e = \frac{RT}{B_T} \ln K_T + \frac{RT}{B_T} \ln C_e$		
	K_L	q_L	R^2	K_F	1/n	R^2	K_T	B_T	R^2
MO									
Eggshell	0.621	5.42	0.9917	0.721	0.921	0.9802	2.01	1.089	0.9595
ZnO-Eggshell 500°C	0.521	9.01	0.9947	0.809	0.924	0.9861	3.08	1.107	0.9722
La-ZnO-Eggshell 500°C	0.202	15.41	0.9968	0.899	0.944	0.9907	4.86	2.021	0.9799
Eggshell (RH)	0.112	1.97	0.9613	1.234	0.743	0.9913	2.02	1.018	0.9619
ZnO-Eggshell 500°C (RH)	0.402	2.78	0.9855	1.814	0.789	0.9922	4.39	1.327	0.9735
La-ZnO-Eggshell 500°C (RH)	0.119	4.21	0.9908	2.202	0.798	0.9978	5.16	2.223	0.9802
MB									
Eggshell	0.623	2.01	0.9903	0.713	0.969	0.9791	1.67	1.023	0.9536
ZnO-Eggshell 500°C	0.359	10.14	0.9961	0.822	0.768	0.9899	4.06	1.487	0.9752
La-ZnO-Eggshell 500°C	0.334	9.92	0.9962	0.817	0.941	0.9897	4.12	1.342	0.9737
Eggshell (RH)	0.557	1.07	0.9522	1.012	0.904	0.9909	1.99	1.075	0.9536
ZnO-Eggshell 500°C (RH)	0.417	3.99	0.9903	2.178	0.712	0.9971	5.11	2.321	0.9802
La-ZnO-Eggshell 500°C (RH)	0.419	2.96	0.9861	1.976	0.783	0.9934	4.23	1.339	0.9743

Table 4.6. Langmuir type of adsorption: Separation Factor (R_L) values for different initial concentrations (C_0) of MO and MB on Eggshell, ZnO-Eggshell 500ºC, La-ZnO-Eggshell 500ºC.

Separation Factor (R_L) $R_L = \frac{1}{1+K_L C_0}$			
$[MO]_0$ (mg L^{-1})	**Eggshell**	**ZnO-Eggshell 500ºC**	**La-ZnO-Eggshell 500ºC**
32.7	0.18	0.33	0.32
16.8	0.32	0.40	0.41
8.17	0.40	0.52	0.55
3.27	0.43	0.59	0.60
1.64	0.55	0.73	0.78
0.82	0.66	0.79	0.81
0.32	0.78	0.85	0.88
$[MB]_0$ (mg L^{-1})	**Eggshell**	**ZnO-Eggshell 500ºC**	**La-ZnO-Eggshell 500ºC**
31.9	0.19	0.29	0.28
15.9	0.33	0.35	0.34
7.97	0.43	0.43	0.48
3.19	0.48	0.55	0.54
1.59	0.53	0.61	0.78
0.79	0.61	0.73	0.81
0.319	0.77	0.82	0.88

Table 4.7. Adsorption models for MO and MB on HAP 100ºC, HAP 500ºC, ZnO-HAP 500ºC, La-ZnO-HAP 500ºC, HAP 100ºC (RH), HAP 500ºC (RH), ZnO-HAP 500ºC (RH), La-ZnO-HAP 500ºC (RH).

	Langmuir $\frac{C_e}{q_e} = \frac{1}{K_L q_L} + \frac{C_e}{q_L}$			**Freundlich** $\ln q_e = \ln K_F + \frac{1}{n} \ln C_e$			**Tempkin** $q_e = \frac{RT}{B_T} \ln K_T + \frac{RT}{B_T} \ln C_e$		
	K_L	q_L	R^2	K_F	1/n	R^2	K_T	B_T	R^2
MO									
HAP 100ºC	0.543	7.75	0.9939	0.756	0.706	0.9851	3.03	1.087	0.9702
HAP 500ºC	0.419	8.78	0.9951	0.811	0.685	0.9892	3.98	1.216	0.9732
ZnO-HAP 500ºC	0.196	17.2	0.9976	0.978	0.670	0.9906	4.99	2.099	0.9805
La-ZnO-HAP 500ºC	0.070	19.4	0.9986	1.112	0.591	0.9918	5.34	2.654	0.9816
HAP 100ºC (RH)	0.476	2.34	0.9851	1.423	0.711	0.9917	3.43	1.198	0.9715
HAP 500ºC (RH)	0.276	3.45	0.9879	2.004	0.676	0.9946	4.32	1.888	0.9766
ZnO-HAP 500ºC (RH)	0.054	5.08	0.9917	2.398	0.789	0.9984	5.89	2.678	0.9863
La-ZnO-HAP 500ºC (RH)	0.029	6.21	0.9928	2.671	0.739	0.9996	6.74	3.437	0.9905
MB									
HAP 100ºC	0.337	11.9	0.9963	0.854	0.911	0.9902	4.33	1.674	0.9761
HAP 500ºC	0.213	14.9	0.9966	0.879	0.882	0.9907	4.77	2.001	0.9797
ZnO-HAP 500ºC	0.192	16.1	0.9971	0.972	0.767	0.9909	5.01	2.089	0.9800
La-ZnO-HAP 500ºC	0.082	18.4	0.9979	1.024	0.783	0.9913	5.18	2.399	0.9803
HAP 100ºC (RH)	0.233	3.67	0.9882	2.048	0.925	0.9951	4.75	1.978	0.9773
HAP 500ºC (RH)	0.179	4.33	0.9899	2.154	0.833	0.9958	5.07	2.123	0.9801
ZnO-HAP 500ºC (RH)	0.077	4.19	0.9911	2.268	0.672	0.9980	5.23	2.587	0.9807
La-ZnO-HAP 500ºC (RH)	0.037	5.89	0.9925	2.442	0.769	0.9993	6.72	2.989	0.9888

Table 4.8. Langmuir type of adsorption: Separation Factor (R_L) values for different initial concentrations (C_0) of MO and MB (mg L^{-1}) on HAP 100ºC, HAP 500ºC, ZnO-HAP 500ºC, La-ZnO-HAP 500ºC.

Separation Factor (R_L) $R_L = \frac{1}{1+K_L C_0}$				
$[MO]_0$	**HAP 100ºC**	**HAP 500ºC**	**ZnO-HAP 500ºC**	**La-ZnO-HAP 500ºC**
32.7	0.29	0.31	0.33	0.35
16.8	0.30	0.33	0.39	0.34
8.17	0.37	0.44	0.40	0.43
3.27	0.43	0.53	0.52	0.55
1.64	0.58	0.61	0.60	0.63
0.82	0.70	0.72	0.71	0.76
0.32	0.76	0.78	0.88	0.89
$[MB]_0$	**HAP 100ºC**	**HAP 500ºC**	**ZnO-HAP 500ºC**	**La-ZnO-HAP 500ºC**
31.9	0.21	0.22	0.31	0.32
15.9	0.30	0.29	0.30	0.43
7.97	0.40	0.41	0.43	0.45
3.19	0.49	0.50	0.53	0.54
1.59	0.58	0.64	0.61	0.60
0.79	0.67	0.69	0.73	0.79
0.319	0.76	0.78	0.80	0.83

4.3.7. Kinetic Analysis Under Irradiation

The effect of initial concentration variations (in the range of 32.7-0.327 mg L^{-1} for MO and in the range of 31.9-0.319 mg L^{-1} for MB) on the photocatalytic reactions is evaluated in the presence of eggshell, ZnO-Eggshell 500°C, La-ZnO-Eggshell 500°C, HAP 100°C, HAP 500°C, ZnO-HAP 500°C, La-ZnO-HAP 500°C (Figure A.25 and A.26) and humidified samples (Figure A.27 and A.28). The rates of MO and MB degradations are calculated on the basis of pseudo-first order kinetic model via ln ($[MO]_0/[MO]_t$) or ($[MB]_0/[MB]_t$) versus time plots where $[MO]_0$ and $[MB]_0$ represent the concentrations of MO and MB after dark equilibrium adsorption, while $[MO]_t$ and $[MB]_t$ correspond to the concentrations at time t (min). The rate constants k (min^{-1}) obtained from the slopes of the lines reveal an inverse correlation between degradation rate and initial concentrations of MO and MB (Table 4.9-12). At high concentrations, MO or MB molecules may accumulate on the active catalysts sites, block the light penetration through these sites and eventually decrease the rates.

Langmuir-Hinshelwood kinetic analysis is also applied to describe the degradation processes of MO and MB. Accordingly, La-ZnO-Eggshell 500°C, La-ZnO-Eggshell 500°C (RH), La-ZnO-HAP 500°C and La-ZnO-HAP 500°C (RH) show the highest rates and regressions for both MO and MB (Figure 4.16 and 4.17). In each rate (R) versus $[MO]_0$ or $[MB]_0$ plot a saturation level is noticed, following zero order kinetics (Figure 4.16a,c,e and g and Figure 4.17a,c,e and g). The plots of reciprocal rate (1/R) versus reciprocal of initial concentration of MO or MB ($1/[MO]_0$ or $1/[MB]_0$) give the adsorption coefficients (K, L mg^{-1}) from the slopes and the reaction rate constants (k, mg^{-1} L) from the intercepts (Figure 4.16b,d,f and h and Figure 4.17b,d,f and h and Table 4.14). La-ZnO-Eggshell 500°C, La-ZnO-Eggshell 500°C (RH), La-ZnO-HAP 500°C and La-ZnO-HAP 500°C (RH) reveal the highest rate constants, being corroborated with the degradation results.

Table 4.9. First-order rate constants (k, min^{-1}) and linear regression values (R) for the photocatalytic degradation initial concentrations of MO (mg L^{-1}) and MB (mg L^{-1}) in the presence of eggshell, ZnO-Eggshell 500ºC and La-ZnO-Eggshell 500ºC.

	Eggshell		**ZnO-Eggshell 500ºC**		**La-ZnO-Eggshell 500ºC**	
$[MO]_0$	**k**	**R^2**	**k**	**R^2**	**k**	**R^2**
32.7	0.0009	0.9462	0.0023	0.9593	0.0105	0.9618
16.3	0.0012	0.9334	0.0044	0.9643	0.0195	0.9790
8.17	0.0014	0.9492	0.0077	0.9909	0.0216	0.9821
3.27	0.0021	0.9692	0.0156	0.9962	0.0366	0.9971
1.63	0.0028	0.9769	0.0161	0.9945	0.0441	0.9867
0.81	0.0034	0.9771	0.0171	0.9940	0.0574	0.9901
0.32	0.0048	0.9789	0.0212	0.9877	0.0615	0.9921
$[MB]_0$	**k**	**R^2**	**k**	**R^2**	**k**	**R^2**
31.9	0.0007	0.8512	0.0032	0.9612	0.0115	0.9821
15.9	0.0023	0.8783	0.0059	0.9712	0.0202	0.9879
7.95	0.0029	0.9298	0.0071	0.9812	0.0241	0.9902
3.19	0.0032	0.9345	0.0163	0.9945	0.0371	0.9962
1.59	0.0022	0.9434	0.0175	0.9824	0.0469	0.9943
0.79	0.0025	0.9683	0.0192	0.9845	0.0571	0.9952
0.31	0.0033	0.9767	0.0218	0.9876	0.0603	0.9953

Table 4.10. First-order rate constants (k, min^{-1}) and linear regression values (R) for the photocatalytic degradation initial concentrations of MO (mg L^{-1}) and MB (mg L^{-1}) in the presence of eggshell (RH), ZnO-Eggshell 500ºC (RH) and La-ZnO-Eggshell 500ºC (RH).

	Eggshell (RH)		**ZnO-Eggshell 500ºC (RH)**		**La-ZnO-Eggshell 500ºC (RH)**	
$[MO]_0$	**k**	**R^2**	**k**	**R^2**	**k**	**R^2**
32.7	0.0009	0.9278	0.0045	0.9698	0.0102	0.9912
16.3	0.0012	0.9301	0.0078	0.9712	0.0203	0.9920
8.17	0.0016	0.9334	0.0101	0.9791	0.0276	0.9933
3.27	0.0025	0.9483	0.0130	0.9852	0.0299	0.9941
1.63	0.0037	0.9532	0.0162	0.9872	0.0359	0.9949
0.81	0.0042	0.9634	0.0182	0.9899	0.0423	0.9952
0.32	0.0052	0.9732	0.0244	0.9910	0.0587	0.9961
$[MB]_0$	**k**	**R^2**	**k**	**R^2**	**k**	**R^2**
31.9	0.0012	0.9401	0.0103	0.9812	0.0119	0.9900
15.9	0.0013	0.9502	0.0143	0.9832	0.0221	0.9902
7.95	0.0019	0.9556	0.0158	0.9863	0.0321	0.9916
3.19	0.0021	0.9602	0.0168	0.9872	0.0354	0.9923
1.59	0.0029	0.9678	0.0210	0.9891	0.0401	0.9931
0.79	0.0034	0.9721	0.0220	0.9906	0.0421	0.9942
0.31	0.0045	0.9832	0.0231	0.9912	0.0553	0.9959

Table 4.11. First-order rate constants (k, min^{-1}) and linear regressions (R) for the photodegradation initial concentrations of MO (mg L^{-1}) and MB (mg L^{-1}) in the presence of HAP 100ºC, HAP 500ºC, ZnO-HAP 500ºC and La-ZnO-HAP 500ºC.

	HAP 100ºC		**HAP 500ºC**		**ZnO-HAP 500ºC**		**La-ZnO-HAP500ºC**	
$[MO_0$	**k**	**R^2**	**k**	**R^2**	**k**	**R^2**	**k**	**R^2**
32.7	0.0042	0.9698	0.0059	0.9702	0.0090	0.9798	0.0119	0.9845
16.3	0.0073	0.9793	0.0107	0.9791	0.0163	0.9893	0.0222	0.9899
8.17	0.0086	0.9892	0.0139	0.9834	0.0218	0.9899	0.0303	0.9906
3.27	0.0102	0.9906	0.0145	0.9899	0.0243	0.9903	0.0473	0.9934
1.63	0.0139	0.9920	0.0167	0.9913	0.0297	0.9925	0.0596	0.9952
0.81	0.0168	0.9921	0.0188	0.9941	0.0323	0.9943	0.0699	0.9966
0.32	0.0200	0.9932	0.0227	0.9945	0.0383	0.9953	0.0791	0.9971
$[MB]_0$	**k**	**R^2**	**k**	**R^2**	**k**	**R^2**	**k**	**R^2**
31.9	0.0047	0.9708	0.0061	0.9732	0.0092	0.9803	0.0121	0.9883
15.9	0.0081	0.9787	0.0116	0.9802	0.0185	0.9895	0.0220	0.9901
7.95	0.0090	0.9890	0.0151	0.9845	0.0214	0.9903	0.0356	0.9903
3.19	0.0113	0.9902	0.0174	0.9867	0.0266	0.9912	0.0477	0.9936
1.59	0.0144	0.9911	0.0186	0.9901	0.0313	0.9928	0.0645	0.9956
0.79	0.0171	0.9913	0.0205	0.9921	0.0359	0.9950	0.0742	0.9969
0.31	0.0203	0.9925	0.0238	0.9939	0.0404	0.9959	0.0804	0.9975

Table 4.12. First-order rate constants (k, min^{-1}) and linear regressions (R) for the photodegradation initial concentrations of MO (mg L^{-1}) and MB (mg L^{-1}) in the presence of HAP 100ºC (RH), HAP 500ºC (RH), ZnO-HAP 500ºC (RH) and La-ZnO-HAP 500ºC (RH).

	HAP 100ºC (RH)		**HAP 500ºC (RH)**		**ZnO-HAP 500ºC (RH)**		**La-ZnO-HAP 500ºC (RH)**	
$[MO_0$	**k**	**R^2**	**k**	**R^2**	**k**	**R^2**	**k**	**R^2**
32.7	0.0054	0.9832	0.0061	0.9840	0.0101	0.9878	0.0120	0.9902
16.3	0.0079	0.9843	0.0113	0.9864	0.0172	0.9889	0.0121	0.9912
8.17	0.0099	0.9882	0.0156	0.9889	0.0234	0.9900	0.0231	0.9920
3.27	0.0106	0.9901	0.0189	0.9919	0.0254	0.9912	0.0321	0.9940
1.63	0.0231	0.9912	0.0231	0.9934	0.0300	0.9931	0.0543	0.9943
0.81	0.0244	0.9930	0.0321	0.9942	0.0432	0.9952	0.0674	0.9973
0.32	0.0256	0.9942	0.0401	0.9956	0.0472	0.9962	0.0873	0.9987
$[MB]_0$	**k**	**R^2**	**k**	**R^2**	**k**	**R^2**	**k**	**R^2**
31.9	0.0053	0.9861	0.0072	0.9845	0.0099	0.9898	0.0102	0.9873
15.9	0.0091	0.9873	0.0121	0.9854	0.0197	0.9901	0.0132	0.9901
7.95	0.0110	0.9892	0.0145	0.9876	0.0245	0.9911	0.0133	0.9932
3.19	0.0123	0.9912	0.0178	0.9916	0.0321	0.9924	0.0344	0.9945
1.59	0.0178	0.9915	0.0199	0.9921	0.0445	0.9933	0.0432	0.9921
0.79	0.0201	0.9923	0.0234	0.9934	0.0586	0.9953	0.0561	0.9967
0.31	0.0231	0.9934	0.0342	0.9944	0.0601	0.9959	0.0834	0.9980

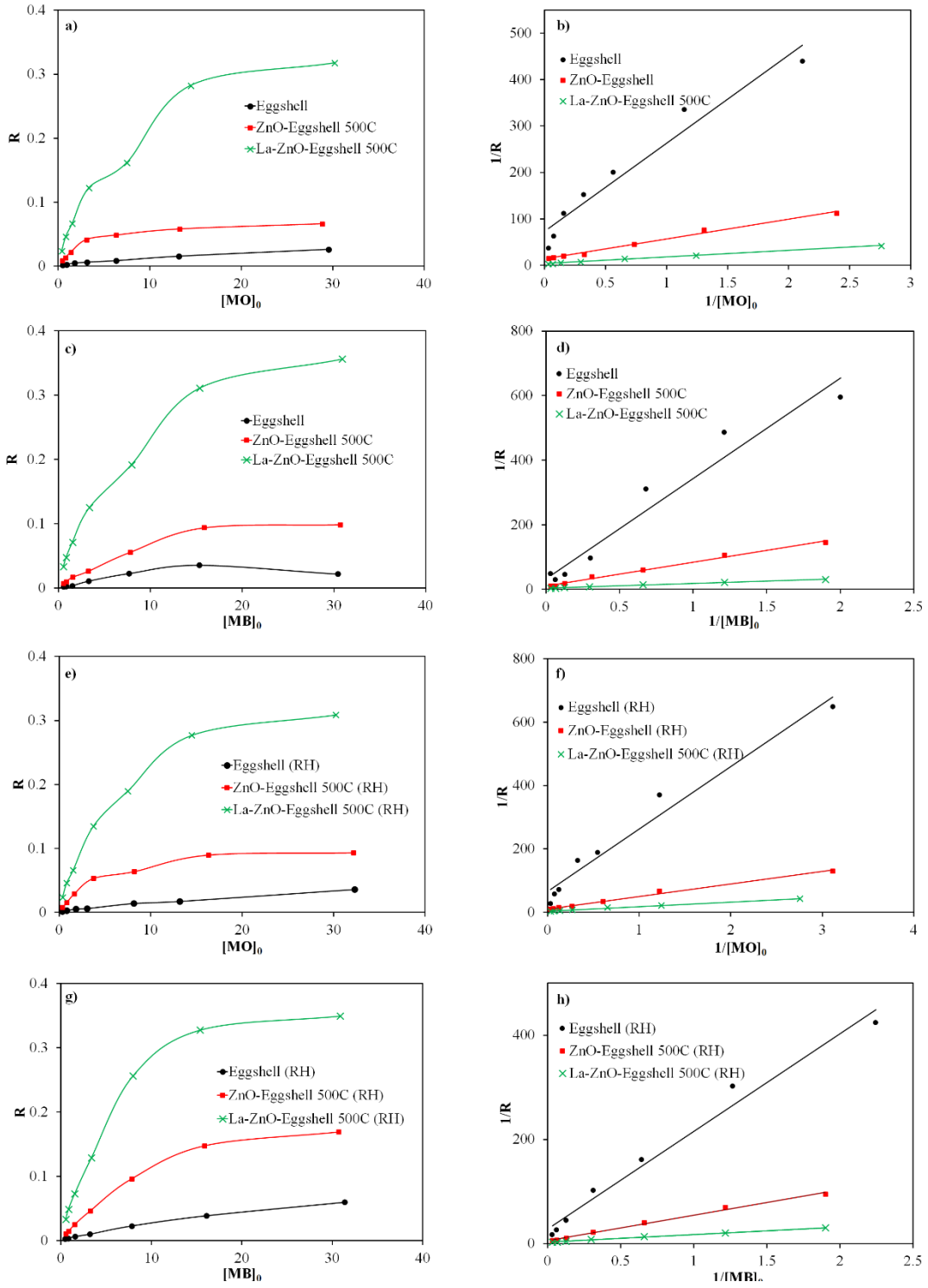

Figure 4.17. Langmuir-Hinshelwood kinetic analysis (a,c) for MO and (b,d) for MB in the presence of eggshell, ZnO-Eggshell 500°C, La-ZnO-Eggshell 500°C.

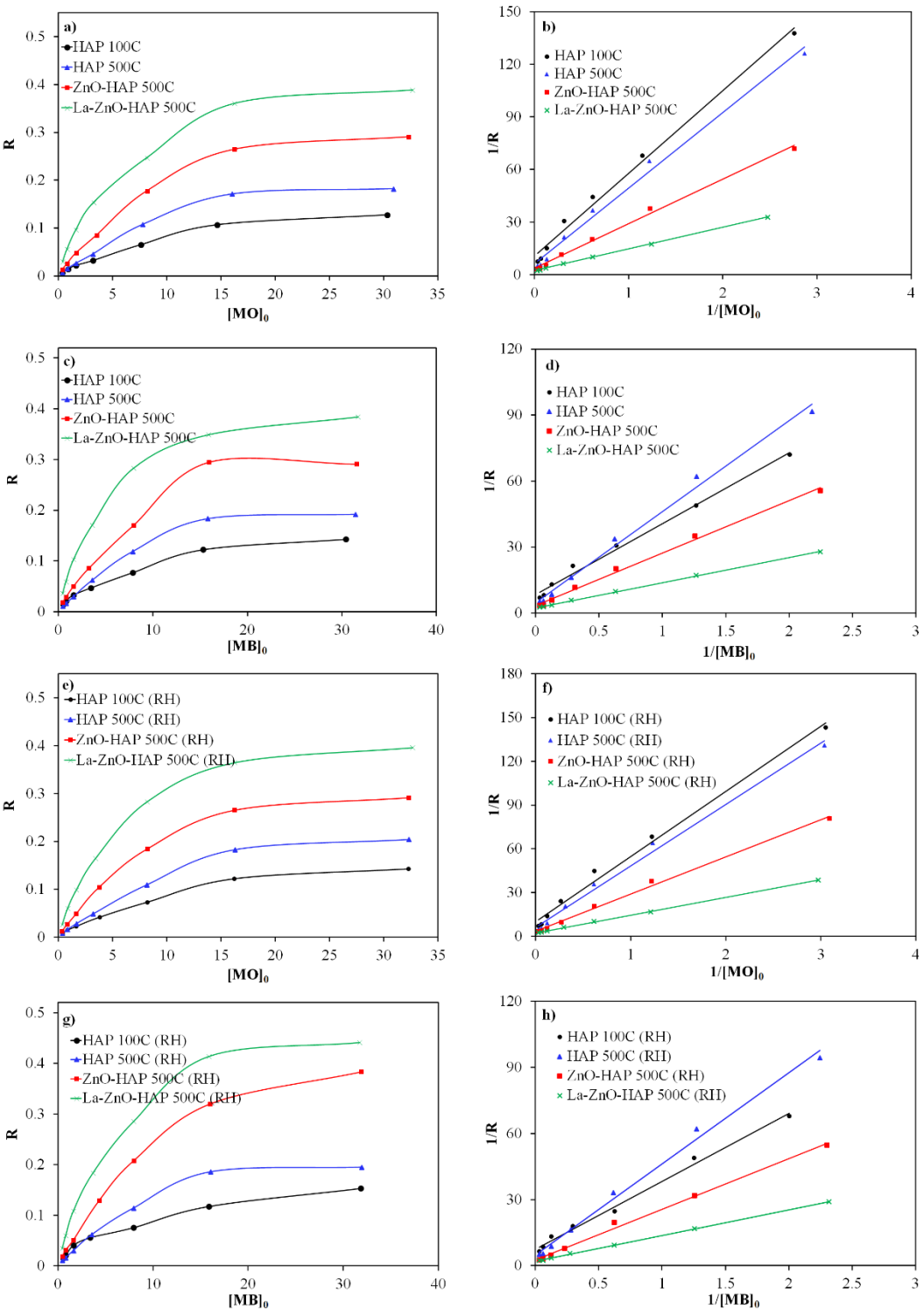

Figure 4.18. Langmuir-Hinshelwood kinetic analysis (a,c) for MO and (b,d) for MB in the presence of HAP 100ºC, HAP 500ºC, ZnO-HAP 500ºC, La-ZnO-HAP 500ºC.HAP 100ºC (RH), HAP 500ºC (RH), ZnO-HAP 500ºC (RH), La-ZnO-HAP 500ºC (RH).

Table 4.13. Adsorption coefficients (K) and the rate constants (k) of eggshell, ZnO-Eggshell 500ºC, La-ZnO-Eggshell 500ºC, HAP 100ºC, HAP 500ºC, ZnO-HAP 500ºC, La-ZnO-HAP 500ºC and humidified samples for Langmuir-Hinshelwood kinetic model.

	K (L mg^{-1})	**k ($L^{-1}min^{-1}$)**
MO		
Eggshell	0.3823	0.0137
ZnO-Eggshell 500ºC	0.3222	0.0724
La-ZnO-Eggshell 500ºC	0.2671	0.2652
Eggshell (RH)	0.3340	0.0152
ZnO-Eggshell 500ºC (RH)	0.2715	0.0935
La-ZnO-Eggshell 500ºC (RH)	0.2439	0.2825
HAP 100ºC	0.2268	0.0935
HAP 500ºC	0.1497	0.1554
ZnO-HAP 500ºC	0.1446	0.2721
La-ZnO-HAP 500ºC	0.1940	0.4161
HAP 100ºC (RH)	0.2223	0.1007
HAP 500ºC (RH)	0.1446	0.1640
ZnO-HAP 500ºC (RH)	0.1443	0.2727
La-ZnO-HAP 500ºC (RH)	0.1836	0.4466
MB		
Eggshell	0.1047	0.0307
ZnO-Eggshell 500ºC	0.1386	0.0980
La-ZnO-Eggshell 500ºC	0.2105	0.3219
Eggshell (RH)	0.1487	0.0358
ZnO-Eggshell 500ºC (RH)	0.1123	0.1825
La-ZnO-Eggshell 500ºC (RH)	0.1828	0.3721
HAP 100ºC	0.2607	0.1191
HAP 500ºC	0.1127	0.2140
ZnO-HAP 500ºC	0.1428	0.2934
La-ZnO-HAP 500ºC	0.2036	0.4281
HAP 100ºC (RH)	0.2402	0.1347
HAP 500ºC (RH)	0.1150	0.2102
ZnO-HAP 500ºC (RH)	0.1102	0.3895
La-ZnO-HAP 500ºC (RH)	0.1687	0.5076

4.3.8. Stability Tests

Stabilities of the eggshell, ZnO-Eggshell 500ºC, La-ZnO-Eggshell 500ºC, HAP 100ºC, HAP 500ºC, ZnO-HAP 500ºC, La-ZnO-HAP 500ºC are also controlled (Figure 4.18 and 4.19). Samples are gathered by centrifugation, then following the washing runs, they are reused in the next photocatalytic reaction under identical experimental conditions for four consecutive cycles. The variation in photocatalytic degradation percentages from the first cycle to the fourth cycle is as follows; eggshell (from 25.2 to 23.9% for MO and from 33.2 to 31% for MB), ZnO-Eggshell 500ºC (from 81.1 to 79.3% for MO and from 86.2 to 85.4% for MB), La-ZnO-Eggshell 500ºC (from 99.7 to 99.4% for MO and from 99.8 to 99.6% for MB) and HAP 100ºC (from 63.1 to 61.1% for MO and from 64.3 to 62.1% for MB). HAP 500ºC (from 77.7 to 76.8% for MO and from 63.2 to 62.4% for MB), ZnO-HAP 500ºC (from 95.5 to 94.5% for MO and from 98.4 to 98% for MB), La-ZnO-HAP 500ºC (from 99.8 to 99.6% for MO and from 99.8 to 99.6% for MB). The negligible decrements in the percentages indicate stabilities of the eggshell, ZnO-Eggshell 500ºC, La-ZnO-Eggshell 500ºC, HAP 100ºC, HAP 500ºC, ZnO-HAP 500ºC, La-ZnO-HAP 500ºC.

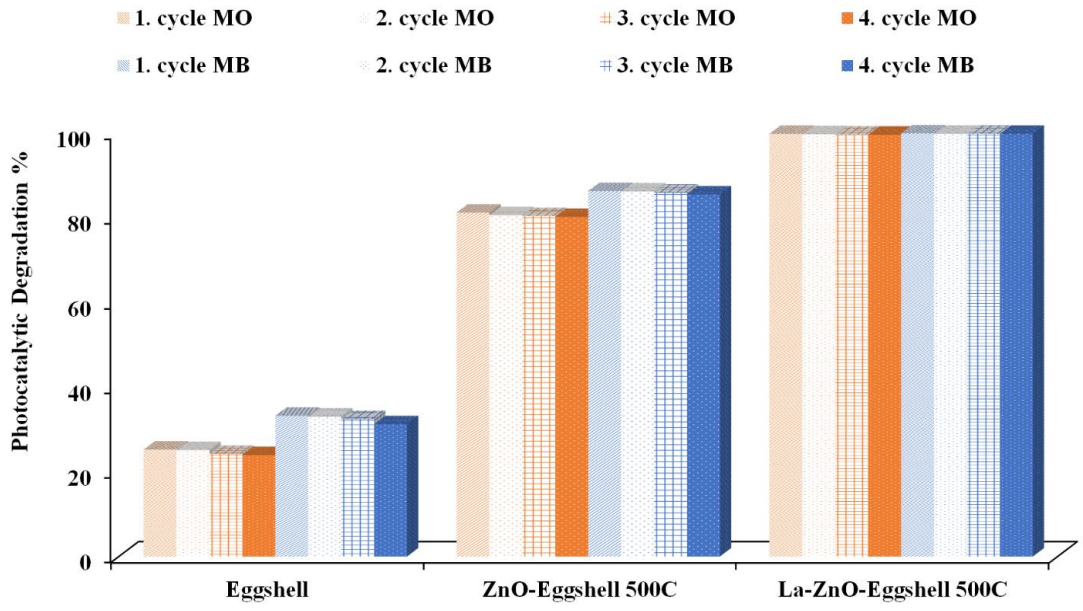

Figure 4.19. Stability tests of eggshell, ZnO-Eggshell 500ºC and La-ZnO-Eggshell 500ºC.

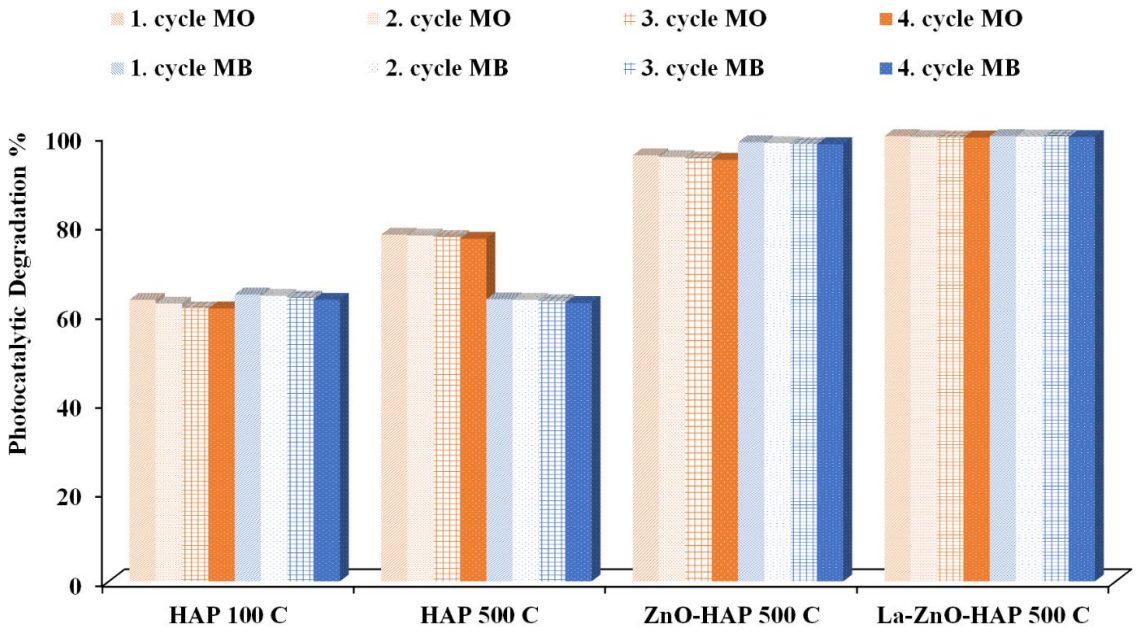

Figure 4.20. Stability tests of HAP 100ºC, HAP 500ºC, ZnO-HAP 500ºC and La-ZnO-HAP 500ºC.

4.4. Conclusion

In this chapter, ZnO-eggshell and La-ZnO-eggshell, ZnO-eggshell (RH) and La-ZnO-eggshell (RH) and ZnO-HAP and La-ZnO-HAP, ZnO-HAP (RH) and La-ZnO-HAP (RH) catalysts are examined.

In the first catalyst group where eggshell is used as a support material, characterization results confirm the in-situ generation of ZnO crystallites. Moreover, ZnO and La-ZnO loading onto the eggshell increase the surface areas and induce mesoporous structures. Thus, MO and MB adsorptions and degradations are improved via enhanced electrostatic interactions, Lewis acid-base interactions and H-bonding. The higher photodegradation efficiencies of the humidified catalysts compared to the unhumidified forms are attributed to the increased adsorption abilities due to the interactions of water molecules with MO and MB as well as the generation of more hydroxyl radicals.

In the second catalyst group, HAP is synthesized from the eggshell and used as a support material. The as-prepared HAP 100ºC displays higher surface area and porosity compared to the eggshell. To examine the thermal stability and structural variations, HAP is calcined at 500ºC. It is observed that the calcination of HAP at 500ºC increases the surface area and expands the pore volume due to the improvement of the crystallinity. The ZnO generation in the ZnO-HAP 500ºC and La-ZnO-HAP 500ºC frames is verified by the characterization studies. The higher surface area and porosity of ZnO-HAP 500ºC compared to HAP 100ºC and HAP 500ºC is attributed to the formation of interparticle voids among ZnO nanoparticles. La-ZnO-HAP 500ºC has the highest surface area and porosity since existence of La ions inhibits the formation of ZnO aggregates. HAP 100ºC and HAP 500ºC show photoactivity under UV irradiation being consisted with their UV-vis DRS profiles. The decrement in the band energy of HAP 500ºC relative to the HAP 100ºC is attributed to the creation of more oxygen deficiencies upon calcination. ZnO-HAP 500ºC and La-ZnO-HAP 500ºC exhibit the characteristic absorption edge of ZnO. Accordingly, ZnO-HAP 500ºC exhibits higher photocatalytic performance compared to HAP 100ºC and HAP 500ºC due to the existence of ZnO in the frame. The highest photocatalytic degradation rate is achieved in the case of La-ZnO-HAP 500ºC owing to the synergy established between La-ZnO and HAP. Similar to the eggshell supported catalysts, the humidified samples reveal structural stabilities and improved activities in adsorption and photocatalytic degradation processes, attributed to the existence of water molecules on the surface of the catalysts, formation of more H-bonds and generation of more hydroxyl radicals.

5. BINARY AND TERNARY LAYERED DOUBLE HYDROXIDES, FLY ASH, ZEOLITE AND ZIF-8 SUPPORTED LAYERED DOUBLE HYDROXIDES

5.1. Introduction

Layered double hydroxides (LDHs) are an emerging class of two-dimensional (2D) layered materials from the family of hydrotalcite-like compounds. Hydrotalcite is a naturally occurring layered mineral with the formula of ($Mg_6Al_2(OH)_{16}CO_3.4H_2O$), consisting of stacked brucite layers of $Mg(OH)_2$ [199]. The structure of LDHs is also described based on the stacking of charged brucite-like layers. LDHs are represented by the general formula of $[M^{2+}{}_{1-x}M^{3+}{}_x(OH)_2]^{x+}$ $[A^{n-}{}_{x/n}.mH_2O]^{x-}$ where M^{2+} and M^{3+} are divalent and trivalent metal cations while A^{n-} is an exchangeable interlayer anion of valence n. The value of x in between 0.18 and 0.33 signifies the mole fraction of trivalent metal cations ($M^{3+}/(M^{2+}+M^{3+})$), which also determines the phase purity of the LDH material [200]. The number of interlayer water is shown by the sign of m. The $[M^{2+}{}_{1-x}M^{3+}(OH)_2]$ part in the formula of LDHs defines the composition of brucite-like layers and $[A^{n-}{}_{x/n}.mH_2O]^{x-}$ part denotes the composition of interlayer space. A schematic representation of a LDH is displayed in Figure 3.1. The brucite-like layers are assembled of octahedral units in which divalent or trivalent cations occupy the center of the octahedron whose vertexes contain six OH^- ions that connect to construct 2D layers. The predominant positive charge on the layers which is generated via the partial substitution of divalent cations by trivalent cations is compensated with interlayer anions to maintain electroneutrality. Besides, the water molecules complete interlayer voids [199, 201, 202]. The interlayer distance (basal spacing) in LDH structure is influenced by the ionic radius, charge density and electronegativity of metal cations as well as the nature of the interlayer anions [201, 202].

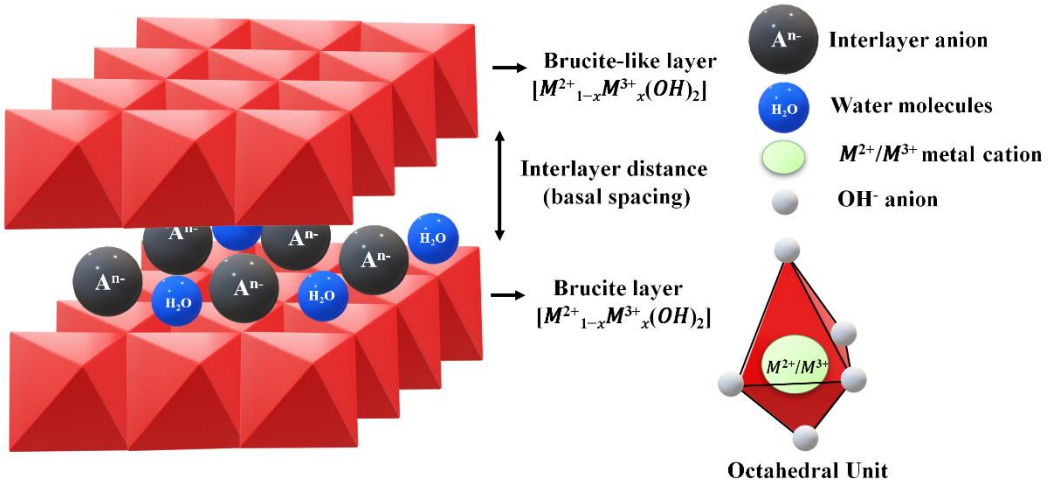

Figure 5. 1. Schematic representation of LDH.

The structural features of LDHs can be tailored by tuning the types of M^{2+} (e.g. Mg^{2+}, Zn^{2+}, Cu^{2+}, Mn^{2+} etc.) and M^{3+} (e.g. Al^{3+} Fe^{3+}, Cr^{3+}, Co^{3+} etc.), the molar ratio of M^{2+}/M^{3+}, the nature of interlayer anions (e.g. NO_3^-, Cl^-, CO_3^{2-}, SO_4^{2-} etc.) and preparation temperature in order to meet the requirements for the application areas [203–205]. In particular, LDHs are regarded as promising versatile adsorbents considering the attractive properties such as effective surface area, anion exchange capacity and flexible interlayer space [206–208]. The charged layers and a large number of accessible sites endow LDHs ability to capture anionic or cationic substances [209]. Secondly, the lack of crosslinking between cation layers of LDHs and the weak interlayer bonding allow the exchange of the interlayer anions with many inorganic or organic anions via simple ion exchange mechanism [210]. Moreover, the layers of LDHs provide a flexible confined space to host various guest anions and enable to formation of probable interactions such as electrostatic attraction and hydrogen bonding [211].

LDHs are transformed into layered double oxides (LDOs) upon thermal treatment at and above temperatures of 400°C-500°C under the ambient air [212]. The decomposition of the layered structure of LDHs by calcination initiates the formation of mixed metal oxides. Several works in the literature report the adsorption capacities of LDOs for the removal of dye molecules such as methyl orange [213], acid blue 113 [212], congo red [214], indigo carmine [215], acid yellow 42 [216] and acid brown 14 [217].

The photoactivity of LDHs is attributed to the formation of photoinduced defects on the surface oxides which can act as active centers for surface reactions. Additionally, the layered structure enhances the photoactivity of LDHs by providing mobility for photoexcited charge carriers [205]. It is also noticed that LDOs show improved photoactivity for the degradation of dyes compared to the LDHs owing to the formation of mixed metal oxides such as ZnO, Fe_2O_3 etc. depending on the nature of the metal cations in the structure [205, 218, 219]. Despite the excellent properties of LDHs and LDOs in the adsorption and photocatalytic processes, there are still drawbacks that limit their utilization in practical applications. For instance, the agglomeration of nano-sized particles of LDHs and LDOs is recognized to diminish the effective surface area and reaction reactivity, which eventually causes an adverse effect on the adsorption and photocatalytic performance [220]. In recent studies, a construction strategy with the combination of LDHs (or LDOs) by multiscale porous materials such as graphene oxide [221], biochar [222], activated carbon [213] and sepiolite [223] is explored to offer potential solution on problematic issues.

In the line of these studies, fly ash, zeolite and ZIF-8 are used as support materials in this study for the as-synthesized LDHs and LDOs. Fly ash is a massive industrial by-product discharged from power plants through the coal combustion process [224, 225]. It is defined as an inorganic ferro-alumino-silicate material [226]. The powder of fly ash ensembles of different crystalline and amorphous phases. The main mineral crystalline phases in fly ash are quartz (SiO_2), mullite ($Al_2O_3.2SiO_3$), lime (CaO) and hematite (Fe_2O_3), while the amorphous content is associated with the glassy phase being rounded cenospheres [227, 228]. The physical properties of fly ash depend on the type of coal burned and burning conditions [224]. In the thermochemical transformation of minerals during the coal combustion process, small droplets occur upon melting of minerals and surface tension forces adopt the spherical shape of hollow particles which are called as cenospheres. The structure of fly ash is composed of cenosphere aggregates of about 01-100 μm in size [229]. The superior features of fly ash such as high porosity, thermal stability, large surface area, ultralight weight, inert nature and low-cost make it a demanding material to use in dye adsorption processes [230, 231]. Besides, fly ash is proposed as a support material to develop composite materials to enhance the effectiveness of various adsorbents and photocatalysts [226, 227, 232, 233].

Zeolite is an hydrated alumina-silicate material with the empirical formula of $M_{(2/n)}O.Al_2O_3.xSiO_2.yH_2O$, where M defines alkali or alkaline earth metal, n is a sign of the charge on the metal atom, x is the number of silicon oxide that exists in the matrix, and y is the number of water molecules [234]. In the matrix of zeolite, SiO_2 and AlO_4 tetrahedra are linked to each other by sharing oxygen atoms to construct a three-dimensional (3D) framework [235, 236]. The substitution of tetravalent Si ions by trivalent Al ions in the in the tectosilicate framework creates a net negative charge on the surface of zeolite [234]. The resulting negative charge is balanced by counter ions of the alkali or alkali earth metal cations that situate in the cavities of zeolite [236]. These ions on the external surface of zeolite, bound with the aluminosilicate structure by weak electrostatic interactions. Zeolite possesses a rigid microporous structure with well-defined channels. The attractive structural properties of zeolite such as the large specific surface area and ordered microporosity as well as its low-cost and abundant availability gather attention from researchers to develop zeolite-based composites for adsorption processes [235, 237, 238]. Besides, zeolite contains both Lewis acid sites derived from the existence of Al in the matrix and Lewis basic sites derived from the oxygen adjacent in the Si-O-Al coordination [239]. These Lewis acidic-basic sites act as electron acceptor and electron donor parts in the framework. Thus, these features encourage the usage of zeolite as an ideal support material to host the photocatalysts [240-244].

This chapter has four sections; in the first section, binary LDHs at 100°C and their corresponding LDOs at 500°C are prepared, characterized and investigated in terms of adsorption properties and photoactivity for MO, MB and SA (Section 5.3). The constituents of these binary systems; Mg^{2+} and Zn^{2+} are used as divalent metal cations, Al^{3+} and Fe^{3+} are used as trivalent metal cations and NO_3^- are used as interlayer anions. In the second and third sections, as-synthesized binary LDHs and LDOs are supported by fly ash and zeolite materials to improve their adsorption abilities and photocatalytic performances (Section 5.4 and Section 5.5). In the fourth section, two different ternary LDHs and LDOs are prepared, characterized and evaluated. The first ternary system includes a combination of co-existing divalent metal cations (Mg^{2+} and Zn^{2+}) with trivalent cations (Al^{3+} and Fe^{3+}). In the second ternary system, ZIF-8 support material is used as a Zn^{2+} precursor for the binary Mg-Al and Mg-Fe LDHs and LDOs (Section 5.6).

5.2. Experimental

5.2.1. Preparation of LDHs and LDOs

5.2.1.1. Preparation of Binary LDHs and LDOs. Mg-Al 100°C, Mg-Al 500°C, Mg-Fe 100°C, Mg-Fe 500°C, Zn-Al 100°C, Zn-Al 500°C, Zn-Fe 100°C and Zn-Fe 500°C are synthesized by a co-precipitation method. The details are explained based on the preparation of Mg-Al 100°C and Mg-Al 500°C. Briefly, 5.128 gr of $Mg(NO_3)_2 \cdot 6H_2O$ (Sigma-Aldrich) and 3.751 gr of $Al(NO_3)_3 \cdot 9H_2O$ (Merck) are dissolved in 100 mL deionized water to adjust the molar ratio of Mg^{2+}/Al^{3+} to 2:1. Then, 6.06 gr of urea (Sigma-Aldrich) is prepared in a separate flask, to regulate the pH at around 7-9, known as an ideal media for the formation of nitrate-containing LDHs [245]. The urea solution is added dropwise to the metal solution under the continuous stirring. The molar ratio of metal ions to urea is fixed to $(Mg^{2+}+Al^{3+})$/urea 1:10. The mixture is agitated by a magnetic stirrer for 2 h at room temperature, then stored in the oven for aging at 98°C for one week. The residual gel is separated by centrifugation and washed several times with deionized water. After drying at 100°C for 12 h, the obtained powder is named as Mg-Al 100°C. Mg-Al 100°C is also calcined in the muffle furnace at 500°C for 5 h with a heating rate of 10°C min^{-1} and named as Mg-Al 500°C. In order to synthesize Mg-Fe 100°C and Mg-Fe 500°C, Zn-Al 100°C and Zn-Al 500°C, Zn-Fe 100°C and Zn-Fe 500°C, the above-mentioned procedure is applied by utilizing $Mg(NO_3)_2 \cdot 6H_2O$ (Sigma-Aldrich), $Fe(NO_3)_3.6H_2O$ (Sigma-Aldrich), $Zn(NO_3)_2 \cdot 6H_2O$ (Merck) and urea as precursors with the molar ratios of M^{2+}/M^{3+}=2:1 and $(M^{2+}+M^{3+})$/urea=1:10.

5.2.1.2. Preparation of Fly Ash-Supported LDHs. Fly ash powder is obtained from a lignite power plant in Soma/Manisa/Türkiye. The fly ash suspension is prepared by the dispersion of 1 gr of fly ash in 100 mL of deionized water. Requisite amounts of $Mg(NO_3)_2 \cdot 6H_2O$, $Al(NO_3)_3 \cdot 9H_2O$ and urea are dissolved in 100 mL deionized water by fixing the molar ratio to M^{2+}/M^{3+}/urea=2:1:10. Then, Mg-Al solution is mixed with the fly ash suspension for 12 h at room temperature and aged for one week at 98°C. The resultant gel is separated by centrifugation, washed several times with deionized water and dried at 100°C for 12 h. The synthesized powders are denoted as Mg-Al-Fly Ash 100°C. It is also calcined at 500°C to obtain Mg-Al-Fly Ash 500°C. Similarly, Mg-Fe-Fly Ash 100°C and Mg-Fe-Fly Ash 500°C,

Zn-Al-Fly Ash 100ºC and Zn-Al-Fly Ash 500ºC, Zn-Fe-Fly Ash 100ºC and Zn-Fe-Fly Ash 500ºC are prepared under the same experimental conditions.

5.2.1.3. Preparation of Zeolite-Supported LDHs. H-type aluminosilicate zeolite is obtained from Eskişehir/Türkiye. The zeolite suspension is prepared by adding 1 g of zeolite into 100 mL of deionized water. Mg-Al, Mg-Fe, Zn-Al and Zn-Fe are prepared by applying the M^{2+}/M^{3+}/urea=2:1:10 molar ratio. The LDH solutions are mixed with the zeolite suspension for 12 h at room temperature. Then, the resultant mixture is aged at 98ºC for one week. The precipitate is separated by centrifugation, purified with the deionized water and dried at 100ºC for 12 h. The final products are denoted as Mg-Al-Zeolite 100°C, Mg-Fe-Zeolite 100°C, Zn-Al-Zeolite 100°C and Zn-Fe-Zeolite 100°C. The calcined forms are prepared at 500ºC for 5 h in the muffle furnace and labeled as Mg-Al-Zeolite 500°C, Mg-Fe-Zeolite 500°C, Zn-Al-Zeolite 500°C and Zn-Fe-Zeolite 500°C.

5.2.1.4. Preparation of Ternary LDHs. Zn-Mg-Al 100ºC, Zn-Mg-Al 500ºC, Zn-Mg-Fe 100ºC and Zn-Mg-Fe 500ºC are synthesized via the same co-precipitation method using the $Al(NO_3)_3 \cdot 9H_2O$, $Mg(NO_3)_2 \cdot 6H_2O$, $Zn(NO_3)_2 \cdot 6H_2O$ and urea as precursors. The molar ratio of Zn^{2+}/Mg^{2+} is kept at 1:1 and the molar ratio of $(Zn^{2+}+Mg^{2+})/Al^{3+}$/urea is adjusted as 2:1:10. The prepared solutions are aged at 98ºC for one week. Then, the resultant gels are dried at 100°C after centrifugation and washing steps. The obtained solids are named as Zn-Mg-Al 100ºC and Zn-Mg-Fe 100ºC, while the calcined forms at 500ºC are labeled as Zn-Mg-Al 500ºC and Zn-Mg-Fe 500ºC.

5.2.1.5. Preparation of ZIF-8-Supported LDHs. 1 gr ZIF-8 (Sigma-Aldrich) is dissolved in 100 mL deionized water. In the meantime, Mg-Al and Mg-Fe solutions are prepared using the co-precipitation method by fixing the molar ratios of Mg^{2+}/Al^{3+}/urea and Mg^{2+}/Fe^{3+}/urea at 2:1:10. Then, ZIF-8 solution is added into the Mg-Al and Mg-Fe solutions. After the aging process at 98ºC for one week, the resultant gels are centrifuged and washed several times. The obtained precipitates are dried at 100ºC for 12 h and named as Mg-Al-ZIF-8 100ºC and Mg-Fe-ZIF-8 100ºC. The calcined forms at 500ºC for 5 h in the muffle furnace are named as Mg-Al-ZIF-8 500ºC and Mg-Fe-ZIF-8 500ºC.

5.2.2. Characterization Techniques

Similar to the characterization studies of Chapter 1 and Chapter 2, elemental and morphological analysis of as-prepared LDHs and LDOs are performed by X-ray diffraction (XRD) through Rigaku-D/MAX Ultima diffractometer with Cu Kα radiation (λ =1.54 Å) operating at 40 kV and 40 mA with the scanning rate 2 min^{-1}, Quantachrome Nova 2200e automated gas adsorption system at liquid nitrogen temperature (77 K), scanning electron microscopy (SEM) coupled to energy-dispersive X-ray analysis on an ESEM-FEG/EDAX Philips XL-30 instrument operating at 20 kV and UV–vis diffuse reflectance spectroscopy (UV-2450, Shimadzu).

5.2.3. Adsorption and Photocatalytic Tests

The adsorption and photocatalytic performances of the as-prepared materials are explored in the presence of MO, MB and SA. The degradation of SA is followed by a decrement in its absorbance peak at 296 nm. The experimental equipment, procedures followed and technical analysis are discussed in detail in Chapter 1.

5.3. Results and Discussion of Binary LDHs and LDOs

5.3.1. XRD Analysis

The XRD patterns of Mg-Al 100^{o}C, Mg-Al 500^{o}C, Mg-Fe 100^{o}C, Mg-Fe 500^{o}C, Zn-Al 100^{o}C, Zn-Al 500^{o}C, Zn-Fe 100^{o}C and Zn-Fe 500^{o}C are displayed in Figure 5.2. The diffraction peaks of the Mg-Al 100^{o}C at 11.5°, 23.2°, 34.8°, 39.2°, 46.5°, 60.8°, 62.2° (2θ) are indexed to the (003), (006), (012), (015), (018), (110) and (113) planes of talcite (MDI-JADE6), respectively (Figure 5.2a). These peaks are in good accordance with the values of layered double hydroxides in the literature, suggesting the well-ordered crystallization of the synthesized Mg-Al 100^{o}C [215]. An impurity peak is not detected. Thermal stability of the Mg-Al is confirmed by the remaining talcite peaks after calcination at 500^{o}C. After calcination at 500^{o}C, the characteristic talcite peaks are retained with wider and decreased

peak intensities. A small peak appeared at 43.6° (2θ) in the patterns of Mg-Al 500ºC is assigned to the (113) crystal plane of Al_2O_3 as a result of the oxidation of aluminum in the structure.

For Mg-Fe 100ºC, the characteristic talcite peaks are detected at 22.2°, 34.7°, 39.9°, 46.9°, 60.7°, 62.3° (2θ) (Figure 5.2b). In addition, peaks at 24.0°, 33.0°, 35.6°, 40.7°, 49.3°, 53.9° and 63.8° (2θ) are matched with the (012), (104), (110), (130), (024), (116) and (200) crystal planes of face-centered cubic Fe_2O_3, respectively [246]. The existence of $Fe(OH)_3$ is also noticed at 17.6°, 26.2°, 36.6° (2θ). In the pattern of Mg-Fe 500ºC, Fe_2O_3 peaks become more precise while $Fe(OH)_3$ peaks disappear due to the removal of interlayer hydroxyl groups and partial dehydroxylation of the double hydroxide layers [247]. Formation of metal oxides after calcination is also verified with the observation of MgO peaks at 42.9° and 62.7° (2θ) which belong to the (200) and (220) reflections, respectively.

Zn-Al 100ºC displays the diffraction peaks at 11.8º, 22.7º, 34.9º, 39.5º, 46.2º, 60.9º, 62.2º (2θ) which are well agreed with (003), (006), (012), (015), (018), (110) and (113) planes of talcite, respectively (Figure 5.2c). This demonstrates the successful generation of the layered double hydroxide assembly. In the spectrum of Zn-Al 500ºC, the peak intensities of talcite decrease due to the removal of the interlayer anions and partial destruction of lamellar structure, which ultimately points out the formation of a layered double oxide [248]. Meanwhile, the sharp peaks emerged at 32.1°, 34.5°, 36.3°, 56.7°, 62.9°, and 68.1° (2θ) are ascribable to the (100), (002), (101), (110), (103) and (112) planes of ZnO wurtzite phase, respectively. The suppression of the talcite peaks can also be explained by the distribution of the ZnO nanoparticles on the layered double hydroxide (talcite) surface [249].

Zn-Fe 100ºC pattern reveals the typical talcite peaks at 11.3°, 23.4°, 34.8° and 39.2° (2θ) and also $Fe(OH)_3$ peaks at 18.0°, 26.3° and 36.7° (2θ) (Figure 5.2d). Moreover, $Zn(OH)_2$ generation is noticed at the 32.2°, 34.8°, 36.2°, 56.7° (2θ) with corresponding (211), (002), (101) and (110) planes, respectively. In the profile of Zn-Fe 500ºC, ZnO peaks become dominant owing to the oxidation of the zinc cation and transformation of $Zn(OH)_2$ to ZnO. In the meantime, $Fe(OH)_3$ peaks disappear and Fe_2O_3 and Fe_3O_4 peaks are detected [250, 251].

The basal spacing (d-spacing) value represents an interlayer distance between cations in a layered double hydroxide [201]. The values of the as-synthesized samples are reported based on (003) reflections (Table 5.1). For Mg-Al 100ºC and Mg-Al 500ºC, d-spacing values are found as 0.766 nm and 0.753 nm, respectively, being consistent with the previously reported values [213, 252]. Since there is an insignificant difference between basal spacings of Mg-Al 100ºC and Mg-Al 500ºC, Mg-Al layered structure seems to be preserved after calcination. On the other hand, the decrement in the d-spacing values of Mg-Fe 100ºC (0.626 nm) after calcination (0.368 nm for Mg-Fe 500ºC) is attributed to the destruction of the lamellar structure upon oxidation of metals cations via formation of MgO and Fe_2O_3. The basal spacings are determined to be 0.987 nm and 0.819 nm for Zn-Al 100ºC and Zn-Al 500ºC, respectively. The decrement in the d-spacing value of Zn-Al 500ºC compared to Zn-Al 100ºC may stem from the charge imbalance between the layers due to the formation of ZnO crystallites. The d-spacing values are found as 1.22 nm for Zn-Fe 100ºC and 1.01 nm for Zn-Fe 500ºC. The higher interlayer distances of Zn-Al and Zn-Fe LDHs in comparison to those of Mg-Al and Mg-Fe LDHs are attributed to the larger ionic radius of Zn^{2+} (0.074 nm) than that of Mg^{2+} (0.065 nm) [201]. It is known that the charge density on the layers decreases in the presence of a cation with a larger ionic radius. Since Coulumbic attractions among negatively charged interlayer anions and positively charged cations decrease, the interlayer distance increases [253].

The crystalline sizes of ZnO are evaluated using Scherrer's equation regarding the most prominent (101) diffractions at 36.2° (2θ). For Zn-Al 100ºC and Zn-Fe 100ºC, the crystalline size of ZnO cannot be calculated due to the absence of the ZnO reflections. The crystal growth of ZnO is enhanced upon calcination. Hence, the sizes of the ZnO crystallites are found as 20.7 nm for Zn-Al 500ºC and 25.5 nm for Zn-Fe 500ºC. Although Zn-Fe 500ºC has a larger interlayer spacing value compared to that of Zn-Al 500ºC, it cannot host ZnO crystallites.

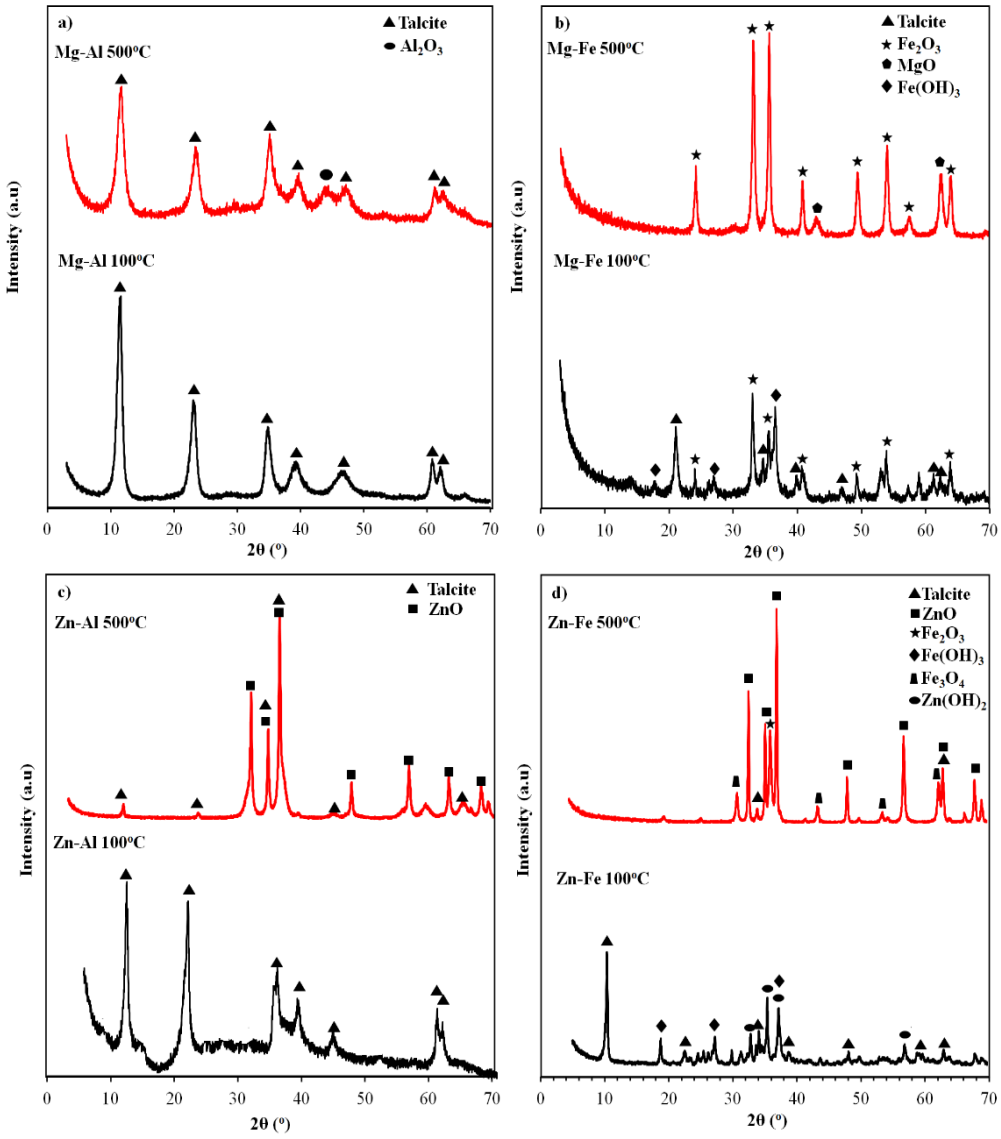

Figure 5.2. XRD patterns of (a) Mg-Al 100°C and Mg-Al 500°C, (b) Mg-Fe 100°C and Mg-Fe 500°C, (c) Zn-Al 100°C and Zn-Al 500°C, (d) Zn-Fe 100°C and Zn-Fe 500°C.

5.3.2. Nitrogen Adsorption-Desorption Tests

Nitrogen adsorption-desorption isotherms of Mg-Al 100°C, Mg-Al 500°C, Mg-Fe 100°C, Mg-Fe 500°C, Zn-Al 100°C, Zn-Al 500°C, Zn-Fe 100°C and Zn-Fe 500°C are shown in Figure 5.3. The isotherms of all samples are classified as type IV, corresponding to mesoporous materials. Mg-Al 100°C, Mg-Fe 100°C and Zn-Fe 100°C exhibit H3 hysteresis loops in the relative pressure range of 0.48-0.96 which is associated with the slit-shaped pores of the aggregates in plate-like/layered materials such as layered double hydroxides

[254–256]. However, these loops become narrower in the isotherms of Mg-Al 500ºC, Mg-Fe 500ºC and Zn-Fe 500ºC relative to the uncalcined forms, implying the distraction of the plate-like structures upon calcination and decrements in the values of the surface area and pore volumes (Table 5.1). Contrarily, the hysteresis loop is observed in the Zn-Al 500ºC isotherm rather than Zn-Al 100ºC. A considerable increase in the surface area and pore volume of Zn-Al 500ºC in comparison to Zn-Al 100ºC can be explained by the cratering effect due to the removal of water, hydroxyl and NO_3 groups and the rearrangement of the matrix through this weight loss at 500ºC [249, 253, 257].

Table 5.1. Basal spacings (d-spacing), surface areas (BET), pore volumes (V_{pore}) and pore radius (r_{pore}) of Mg-Al 100ºC, Mg-Al 500ºC, Mg-Fe 100ºC, Mg-Fe 500ºC, Zn-Al 100ºC, Zn-Al 500ºC, Zn-Fe 100ºC and Zn-Fe 500ºC.

Materials	**d-spacing (nm)**	**BET (m^2g^{-1})**	**V_{pore} (cm^3 g^{-1})**	**r_{pore} (Å)**
Mg-Al 100ºC	0.766	32.7	0.068	18.4
Mg-Al 500ºC	0.753	30.3	0.054	16.0
Mg-Fe 100ºC	0.626	24.5	0.039	20.1
Mg-Fe 500ºC	0.368	21.3	0.030	14.9
Zn-Al 100ºC	0.987	10.2	0.003	17.6
Zn-Al 500ºC	0.819	22.8	0.047	15.7
Zn-Fe 100ºC	1.220	12.9	0.026	14.9
Zn-Fe 500ºC	1.010	11.3	0.019	20.3

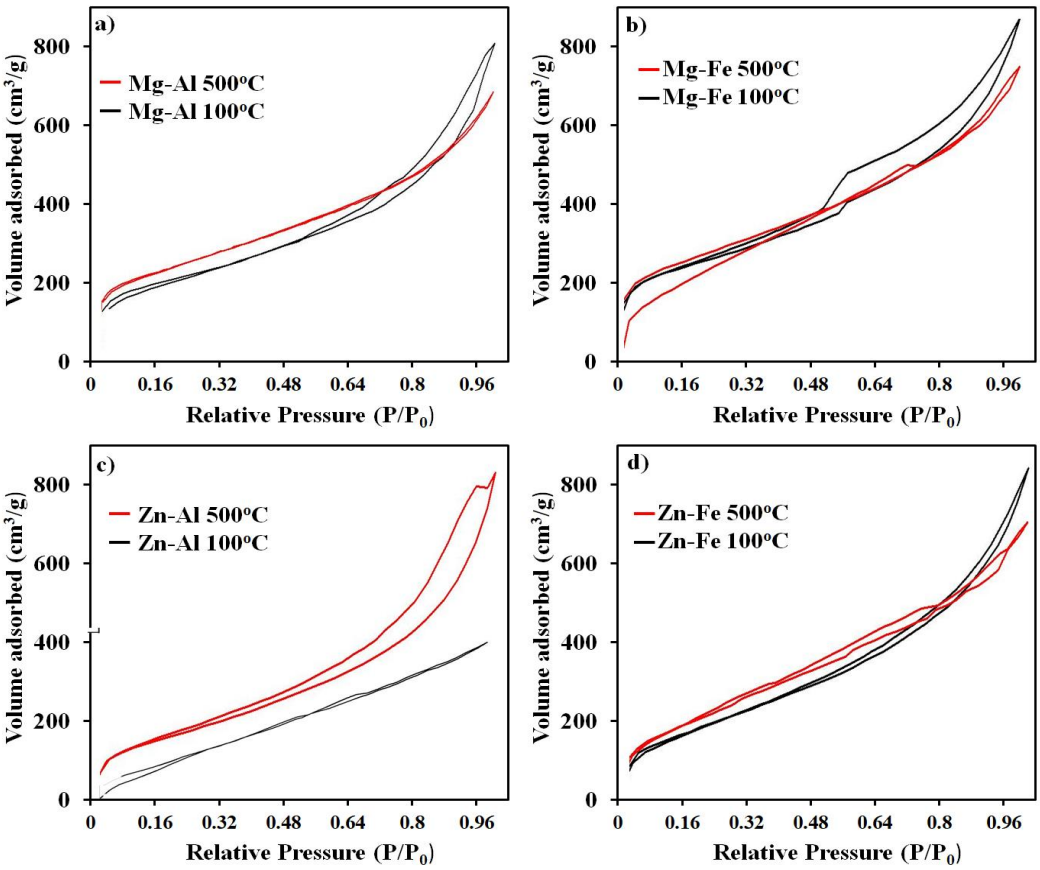

Figure 5.3. Nitrogen adsorption-desorption isotherms of (a) Mg-Al 100°C and Mg-Al 500°C, (b) Mg-Fe 100°C and Mg-Fe 500°C, (c) Zn-Al 100°C and Zn-Al 500°C, (d) Zn-Fe 100°C and Zn-Fe 500°C.

5.3.3. SEM-EDX Analysis

The morphological features of the Mg-Al 100°C, Mg-Al 500°C, Mg-Fe 100°C, Mg-Fe 500°C, Zn-Al 100°C, Zn-Al 500°C, Zn-Fe 100°C and Zn-Fe 500°C are investigated by the SEM-EDX analysis (Figure 5.4). The images of Mg-Al 100°C and Mg-Al 500°C display irregular rock-like particles with sharp edges and corners (Figure 5.4a and c). These particles build from stacked plate-like layers as a common structure for talcite-like materials [258]. After calcination, the lamellar structure is retained confirming the thermal stability of Mg-Al, being consistent with the XRD results [249, 259]. EDX analysis of Mg-Al 100°C and Mg-Al 500°C are discussed in terms of the selected areas (Figure 5.4b and d). The molar ratios of Mg/Al are found as 2.01 for Mg-Al 100°C and 2.08 for Mg-Al 500°C which are well matched with the molar ratio of 2.0 applied during the preparation procedure. Also, the

percentage N decreases after calcination due to the release of the interlayer anionic NO_3 groups.

The particles in the image of Mg-Fe 100°C exhibit lamellar structure (Figure 5e). The bright ones attributed to the formation of Fe_2O_3 create a rough surface on the aggregates. After calcination, Fe_2O_3 nanoparticles are distributed on the whole surface of Mg-Fe 500° due to the oxidation of the metals and enhancement of the Fe_2O_3 crystallites (Figure 5g) [256]. The EDX analysis of the labeled areas verifies the existence of the Mg, Fe, N and O as the major components of the Mg-Fe 100° and Mg-Fe 500° (Figure 5.4f and h). In contrast to Mg-Al LDHs, the ratio among Mg and Fe cations is not consistent with the ratio of the synthesis which suggests the incomplete formation of the LDH structure. The higher percentages of Fe than Mg in both Mg-Fe 100° and Mg-Fe 500° can be attributed to the formation of Fe_2O_3 and the dissolution of Mg instead of building a layered double hydroxide structure. The increment in the atomic percentages of O in Mg-Fe 500° compared to Mg-Fe 100° also confirm the oxidation of metals upon calcination.

Zn-Al 100°C reveals big layered rock-like particles of talcite and smaller unshaped fragments stacked around the layers of talcite particles (Figure 5.4i). After calcination, layers are covered with the grains of ZnO nanoparticles as determined in the XRD analysis (Figure 3k). The EDX spectrums of Zn-Al 100°C and Zn-Al 500°C depict that the samples contain Zn, Al, N and O elements (Figure 5.4j and l). Upon calcination, the Zn percentage increases owing to the formation of ZnO crystallites, while O and N percentages reduce through the removal of the interlayer anions. The decrement in the molar ratio of Zn/Al in Zn-Al 500°C (1.96) compared to Zn-Al 100°C (2.02) is not significant, hence partial destruction in the lamellar structure is expected.

In the images of Zn-Fe 100°C and Zn-Fe 500°C, irregular-shaped particles with spongy morphology are detected (Figure 5.4m and o). The formation of holes and craters on the Zn-Fe 500°C particles can be attributed to the removal of surface hydroxyl groups following the thermal treatment [257]. This removal is also confirmed via EDX analysis with the reduced N and O percentages in Zn-Fe 500°C as a comparison to Zn-Fe 100°C (Figure 5.4n and p). The Zn/Fe molar ratio are found as 2.01 for Zn-Fe 100°C and 1.95 for Zn-Fe 500°C.

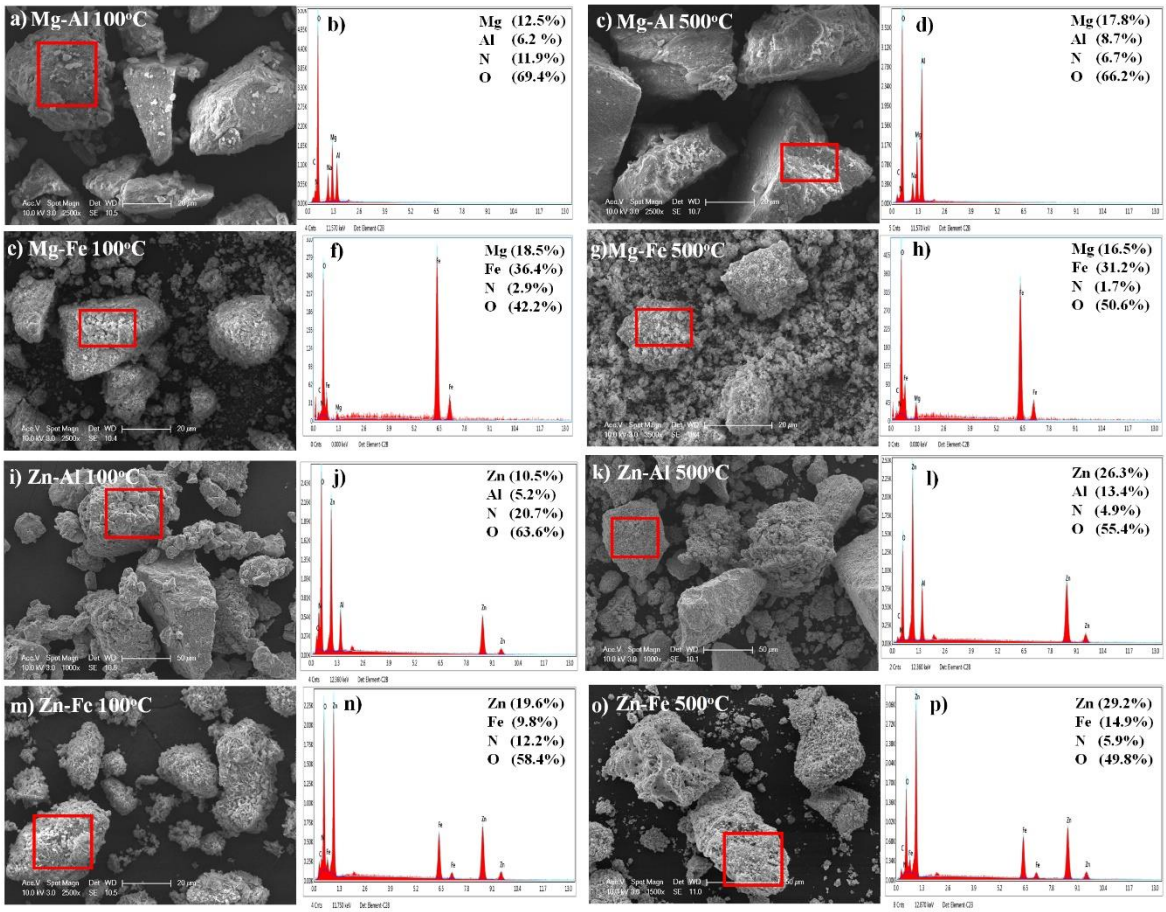

Figure 5.4. SEM images and EDX analysis of (a,b) Mg-Al 100°C (c,d) Mg-Al 500°C, (e,f) Mg-Fe 100°C (g,h) Mg-Fe 500°C, (i,j) Zn-Al 100°C (k,l) Zn-Al 500°C, (m,n) Zn-Fe 100°C (o,p) Zn-Fe 500°C.

5.3.4. UV-Vis DRS Analysis

The absorption spectra and corresponding band gap energy plots of Mg-Al 100°C, Mg-Al 500°C, Mg-Fe 100°C, Mg-Fe 500°C, Zn-Al 100°C, Zn-Al 500°C, Zn-Fe 100°C and Zn-Fe 500°C are illustrated in Figure 5.5. Layered double hydroxides, despite not being considered as semiconductors, can induce photoactivity owing to the existence of metal cations and surface defects in their frames [260]. Mg-Al 100°C shows a minor absorption peak in the 230-290 nm which is related to the existence of nitrate anions in the interlayer galleries (Figure 5.5a) [261]. In the spectrum of Mg-Al 500°C, the intensity of this peak decreases due to the release of the nitrate groups after thermal treatment as also confirmed by the lower atomic percentages of N in the EDX analysis. The band-gap energies are

estimated from the intercept of the tangent in the plots of $(Abs\ hv)^2$ versus photon energy (hv). The calculated values for Mg-Al 100°C and Mg-Al 500°C are found as 3.8 and 3.9 eV, respectively, in agreement with the values of previous studies (Figure 5.5b) [262]. The increased band gap energy after calcination stems from the releasing nitrate groups. The absorbance spectra of Mg-Fe 100°C and Mg-Fe 500°C exhibit broad absorption bands at around 550 nm which refer to the formation of Fe_2O_3, being detected in the XRD analysis (Figure 5.5c) [263]. This absorption of Fe_2O_3 may arise from the spin-forbidden-excitation between 2p orbitals of O and 4s orbitals of Fe [264, 265]. The edge of the absorption band becomes sharper in the spectrum of Mg-Fe 500°C, confirming the crystalline growth of Fe_2O_3 [263].The band gap energies are determined as 2.21 eV for Mg-Fe 100°C and 2.20 eV for Mg-Fe 500°C as consistent with the reported values of Fe_2O_3 (Figure 5.5d) [266].

The pattern of Zn-Al 100°C has an absorption peak in between 280-320 nm which is ascribed to the interlayer nitrate anions (Figure 5.5e). The minor peak detected at around 380 nm implies the $Zn(OH)_2$ presence in the matrix. These peaks disappear upon thermal treatment. The characteristic absorption edge of ZnO becomes predominant in the spectrum of Zn-Al 500°C owing to the formation of ZnO crystallites as collaborated with the XRD results. The band gap energies of Zn-Al 100°C and Zn-Al 500°C are calculated as 3.60 eV and 2.90 eV, respectively [267, 268]. The lower band gap value of Zn-Al 500°C in comparison to the bare ZnO (3.2 eV) is attributed to additional energy levels derived from the presence of Al^{3+} ions in the matrix. Thus, the photoactivity is assumed to be higher than that of the bare ZnO, following the calcination at 500°C [268].

The Zn-Fe 100°C exhibits an absorption peak owing to the nitrate anions in the range of 280-320 nm (Figure 5.5g). In the spectrum of Zn-Fe 500°C, this peak disappears and the characteristic absorption edge of ZnO becomes observable at around 380 nm (Figure 5.5g). Also, a broad absorption band is noticed between 450-550 nm which is ascribed to the generation of mixed metal oxides (such as Fe_2O_3 and Fe_3O_4) upon calcination. The band gap energy of Zn-Fe 100°C (3.6 eV) is similar to the values calculated for Mg-Al 100°C (3.8 eV) and Zn-Al 100°C (3.23 eV) (Figure 3.5h). Zn-Fe 500°C presents two band gap energy values: the first is found as 2.3 eV due to the formation of Fe_2O_3 and Fe_3O_4, and the second one is located at 3.1 eV, attributed to the ZnO crystal growth.

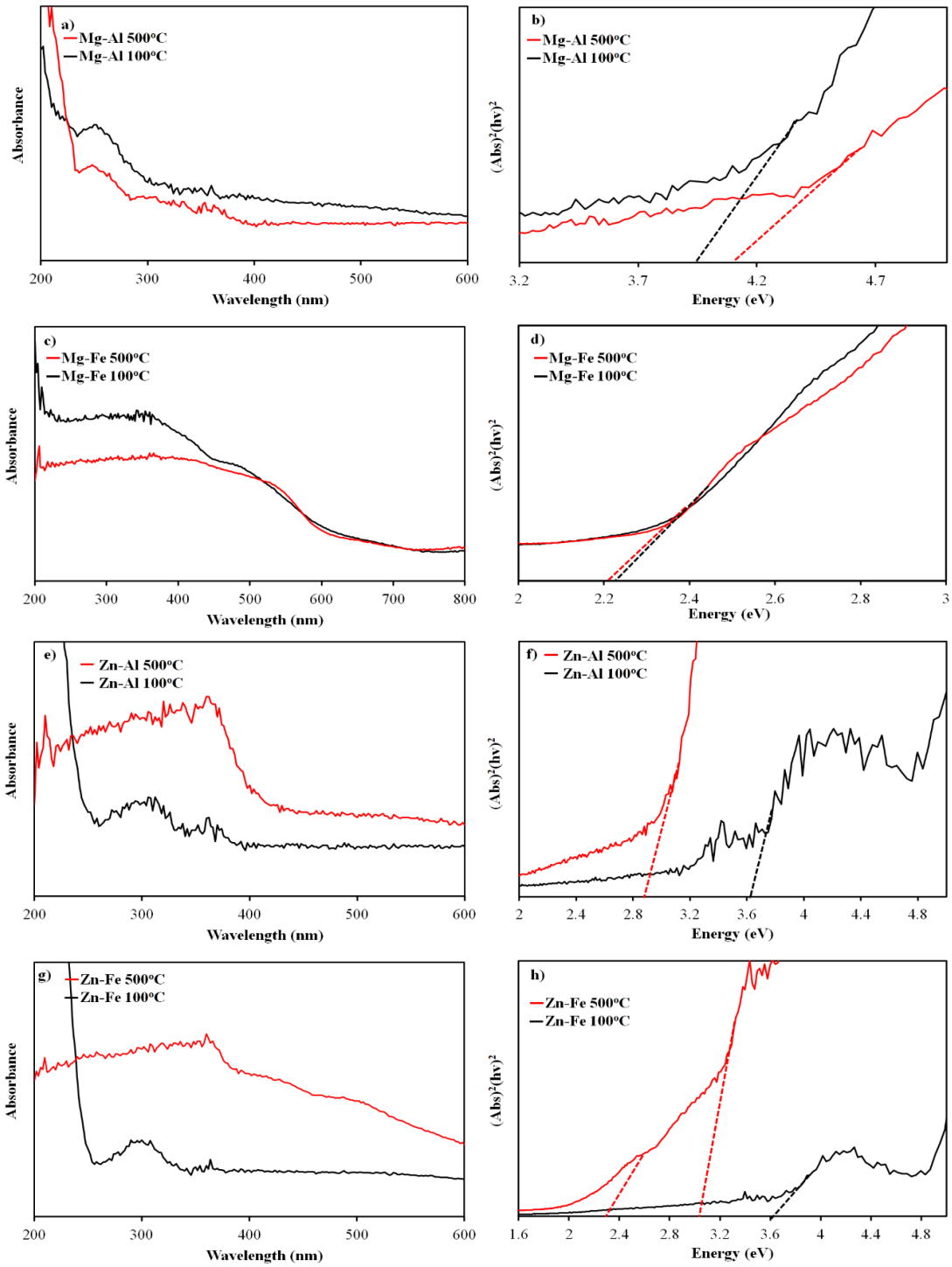

Figure 5.5. UV-vis DRS spectra and band gap absorption plots of (a,b) Mg-Al 100°C and Mg-Al 500°C, (c,d) Mg-Fe 100°C and Mg-Fe 500°C, (e,f) Zn-Al 100°C and Zn-Al 500°C, and (g,h) Zn-Fe 100°C and Zn-Fe 500°C.

5.3.5. Adsorption and Photocatalytic Tests

Figure 5.6a, Figure 5.6c and Figure 5.6e show dark adsorption capacities of Mg-Al 100°C, Mg-Al 500°C, Mg-Fe 100°C, Mg-Fe 500°C, Zn-Al 100°C, Zn-Al 500°C, Zn-Fe 100°C and Zn-Fe 500°C for MO, MB and SA.

In the adsorption processes of the layered double hydroxides, two kinds of mechanisms can be pronounced; the first one is surface adsorption and the second one is the intercalation among the layers. In this respect, two-dimensional forms of MO, MB and SA are shown in Figure 5.7 for a detailed discussion in the presence of as-prepared LDH and LDOs. The high surface area and porous structure of Mg-Al 100°C and Mg-Al 500°C provide a wide contact area for the electrostatic interactions, thus the adsorption of MO is completed within 100 min. (Figure 5.6a). MO ions are predominantly present as monovalent anions in the solution and attract to the positively charged layers of Mg-Al 100°C and Mg-Al 500°C. Moreover, positively charged metal cations on the surface of Mg-Al 100°C and Mg-Al 500°C can interact with the negatively charged electron clouds of π system in benzene rings and thus the dipole-π interaction can enhance the adsorption of MO [269-271]. Meanwhile, MO molecules can be intercalated into the interlayers of Mg-Al 100°C and Mg-Al 500°C through horizontal axis owing to the smaller width of the MO molecule (0.552 nm) than the interlayer spacings of Mg-Al 100°C (0.766 nm) and Mg-Al 500°C (0.753 nm) (Figure 5.7a). This intercalation is driven by the anion exchange mechanism among the NO_3^- groups and anionic MO molecules. Besides, Mg-Al 100°C and Mg-Al 500°C show similar adsorption behavior due to the retained talcite structure and insignificant variation in the surface areas and pore sizes even after calcination.

The remaining percentages of MB are found as 61% end 81% in the presence of Mg-Al 100°C and Mg-Al 500°C, respectively (Figure 5.6c). The lower adsorption ability of Mg-Al 100°C and Mg-Al 500°C toward MB compared to MO can be explained by the electrostatic repulsion between the positively charged surfaces of Mg-Al 100°C and Mg-Al 500°C and the cationic MB molecules [272]. The limited adsorption is attributed to the surface interactions which can be established via hydrogen bonding with surface hydroxyl groups of Mg-Al 100°C and Mg-Al 500°C and N atoms of MB. Despite the appropriate dimension of MB molecule to intercalate within the layers, the ion exchange process cannot

occur due to the disruption of charge balance in the structure (Figure 5.7b). Instead, positively charged MB molecules may interact with the interlayer anionic nitrate groups in the Mg-Al 100ºC and Mg-Al 500ºC structure. Therefore, lower adsorption of MB in the presence of Mg-Al 500ºC than that of Mg-Al 100ºC is attributed to the removal of nitrate groups upon thermal treatment.

The pH (2.7) of SA in the solution creates the net positive charge on the surfaces of Mg-Al 100ºC and Mg-Al 500ºC. Thus, hydrogen bonding can be formed between carboxylic acid and hydroxyl groups of SA and surface hydroxyl groups of Mg-Al 100ºC and Mg-Al 500ºC. However, the electron-withdrawing behavior of the carboxylic acid group attached to the benzene ring in the SA structure takes electrons toward itself and forces the adjacent hydroxyl group to give electrons. This intramolecular hydrogen bonding leads to lower adsorption of SA on the surface of Mg-Al 100ºC and Mg-Al 500ºC [273]. Hence, the adsorption of SA is mostly driven by the intercalation mechanism via suitable molecular dimensions of SA (0.512 nm width and 0.66 nm length) (Figure 5.7c) [203]. The remaining amount of SA is found as 48% and 53% in the presence of Mg-Al 100ºC and Mg-Al 500ºC, respectively (Figure 5.6e). The small difference in the adsorption capacities of Mg-Al 100ºC and Mg-Al 500ºC may be attributed to the lower interlayer spacing of Mg-Al 500ºC than that of the Mg-Al 100ºC.

The lower interlayer distances of the Mg-Fe 100ºC (0.626 nm) and Mg-Fe 500ºC (0.368 nm) relative to that of Mg-Al 100ºC (0.766 nm) and Mg-Al 500ºC (0.753 nm) may also indicate the incomplete build-up of the lamellar structure. Therefore, an intercalation mechanism cannot be suggested for the adsorption processes of MO, MB and SA on Mg-Fe 100ºC and Mg-Fe 500ºC. The existence of metal oxides creates repulsive forces for adsorption of MO. The restricted adsorption of MO (76% remaining percentage for Mg-Fe 100ºC and 81% remaining percentage for Mg-Fe 500ºC) may be attributed to the Fe-O coordination in between Fe^{3+} ions and oxygens of sulphonic groups of MO (Figure 5.6a) [274].

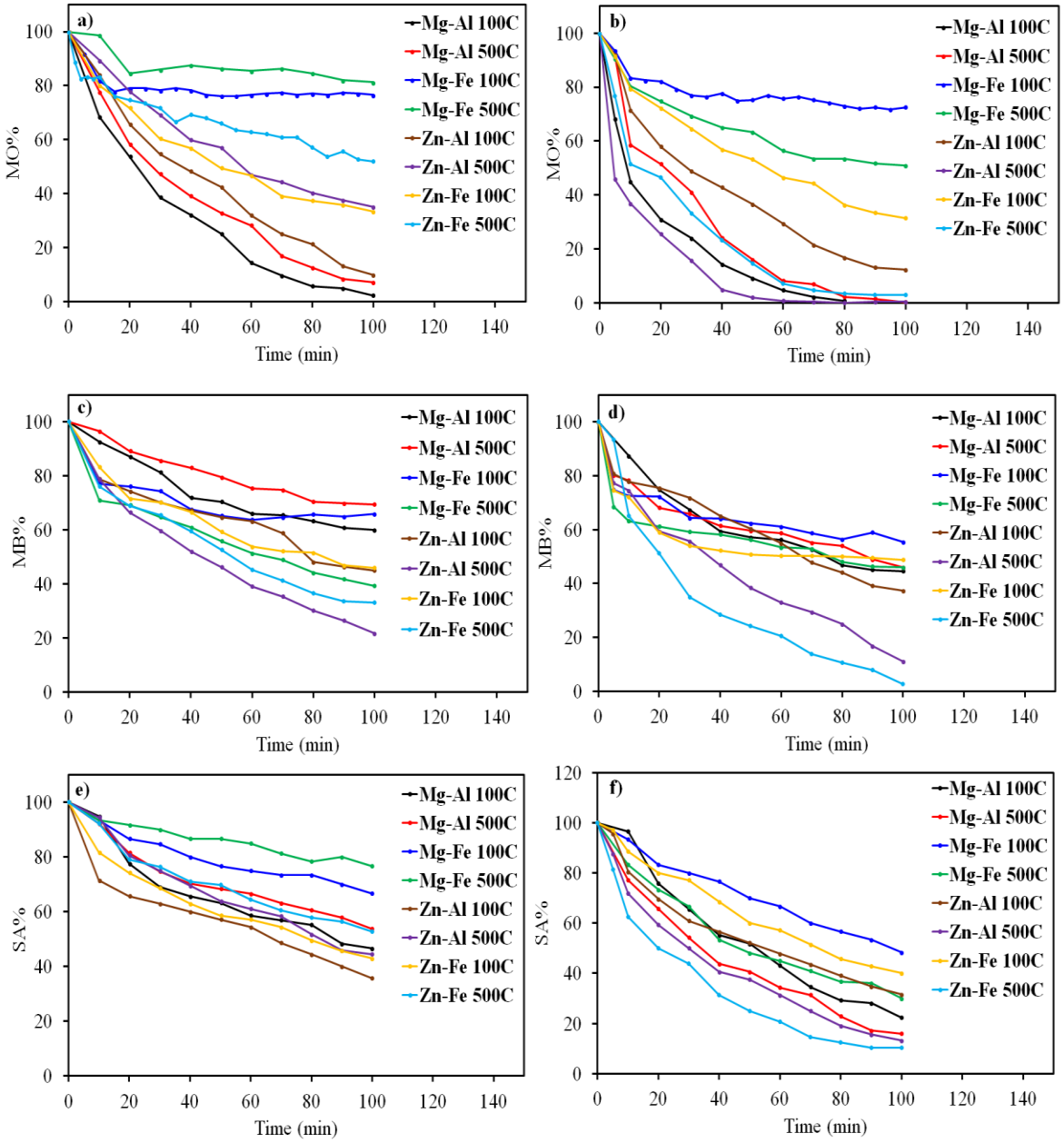

Figure 5.6. Dark adsorption and photocatalytic degradation (a,b) of MO, (c,d) of MB and (e,f) SA in the presence of Mg-Al 100°C, Mg-Al 500°C, Mg-Fe 100°C, Mg-Fe 500°C, Zn-Al 100°C, Zn-Al 500°C, Zn-Fe 100°C and Zn-Fe 500°C.

In contrast to MO, the formation of mixed metal oxides favors the adsorption of positively charged MB due to the interaction between negatively charged electron cloud on oxygen atoms and C-S+=C functional group of MB. Also, the presence of $Fe(OH)_3$ in Mg-Fe 100°C leads to hydrogen bonds with the nitrogen atoms of MB. Thus, the remaining MB

percentages are found as 51% and 45% in the presence of Mg-Fe 100ºC and Mg-Fe 500ºC, respectively (Figure 5.6c). The adsorption of MB is relatively enhanced in the presence of Mg-Fe 500ºC compared to Mg-Fe 100ºC by the generation of Fe_2O_3 crystallites which creates more negative adsorption sites for MB. In the presence of Mg-Fe 100ºC and Mg-Fe 500ºC, the residual SA percentages are found as 71% and 81%, respectively (Figure 5.6e). The adsorption of SA may arise from the coordination between the Fe cations in the outermost layers of Mg-Fe 100ºC and Mg-Fe 500ºC, and oxygens in the carboxylic acid groups of SA.

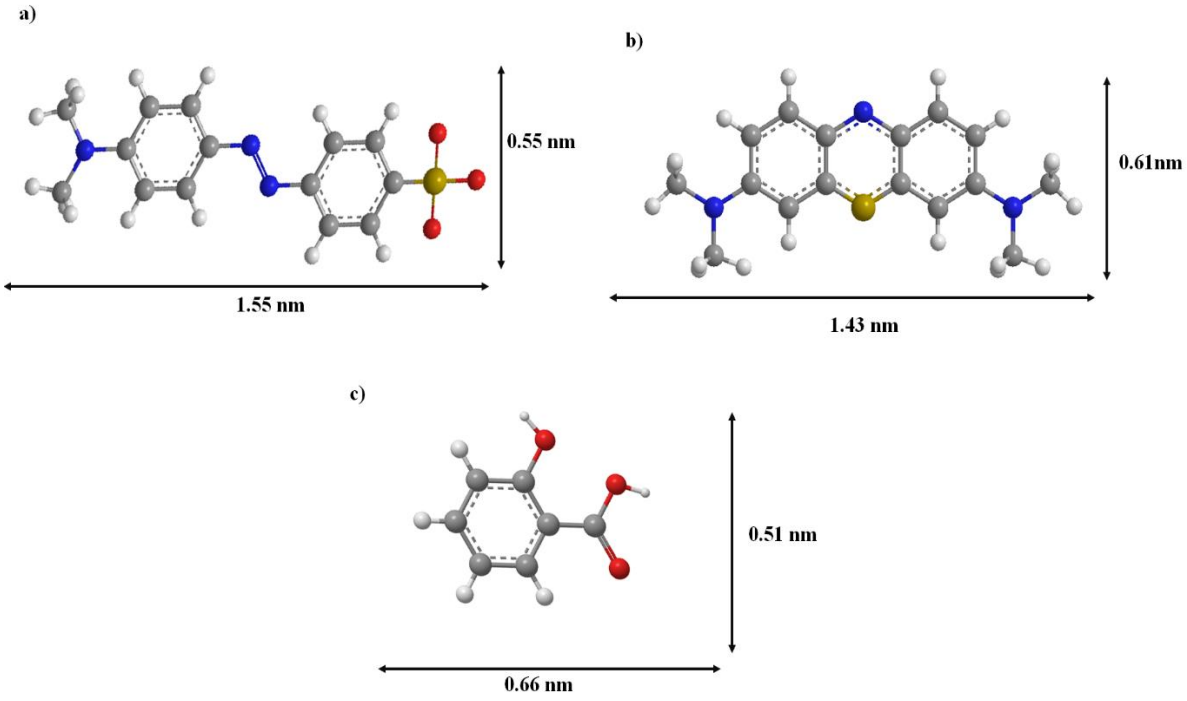

Figure 5.7. Two-dimensional forms of (a) MO, (b) MB and (c) SA.

The remaining MO percentages are found as 10% and 35%, in the existence of Zn-Al 100ºC and Zn-Al 500ºC respectively (Figure 5.6a). The high interlayer spacing of Zn-Al 100ºC (0.987 nm) enables the intercalation of MO molecules via an anion exchange process with the interlayer nitrate groups. Moreover, the positively charged surface of Zn-Al 100ºC has a tendency towards anionic MO molecules. Such attractions can also be formed among metal cations and benzene rings of MO through dipole-π interactions [269]. The lower adsorption ability of Zn-Al 500ºC compared to Zn-Al 100ºC, can be explained by the formation of ZnO and the generation of a negatively charged surface due to the lone pair electrons of oxygens in the Zn-O bond. Consequently, the adsorption mechanism of MO on

Zn-Al 500^{o}C can be interpreted via the anion exchange process due to the high interlayer distance of Zn-Al 500^{o}C (0.819 nm) instead of surface interactions.

The remaining percentages of MB are found as 45% for Zn-Al 100^{o}C and 22% for Zn-Al 500^{o}C (Figure 5.6c). The surface interactions are restricted by the surface metal cations in the presence of Zn-Al 100^{o}C. Instead, the high interlayer distance of Zn-Al 100^{o}C can provide a contact area for interlayer nitrate anions and MB molecules, thus the adsorption of MB can be driven by intercalation due to the electrostatic attractions. In the existence of Zn-Al 500^{o}C, the crystalline growth of ZnO creates a negatively charged surface and thereby, promotes the adsorption of cationic MB.

The residual percentages of SA are found as 35% and 45% in the presence of Zn-Al 100^{o}C and Zn-Al 500^{o}C, respectively (Figure 5.6e). The high distance between the layers of Zn-Al 100^{o}C provides intercalation of the SA molecules through ion exchange mechanism. The releasing of the nitrate ions during calcination leads to a relatively lower adsorption of SA molecules in the presence of Zn-Al 500^{o}C.

For Zn-Fe 100^{o}C and Zn-Fe 500^{o}C, the remaining percentages of MO are found as 34% and 51%, respectively (figure 5.6a). MO molecules can be intercalated among the layers of Zn-Fe 100^{o}C owing to the high interlayer spacing (1.22 nm). Also, surface adsorption can occur due to the electrostatic attractions between the metal cations and negatively charged sulphonic groups of MO. However, these metal cations participate in the formation of $Zn(OH)_2$ and $Fe(OH)_3$ crystallites in the Zn-Fe 100^{o}C structure and limit the adsorption of MO on the surface. After calcination, the metal hydroxides vary to mixed metal oxides such as ZnO, Fe_2O_3 and Fe_3O_4 which create repulsive forces for MO adsorption. Thus, instead of surface adsorption, the intercalation of MO molecules is responsible for the adsorption process due to the high interlayer spacing of Zn-Fe 500^{o}C (1.01 nm). Contrarily, MB adsorption increases from Zn-Fe 100^{o}C (46% remaining percentage) to Zn-Fe 500^{o}C (33% remaining percentage) due to the increment of negative surface charge with the formation of metal oxides (Figure 5.6c). For SA, the residual percentages are found as 42% and 54% in the presence of Zn-Fe 100^{o}C and Zn-Fe 500^{o}C, respectively (Figure 5.6e).

Figure 5.6b, Figure 5.6d and Figure 5.6f show photocatalytic activities of Mg-Al 100ºC, Mg-Al 500ºC, Mg-Fe 100ºC, Mg-Fe 500ºC, Zn-Al 100ºC, Zn-Al 500ºC, Zn-Fe 100ºC and Zn-Fe 500ºC for MO, MB and SA.

The remaining percentages are found as 0.5% for MO, 44% for MB and 22% for SA at the end of 100 min, in the presence of Mg-Al 100ºC (Figure 5.6b,d and f). For Mg-Al 500ºC, the remaining MO, MB and SA percentages are found as 2.9%, 45% and 16%, respectively. Although LDHs are not considered as semiconductor materials, they exhibit a certain degree of photoactivity. Photoexcitation can provide mobility of charges in the laminar structures of LDHs and create defects that eventually serve as active centers for photoreactions [260]. The surface OH groups of the talcite layers and oxygens of the interlayer nitrate groups can react with the photogenerated holes and yield hydroxyl radicals with very high oxidation potentials [275]. On the other hand, the photogenerated electrons which are delocalized toward the electron deflections of Al^{3+} react with the dissolved O_2 to form superoxide radicals. Both hydroxyl and superoxide radicals act as photocatalytic oxidant species for the degradation of MO, MB and SA [262]. Besides, photocatalytic degradation abilities of Mg-Al 100ºC and Mg-Al 500ºC for MO, MB and SA follow a similar trend of their dark adsorption capacities. This also confirms the crucial role of adsorption to provide more active sites for redox reactions. Therefore, efficient degradation of MO or MB or SA can be achieved when the corresponding adsorption is more satisfied.

For Mg-Fe 100ºC, the residual percentages of MO, MB and SA are found as 72%, 51% and 45%, respectively (Figure 5.6b,d and f). The higher photoactivity of Mg-Fe 500ºC (50%, 45% and 31% remaining percentages of MO, MB and SA, respectively) compared to Mg-Fe 100ºC may be attributed to the crystalline growth of Fe_2O_3 upon calcination. The photoactivity of Fe_2O_3 can be explained by the promotion of excited electrons from the valence band to empty d^5 orbitals of Fe^{3+} ions. Meanwhile, the photogenerated holes react with water and surface hydroxide groups while photogenerated electrons can react with the oxygens to form superoxide radicals. Such chain reactions initiate to degradation of MO, MB and SA [276].

In the presence of Zn-Al 100ºC, the remaining percentages of MO, MB and SA are found as 12%, 37% and 21%, respectively (Figure 5.6b,d and f). For Zn-Al 500ºC, improved

ZnO crystallinity as detected in XRD analysis and enlarged surface area as measured in BET analysis increase the photocatalytic activity. Also, the synergy established between ZnO and Al is beneficial to interfacial charge transfer. Briefly, the photogenerated electrons in ZnO can migrate from the filled 2p orbitals of O to empty 3s or 3p orbitals of Al. The extended life-time of charge carriers improve photocatalytic performance of Zn-Al 500°C [268, 277].

For Zn-Fe 100°C, the remaining percentages of MO, MB and SA are found to be 31%, 48% and 40%, respectively (Figure 5.6b,d and f). The formation of metal hydroxides (such as $Fe(OH)_3$ and $Zn(OH)_2$) in the structure may be responsible for the photoactivity of Zn-Fe 100°C. The higher photocatalytic efficiency of Zn-Fe 500°C than that of Zn-Fe 100°C is ascribed to the growth of ZnO upon thermal treatment. Moreover, the existence of Fe_2O_3 enhances photocatalytic efficiency by providing additional energy levels. The higher photodegradation performance of Zn-Al 500°C than that of the Zn-Fe 500°C is attributed to the smaller ZnO crystalline size that facilitates the rapid photoelectron transfer from bulk to the surface which can retard the recombination of electron-hole pair and enhance the photoactivity [276].

5.3.6. Dark Adsorption Kinetics and Isotherms

For the dark adsorption studies, samples with the highest adsorption capacities are examined in detail, namely; Mg-Al 100°C for MO, Zn-Al 500°C for MB and Zn-Al 100°C for SA. The pseudo-first order and pseudo-second order kinetic models are employed and their corresponding kinetic parameters are listed (Table 5.2, Figure 5.8). Accordingly, the pseudo-second-order model better fits to the adsorption behaviors of Mg-Al 100°C for MO, Zn-Al 500°C for MB and Zn-Al 100°C with higher correlation coefficients (R^2) than that of the pseudo-first order model. Meanwhile, the calculated qe values of the pseudo-second-order model are found to be closer to the experimental equilibrium adsorption capacities (q_e, (exp)). Thus, chemisorption may be proposed owing to the electrostatic attractions as well as hydrogen bonds among model compounds (MO, MB and SA) and the as-synthesized LDHs. Besides, surface and interlayer interactions in the presence of Mg-Al 100°C for MO adsorption points to the highest rate constant k_2 value in comparison to those of Zn-Al 500°C for MB and Zn-Al 100°C for SA adsorption.

Table 5.2. Kinetic parameters of Mg-Al 100ºC for MO, Zn-Al 500ºC for MB and Zn-Al 100ºC for SA adsorption.

		Pseudo-first order $\ln (q_e - q_t) = \ln q_e - k_1 t$			**Pseudo-second order** $\frac{t}{q_t} = (\frac{1}{k_2 q^2_e}) + \frac{t}{q_e}$		
	$q_{e(exp)}$	**k_1**	**$q_{e\ (calc)}$**	**R^2**	**k_2**	**$q_{e(calc)}$**	**R^2**
Mg-Al 100ºC (MO)	2.97	0.0301	1.15	0.9617	0.484	2.99	0.9972
Zn-Al 500ºC (MB)	2.85	0.0223	1.75	0.9494	0.433	2.84	0.9951
Zn-Al 100ºC (SA)	2.23	0.0101	1.98	0.9918	0.311	2.19	0.9933

Table 5.3. Langmuir and Freundlich isotherm models of Mg-Al 100ºC for MO, Zn-Al 500ºC for MB and Zn-Al 100ºC for SA.

	Langmuir $\frac{C_e}{q_e} = \frac{1}{K_L q_L} + \frac{C_e}{q_L}$			**Freundlich** $\ln q_e = \ln K_F + \frac{1}{n} \ln C_e$		
	K_L	**q_L**	**R^2**	**K_F**	**1/n**	**R^2**
Mg-Al 100ºC (MO)	0.439	18.7	0.9979	0.202	0.839	0.9910
Zn-Al 500ºC (MB)	0.401	14.6	0.9956	0.187	0.831	0.9886
Zn-Al 100ºC (SA)	0.318	11.4	0.9938	0.123	0.721	0.9852

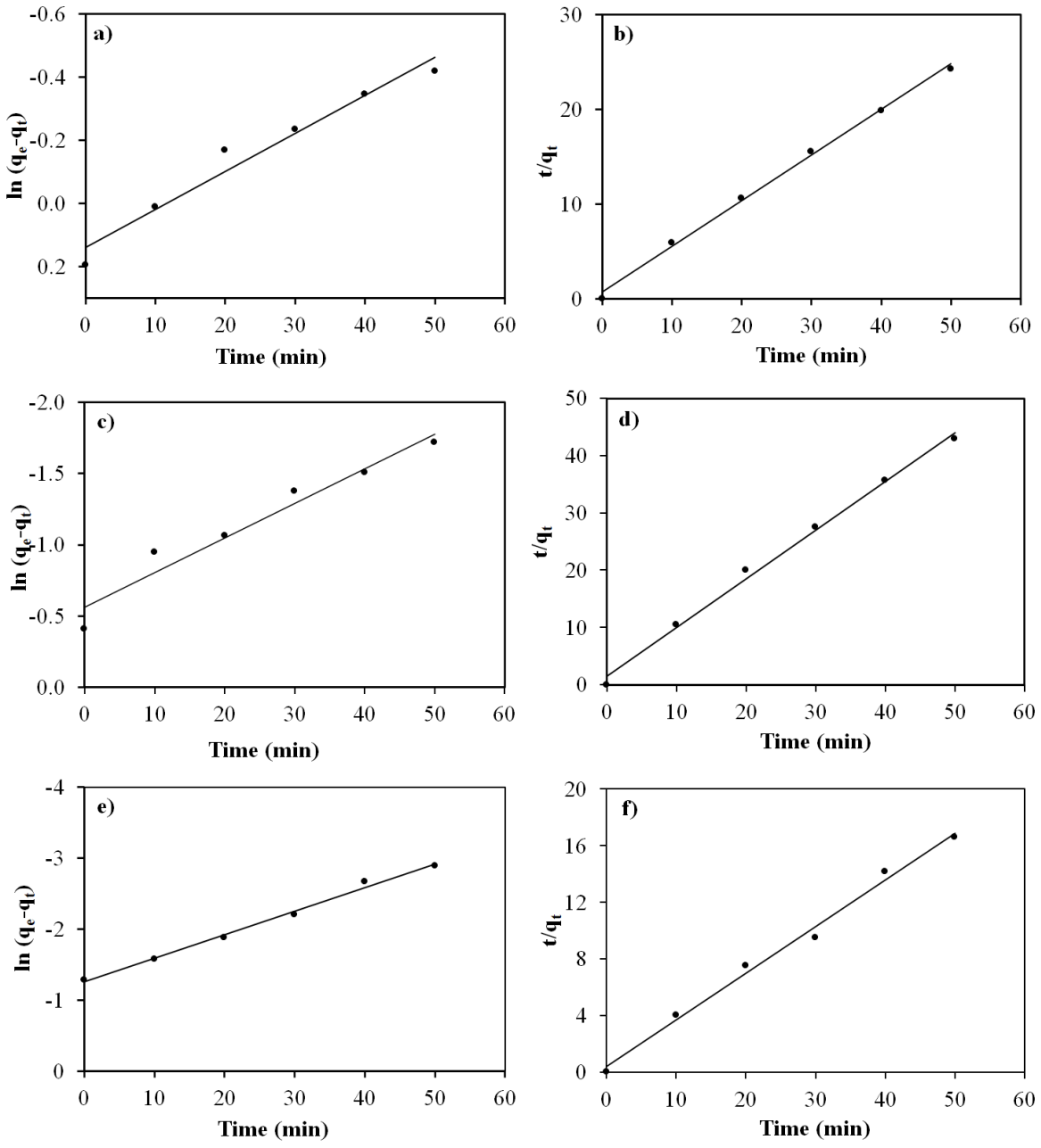

Figure 5.8. Pseudo-first order and pseudo-second order kinetics of (a,b) Mg-Al 100ºC for MO (c,d) Zn-Al 500ºC for MB and (e,f) Zn-Al 100ºC for SA adsorption.

Mg-Al 100ºC for MO, Zn-Al 500ºC for MB and Zn-Al 100ºC for SA adsorption are further analyzed by Langmuir and Freundlich isotherms. The fitting parameters are tabulated in Table 5.3 and the linear plots of the models are presented in Figure 5.9. The highest correlation coefficients (R^2) are obtained with the Langmuir model for Mg-Al 100ºC, Zn-Al 500ºC and Zn-Al 100ºC. Thus, MO, MB and SA adsorptions are assumed to occur on Mg-

Al 100ºC, Zn-Al 500ºC surfaces, respectively, as a monolayer coverage due to the existence of functional groups for electrostatic interactions and hydrogen bonding. The highest monolayer adsorption capacity (q_L) and the lowest adsorption energy value (K_L) are obtained in the presence of Mg-Al 100ºC for MO adsorption. The separation factor values (R_L) of Mg-Al 100ºC (0.56), Zn-Al 500ºC (0.49) and Zn-Al 100ºC (0.40) range in between 0 and 1, indicating the favorable adsorptions of MO, MB and SA, respectively, via application of the Langmuir model.

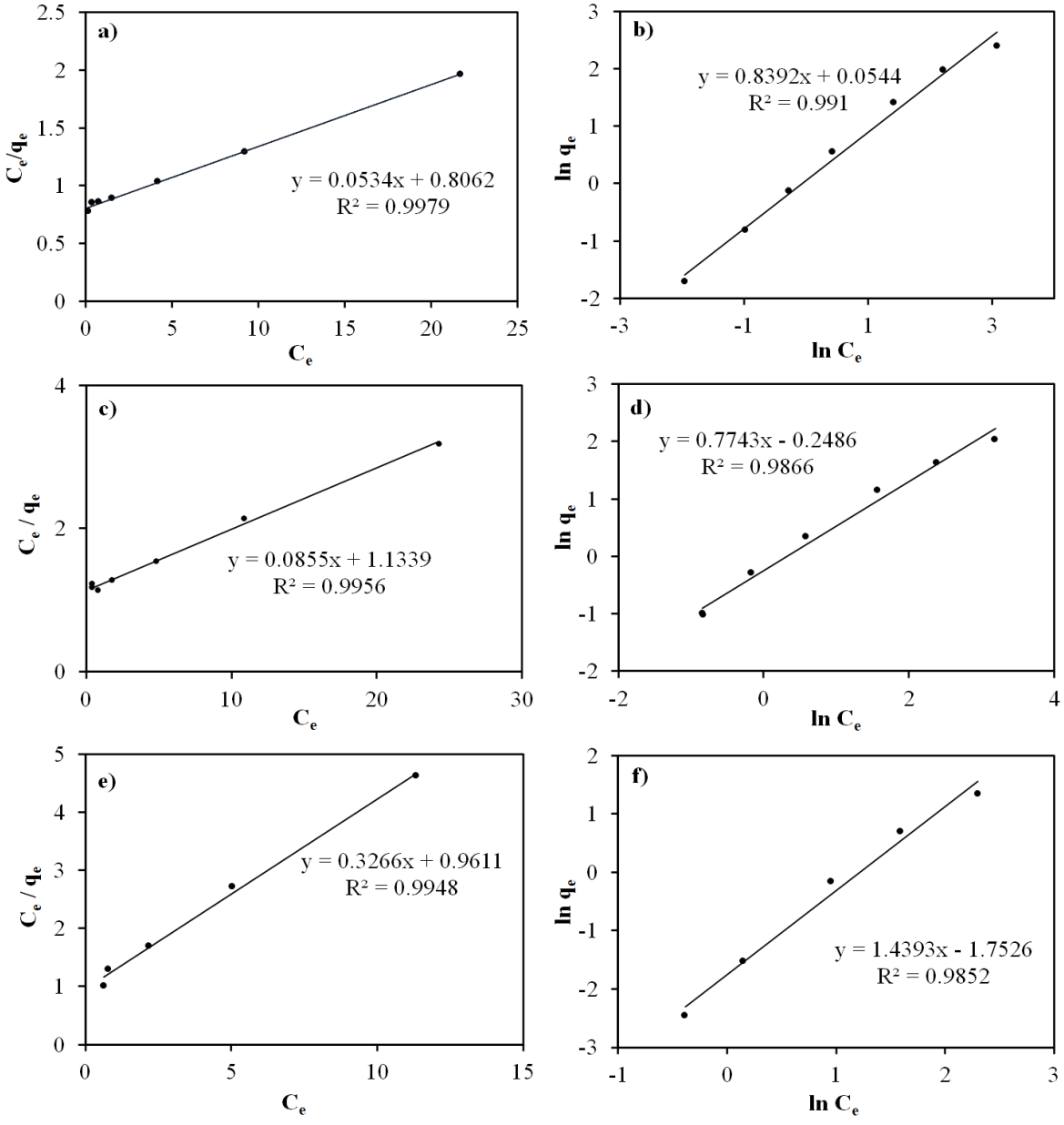

Figure 5.9. Langmuir and Freundlich isotherms of (a,b) Mg-Al 100ºC for MO (c,d) Zn-Al 500ºC for MB and (e,f) Zn-Al 100ºC for SA adsorption.

5.3.7. Kinetic Analysis Under Irradiation

In this part of the study, the most photo-active LDHs are selected, namely; Zn-Al 500ºC for MO degradation, Zn-Fe 500ºC for MB degradation and Zn-Fe 500ºC for SA degradation. The kinetics of such photocatalytic reactions are analyzed in the initial concentration range of MO from 32.7 to 0.327 mg L^{-1}, MB from 31.9 to 0.319 mg L^{-1} and SA 13.8 to 0.138 mg L^{-1}, in the presence of Zn-Al 500ºC, Zn-Fe 500ºC and Zn-Fe 500ºC, respectively. The linearity of plots for ln ($[MO]_0/[MO]_t$), ln ($[MB]_0/[MB]_t$) and ln ($[SA]_0/[SA]_t$) versus time confirms the applicability of pseudo-first-order model (Figure A.29). The rate constants k (min^{-1}) are determined from the slopes of the lines and listed in Table 5.4. The highest rate constants and the linear regression values (R^2) are obtained with the lowest initial concentrations of MO, MB and SA. High concentrations of MO, MB and SA molecules may accumulate on the active sites of Zn-Al 500ºC, Zn-Fe 500ºC and Zn-Fe 500ºC, inhibit the light penetration, and thereby reduce the activities.

Table 5.4. First-order rate constants (k, min^{-1}) and linear regression values (R^2) for different initial concentrations of MO, MB and SA in the presence of Zn-Al 500ºC, Zn-Fe 500ºC and Zn-Fe 500ºC.

	Zn-Al 500ºC		**Zn-Fe 500ºC**			**Zn-Fe 500ºC**		
$[MO]_0$	**k**	**R^2**	**$[MB]_0$**	**k**	**R^2**	**$[SA]_0$**	**k**	**R^2**
32.7	0.0284	0.9662	**31.9**	0.0214	0.9601	**13.8**	0.0087	0.8283
16.3	0.0292	0.9762	**15.9**	0.0220	0.9621	**6.90**	0.0089	0.9442
8.17	0.0297	0.9803	**7.95**	0.0229	0.9683	**3.45**	0.0092	0.9523
3.27	0.0347	0.9954	**3.19**	0.0321	0.9733	**1.38**	0.0179	0.9721
1.63	0.0449	0.9960	**1.59**	0.0442	0.9873	**0.69**	0.0261	0.9872
0.82	0.0499	0.9962	**0.79**	0.0482	0.9932	**0.35**	0.0342	0.9931
0.33	0.0578	0.9970	**0.31**	0.0523	0.9962	**0.14**	0.0453	0.9952

Langmuir-Hinshelwood model is also employed to describe the degradation processes of MO, MB and SA. Rate (R) versus initial concentration ($[MO]_0$, $[MB]_0$ and $[SA]_0$) plots approach a saturation region at high concentration values (Figure 5.10a,c and e). Thus, the reaction rate follows the zero-order kinetics beyond these regions and may also

suggest occupation of all active surface sites and interlayer galleries of Zn-Al 500ºC, Zn-Fe 500ºC and Zn-Fe 500ºC with the functional groups of MO, MB and SA, respectively. The linear plots of the reciprocals rates (1/R) versus reciprocal initial concentrations ((1/$[MO]_0$), (1/$[MB]_0$), (1/$[SA]_0$)) yield the adsorption coefficients (K) and the degradation rate constants (k) (Figure 5.10b,d and f). The values of K and k are found to be 0.250 L mg^{-1} and 0.346 mg L^{-1} min^{-1} for Zn-Al 500ºC (MO) and 0.174 L mg^{-1} and 0.249 mg L^{-1} min^{-1} for Zn-Fe 500ºC (MB) and 0.171 L mg^{-1} and 0.233 mg L^{-1} min^{-1} for Zn-Fe 500ºC (SA). Accordingly, the highest reaction rate constant is determined in the presence of Zn-Al 500ºC for MO degradation process, being consistent with the photocatalytic degradation results.

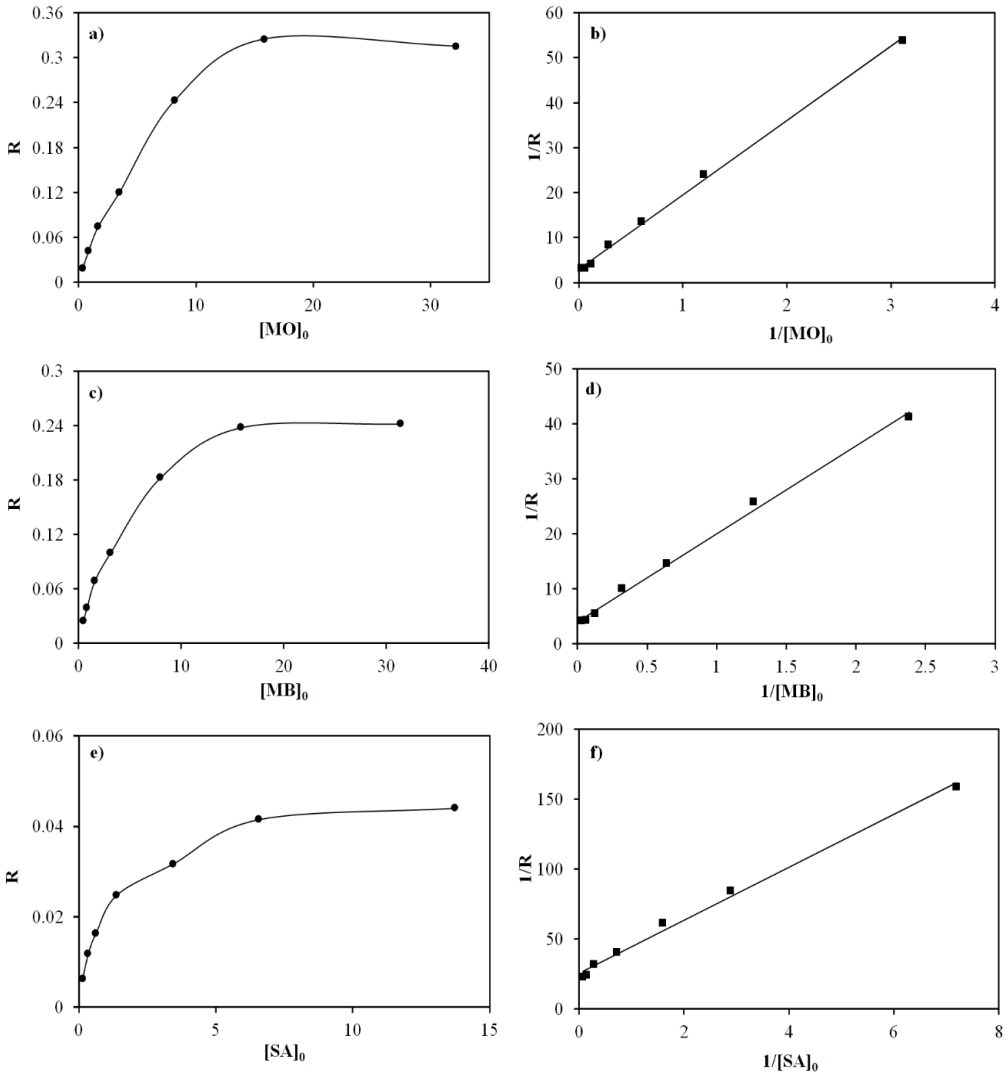

Figure 5.10. Langmuir-Hinshelwood kinetic analysis of (a,b) Zn-Al 500ºC for MO, (c,d) Zn-Fe 500ºC for MB and (e,f) Zn-Fe 500ºC for SA degradation.

5.4. Results and Discussion of Fly Ash Supported LDHs and LDOs

5.4.1. XRD Analysis

Fly ash exhibits the main crystalline phases of mullite ($Al_2O_3.2SiO_3$), quartz (SiO_2), lime (CaO) and Fe_2O_3 (Figure 5.11a). For Mg-Al-Fly Ash 100ºC and Mg-Al-Fly Ash 500ºC, the peaks at 20.8º and 26.6º (2θ) are indexed to the (100) and (101) planes of the quartz while 26.1º and 33.2º (2θ) reflections are matched with the (210) and (220) planes of mullite phase. The specific talcite peaks are not detected. After calcination, the intensity of the mullite peak increases since Al_2O_3 growth is enhanced due to the existence of aluminum in both fly ash and LDH structures. In the profiles of Mg-Fe-Fly Ash 100ºC and Mg-Fe-Fly Ash 500ºC, quartz and Fe_2O_3 peaks are observed (Figure 5.11b). The Fe_2O_3 peaks become more distinctive in the spectrum of Mg-Fe-Fly Ash 500ºC compared to Mg-Fe-Fly Ash 100ºC owing to the better crystallization of iron content through oxidation. The patterns of Zn-Al-Fly Ash 100ºC reveal 11.5º, 23.2º, 34.7º, 39.1º, 46.6º, 60.6º, 62.1º (2θ) reflections of the (003), (006), (012), (015), (018), (110) and (113) planes of talcite, respectively (Figure 5.11c). Also, quartz peaks are detected at 20.8º and 27.6º (2θ). The reflections obtained at 32.2º, 34.8º, 36.8º and 56.7º are ascribed to the planes (211), (002), (101) and (110) of $Zn(OH)_2$. For Zn-Al-Fly Ash 500ºC, the remaining talcite and quartz peaks confirm the preserved structure of both fly ash and LDH in the matrix. Besides, the transformation of $Zn(OH)_2$ into ZnO is verified with the peaks noticed at 31.8º, 34.4º, 36.3º, 56.6º and 67.8º (2θ), indexed to the (100), (002), (101), (110) and (112) planes of wurtzite phase of ZnO. The Zn-Fe-Fly Ash 100ºC exhibits mainly characteristic $Zn(OH)_2$ peaks in addition to the small peaks of talcite and quartz (Figure 5.11d). For Zn-Fe-Fly Ash 500ºC, a single peak of fly ash is detected at 27.6º (2θ) while talcite peak disappears. Also, observation of the distinct ZnO peaks confirms the crystal growth of ZnO. The interlayer spacing values corresponding to the (003) planes of Zn-Al-Fly Ash 100ºC and Zn-Al-Fly Ash 500ºC are determined as 0.766 nm and 0.753 nm, respectively (Table 5.5). The negligible decrement in the basal spacings of Zn-Fe-Fly Ash 100ºC and Zn-Fe-Fly Ash 500ºC is attributed to the formation of ZnO nanoparticles through thermal treatment. The d-spacing value of Zn-Fe-Fly Ash 100ºC is found as 0.911 nm based on the main talcite reflection of (003).

The crystalline sizes of ZnO are calculated as 18.4 nm for Zn-Al-Fly Ash 500°C and 25.5 nm for Zn-Fe-Fly Ash 500°C by employing Scherrer's equation based on the most intense ZnO peak located at 36.3° (2θ).

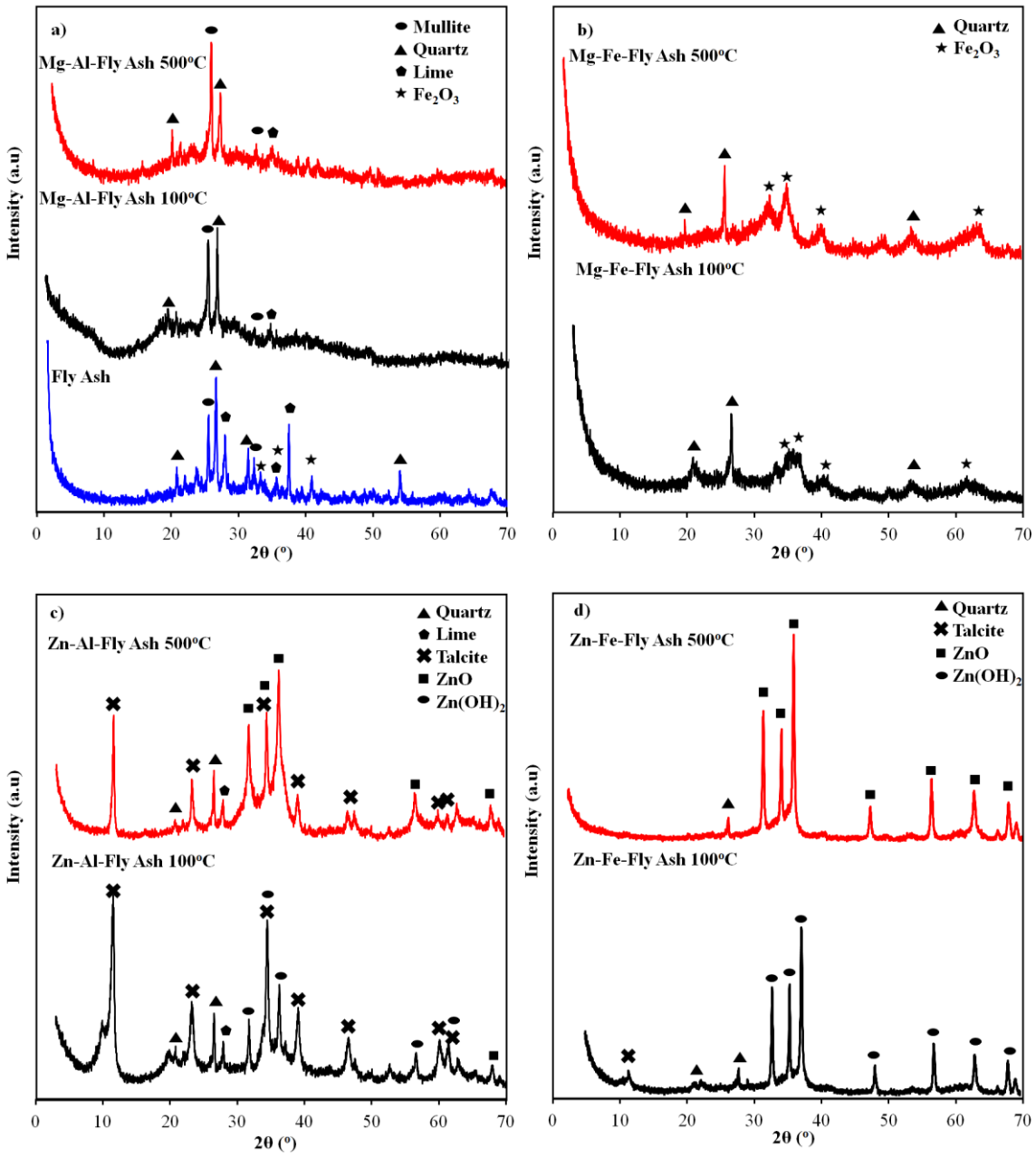

Figure 5.11. XRD patterns of (a) Fly Ash, Mg-Al-Fly Ash 100°C and Mg-Al-Fly Ash 500°C, (b) Mg-Fe-Fly Ash 100°C and Mg-Fe-Fly Ash 500°C, (c) Zn-Al-Fly Ash 100°C and Zn-Al-Fly Ash 500°C, (d) Zn-Fe-Fly Ash 100°C and Zn-Fe-Fly Ash 500°C.

5.4.2. Nitrogen Adsorption-Desorption Tests

The nitrogen adsorption/desorption isotherms of fly ash, Mg-Al-Fly Ash 100ºC, Mg-Al-Fly Ash 500ºC, Mg-Fe-Fly Ash 100ºC, Mg-Fe-Fly Ash 500ºC, Zn-Al-Fly Ash 100ºC, Zn-Al-Fly Ash 500ºC, Zn-Fe-Fly Ash 100ºC and Zn-Fe-Fly Ash 500ºC are illustrated in Figure 5.12. The fly ash and Mg-Al-Fly Ash 500ºC reveal type II isotherm which refers to nonporous or microporous structures (Figure 3.12a). Contrarily, the isotherms of Mg-Al-Fly Ash 500ºC, Mg-Fe-Fly Ash 100ºC, Mg-Fe-Fly Ash 500ºC, Zn-Al-Fly Ash 100ºC, Zn-Al-Fly Ash 500ºC, Zn-Fe-Fly Ash 100ºC and Zn-Fe-Fly Ash 500ºC concur type IV isotherm model accompanying the H3 hysteresis loop at the high relative pressure (0.48-0.96) which is associated with the slit-shaped pores formed by platelet aggregation (Figure 5.12a-d) [278]. The specific surface area, pore volume and pore radius of the samples are presented in Table 5.5. The fly ash exhibits low surface area and pore radius compared to the LDH samples. The surface area and pore features of Mg-Al-Fly Ash 500ºC, Mg-Fe-Fly Ash 500ºC, Zn-Al-Fly Ash 500ºC and Zn-Fe-Fly Ash 500ºC are found to be higher than those of the uncalcined analogous (Mg-Fe-Fly Ash 100ºC, Zn-Al-Fly Ash 100ºC and Zn-Fe-Fly Ash 100ºC). This enhancement in the structure of calcined samples is attributed to the formation of mixed metal oxides upon thermal treatment. Moreover, the fly ash-supported samples possess higher surface areas and pore sizes in comparison to the samples prepared in the absence of fly ash (Section 5.3). Thus, the existence of fly ash in the matrix provides an increment in the surface areas and porosities, which is ultimately expected to improve the adsorption abilities and photoactivities of the studied LDHs.

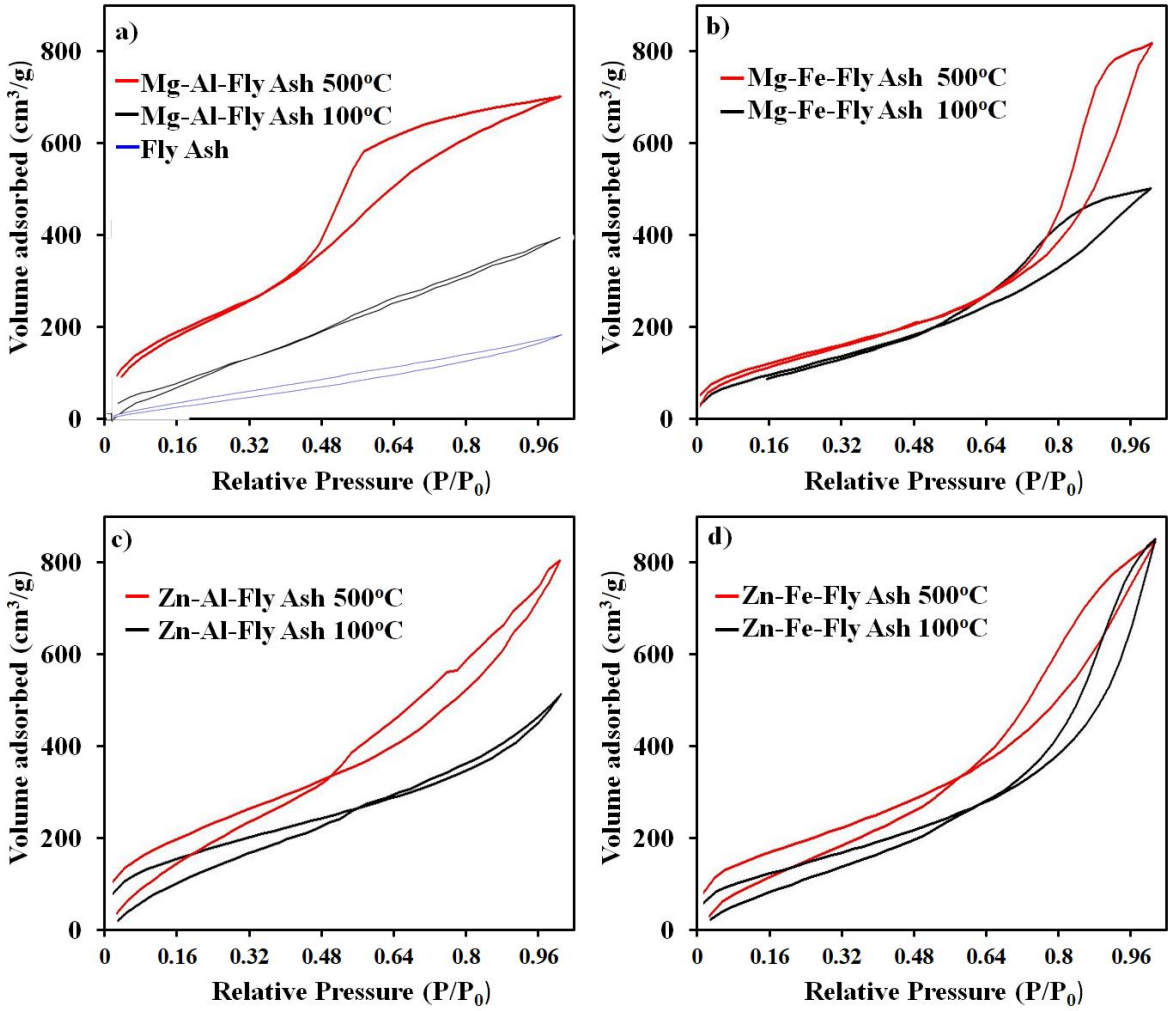

Figure 5.12. Nitrogen adsorption-desorption isotherms of (a) Mg-Al-Fly Ash 100°C and Mg-Al-Fly Ash 500°C, (b) Mg-Fe-Fly Ash 100°C and Mg-Fe-Fly Ash 500°C, (c) Zn-Al-Fly Ash 100°C and Zn-Al-Fly Ash 500°C, (d) Zn-Fe-Fly Ash 100°C and Zn-Fe-Fly Ash 500°C.

Table 5.5. Basal spacings (d-spacing), surface areas (BET), pore volumes (V_{pore}) and pore radius (r_{pore}) of fly ash, Mg-Al-Fly Ash 100°C, Mg-Al-Fly Ash 500°C, Mg-Fe-Fly Ash 100°C, Mg-Fe-Fly Ash 500°C, Zn-Al-Fly Ash 100°C, Zn-Al-Fly Ash 500°C, Zn-Fe-Fly Ash 100°C and Zn-Fe-Fly Ash 500°C.

Materials	**d-spacing (nm)**	**BET (m^2g^{-1})**	**V_{pore} (cm^3 g^{-1})**	**r_{pore} (Å)**
Fly Ash		5.6	0.009	15.1
Mg-Al-Fly Ash 100°C	-	19.9	0.003	16.5
Mg-Al-Fly Ash 500°C	-	39.9	0.053	18.2
Mg-Fe-Fly Ash 100°C	-	83.2	0.151	20.0
Mg-Fe-Fly Ash 500°C	-	109.4	0.255	24.0
Zn-Al-Fly Ash 100°C	0.766	16.7	0.240	15.0
Zn-Al-Fly Ash 500°C	0.763	35.2	0.420	16.4
Zn-Fe-Fly Ash 100°C	0.911	72.5	0.138	28.9
Zn-Fe-Fly Ash 500°C	0.989	81.6	0.146	58.2

5.4.3. SEM-EDX Analysis

The morphologies of fly ash, Mg-Al-Fly Ash 100°C, Mg-Al-Fly Ash 500°C, Mg-Fe-Fly Ash 100°C, Mg-Fe-Fly Ash 500°C, Zn-Al-Fly Ash 100°C, Zn-Al-Fly Ash 500°C, Zn-Fe-Fly Ash 100°C and Zn-Fe-Fly Ash 500°C are examined via SEM-EDX analysis (Figure 5.13). The spherical structure is the predominant shape of fly ash particles (Figure 5.13a). The EDX analysis reports that Si, Al and Ca as major and Mg and Fe as minor constituents of the fly ash. In the image of Mg-Al-Fly Ash 100°C, fly ash nanoparticles are interweaved into layers and on the surface of talcite (Figure 5.13b). After calcination, the layers are preserved with more cracks and also spheres of fly ash are anchored on the talcite (Figure 5.13d). The elemental composition of Mg-Al-Fly Ash 100°C and Mg-Al-Fly Ash 500°C confirm the presence of both fly ash and talcite with Mg, Al, N, O, Si, Ca and Fe signals

(Figure 5.13c and e). The N percentage which is derived from the interlayer anions in the talcite structure decreases upon calcination in the selected area. To calculate Mg/Al ratio is not meaningful for Mg-Al-Fly Ash 100ºC and Mg-Al-Fly Ash 500ºC because of the high percentage of Al as a common element in both fly ash and talcite structure.

The layers of the talcite particles are observed in the images of Mg-Fe-Fly Ash 100ºC and Mg-Fe-Fly Ash 500ºC (Figure 5.13f and h). After calcination, fly ash spheres of different sizes are attached to talcite surface. Also, the bright aggregates are attributed to the formation Fe_2O_3 crystallites in the matrix of Mg-Fe-Fly Ash 500ºC. This is supported by the EDX analysis with the higher percentage of Fe in Mg-Fe-Fly Ash 500ºC compared to that of Mg-Fe-Fly Ash 100ºC (Figure 5.13g and i). Other percentages are not varied significantly, indicating preserved structures of fly ash and LDH. The decrement in the N amount points to the removal of the interlayer anions during the calcination process.

Zn-Al-Fly Ash 100ºC and Zn-Al-Fly Ash 500ºC images consist of talcite particles with rough surfaces and spherical fly ash particles (Figure 5.13j and l). The formation of the layered structure is verified by the Zn/Al molar ratio (2.01) of Zn-Al-Fly Ash 100ºC and (2.02) Zn-Al-Fly Ash 500ºC as revealed by the EDX analysis (Figure 5.13k and m).

In the images Zn-Fe-Fly Ash 100ºC and Zn-Fe-Fly Ash 500ºC, the needle-like nanoparticles overlapped on the whole surface, are attributed to the formation of $Zn(OH)_2$ and ZnO crystallites (Figure 5.13n and p). The high surface area and porosity obtained by the BET analysis may be derived from these coarse particles. The molar ratio of Zn/Fe is found to be consistent for both (1.99) Zn-Fe-Fly Ash 100ºC and (1.99) Zn-Fe-Fly Ash 500ºC (Figure 5.13o and r).

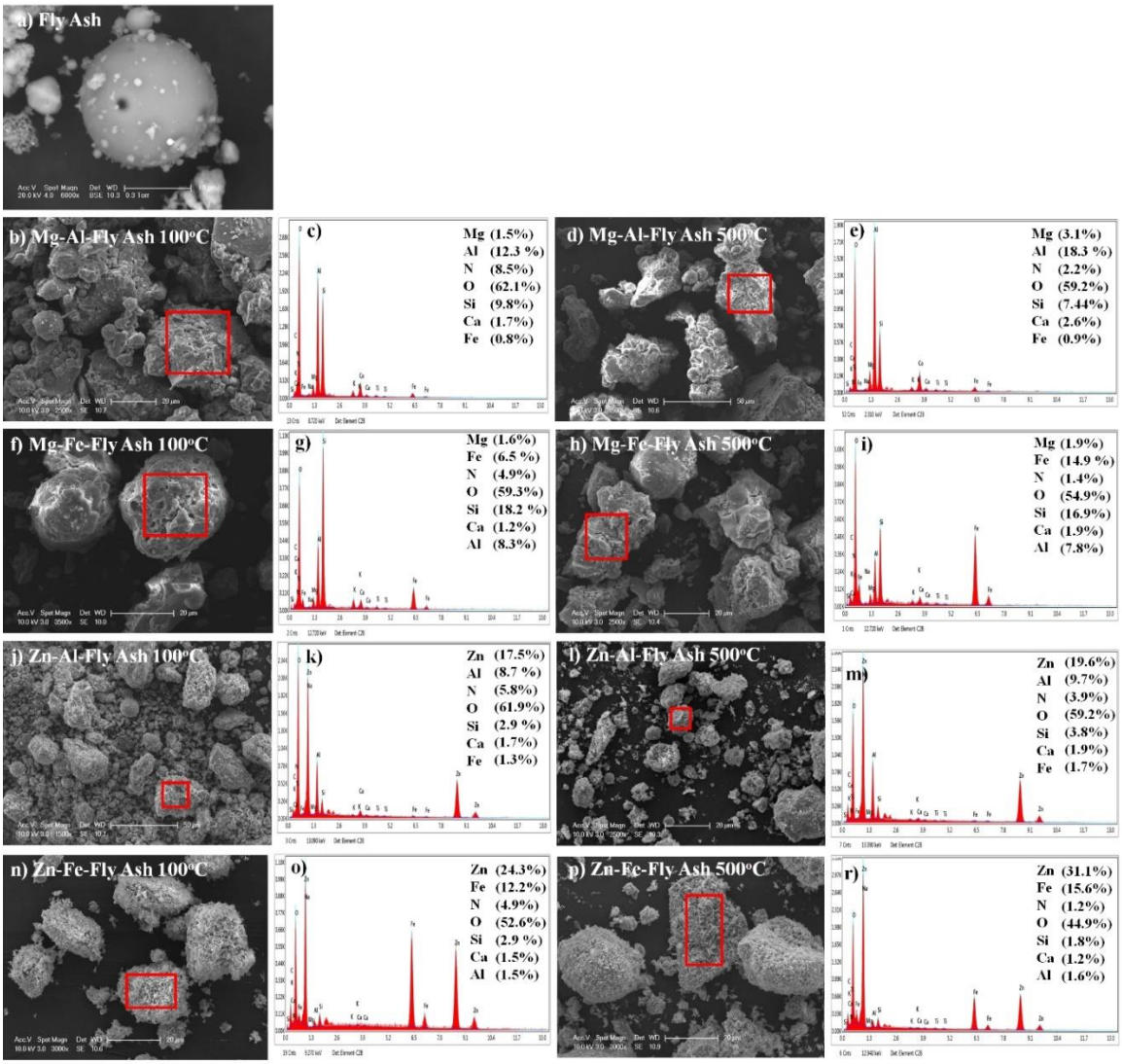

Figure 5.13. SEM images and EDX analysis of (a,b) Mg-Al-Fly Ash 100°C (c,d) Mg-Al-Fly Ash 500°C, (e,f) Mg-Fe-Fly Ash 100°C (g,h) Mg-Fe-Fly Ash 500°C, (i,j) Zn-Al-Fly Ash 100°C (k,l) Zn-Al-Fly Ash 500°C, (m,n) Zn-Fe-Fly Ash 100°C (o,p) Zn-Fe-Fly Ash 500°C.

5.4.4. UV-Vis DRS Analysis

Figure 5.14 shows the absorption spectra and corresponding band gap energy curves of fly ash, Mg-Al-Fly Ash 100°C, Mg-Al-Fly Ash 500°C, Mg-Fe-Fly Ash 100°C, Mg-Fe-Fly Ash 500°C, Zn-Al-Fly Ash 100°C, Zn-Al-Fly Ash 500°C, Zn-Fe-Fly Ash 100°C and Zn-Fe-Fly Ash 500°C. The fly ash presents an extending absorption band in between the range

of 200 and 600 nm (Figure 5.14a). In the spectrum of Mg-Al-Fly Ash 100ºC, a minor absorption peak at around 300 nm is associated with the existence of interlayer nitrate anions and the Al content. After calcination, the intensity of this peak increases due to the formation of Al_2O_3. The band-gap energies of the Mg-Al-Fly Ash 100ºC and Mg-Al-Fly Ash 500ºC based on the intercept of the tangent in the plots of $((Abs)^2 hv)^2)$ versus photon energy (hv), are determined as 2.75 eV and 2.59 eV, respectively, (Figure 5.14b).

In the spectrum of Mg-Fe-Fly Ash 100ºC and Mg-Fe-Fly Ash 500ºC, the broad absorption band in between 500-600 nm is derived from the spin-forbidden-excitation and straight transition in Fe_2O_3 structure (Figure 5.14c) [279]. After calcination, this peak becomes sharper with higher intensity due to the improved crystallization of Fe_2O_3 via oxidation of iron content in both talcite and fly ash, being consistent with the XRD results. The band gap energies are found as 2.20 eV for Mg-Fe-Fly Ash 100ºC and 2.11 eV for Mg-Fe-Fly Ash 500ºC (Figure 5.14d).

In the profiles of Zn-Al-Fly Ash 100ºC and Zn-Al-Fly Ash 500ºC, the absorption edge at around 390 nm is attributed to the $Zn(OH)_2$ and ZnO nanoparticles formed in the matrix, being corroborated with the XRD patterns (Figure 5.14e). The sharpness and the intensity of the ZnO peak increase after being calcined at 500ºC. The band gap energy values are found as 3.10 eV for Zn-Al-Fly Ash 100ºC and 3.05 eV for Zn-Al-Fly Ash 500ºC.

The characteristic absorption edge of ZnO at 390 nm is also observed in the spectra of Zn-Fe-Fly ash 100ºC and Zn-Fe-Fly ash 500ºC (Figure 5.14g). Besides, extension in the range of 500-600 nm may be attributed to the iron content in the structure. The band gap energy values are estimated as 3.10 eV for Zn-Fe-Fly ash 100ºC and 3.02 eV for Zn-Fe-Fly ash 500ºC (Figure 5.14h).

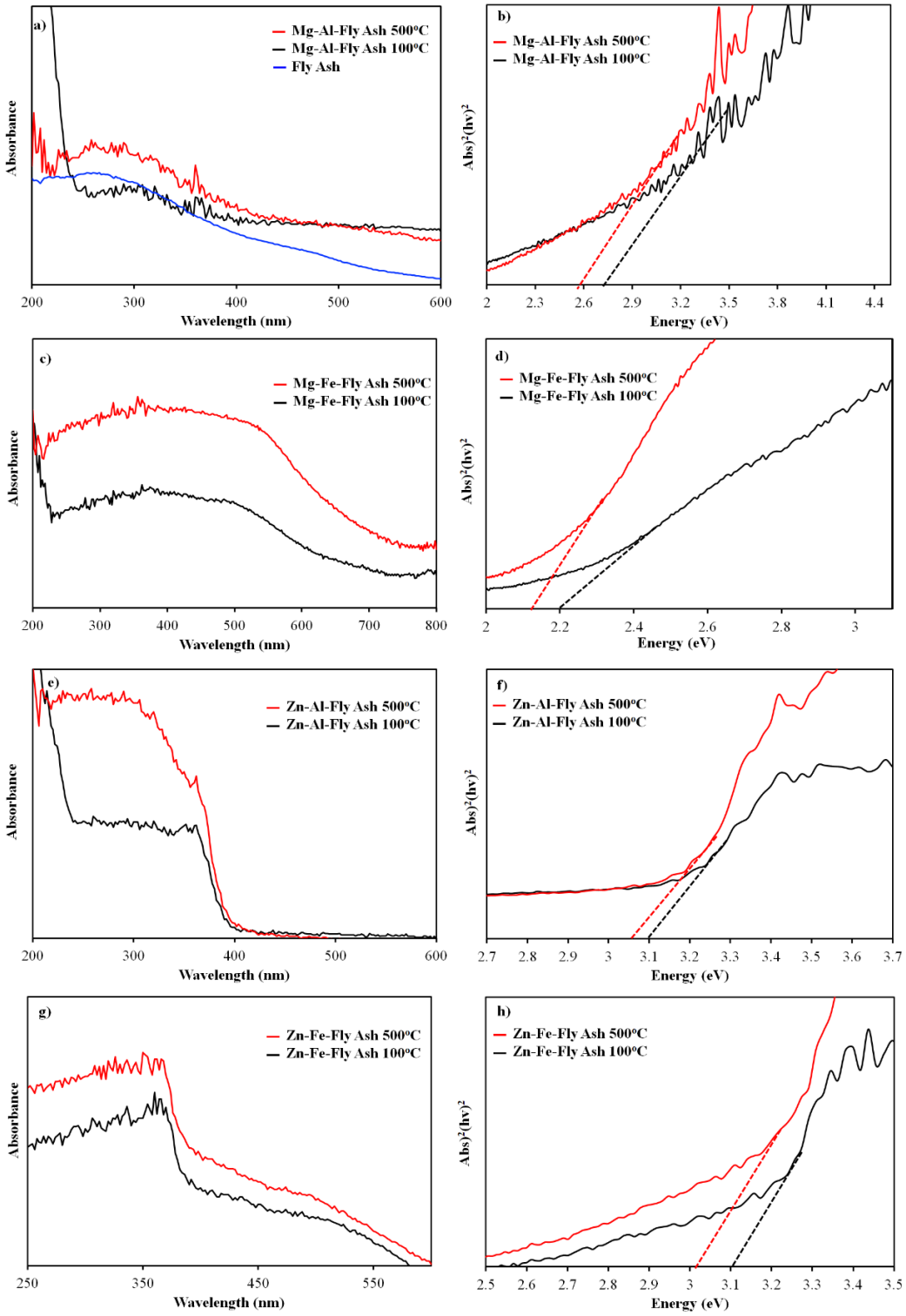

Figure 5.14. UV-vis DRS spectra and band gap absorption plots of (a,b) Mg-Al-Fly Ash 100°C, Mg-Al-Fly Ash 500°C, (c,d) Mg-Fe-Fly Ash 100°C, Mg-Fe-Fly Ash 500°C, (e,f) Zn-Al-Fly Ash 100°C, Zn-Al-Fly Ash 500°C, and (g,h) Zn-Fe-Fly Ash 100°C, Zn-Fe-Fly Ash 500°C.

5.4.5. Adsorption and Photocatalytic Tests

The dark adsorption capacities of the Mg-Al-Fly Ash 100ºC, Mg-Al-Fly Ash 500ºC, Mg-Fe-Fly Ash 100ºC, Mg-Fe-Fly Ash 500ºC, Zn-Al-Fly Ash 100ºC, Zn-Al-Fly Ash 500ºC, Zn-Fe-Fly Ash 100ºC and Zn-Fe-Fly Ash 500ºC in the presence of MO, MB and SA are displayed in Figure 5.15a,c and e.

The remaining MO percentages are found as 11.2% and 3.5% for Mg-Al-Fly Ash 100ºC and Mg-Al-Fly Ash 500ºC, respectively (Figure 5.15a). Despite the low surface area and porosity of Mg-Al-Fly Ash 100ºC, electrostatic attractions between metal cations of Mg-Al-Fly Ash 100ºC and the negatively charged sulphonic group of MO contribute to the adsorption of MO. The higher adsorption ability of Mg-Al-Fly Ash 500ºC than that of the Mg-Al-Fly Ash 100ºC is attributed to the increment in the surface area and formation of the mesoporous structure after calcination. In the presence of MB, a similar trend is observed. Besides, the surface oxide groups may enhance the adsorption of cationic dye MB, thus remaining percentages reach 3.6% for Mg-Al-Fly Ash 100ºC and 3.7% for Mg-Al-Fly Ash 500ºC, at the end of the 100 min (Figure 5.15c). In the case of SA, the remaining percentages are found as 30.1% and 25.2% in the presence of Mg-Al-Fly Ash 100ºC and Mg-Al-Fly Ash 500ºC, respectively (Figure 5.15e). The high surface area and porosity of Mg-Al-Fly Ash 500ºC increase its adsorption ability in comparison to that of Mg-Al-Fly Ash 100ºC. The adsorption of SA can be driven by the hydrogen bonding, formed in between carboxylic acid functional group of SA and surface hydroxyl groups of Mg-Al-Fly Ash 100ºC and Mg-Al-Fly Ash 500ºC.

The residual amounts of MO are found as 30% for Mg-Fe-Fly Ash 100ºC and 38% for Mg-Fe-Fly Ash 500ºC, respectively (Figure 5.15a). The existence of fly ash in the matrix leads to a higher surface area and porosity, thus enhancing the adsorption ability of Mg-Fe-Fly Ash 100ºC and Mg-Fe-Fly Ash 500ºC compared to the samples prepared in the absence of fly ash (Section 5.3.5). In the case of Mg-Fe-Fly Ash 500ºC, the existence of Fe_2O_3 crystallites induces the repulsive forces for MO molecules and leads to the lower adsorption of MO in comparison to Mg-Fe-Fly Ash 100ºC.

In contrast to MO, the adsorption of MB is enhanced due to the generation of a negatively charged surface with the formation of metal oxides after calcination (Figure 5.15c). The residual percentages of SA are found as 51% and 38% in the presence of Mg-Fe-Fly Ash 100ºC and Mg-Fe-Fly Ash 500ºC, respectively (Figure 5.15e). The higher surface area and pore sizes of Mg-Fe-Fly Ash 500ºC also enhance the adsorption of SA.

In the presence of Zn-Al-Fly Ash 100ºC and Zn-Al-Fly Ash 500ºC, the removal of MO is completed in 100 min (Figure 5.15a). The electrostatic attractions between the cations of Zn-Al-Fly Ash 100ºC and Zn-Al-Fly Ash 500ºC surfaces and anionic MO molecules improve the adsorption of MO. Moreover, the basal spacing values of Zn-Al-Fly Ash 100ºC (as 0.766 nm) and Zn-Al-Fly Ash 500ºC (as 0.753 nm) ensure intercalation of MO molecule with a width of 0.555 nm. Thus, the anion exchange mechanism facilitates MO adsorption. Despite the suitable basal spacing values for intercalation, the MB adsorption is found to be lower than MO with 42% and 21% remaining percentages in the presence of Zn-Al-Fly Ash 100ºC and Zn-Al-Fly Ash 500ºC, respectively (Figure 5.15c). This can be explained by the repulsive forces between the surface metallic cations and positively charged MB molecules. After calcination, ZnO nanoparticles induce the negative charge on the Zn-Al-Fly Ash 500ºC and provide more attraction for MB molecules. The residual percentages of SA are found as 42% for Zn-Al-Fly Ash 100ºC and 35% Zn-Al-Fly Ash 500ºC, respectively (Figure 5.15e). The interlayer distances in the Zn-Al-Fly Ash 100ºC and Zn-Al-Fly Ash 500ºC can supply intercalation channels for SA. Also, the formation of the ZnO nanoparticles supports the electrostatic attractions among carboxylic acid groups of SA and oxygen atoms in ZnO crystallites.

The high surface area and porous structure of Zn-Fe-Fly Ash 100ºC (23% remaining MO) and Zn-Fe-Fly Ash 500ºC (28% remaining MO) play a significant role in the adsorption of MO (Figure 5.15a). In the structure of Zn-Fe-Fly Ash 100ºC, hydrogen bonding on the surface can be established between $Zn(OH)_2$ crystallites and sulphonic groups of MO. However, after calcination, repulsive forces between oxygen atoms in Zn-O bond and MO molecules lead to the lower adsorption of MO. The remaining MB percentages are determined as 28% and 20% in the presence of Zn-Fe-Fly Ash 100ºC and Zn-Fe-Fly Ash 500ºC, respectively (Figure 5.15c). The increment of the MB adsorption after calcination is attributed to the variations of the surface charge with the formation of ZnO nanoparticles.

The SA amount is found as 30% for Zn-Fe-Fly Ash 100ºC and 38% for Zn-Fe-Fly Ash 500ºC (Figure 5.15e). The intercalation of the SA molecules into the structure of the Zn-Fe-Fly Ash 100ºC can be possible due to the smaller size of SA molecule. And, surface electrostatic interactions can also be proposed between the carboxylic acid groups of SA and anionic groups of Zn-Fe-Fly Ash 500ºC.

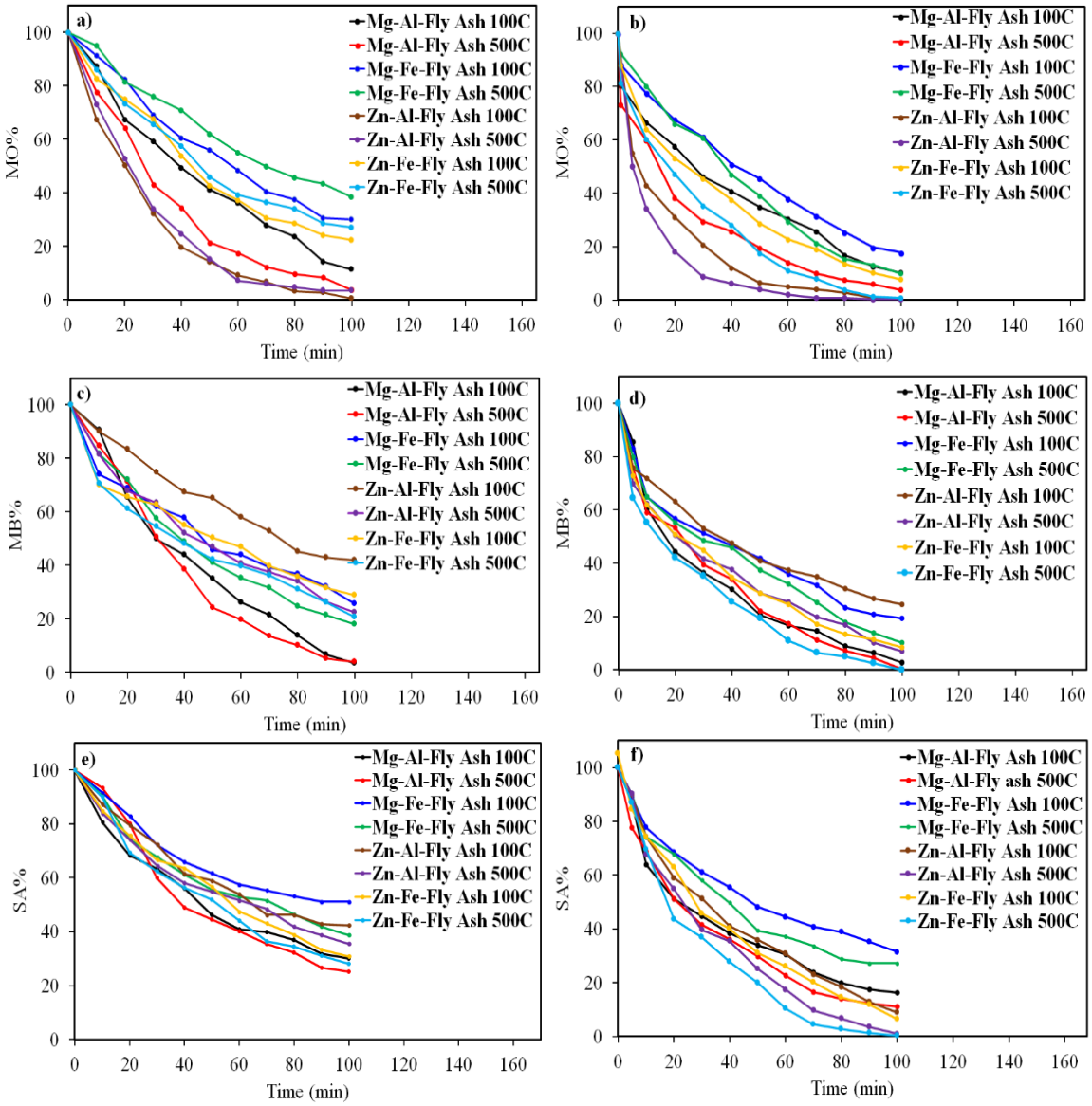

Figure 5.15. Dark adsorption and photocatalytic degradation (a,b) of MO, (c,d) of MB and (e,f) SA in the presence of Mg-Al-Fly Ash 100ºC, Mg-Al-Fly Ash 500ºC, Mg-Fe-Fly Ash 100ºC, Mg-Fe-Fly Ash 500ºC, Zn-Al-Fly Ash 100ºC, Zn-Al-Fly Ash 500ºC, Zn-Fe-Fly Ash 100ºC and Zn-Fe-Fly Ash 500ºC.

The photocatalytic performances of the Mg-Al-Fly Ash 100ºC, Mg-Al-Fly Ash 500ºC, Mg-Fe-Fly Ash 100ºC, Mg-Fe-Fly Ash 500ºC, Zn-Al-Fly Ash 100ºC, Zn-Al-Fly Ash 500ºC, Zn-Fe-Fly Ash 100ºC and Zn-Fe-Fly Ash 500ºC are examined for the degradation processes of MO, MB and SA (Figure 5.15b,d and f).

In the presence of Mg-Al-Fly Ash 100ºC, the remaining percentages of MO, MB and SA are found as 10%, 5% and 16%, respectively (Figure 5.15b,d and f). The photocatalytic degradation of the calcined sample (Mg-Al-Fly Ash 500ºC) is relatively higher than the uncalcined form (Mg-Al-Fly Ash 100ºC) due to the increased Al in the structure.

The residual percentages of MO, MB and SA are determined as 18%, 19% and 31% in the presence of Mg-Fe-Fly Ash 100ºC, while 10%, 11% and 25% in the presence of Mg-Fe-Fly Ash 500ºC (Figure 5.15b,d and f). The higher photocatalytic performance of Mg-Fe-Fly Ash 500ºC can be explained by the formation of Fe_2O_3 crystallites after thermal treatment. The photoactivity of Fe_2O_3 stems from the promotion of excited electrons from the valence band to the empty d^5 orbitals of Fe^{3+} ions. The photogenerated holes react with water and surface hydroxide groups while photogenerated electrons react with the oxygens to form superoxide radicals. Thus, the attack of these radicals to MO, MB and SA moieties improves the photoactivity of Mg-Fe-Fly Ash 500ºC [280].

The MO degradation is completed in 70 min while the remaining percentages of MB and SA percentages are found as 24% and 8%, in the presence of Zn-Al-Fly Ash 100ºC. The photoactivity of Zn-Al-Fly Ash 100ºC is attributed to the existence of $Zn(OH)_2$. The degradation of MO, MB and SA are accomplished in 100 min in presence of Zn-Al-Fly Ash 500ºC due to the formation of ZnO crystallites in the matrix.

In the case of Zn-Fe-Fly Ash 100ºC, the remaining percentages are found as 7% for MO, 8% for MB and 6% for SA (Figure 5.15b,d and f). The complete photocatalytic degradation of MO, MB and SA is accomplished at the end of the 100 min in the presence of Zn-Fe-Fly Ash 500ºC. The existence of both ZnO and Fe_2O_3 enhances the photoactivity. The higher photocatalytic performance of Zn-Al-Fly Ash 500ºC than that of Zn-Fe-Fly Ash 500ºC is attributed to the smaller ZnO crystalline size that facilitates the rapid photoelectron

transfer from bulk to the surface which can retard the recombination of electron-hole pair and enhance the photoactivity [280].

5.4.6. Dark Adsorption Kinetics and Isotherms

Zn-Al-Fly Ash 500°C, Mg-Al-Fly Ash 500°C and Mg-Al-Fly Ash 500°C demonstrate the highest dark adsorption capacities for MO, MB and SA, respectively. Accordingly, kinetic analysis under dark conditions are carried out in the presence of these samples. Pseudo-first order and pseudo-second order models are studied, and their kinetic parameters and correlation coefficients are summarized (Table 5.6 and Figure 5.16). The correlation coefficients (R^2) of Zn-Al-Fly Ash 500°C, Mg-Al-Fly Ash 500°C and Mg-Al-Fly Ash 500°C for pseudo-second order model are found to be higher than those for the pseudo-first-order model. In addition, calculated q_e values (q_e (calc)) of the pseudo-second order model are closer to the experimental q_e values (q_e (exp)). Therefore, pseudo-second order kinetic model is accepted as a more precise model through the electrostatic interactions and hydrogen bonding to explore the adsorption behaviors of Zn-Al-Fly Ash 500°C for MO, Mg-Al-Fly Ash 500°C for MB and Mg-Al-Fly Ash 500°C for SA.

Table 5.6. Kinetic parameters of Zn-Al-Fly Ash 500°C for MO, Mg-Al-Fly Ash 500°C for MB and Mg-Al-Fly Ash 500°C for SA adsorption.

		Pseudo-first order $\ln (q_e - q_t) = \ln q_e - k_1 t$			**Pseudo-second order** $\frac{t}{q_t} = (\frac{1}{k_2 q^2_e}) + \frac{t}{q_e}$		
	$q_{e\ (exp)}$	**k_1**	**$q_{e\ (calc)}$**	**R^2**	**k_2**	**$q_{e(calc)}$**	**R^2**
Zn-Al-Fly Ash 500°C (MO)	3.17	0.0339	2.34	0.9908	0.554	3.23	0.9992
Mg-Al-Fly Ash 500°C (MB)	2.78	0.0210	2.14	0.9827	0.402	2.70	0.9976
Mg-Al-Fly Ash 500°C (SA)	2.41	0.0116	1.67	0.9744	0.356	2.39	0.9959

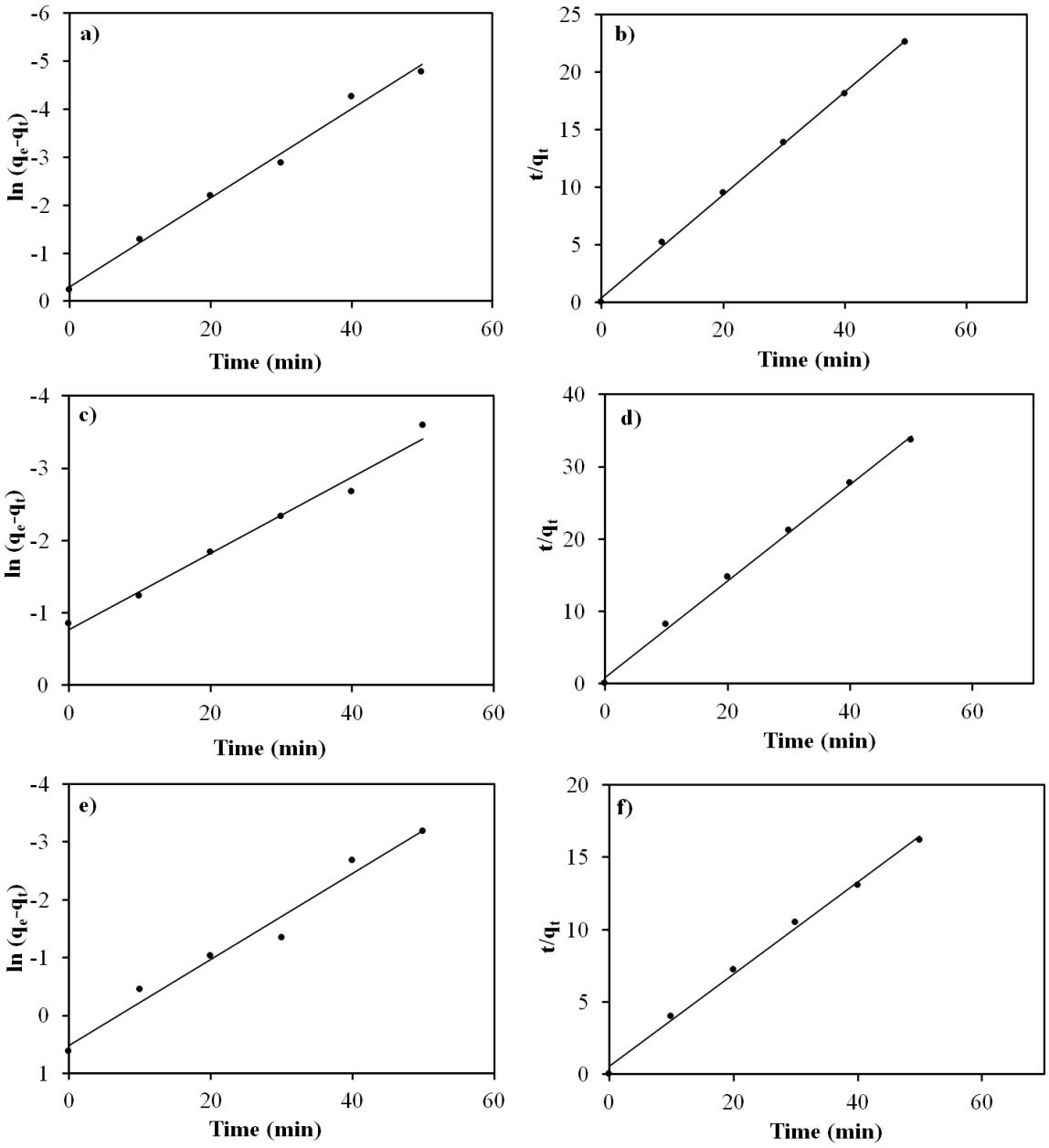

Figure 5.16. Pseudo-first order and pseudo-second order kinetics of (a,b) Zn-Al-Fly Ash 500^{o}C for MO (c,d) Mg-Al-Fly Ash 500^{o}C for MB and (e,f) Mg-Al 500^{o}C for SA adsorption.

Dark kinetic studies continue with the application of Langmuir and Freundlich models and their corresponding kinetic parameters with the correlation coefficients (R^2) (Table 5.7, Figure 5.17). Accordingly, Zn-Al-Fly Ash 500^{o}C for MO, Mg-Al-Fly Ash 500^{o}C for MB and Mg-Al-Fly Ash 500^{o}C for SA adsorption are well-matched to the Langmuir

model with the highest R^2 values. Thus, the monolayer adsorption of MO, MB and SA is postulated on the surfaces of Zn-Al-Fly Ash 500ºC, Mg-Al-Fly Ash 500ºC and Mg-Al-Fly Ash 500ºC, respectively. The highest maximum adsorption capacity (q_L) is detected in the presence of Zn-Al-Fly Ash 500ºC for MO adsorption. Also, the separation factor (R_L) calculated in between 0 and 1 confirms the favorable adsorptions of MO on Zn-Al-Fly Ash 500ºC (0.60), MB on Mg-Al-Fly Ash 500ºC (0.59) and SA on Mg-Al-Fly Ash 500ºC (0.54) via Langmuir isotherm model.

Table 5.7. Langmuir and Freundlich isotherm models of Zn-Al-Fly Ash 500ºC for MO, Mg-Al-Fly Ash 500ºC for MB and Mg-Al-Fly Ash 500ºC for SA adsorption.

	Langmuir $\frac{C_e}{q_e} = \frac{1}{K_L\, q_L} + \frac{C_e}{q_L}$			**Freundlich** $\ln q_e = \ln K_F + \frac{1}{n} \ln C_e$		
	K_L	**q_L**	**R^2**	**K_F**	**1/n**	**R^2**
Zn-Al-Fly Ash 500ºC (MO)	0.484	19.4	0.9991	0.217	0.853	0.9914
Mg-Al-Fly Ash 500ºC (MB)	0.397	14.1	0.9965	0.176	0.823	0.9878
Mg-Al-Fly Ash 500ºC (SA)	0.327	10.5	0.9942	0.134	0.747	0.9862

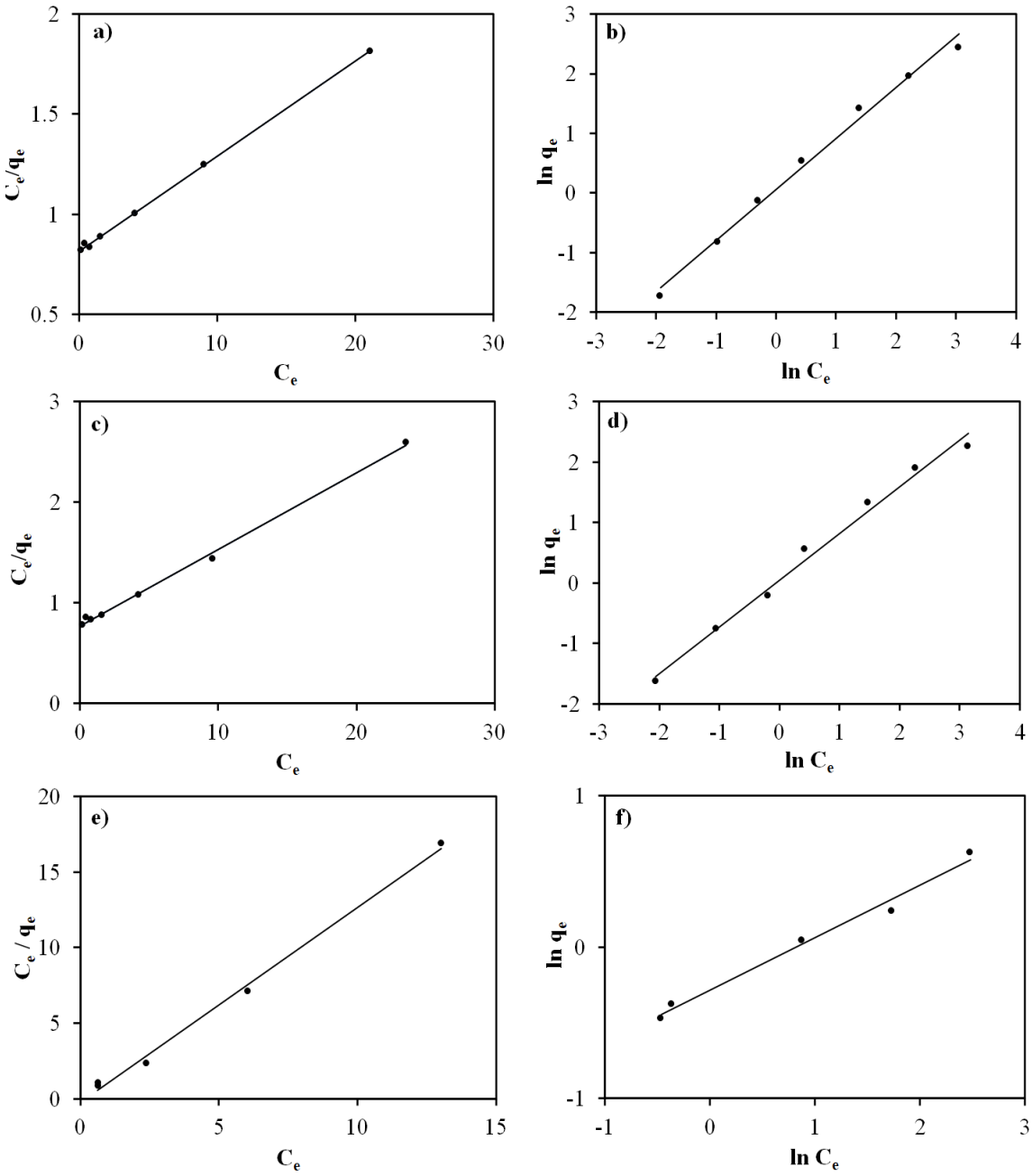

Figure 5.17. Langmuir and Freundlich isotherms of (a,b) Zn-Al-Fly Ash 500^{o}C for MO (c,d) Mg-Al-Fly Ash 500^{o}C for MB and (e,f) Mg-Al 500^{o}C for SA adsorption.

5.4.7. Kinetic Analysis Under Irradiation

Kinetic analysis under irradiation is performed with the samples that show the highest photoactivity, namely: Zn-Al-Fly Ash 500°C for MO degradation, Zn-Fe-Fly Ash 500°C for MB degradation and Zn-Fe-Fly Ash 500°C for SA degradation. The effect of initial concentration variations on the photocatalytic degradations is examined in the range of 32.7-0.327 mg L^{-1} for MO, in the range of 31.9-0.319 mg L^{-1} for MB and in the range of 13.8 to 0.138 mg L^{-1} for SA. The fitted plots and the high correlation coefficients confirm the suitability of pseudo-first order kinetic model for MO. MB and SA degradation (Figure A.30 and Table 5.8). And, the rate constants k (min^{-1}) determined from the slopes of the lines reveal an inverse relation among degradation rate and initial concentrations of MO, MB and SA, since the excess amounts of MO, MB and SA may block the active sites on Zn-Al-Fly Ash 500°C, Zn-Fe-Fly Ash 500°C and Zn-Fe-Fly Ash 500°C, prevent the light penetration and decrease the photoactivities.

Table 5.8. First-order rate constants (k, min^{-1}) and linear regression values (R^2) for different initial concentrations of MO, MB and SA (mg L^{-1}) in the presence of Zn-Al-Fly Ash 500°C, Zn-Fe-Fly Ash 500°C and Zn-Fe-Fly Ash 500°C.

	Zn-Al-Fly Ash500°C		**Zn-Fe-Fly Ash 500°C**			**Zn-Fe-Fly Ash 500°C**		
$[MO]_0$	**k**	**R^2**	**$[MB_0$**	**k**	**R^2**	**$[SA]_0$**	**k**	**R^2**
32.7	0.0410	0.9901	**31.9**	0.0391	0.9871	**13.8**	0.0223	0.9732
16.3	0.0413	0.9912	**15.9**	0.0398	0.9879	**6.90**	0.0229	0.9801
8.17	0.0425	0.9931	**7.95**	0.0401	0.9889	**3.45**	0.0235	0.9831
3.27	0.0465	0.9958	**3.19**	0.0462	0.9921	**1.38**	0.0345	0.9869
1.63	0.0521	0.9967	**1.59**	0.0517	0.9930	**0.69**	0.0431	0.9901
0.82	0.0579	0.9972	**0.79**	0.0557	0.9953	**0.35**	0.0491	0.9912
0.33	0.0624	0.9990	**0.31**	0.0618	0.9973	**0.14**	0.0567	0.9456

The Langmuir-Hinshelwood kinetic model is further tested. The plots of rate (R) versus initial concentrations ($[MO]_0$, $[MB]_0$, $[SA]_0$) show a plateau at high concentrations of MO, MB and SA (Figure 5.18a,c and e). Beyond this, the rate follows zero-order kinetics. The adsorption coefficients (K) and the reaction rate constants (k) are obtained from the

linear plots of reciprocal rate (1/R) versus reciprocal initial concentrations ((1/[MO]$_0$), (1/[MB]$_0$), (1/[SA]$_0$)) (Figure 5.18b,d and f). The values of K and k are found to be 0.322 L mg^{-1} and 0.421 mg L^{-1} min^{-1} for Zn-Al-Fly Ash 500^{o}C (MO) and 0.209 L mg^{-1} and 0.410 mg L^{-1} min^{-1} for Zn-Fe-Fly Ash 500^{o}C (MB) and 0.197 L mg^{-1} and 0.372 mg L^{-1} min^{-1} for Zn-Fe-Fly Ash 500^{o}C (SA).

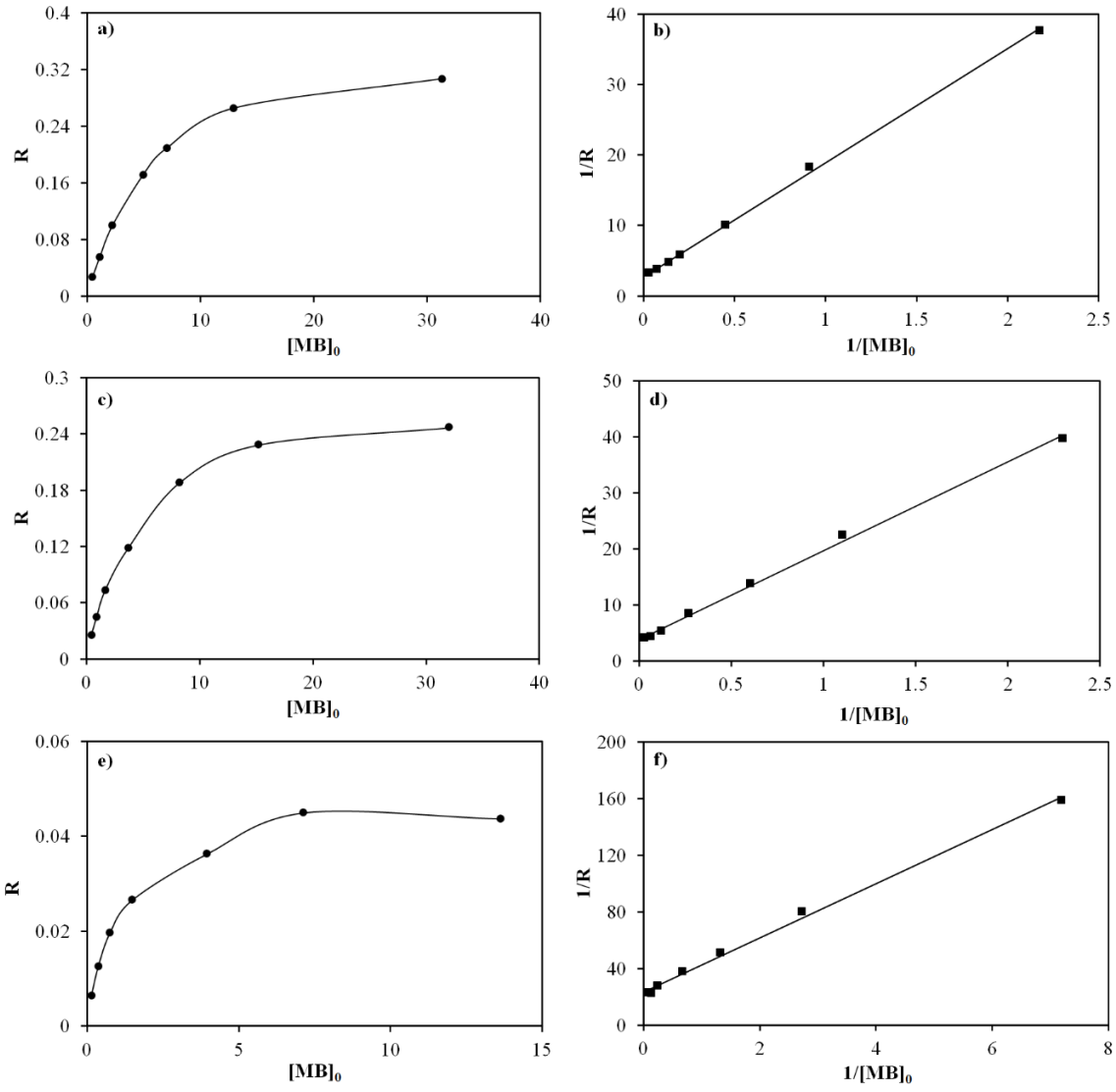

Figure 5.18. Langmuir-Hinshelwood kinetic analysis of (a,b) Zn-Al-Fly Ash 500^{o}C for MO, (c,d) Zn-Fe-Fly Ash 500^{o}C for MB and (e,f) Zn-Fe-Fly Ash 500^{o}C for SA degradation.

5.5. Results and Discussion of Zeolite Supported LDHs and LDOs

5.5.1. XRD Analysis

Figure 5.19 shows the XRD patterns of Zeolite, Mg-Al-Zeolite 100°C, Mg-Al-Zeolite 500°C, Mg-Fe-Zeolite 100°C, Mg-Fe-Zeolite 500°C, Zn-Al-Zeolite 100°C, Zn-Al-Zeolite 500°C, Zn-Fe-Zeolite 100°C and Zn-Fe-Zeolite 500°C. Zeolite displays reflections at 8.9°, 9.9°, 14.9°, 16.7°, 23.2°, 23.9° and 30.1° (2θ) corresponding to the ((101), (020), (031), (122), (051), (303) and (053) planes, respectively (Figure 5.19a). In the spectrum of Mg-Al-Zeolite 100°C, talcite peaks are detected at 11.5°, 23.2°, 34.7°, 39.1° (2θ) indicating the formation of Mg-Al layered double hydroxide. In general, zeolite and talcite peaks overlap. Similar to Mg-Al-Fly ash 500°C, Al_2O_3 peaks are clearly observable in the pattern of Mg-Al-Zeolite 500°C due to the oxidation of Al as a common content in both zeolite and LDH structures.

The Mg-Fe-Zeolite 100°C exhibits typical talcite and zeolite peaks (Figure 5.19b). Also, the minor peaks noticed at 24.0°, 35.9°, 40.5°, 49.5° and 53.9° (2θ) are deduced to the Fe_2O_3 crystal planes of (012), (110), (130), (024) and (116), respectively. After calcination, intensities of talcite and zeolite peaks reduce while intensities of the Fe_2O_3 peaks increase owing to the oxidation of the iron content in the structure.

In the spectrum of Zn-Al-Zeolite 100°C, in addition to the talcite and zeolite peaks, the reflections detected at 31.7°, 34.4°, and 36.3° (2θ) are assigned to (100), (002) and (101) planes of $Zn(OH)_2$, respectively (Figure 5.19c). For Zn-Al-Zeolite 500°C, suppression of the talcite and zeolite peaks can be attributed to the change of the laminate structure with the oxidation of the metal contents in the layers. The generation of characteristic ZnO peaks also confirms the formation of the ZnO crystallites.

Zn-Fe-Zeolite 100°C also exhibits talcite and zeolite peaks (Figure 3.19d). In the meantime, $Zn(OH)_2$ peaks are detected at 31.5, 34.2, and 36.1° (2θ). After calcination, an evident increment in ZnO peaks is noticed, indicating the crystalline growth of ZnO in the matrix.

The basal spacings (d-spacing) corresponding to the (003) planes are determined as 0.773 nm for Mg-Al-Zeolite 100ºC and 0.795 nm for Mg-Al-Zeolite 500ºC (Table 5.9). The small variation may stem from the formation of Al_2O_3 after calcination. The values are found as 0.676 nm, 0.923 nm and 0.936 nm for Mg-Fe-Zeolite 100ºC, Zn-Al-Zeolite 100ºC and Zn-Fe-Zeolite 100ºC, respectively. Since other LDHs prepared at 500ºC do not display (003) planes, their d-spacing values are not measured.

The crystalline sizes of ZnO are calculated as 21.7 nm for Zn-Al-Zeolite 500ºC and 29.9 nm for Zn-Fe-Zeolite 500ºC referring to the most prominent diffraction (101) at 36.2° (2θ).

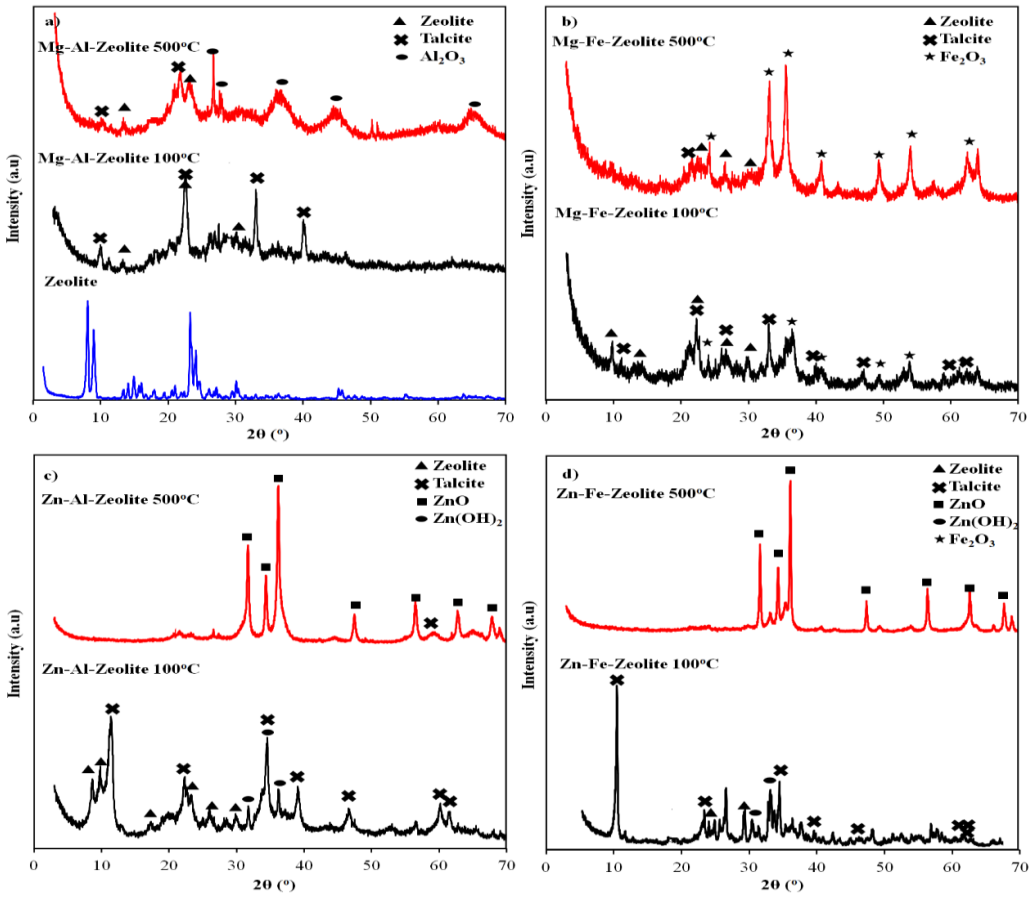

Figure 5.19. XRD patterns of (a) zeolite, Mg-Al-Zeolite 100ºC and Mg-Zeolite 500ºC, (b) Mg-Fe-Zeolite 100ºC and Mg-Fe-Zeolite 500ºC, (c) Zn-Al-Zeolite 100ºC and Zn-Al-Zeolite 500ºC, (d) Zn-Fe-Zeolite 100ºC and Zn-Fe-Zeolite 500ºC.

5.5.2. Nitrogen Adsorption-Desorption Tests

Figure 5.20 displays the nitrogen adsorption-desorption isotherms of zeolite, Mg-Al-Zeolite 100ºC, Mg-Al-Zeolite 500ºC, Mg-Fe-Zeolite 100ºC, Mg-Fe-Zeolite 500ºC, Zn-Al-Zeolite 100ºC, Zn-Al-Zeolite 500ºC, Zn-Fe-Zeolite 100ºC and Zn-Fe-Zeolite 500ºC. The zeolite displays type I isotherm, characteristic of microporous materials (Figure 5.20a). The isotherms of Mg-Al-Zeolite 100ºC and Mg-Al-Zeolite 500ºC are consistent with the type IV isotherm of mesoporous materials (Figure 5.20a). The calcination process results in the generation of a broad hysteresis loop related to the increment in the number of mesopores. Similarly, Mg-Fe-Zeolite 100ºC, Mg-Fe-Zeolite 500ºC, Zn-Al-Zeolite 100ºC, Zn-Al-Zeolite 500ºC, Zn-Fe-Zeolite 100ºC and Zn-Fe-Zeolite 500ºC follow the type IV model accompanied by the H3 hysteresis loop in the high relative pressure range of 0.48–0.96 (Figure 5.20b,c and d). The surface area, pore volume and pore size values of the calcined samples are found to be higher than those of the uncalcined forms, indicating the improvement of mesoporous structures upon thermal treatment (Table 5.9).

Table 5.9. Basal spacings (d-spacing), surface areas (BET), pore volumes (V_{pore}) and pore radius (r_{pore}) of zeolite, Mg-Al-Zeolite 100ºC, Mg-Al-Zeolite 500ºC, Mg-Fe-Zeolite 100ºC, Mg-Fe-Zeolite 500ºC, Zn-Al-Zeolite 100ºC, Zn-Al-Zeolite 500ºC, Zn-Fe-Zeolite 100ºC and Zn-Fe-Zeolite 500ºC.

Materials	**d-spacing *(nm)***	**BET (m^2g^{-1})**	**V_{pore} (cm^3 g^{-1})**	**r_{pore} (Å)**
Zeolite	-	15.02	0.022	17.9
Mg-Al-Zeolite 100ºC	0.773	33.92	0.003	16.6
Mg-Al-Zeolite 500ºC	0.795	49.33	0.042	16.3
Mg-Fe-Zeolite 100ºC	0.676	26.33	0.016	15.5
Mg-Fe-Zeolite 500ºC	-	37.26	0.059	16.4
Zn-Al-Zeolite 100ºC	0.923	18.49	0.026	15.7
Zn-Al-Zeolite 500ºC	-	37.05	0.073	33.3
Zn-Fe-Zeolite 100ºC	0.936	18.42	0.034	16.6
Zn-Fe-Zeolite 500ºC	-	25.01	0.042	15.6

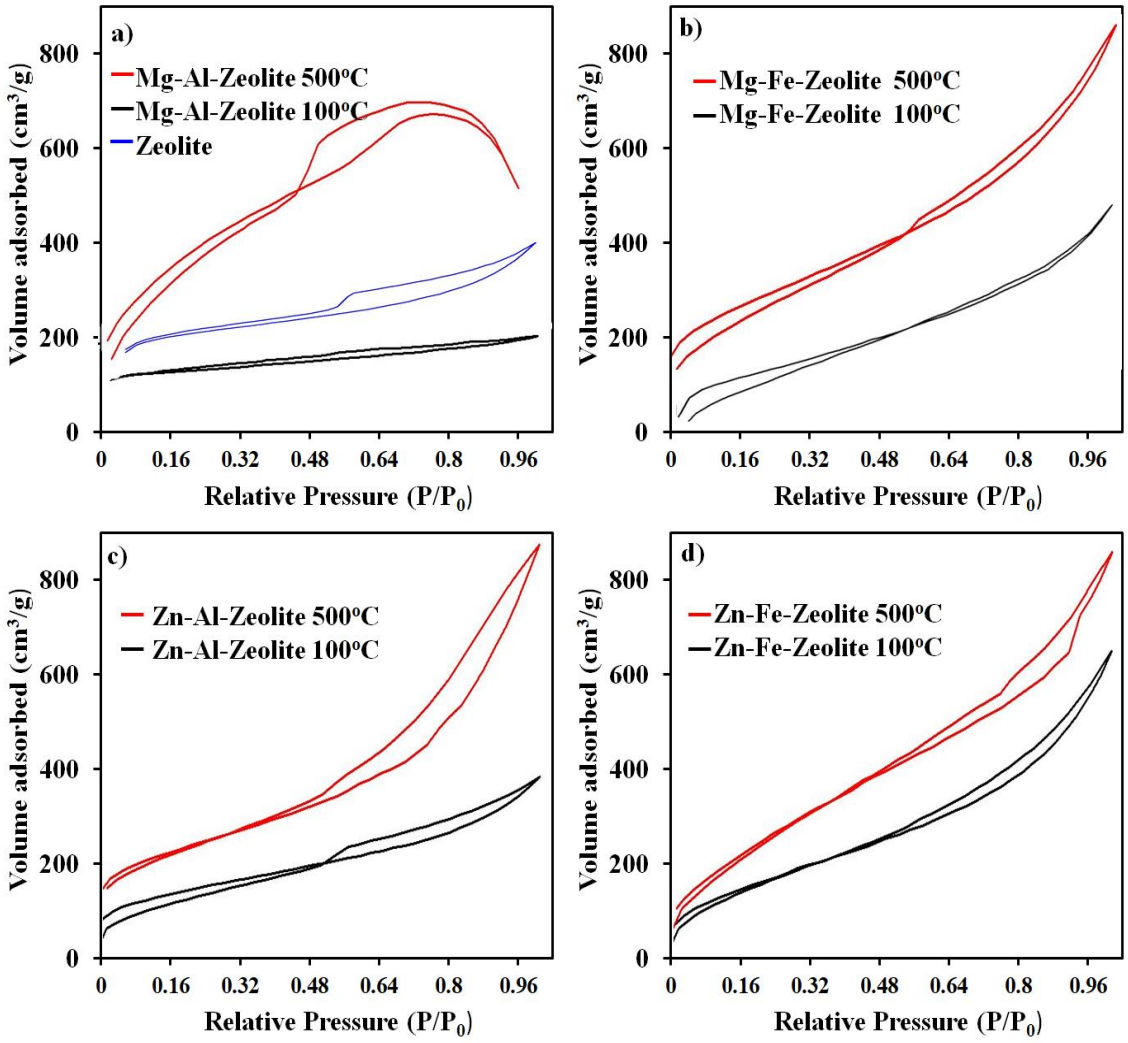

Figure 5.20. Nitrogen adsorption-desorption isotherms of (a) zeolite, Mg-Al-Zeolite 100°C and Mg-Zeolite 500°C, (b) Mg-Fe-Zeolite 100°C and Mg-Fe-Zeolite 500°C, (c) Zn-Al-Zeolite 100°C and Zn-Al-Zeolite 500°C, (d) Zn-Fe-Zeolite 100°C and Zn-Fe-Zeolite 500°C.

5.5.3. SEM-EDX analysis

The morphologies and elemental analysis of the zeolite, Mg-Al-Zeolite 100°C, Mg-Al-Zeolite 500°C, Mg-Fe-Zeolite 100°C, Mg-Fe-Zeolite 500°C, Zn-Al-Zeolite 100°C, Zn-Al-Zeolite 500°C, Zn-Fe-Zeolite 100°C and Zn-Fe-Zeolite 500°C are illustrated in the Figure 5.21. The micrograph of zeolite consists predominantly of plate-like morphology (Figure 5.21a). The main components of zeolite are determined as Si (40.5%), Al (1.4%) and O

(58.0%), being consistent with the previous studies [281]. The Mg-Al-Zeolite 100ºC possesses rock-like particles with lamellar structure and rough surface (Figure 5.21b). The bright spots in the image of Mg-Al-Zeolite 500ºC are attributed to the formation of Al_2O_3 (Figure 5.21d). The Mg/Al ratio of talcite is not calculated for Mg-Al-Zeolite 100ºC and Mg-Al-Zeolite 500ºC due to the presence of Al in both zeolite and talcite composition (Figure 5.21c and e). The decrement of N percentage after calcination indicates the removal of NO_3 groups. The O percentage does not show a significant variation after calcination owing to the formation of Al_2O_3.

Mg-Fe-Zeolite 100ºC reveals clusters on the surface of lamellar rock-like particles (Figure 5.21f). A similar morphology is also observed in the Mg-Fe-Zeolite 500ºC (Figure 5.21h). The molar ratio of Mg/Fe is found as 2.01 in the EDX analysis of Mg-Fe-Zeolite 100ºC which corresponds to the desired ratio of talcite (Figure 5.21g). This ratio is not preserved after calcination owing to the formation of Fe_2O_3 crystallites (Figure 5.21i).

The leaf-like particulates on the talcite surface are observed in the image of Zn-Al-Zeolite 100ºC (Figure 5.21j). After calcination, the bright aggregates distributed on the surface and in the layers of Zn-Al-Zeolite 500ºC are attributed to the ZnO nanoparticles (Figure 5.21l). The existence of Zn in both Zn-Al-Zeolite 100ºC and Zn-Al-Zeolite 500ºC is also verified by the EDX analysis (Figure 5.21k and m). The Zn to Al ratio (Zn/Al) of 2.03 is obtained in Zn-Al-Zeolite 100ºC. This ratio is decreased (1.83) with the formation of ZnO in the matrix after calcination.

The cotton-balls-like particles with different sizes are noticed in the image of Zn-Fe-Zeolite 100ºC and Zn-Fe-Zeolite 500ºC (Figure 5.21n and p). The surface becomes more porous after calcination. The existence of $Zn(OH)_2$ and ZnO nanoparticles is also verified with the detection of Zn signals (Figure 5.21o and r). The decrement in the molar ratio of Zn/Fe from 1.98 (in Zn-Fe-Zeolite 100ºC) to 1.77 (in Zn-Fe-Zeolite 100ºC) indicates the formation of ZnO after calcination.

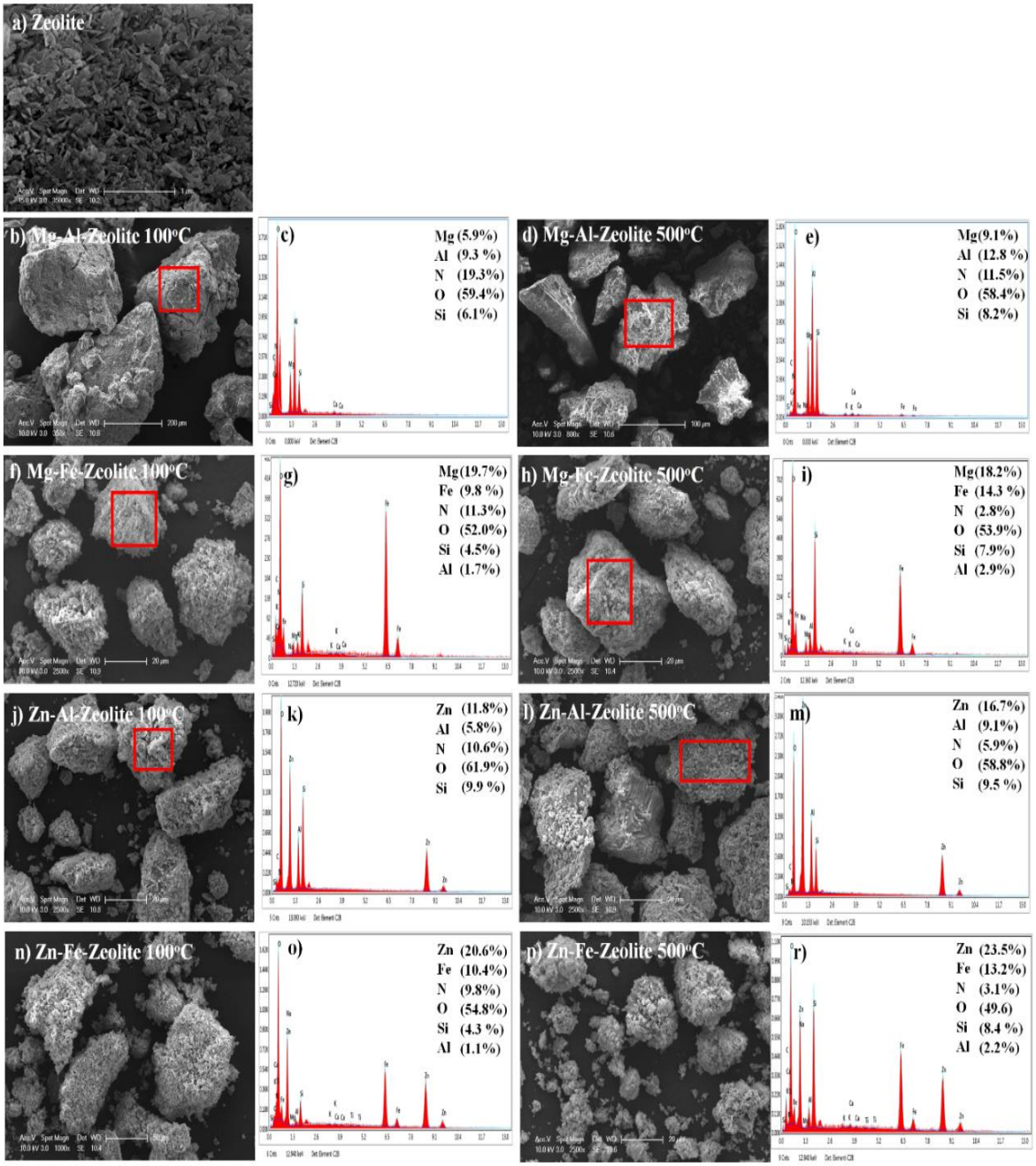

Figure 5.21. SEM images and EDX analysis of (a,b) Mg-Al-Zeolite 100°C (c,d) Mg-Al-Zeolite 500°C, (e,f) Mg-Fe-Zeolite 100°C (g,h) Mg-Fe-Zeolite 500°C, (i,j) Zn-Al-Zeolite 100°C (k,l) Zn-Al-Zeolite 500°C, (m,n) Zn-Fe-Zeolite 100°C (o,p) Zn-Fe-Zeolite 500°C.

5.5.4. UV-vis DRS analysis

Figure 5.22 shows the absorption spectra and band gap energy plots of zeolite, Mg-Al-Zeolite 100^{o}C, Mg-Al-Zeolite 500^{o}C, Mg-Fe-Zeolite 100^{o}C, Mg-Fe-Zeolite 500^{o}C, Zn-Al-Zeolite 100^{o}C, Zn-Al-Zeolite 500^{o}C, Zn-Fe-Zeolite 100^{o}C and Zn-Fe-Zeolite 500^{o}C. Zeolite reveals an extended absorption tail in between 200-600 nm (Figure 5.22a). The specific absorption peak of talcite-like structures is detected at around 300 nm in the spectra of Mg-Al-Zeolite 100^{o}C and Mg-Al-Zeolite 500^{o}C. This absorption peak at the UV region is attributed to the existence of interlayer nitrate anions in the structure. After calcination, the intensity of this peak decreases due to the removal of nitrate groups. The corresponding band gap energies of Mg-Al-Zeolite 100^{o}C and Mg-Al-Zeolite 500^{o}C are calculated as 3.51 eV and 3.62 eV, which is consistent with the values of talcite-like materials (Figure 5.22b).

The spectra of Mg-Fe-Zeolite 100^{o}C and Mg-Fe-Zeolite 500^{o}C exhibit typical Fe_2O_3 absorption edge at around 550-600 nm (Figure 5.22c). The band gap values are determined as 2.12 eV for Mg-Fe-Zeolite 100^{o}C and 2.20 eV for Mg-Fe-Zeolite 500^{o}C (Figure 5.22d). The increment in the crystalline size after calcination implies the crystalline growth of Fe_2O_3 in the matrix.

In the spectrum of Zn-Al-Zeolite 100^{o}C, the small peak of talcite is detected at around 300 nm (Figure 5.22e). This peak disappears after calcination and the characteristic ZnO absorption edge at 390 nm is obtained in the spectrum of Zn-Al-Zeolite 500^{o}C. The band gap energy is found as 3.6 eV for Zn-Al-Zeolite 100^{o}C, being in agreement with the energies of talcite-like materials (Figure 5.22f). For Zn-Al-Zeolite 500^{o}C, the band gap energy is determined as 3.2 eV which is a typical value for ZnO catalyst.

Both Zn-Fe-Zeolite 100^{o}C and Zn-Fe-Zeolite 500^{o}C display characteristic ZnO absorption edge around 390 nm (Figure 5.22h). The increment in the intensity of the peak after calcination indicates the crystallization of ZnO in the Zn-Fe-Zeolite 500^{o}C structure. Band gap energies are determined as 3.17 eV and 3.02 eV for Zn-Fe-Zeolite 100^{o}C and Zn-Fe-Zeolite 500^{o}C, respectively.

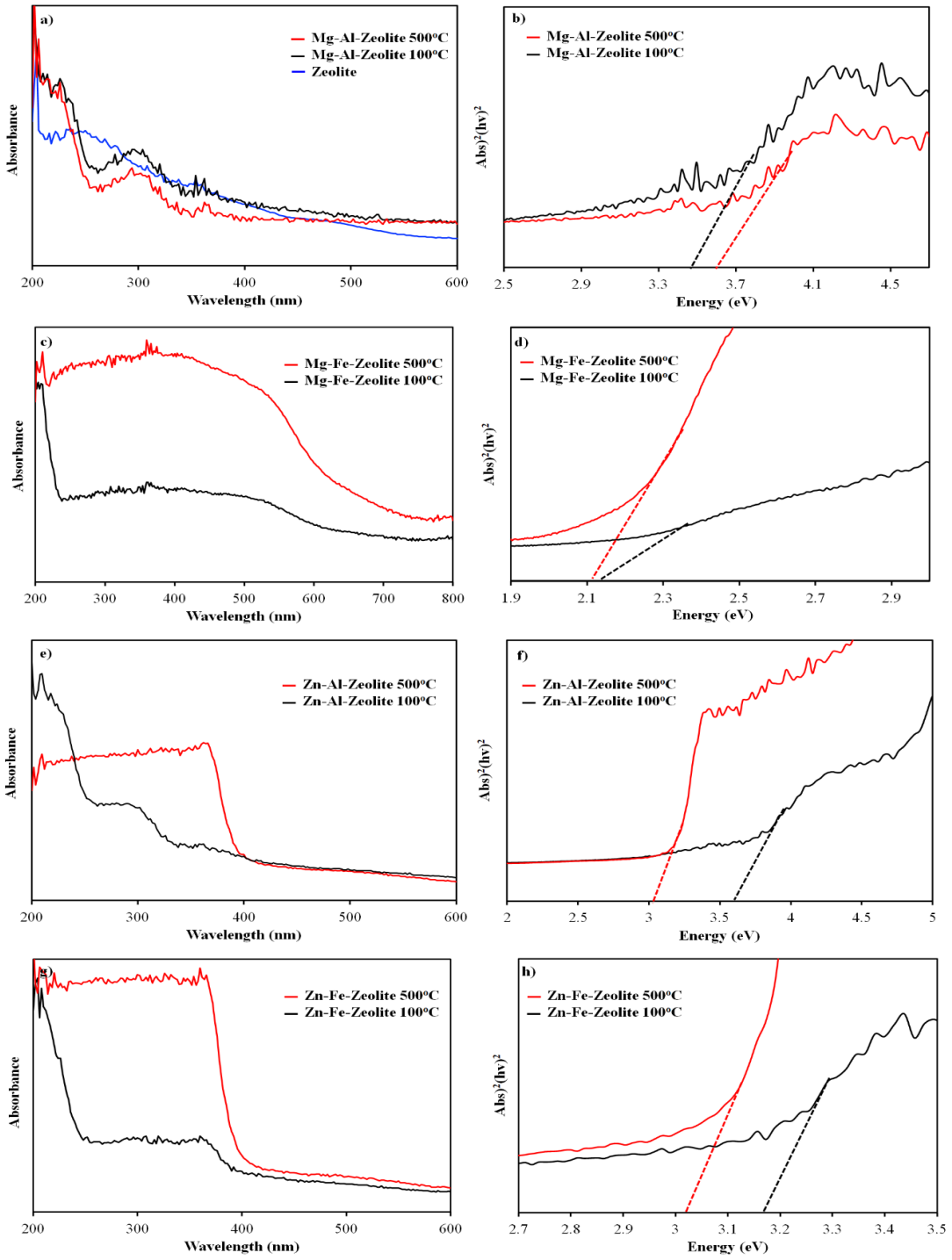

Figure 5.22. UV–vis DRS spectra and band gap absorption plots of (a,b) zeolite, Mg-Al-Zeolite 100°C, Mg-Al-Zeolite 500°C, (c,d) Mg-Fe-Zeolite 100°C, Mg-Fe-Zeolite 500°C, (e,f) Zn-Al-Zeolite 100°C, Zn-Al-Zeolite 500°C, and (g,h) Zn-Fe-Zeolite 100°C, Zn-Fe-Zeolite 500°C.

5.5.5. Adsorption and Photocatalytic Tests

The adsorption properties of Mg-Al-Zeolite 100°C, Mg-Al-Zeolite 500°C, Mg-Fe-Zeolite 100°C, Mg-Fe-Zeolite 500°C, Zn-Al-Zeolite 100°C, Zn-Al-Zeolite 500°C, Zn-Fe-Zeolite 100°C and Zn-Fe-Zeolite 500°C are exhibited in Figure 5.23. In general, the mesoporous structures formed from zeolite and LDH serve as large and strong adsorption sites for the MO, MB and SA molecules.

Mg-Al-Zeolite 100°C and Mg-Al-Zeolite 500°C reveal high adsorption ability toward MO, due to the maintaining talcite and zeolite structures in the matrix (Figure 5.23a). As a desired property of talcite-like structure, the higher interlayer distances of Mg-Al-Zeolite 500°C (0.795 nm) and Mg-Al-Zeolite 100°C (0.773 nm) than the width of MO molecule (0.555 nm) favor the intercalation of MO anions via anion exchange mechanism. Also, the existence of zeolite in the matrix serves Lewis acid sites (Al and Si sites) for the attraction of MO molecules. The relatively faster adsorption ability of Mg-Al-Zeolite 500°C than that of the Mg-Al-Zeolite 100°C toward MO is attributed to the increment in the surface area and porosity and hence, to provide more electrostatic interactions. The remaining percentages of MB are determined as 34% and 20% in the presence of Mg-Al-Zeolite 100°C and Mg-Al-Zeolite 500°C, respectively (Figure 5.23c). The adsorption of MB is found to be lower than that of the MO for both Mg-Al-Zeolite 100°C and Mg-Al-Zeolite 500°C due to the repulsive forces derived from the cations on the layers of talcite structure. For Mg-Al-Zeolite 100°C, the adsorption of MB can be attributed to the electrostatic interactions between the cationic MB and interlayer nitrate anions. Also, the Si-O tetrahedrons in the zeolite structure may contribute to the adsorption of MB by creating negatively charged adsorption sites on the surface of Mg-Al-Zeolite 100°C. The negative charge on the surface increases after calcination by the formation of Al_2O_3 crystallites. Thus, the adsorption of MB is found to be higher in the presence of Mg-Al-Zeolite 500°C compared to Mg-Al-Zeolite 100°C. The residual percentages of SA are found as 32% and 20% for Mg-Al-Zeolite 100°C and Mg-Al-Zeolite 500°C, respectively (Figure 5.23e). The adsorption of SA is driven by the intercalation mechanism owing to the small molecule size of SA (with 0.512 nm width and 0.660 nm length). Mg-Al-Zeolite 500°C adsorbs SA more than Mg-Al-Zeolite 100°C due to the increment in the interlayer spacing after calcination.

In the presence of Mg-Fe-Zeolite 100ºC and Mg-Fe-Zeolite 500ºC, the remaining MO percentages are determined as 29.3% and 43%, respectively (Figure 5.23a). The intercalation of MO molecules into the layers of Mg-Fe-Zeolite 100ºC is expected due to the smaller size of MO (0.555 nm) than the interlayer distance of Mg-Fe-Zeolite 100ºC (0.676 nm). The interlayer distance of Mg-Fe-Zeolite 500ºC cannot be obtained since the lamellar structure is disturbed by the Fe_2O_3 crystalline growth in the matrix. The increased negative charge on the surface of Mg-Fe-Zeolite 500ºC with the existence of Fe_2O_3 induces repulsive forces for anionic MO molecules and leads to the lower adsorption ability of Mg-Fe-Zeolite 500ºC compared to the Mg-Fe-Zeolite 100ºC. The Lewis attractions can be provided by the zeolitic sites of Mg-Fe-Zeolite 100ºC and Mg-Fe-Zeolite 500ºC through azo groups of MO. In contrast to the MO, the adsorption of MB is enhanced with the formation of metal oxides upon thermal treatment. Thus, the residual amount of MB is found to be lower in the presence of Mg-Fe-Zeolite 500ºC (25%) than that of Mg-Fe-Zeolite 100ºC (40%) (Figure 5.23c). The increment in the surface area and porosity after calcination also contributes to the adsorption of MB by providing more active sites for the interactions. SA concentrations in the remaining solutions are found as 33% and 22% in the presence of Mg-Fe-Zeolite 100ºC and Mg-Fe-Zeolite 500ºC, respectively (Figure 5.23e). The intercalation of SA molecules can be achieved due to the smaller particle size of SA than the interlayer space of Mg-Fe-Zeolite 100ºC (0.676 nm). Also, hydrogen bonding can be formed among the Si-O groups of zeolite and hydroxyl groups in SA. The higher surface area and enhanced porous structure of Mg-Fe-Zeolite 500ºC than that of the Mg-Fe-Zeolite 100ºC can be attributed to the higher adsorption of SA. The formation of Fe_2O_3 also improves the adsorption of SA due to the hydrogen bonding between oxygens of Fe_2O_3 and hydroxyl groups of SA.

Adsorption of MO is completed in 80 min in the presence of Zn-Al-Zeolite 100ºC (Figure 5.23a). The high adsorption performance of Zn-Al-Zeolite 100ºC can be attributed to the layered structure and high surface area derived from the existence of both talcite and zeolite structures in the matrix. Besides, hydrogen bonds can be formed between $Zn(OH)_2$ in the Zn-Al-Zeolite 100ºC and sulphonic groups of MO. Lewis interactions among Al^{3+} cations and azo group of MO also enhance the adsorption of MO. Despite the higher surface area of Zn-Al-Zeolite 500ºC than that of Zn-Al-Zeolite 100ºC, the formation of ZnO crystallites dominates the negative charge on the surface and leads to the generation of repulsive forces for MO. Hence, the adsorption of MO is found to be lower for Zn-Al-Zeolite

500ºC compared to Zn-Al-Zeolite 100ºC. MB percentages in the remaining solutions are found as 27% and 21%, in the presence of Zn-Al-Zeolite 100ºC and Zn-Al-Zeolite 500ºC, respectively (Figure 5.23c). The adsorption mechanism of MB on Zn-Al-Zeolite 100ºC is attributed to the electrostatic attractions between the interlayer nitrate anions and cationic MB molecules. Also, Lewis interactions contribute to the adsorption of MB. The formation of ZnO in the structure of Zn-Al-Zeolite 500ºC enhances the adsorption of MB through electrostatic attractions. For SA, the residual amounts are found as 16% and 25% in the presence of Zn-Al-Zeolite 100ºC and Zn-Al-Zeolite 500ºC, respectively (Figure 5.23e). SA molecules can be intercalated into layers of Zn-Al-Zeolite 100ºC by replacing the nitrate anions. Also, the existence of $Zn(OH)_2$ nanoparticles on the surface enable the formation of hydrogen bonding with carboxylic acid and hydroxyl groups of SA. Upon calcination, ZnO crystallites are formed on the surface of Zn-Al-Zeolite 500ºC which leads to repulsive forces between Zn-Al-Zeolite 500ºC and SA molecules. Meanwhile, ZnO crystal growth in the Zn-Al-Zeolite 500ºC contributes to the adsorption of SA via the formation of hydrogen bonds.

The remaining percentages of MO are determined as 25% and 33% for Zn-Fe-Zeolite 100ºC and Zn-Fe-Zeolite 500ºC, respectively (Figure 5.23a). The intercalation of MO can be driven by the anion exchange mechanism among layers of the Zn-Fe-Zeolite 100ºC spacing with 0.916 nm. In addition to the hydrogen bonds formed between $Zn(OH)_2$ and sulphonic groups of MO, Lewis interactions contribute to the adsorption process of MO. The formation of ZnO in the Zn-Fe-Zeolite 500ºC structure leads to the lower adsorption of MO due to the repulsive interactions with increased negative charges on the surface. In the case MB, the residual amounts are found as 20% for Zn-Fe-Zeolite 100ºC and 13 % for Zn-Fe-Zeolite 500ºC (Figure 5.23c). Hydrogen bonds can be formed between the hydroxyl groups of $Zn(OH)_2$ and the nitrogen atoms of MB molecules in the presence of Zn-Fe-Zeolite 100ºC. Also, the Lewis acid sites (Al and Si) can attract the pyridine group of MB. For Zn-Fe-Zeolite 500ºC, MB adsorption is enhanced due to the dominance of negative charge on the surface via the formation of ZnO nanoparticles. This leads to the electrostatic interactions among oxygens of ZnO and positively charged functional groups of MB. The SA percentages in the remaining solutions are found as 23% for Zn-Fe-Zeolite 100ºC and 22% for Zn-Fe-Zeolite 500ºC (Figure 5.23e). The existence of $Zn(OH)_2$ in Zn-Fe-Zeolite 100ºC and ZnO in Zn-Fe-Zeolite 500ºC enables to form of hydrogen bonds with the hydroxyl and carboxylic acid groups of SA and eventually induces SA adsorption.

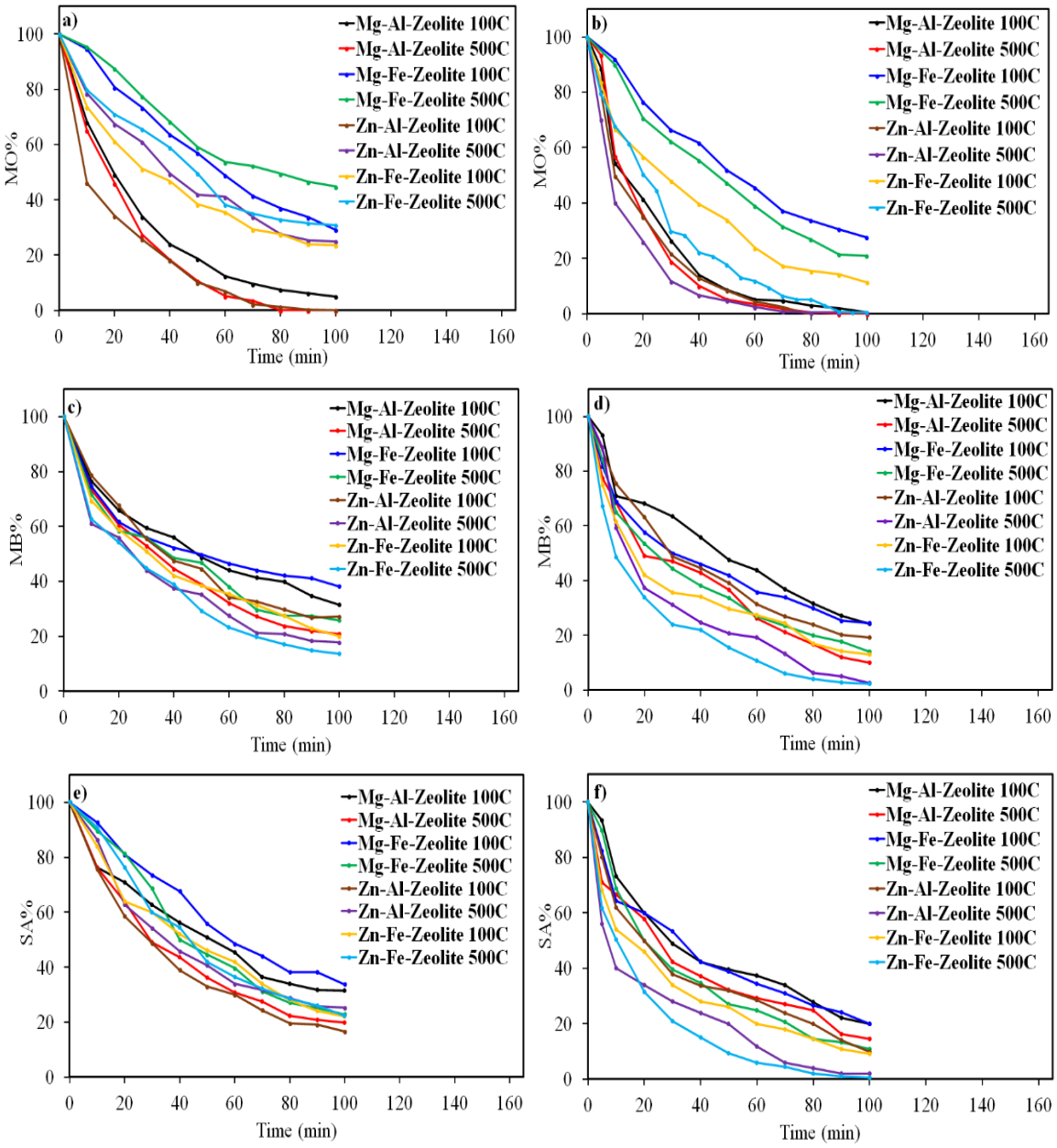

Figure 5.23. Dark adsorption and photocatalytic degradation (a,b) of MO, (c,d) of MB and (e,f) SA in the presence of Mg-Al-Zeolite 100°C, Mg-Al-Zeolite 500°C, Mg-Fe-Zeolite 100°C, Mg-Fe-Zeolite 500°C, Zn-Al-Zeolite 100°C, Zn-Al-Zeolite 500°C, Zn-Fe-Zeolite 100°C and Zn-Fe-Zeolite 500°C.

The photocatalytic performances of the Mg-Al-Zeolite 100°C, Mg-Al-Zeolite 500°C, Mg-Fe- Zeolite 100°C, Mg-Fe-Zeolite 500°C, Zn-Al-Zeolite 100°C, Zn-Al-Zeolite 500°C, Zn-Fe-Zeolite 100°C and Zn-Fe-Zeolite 500°C are examined for the degradation processes of MO, MB and SA (Figure 5.23b,d and f).

In the presence of Mg-Al-Zeolite 100ºC and Mg-Al-Zeolite 500ºC, MO degradation is obtained within 80 min (Figur 5.23b). The high adsorption capacities of these samples enhance their photocatalytic performances. Besides, the photoactivity of Mg-Al-Zeolite 100ºC and Mg-Al-Zeolite 500ºC can be attributed to the talcite-like structure consisting of surface hydroxyl groups and interlayer nitrate anions. The photoexcited electrons can be formed in the oxygens of these groups upon irradiation. The charge carrier separation can be achieved by the migration of photogenerated electrons to 3s or 3p orbitals of Al^{+3} and eventually improves the photocatalytic activities. The residual amounts of MB are found as 24% for Mg-Al-Zeolite 100ºC and 9% for Mg-Al-Zeolite 500ºC (Figure 5.23d). Since repulsive forces between the metal cations among the layers of Mg-Al-Zeolite 100ºC and cationic MB molecules inhibit the adsorption of the MB, its photocatalytic degradation may occur only in the bulk. In the case of Mg-Al-Zeolite 500ºC, photocatalytic degradation of MB is promoted due to the formation of Al_2O_3. The same trend is also observed in the degradation process of SA. The higher photocatalytic performance of Mg-Al-Zeolite 500ºC for SA (14% remaining percentage) than that of the Mg-Al-Zeolite 100ºC (21% remaining percentage) is attributed to the formation of metal oxides upon calcination (Figure 5.23f).

For Mg-Fe-Zeolite 100ºC, the residual amounts of MO, MB and SA are found as 27%, 24% and 21%, respectively (Figure 5.23b,d and f). The photoactivity of Mg-Fe-Zeolite 100ºC is owing to the existence of both talcite structure and Fe_2O_3 nanoparticles. In the case of Mg-Fe-Zeolite 500ºC, MO, MB and SA remaining percentages are determined as 21%, 13% and 12%, respectively (Figure 5.23b,d and f). The higher photoactivity of Mg-Fe-Zeolite 500ºC compared to Mg-Fe-Zeolite 100ºC is attributed to the crystalline growth of Fe_2O_3 upon calcination.

Photocatalytic degradation of MO is completed in 70 min in the presence of both Zn-Al-Zeolite 100ºC and Zn-Al-Zeolite 500ºC (Figure 5.23b). For Zn-Al-Zeolite 100ºC, the remaining percentages of MB and SA are found as 18% and 10%, respectively (Figure 5.23d and f). The high adsorption ability and hence, the photoactivity of Zn-Al-Zeolite 100ºC is induced by the synergy established between talcite structure and $Zn(OH)_2$. For Zn-Al-Zeolite 500ºC, almost complete degradations of MB and SA are noticed in 100 min due to the formation of ZnO crystallites (Figure 5.23d and f).

The remaining percentages of MO, MB and SA are determined as 11%, 12% and 10% for Zn-Fe-Zeolite 100°C (Figure 5.23b,d and f). Similar to Zn-Al-Zeolite 100°C, the photoactivity of Zn-Fe-Zeolite 100°C is attributed to the existence of $Zn(OH)_2$ in the talcite structure. After calcination, the photocatalytic degradation of MO, MB and SA are accomplished in 100 min (Figure 5.23b,d and f). The enhanced photoactivity of Zn-Fe-Zeolite 500°C can be explored by the formation of ZnO crystallites and the existence of Fe content in the matrix.

5.5.6. Dark Adsorption Kinetics and Isotherms

To examine dark adsorption mechanism, pseudo-first order and pseudo-second order models are employed to the samples with the highest adsorption capacities in the dark, namely, Zn-Al-Zeolite 100°C for MO, Zn-Fe-Zeolite 500°C for MB and Zn-Al-Zeolite 100°C for SA. Kinetic parameters and plots demonstrate that pseudo-second order kinetics can better explain the adsorption mechanisms (Table 5.10 and Figure 5.24). This is also supported by the calculated q_e values of the pseudo-second-order model which are closer to the experimental q_e values compared to the calculated qe values of pseudo-first order model.

Table 5.10. Kinetic parameters of Zn-Al-Zeolite 100°C for MO, Zn-Fe-Zeolite 500°C for MB and Zn-Al-Zeolite 100°C for SA adsorption.

		Pseudo-first order $\ln (q_e - q_t) = \ln q_e - k_1 t$			**Pseudo-second order** $\frac{t}{q_t} = (\frac{1}{k_2 q^2_e}) + \frac{t}{q_e}$		
	$q_{e\ (exp)}$	**k_1**	**$q_{e\ (calc)}$**	**R^2**	**k_2**	**$q_{e(calc)}$**	**R^2**
Zn-Al-Zeolite 100°C (MO)	3.18	0.0334	2.21	0.9917	0.534	3.13	0.9993
Zn-Fe-Zeolite 500°C (MB)	3.02	0.0234	1.15	0.9013	0.412	2.87	0.9972
Zn-Al-Zeolite 100°C (SA)	2.51	0.0128	1.38	0.9891	0.377	2.50	0.9965

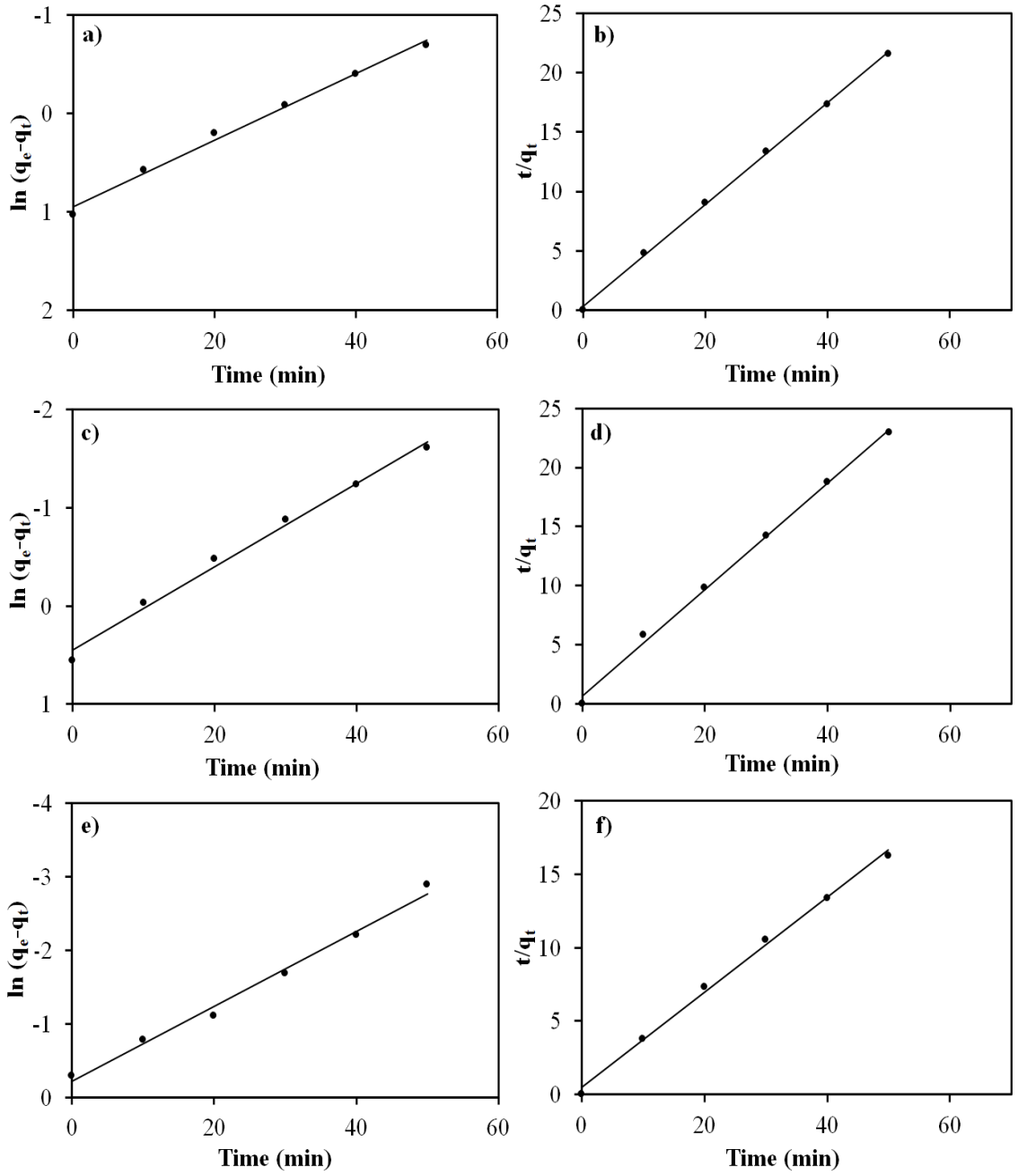

Figure 5.24. Pseudo-first order and pseudo-second order kinetics of (a,b) Zn-Al-Zeolite 100^{o}C for MO, (c,d) Zn-Fe-Zeolite 500^{o}C for MB and (e,f) Zn-Al-Zeolite 100^{o}C for SA adsorption.

The adsorption kinetics of Zn-Al-Zeolite 100^{o}C for MO, Zn-Fe-Zeolite 500^{o}C for MB and Zn-Al-Zeolite 100^{o}C for SA are further explored by Langmuir and Freundlich isotherm models (Figure 5.25). The data fit better to the Langmuir model than Freundlich model in accordance with the correlation coefficients (Table 5.11). Hence, the adsorption of

MO, MB and SA is suggested to proceed as monolayer coverages on Zn-Al-Zeolite 100ºC, Zn-Fe-Zeolite 500ºC and Zn-Al-Zeolite 100ºC surfaces. Zn-Al-Zeolite 100ºC for MO adsorption reveals the highest adsorption capacity (q_L) compared to the Zn-Fe-Zeolite 500ºC for MB and Zn-Al-Zeolite 100ºC for SA adsorption. The conformity of the Langmuir model is supported by the separation factor (R_L) values of Zn-Al-Zeolite 100ºC for MO (0.71), Zn-Fe-Zeolite 500ºC for MB (0.65) and Zn-Al-Zeolite 100ºC for SA (0.62).

Table 5.11. Langmuir and Freundlich isotherm models of Mg-Al 100ºC for MO, Zn-Al 500ºC for MB and Zn-Al 100ºC for SA.

	Langmuir $\frac{C_e}{q_e} = \frac{1}{K_L\, q_L} + \frac{C_e}{q_L}$			**Freundlich** $\ln q_e = \ln K_F + \frac{1}{n} \ln C_e$		
	K_L	**q_L**	**R^2**	**K_F**	**1/n**	**R^2**
Zn-Al-Zeolite 100ºC (MO)	0.489	19.7	0.9995	0.213	0.855	0.9916
Zn-Fe-Zeolite 500ºC (MB)	0.404	16.3	0.9971	0.192	0.842	0.9894
Zn-Al-Zeolite 100ºC (SA)	0.346	9.43	0.9944	0.145	0.753	0.9858

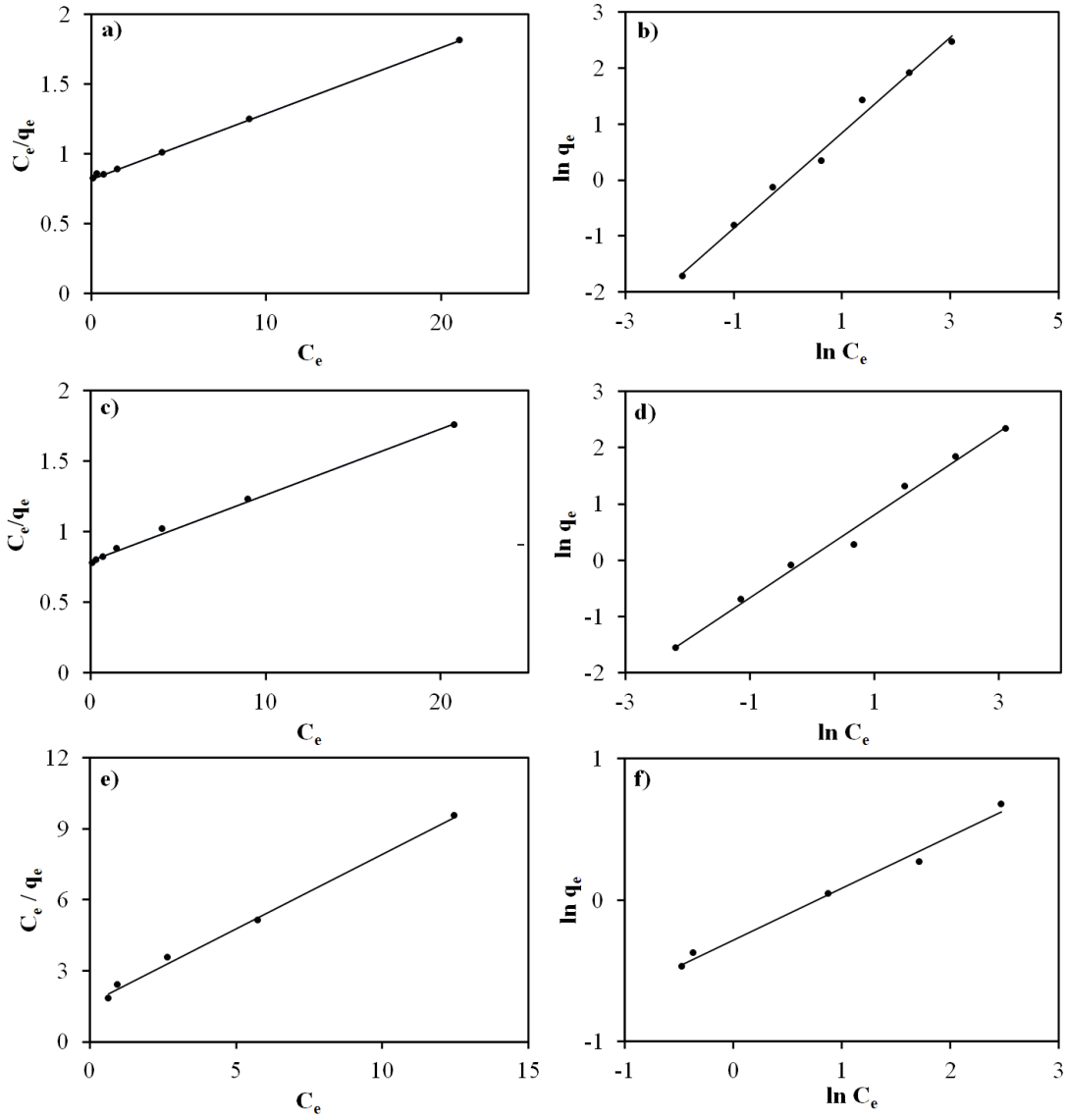

Figure 5.25. Langmuir and Freundlich isotherms of (a,b) Zn-Al-Zeolite 100°C for MO, (c,d) Zn-Fe-Zeolite 500°C for MB and (e,f) Zn-Al-Zeolite 100°C for SA adsorption.

5.5.7. Kinetic Analysis Under Irradiation

For kinetic analysis under irradiation, Zn-Al-Zeolite 500°C, Zn-Fe-Zeolite 500°C and Zn-Fe-Zeolite 500°C are selected as the most photoactive samples for MO, MB and SA degradations, respectively. The effect of initial concentration is investigated in the range of 32.7-0.327 mg L^{-1} for MO, in the range of 31.9-0.319 mg L^{-1} for MB and in the range of 13.8 to 0.138 mg L^{-1} for SA. The linearity of the plots and high correlation coefficients indicate that the photocatalytic processes follow the pseudo-first order kinetics (Figure

A.31). An inverse correlation between the rate constants k (min^{-1}) and initial concentrations of MO, MB and SA is obtained (Table 5.12). This indicates that photocatalytic reactions proceed at a slower rate for the high initial concentrations of MO, MB and SA due to the inhibition of the light access to the active surface sites of Zn-Al-Zeolite 500°C, Zn-Fe-Zeolite 500°C and Zn-Fe-Zeolite 500°C.

Table 5.12. First-order rate constants (k, min^{-1}) and linear regression values (R^2) for different initial concentrations of MO, MB and SA (mg L^{-1}) in the presence of Zn-Al-Zeolite 500°C, Zn-Fe-Zeolite 500°C and Zn-Fe-Zeolite 500°C, respectively.

Zn-Al-Zeolite 500°C			**Zn-Fe-Zeolite 500°C**			**Zn-Fe-Zeolite 500°C**		
$[MO]_0$	**k**	**R^2**	**$[MB]_0$**	**k**	**R^2**	**$[SA]_0$**	**k**	**R^2**
32.7	0.0233	0.9771	**31.9**	0.0223	0.9623	**13.8**	0.0112	0.9678
16.3	0.0241	0.9789	**15.9**	0.0228	0.9755	**6.90**	0.0118	0.9734
8.17	0.0245	0.9882	**7.95**	0.0234	0.9892	**3.45**	0.0123	0.9887
3.27	0.0441	0.9957	**3.19**	0.0379	0.9932	**1.38**	0.0151	0.9909
1.63	0.0502	0.9972	**1.59**	0.0478	0.9954	**0.69**	0.0278	0.9921
0.82	0.0610	0.9980	**0.79**	0.0512	0.9975	**0.35**	0.0283	0.9967
0.33	0.0623	0.9983	**0.31**	0.0563	0.9979	**0.14**	0.0302	0.9974

The Langmuir-Hinshelwood kinetic model is adopted for further analysis of the photocatalytic processes. Plots of rate (R) versus initial concentrations of $[MO]_0$, $[MB]_0$, $[SA]_0$ reach a stationary state at high concentrations, beyond this, the reaction rate becomes independent of MO, MB and SA concentrations, following the zero-order kinetics (Figure 5.26a,c and e). The adsorption coefficients (K) and the rate constants (k) are attained from the linearized plots of reciprocals rates (1/R) versus reciprocal initial concentrations ($(1/[MO]_0)$, $(1/[MB]_0)$, $(1/[SA]_0)$) (Figure 5.26b,e and f). Accordingly, the K values are found to be 0.335 L mg^{-1} for Zn-Al-Zeolite 500°C (MO), 0.313 L mg^{-1} for Zn-Fe-Zeolite 500°C (MB) and 0.307 L mg^{-1} for Zn-Fe-Zeolite 500°C (SA), while k values are determined as 0.430 mg L^{-1} min^{-1} for Zn-Al-Zeolite 500°C (MO), 0.408 mg L^{-1} min^{-1} for Zn-Fe-Zeolite 500°C (MB) and 0.403 mg L^{-1} min^{-1} for Zn-Fe-Zeolite 500°C (SA). The highest value for

rate constant is obtained in the presence of Zn-Al-Zeolite 500ºC for MO degradation, being consistent with the photocatalytic degradations results.

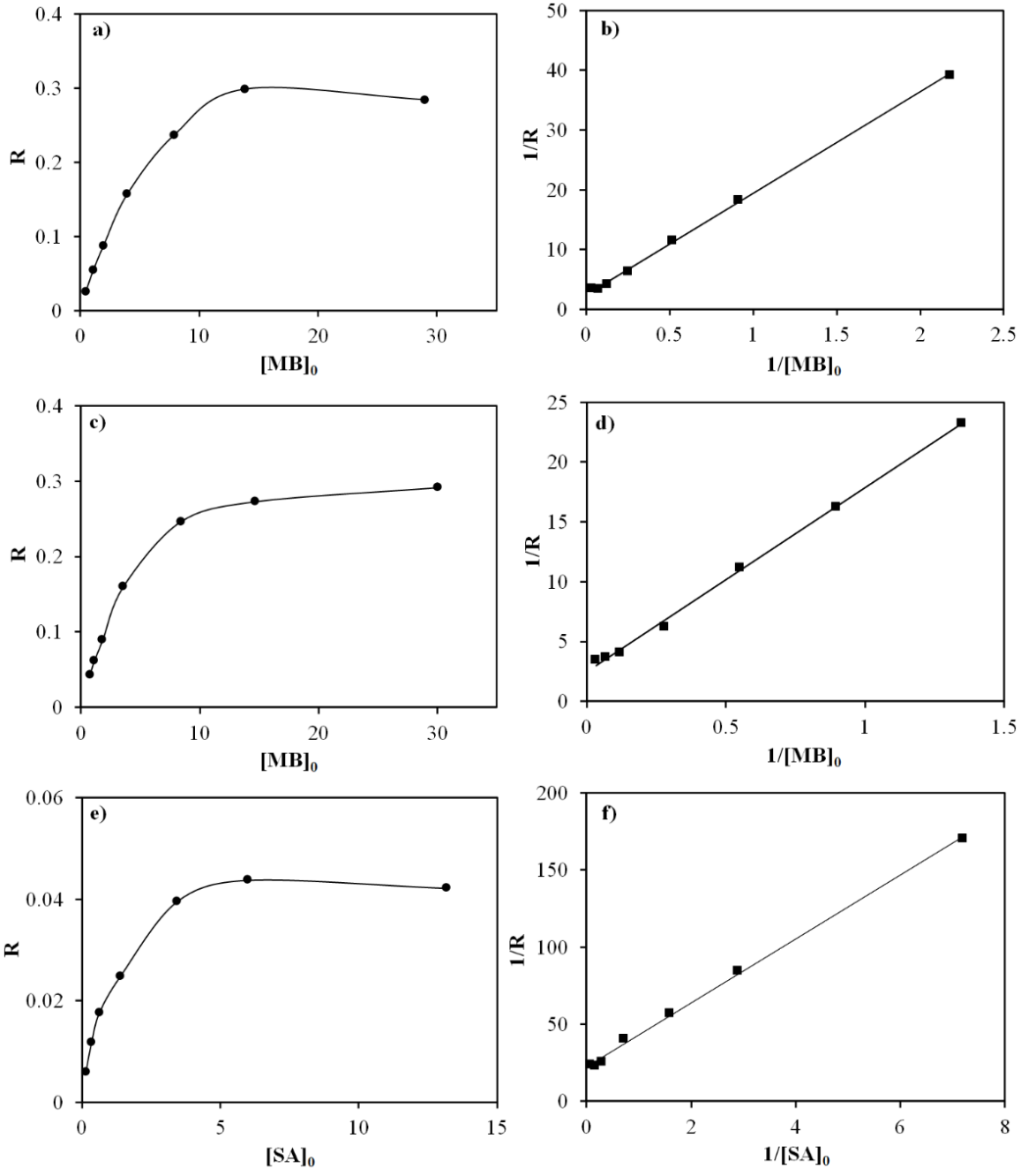

Figure 5.26. Langmuir-Hinshelwood kinetic analysis of (a,b) Zn-Al-Zeolite 500ºC for MO, (c,d) Zn-Fe-Zeolite 500ºC for MB and (e,f) Zn-Fe-Zeolite 500ºC for SA adsorption.

5.6. Results and Discussion of Ternary LDHs and LDOs and ZIF-8 Supported Binary LDHs and LDOs

5.6.1. XRD Analysis

Figure 5.27 shows XRD patterns of Zn-Mg-Al 100ºC, Zn-Mg-Al 500ºC, Zn-Mg-Fe 100ºC, Zn-Mg-Fe 500ºC, ZIF-8, Mg-Al-ZIF-8 100ºC, Mg-Al-ZIF-8 500ºC, Mg-Fe-ZIF-8 100ºC and Mg-Fe-ZIF-8 500ºC. The diffraction peaks of talcite are detected at 11.1º, 23.1º, 34.9º and 62.1º (2θ) in the spectrum of Zn-Mg-Al 100ºC, confirming the successful synthesis of LDH (Figure 5.27a) [282]. After calcination, ZnO crystals are formed with the detection of characteristic peaks at 31.7º, 34.5º, 36.2º and 62.8º (2θ). This leads to a decrement in the intensities of talcite peaks. The patterns of Zn-Mg-Fe 100ºC reveal the $Zn(OH)_2$ and Fe_2O_3 peaks in addition to the talcite reflections (Figure 5.27b). For Zn-Mg-Fe 500ºC, intensities of ZnO and Fe_2O_3 increase and also MgO peak at 42.3º (2θ) is detected. Such observations verify the formation of mixed metal oxides in the matrix.

The ZIF-8 reflections are observed at 7.5º, 10.4º, 12.7º, 18.5º (2θ) with corresponding planes of (011), (002), (112), (222), respectively (Figure 5.27c). These peaks are not detected in the spectra of Mg-Al-ZIF-8 100ºC and Mg-Al-ZIF-8 500ºC. Instead, the characteristic talcite peaks are noticed at 11.2º and 23.3º (2θ) in Mg-Al-ZIF-8 100ºC. Besides, peaks of $Zn(OH)_2$ appear with low intensities. After calcination, the talcite peak is detected only at 11.1º (2θ) and dominant ZnO peaks are generated. In the profile of Mg-Fe-ZIF-8 100ºC, the dominant Fe_2O_3 reflections are observed, in addition to the typical talcite and $Zn(OH)_2$ peaks with lower intensities. For Mg-Fe-ZIF-8 500ºC, the crystallization of ZnO is confirmed by the appearance of 31.6º, 34.4º, 36.4º, 47.2º, 56.1º, 63.6º and 66.0º (2θ) peaks (Figure 5.27d). Accordingly, while intensities of both ZnO and Fe_2O_3 peaks increase, talcite reflections disappear.

The basal spacing values calculated based on the (003) reflections of Zn-Mg-Al 100ºC and Zn-Mg-Al 500ºC are 0.887 nm and 0.767 nm, respectively (Table 5.13). The decrease in the distance between the layers of Zn-Mg-Al 500ºC compared to Zn-Mg-Al 100ºC is attributed to the formation of ZnO nanoparticles and the removal of the interlayer

anions. The d-spacing of Zn-Mg-Fe 100ºC is found to be 0.633 nm. Despite the higher ionic radius of Fe^{3+} (0.065 nm) than that of the Al^{3+} (0.056 nm), the generation of Fe_2O_3 and $Zn(OH)_2$ in the matrix of Zn-Mg-Fe 100ºC leads to a lower basal spacing compared to Zn-Mg-Al 100ºC. The d-spacing value of Zn-Mg-Fe 500ºC cannot be reported due to the disappearance of (003) reflection via the formation of Fe_2O_3 and ZnO. The lower interlayer spacing of Mg-Al-ZIF-8 500ºC (0.793 nm) in comparison to Mg-Al-ZIF-8 100ºC (0.907 nm) is owing to the formation of ZnO crystallites. The basal spacing value is found to be 0.659 nm for Mg-Fe-ZIF-8 100ºC. Similar to Zn-Mg-Fe 500ºC, for Mg-Fe-ZIF-8 500ºC, the basal spacing value is not determined due to the loss of talcite peak. In this respect, LDHs prepared in the presence of ZIF-8 (Mg-Al-ZIF-8 100ºC, Mg-Al-ZIF-8 500ºC, Mg-Fe-ZIF-8 100ºC, Mg-Fe-ZIF-8 500ºC) exhibit higher interlayer spacing values than those of ternary LDHs (Zn-Mg-Al 100ºC, Zn-Mg-Al 500ºC, Zn-Mg-Fe 100ºC and Zn-Mg-Fe 500ºC). The interactions among metal cations of LDH structures and imidazole ligand groups of ZIF-8 may induce such an increment in the d-spacings of the layers.

The ZnO crystalline sizes in Zn-Mg-Al 500ºC, Zn-Mg-Fe 500ºC, Mg-Al-ZIF-8 500ºC and Mg-Fe-ZIF-8 500ºC are evaluated based on (101) diffraction at 36.2° (2θ). For Zn-Mg-Al 500ºC and Zn-Mg-Fe 500ºC, the size of the ZnO crystallites are found as 14.8 nm and 22.7 nm, respectively. For Zn-Mg-Fe 500ºC, ZnO crystalline formation seems to be improved in the existence of Fe ions. Similarly, the crystalline size of ZnO is found to be higher in the structure of Mg-Fe-ZIF-8 500ºC (25.4 nm) than that of Mg-Al-ZIF-8 500ºC (17.2 nm).

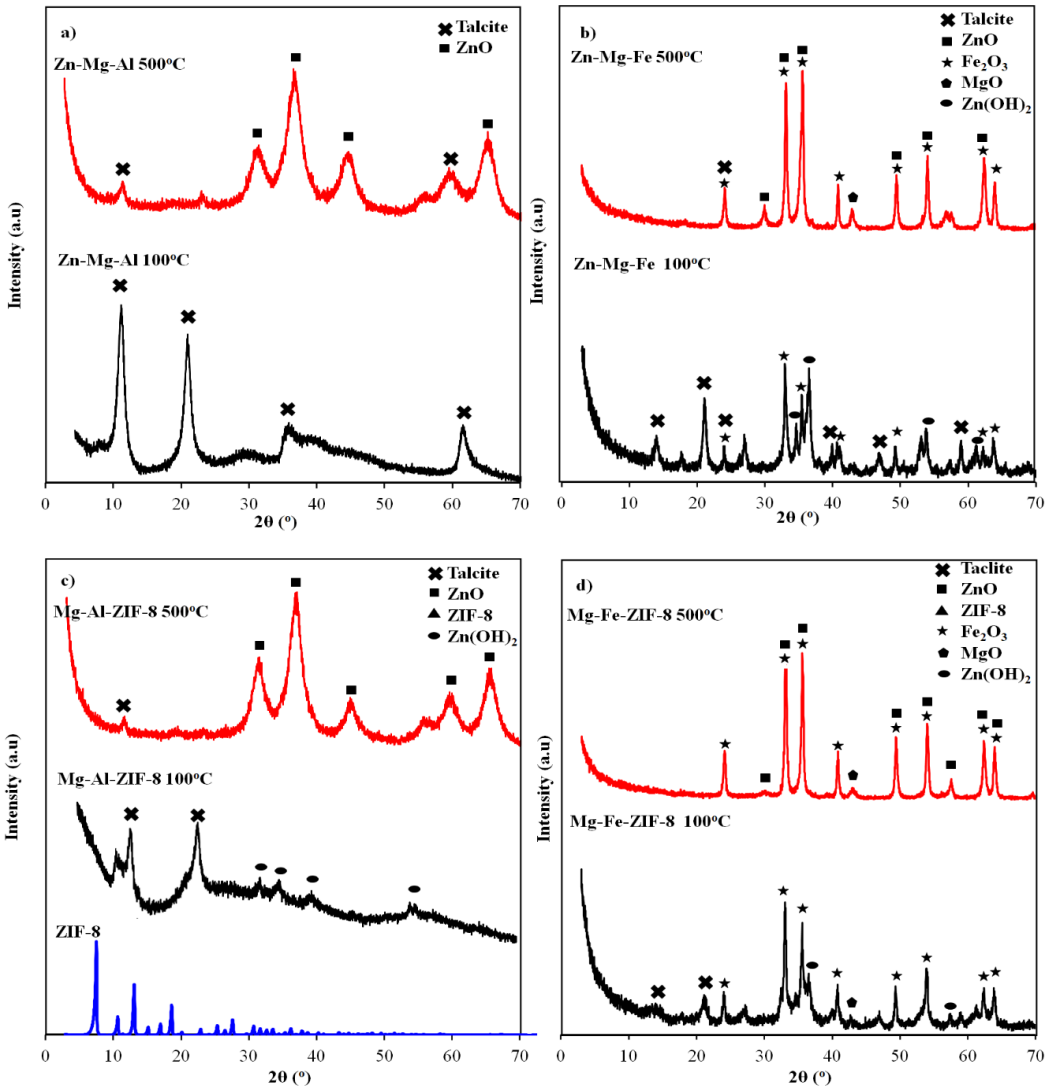

Figure 5. 27. XRD patterns of (a) Zn-Mg-Al 100°C and Zn-Mg-Al 500°C, (b) Zn-Mg-Fe 100°C and Zn-Mg-Fe 500°C, (c) ZIF-8, Mg-Al-ZIF-8 100°C and Mg-Al-ZIF-8 500°C, (d) Mg-Fe-ZIF-8 100°C and Mg-Fe-ZIF-8 500°C.

5.6.2. Nitrogen Adsorption-Desorption Tests

Nitrogen adsorption-desorption isotherms and pore properties of Zn-Mg-Al 100°C, Zn-Mg-Al 500°C, Zn-Mg-Fe 100°C, Zn-Mg-Fe 500°C, ZIF-8, Mg-Al-ZIF-8 100°C, Mg-Al-ZIF-8 500°C, Mg-Fe-ZIF-8 100°C and Mg-Fe-ZIF-8 500°C are presented in Figure 5.28 and Table 5.13. The isotherms of Zn-Mg-Al 100°C and Zn-Mg-Al 500°C are classified as type IV, indicating mesoporous structures (Figure 5.28a). The capillary condensation in the H3 hysteresis loop of Zn-Mg-Al 500°C increases compared to Zn-Mg-Al 100°C due to the

calcination. The isotherms of Zn-Mg-Fe 100ºC and Zn-Mg-Fe 500ºC are consistent with the type IV isotherm of mesoporous materials. Zn-Mg-Fe 100ºC isotherm exhibits H3 hysteresis loop in the relative pressure range of 0.80-0.96 (Figure 5.28b).

The ZIF-8 possesses type I isotherm with a sharp increase in adsorption quantity at low relative pressures ($P/P_0 < 0.08$) due to the existence of intrinsic microporosity. The curves of Mg-Al-ZIF-8 100ºC and Mg-Al-ZIF-8 500ºC fit well with the type IV isotherm. H3 hystereses loop is detected in the isotherm of Mg-Al-ZIF-8 500ºC at the high relative pressure (0.48-0.96) due to the increment of the pores in the structure (Figure 5.28c). The type IV isotherms are also obtained in the case of Mg-Fe-ZIF-8 100ºC and Mg-Fe-ZIF-8 500ºC (Figure 5.28d). An increment in the surface area and pore volume of Zn-Mg-Al 500ºC compared to Zn-Mg-Al 100ºC is attributed to the formation of ZnO nanoparticles. Similarly, the Mg-Al-ZIF-8 500ºC possesses higher surface area and pore volume compared to Mg-Al-ZIF-8 100ºC. Contrarily, Zn-Mg-Fe 500ºC and Mg-Fe-ZIF-8 500ºC reveal lower surface areas and pore volumes than those of Zn-Mg-Fe 100ºC and Mg-Fe-ZIF-8 100ºC due to the destruction of talcite structures after calcination.

Table 5.13. Basal spacings (d-spacing), surface areas (BET), pore volumes (Vpore) and pore radius (r_{pore}) of the Zn-Mg-Al 100ºC, Zn-Mg-Al 500ºC, Zn-Mg-Fe 100ºC, Zn-Mg-Fe 500ºC, ZIF-8, Mg-Al-ZIF-8 100ºC, Mg-Al-ZIF-8 500ºC, Mg-Fe-ZIF-8 100ºC and Mg-Fe-ZIF-8 500ºC.

Materials	**d-spacing (nm)**	**BET (m^2g^{-1})**	**V_{pore} ($cm^3\ g^{-1}$)**	**r_{pore} (Å)**
Zn-Mg-Al 100ºC	0.887	31.44	0.013	15.65
Zn-Mg-Al 500ºC	0.767	61.96	0.128	23.87
Zn-Mg-Fe 100ºC	0.633	42.80	0.050	15.55
Zn-Mg-Fe 500ºC	-	27.97	0.026	15.71
ZIF-8	-	1218	0.011	18.61
Mg-Al-ZIF-8 100ºC	0.907	49.12	0.029	16.39
Mg-Al-ZIF-8 500ºC	0.793	99.58	0.158	19.03
Mg-Fe-ZIF-8 100ºC	0.709	73.62	0.109	15.66
Mg-Fe-ZIF-8 500ºC	-	36.73	0.076	15.68

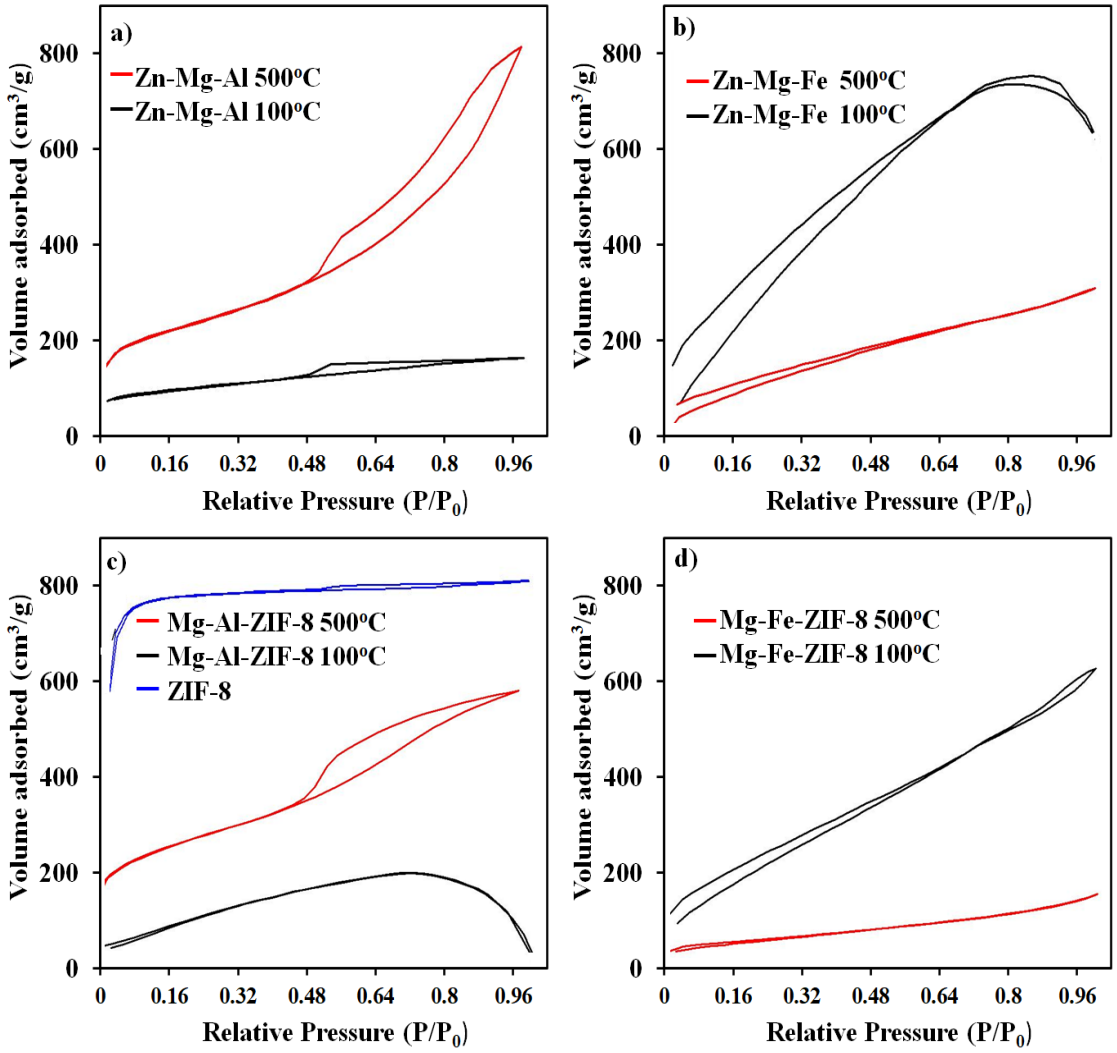

Figure 5.28. Nitrogen adsorption-desorption isotherms of (a) Zn-Mg-Al 100°C and Zn-Mg-Al 500°C, (b) Zn-Mg-Fe 100°C and Zn-Mg-Fe 500°C, (c) ZIF-8, Mg-Al-ZIF-8 100°C and Mg-Al-ZIF-8 500°C, (d) Mg-Fe-ZIF-8 100°C and Mg-Fe-ZIF-8 500°C.

5.6.3. SEM-EDX Analysis

The ZIF-8 exhibits polyhedron facet morphology with Zn (39.7%), C (50.6%) and N (9.7%) (Figure 5.29a). The Zn-Mg-Al 100°C exhibits the layered particles of talcite with different sizes (Figure 3.29b). The EDX analysis confirms the formation of layered structure by (Zn+Mg)/Al ratio as 1.98 for Zn-Mg-Al 100°C (Figure 5.29c). The surface of talcite displays cracks and pores after calcination (Figure 5.29d). The molar ratio of (Zn+Mg)/Al is found as 1.83 for The Zn-Mg-Al 500°C (Figure 5.29e). The lower value compared to the Zn-

Mg-Al 100°C is attributed to the formation of ZnO crystallites. A rough surface on cotton-like particles with different sizes is noticed in the images of Zn-Mg-Fe 100°C and Zn-Mg-Fe 500°C (Figure 5.29f and h). The molar ratio of (Zn+Mg)/Fe is found as 1.3, indicating the poor formation of talcite (Figure 5.29g). The existence of $Zn(OH)_2$ and Fe_2O_3 in the framework may be responsible from this lower ratio. A much lower ratio (1.11) is noticed in the presence of Zn-Mg-Fe 500°C owing to the formation of ZnO. Fe_2O_3 and MgO, detected in the XRD analysis (Figure 5.29i). Moreover, the decrement in the N percentage supports the disturbed talcite structure. The image of Mg-Al-ZIF-8 100°C reveals polyhedron shaped ZIF-8 crystals on and around the talcite layers (Figure 5.29j). The appearance of Zn and C signals is due to the presence of ZIF-8 in the matrix (Figure 5.29k). The molar ratio of (Mg+Zn)/Al is not calculated since ZIF-8 is used as a Zn precursor within the frame. For Mg-Al-ZIF-8 500°C, aggregates with different sizes of pores and cracks are observed (Figure 5.29l). The decrement of the N percentage confirms the distortion of both ZIF-8 and talcite (Figure 5.29m). Meanwhile, increments in the percentages of Zn, Mg and Al indicate the formation of metal oxides after calcination. The Mg-Fe-ZIF-8 100°C possesses cotton-like particles with irregular shapes (Figure 5.29n). The bright agglomerates show the existence of metals on the surface. EDX analysis confirms the existence of Zn, Mg and Fe in the matrix (Figure 5.29o). Mg-Fe-ZIF-8 500°C displays similar morphology (Figure 5.29p). The reduction in the C percentage is attributed to the destruction of ZIF-8 structure after calcination (Figure 5.29r). Moreover, Mg and Fe percentages increase due to the crystalline growth of MgO and Fe_2O_3.

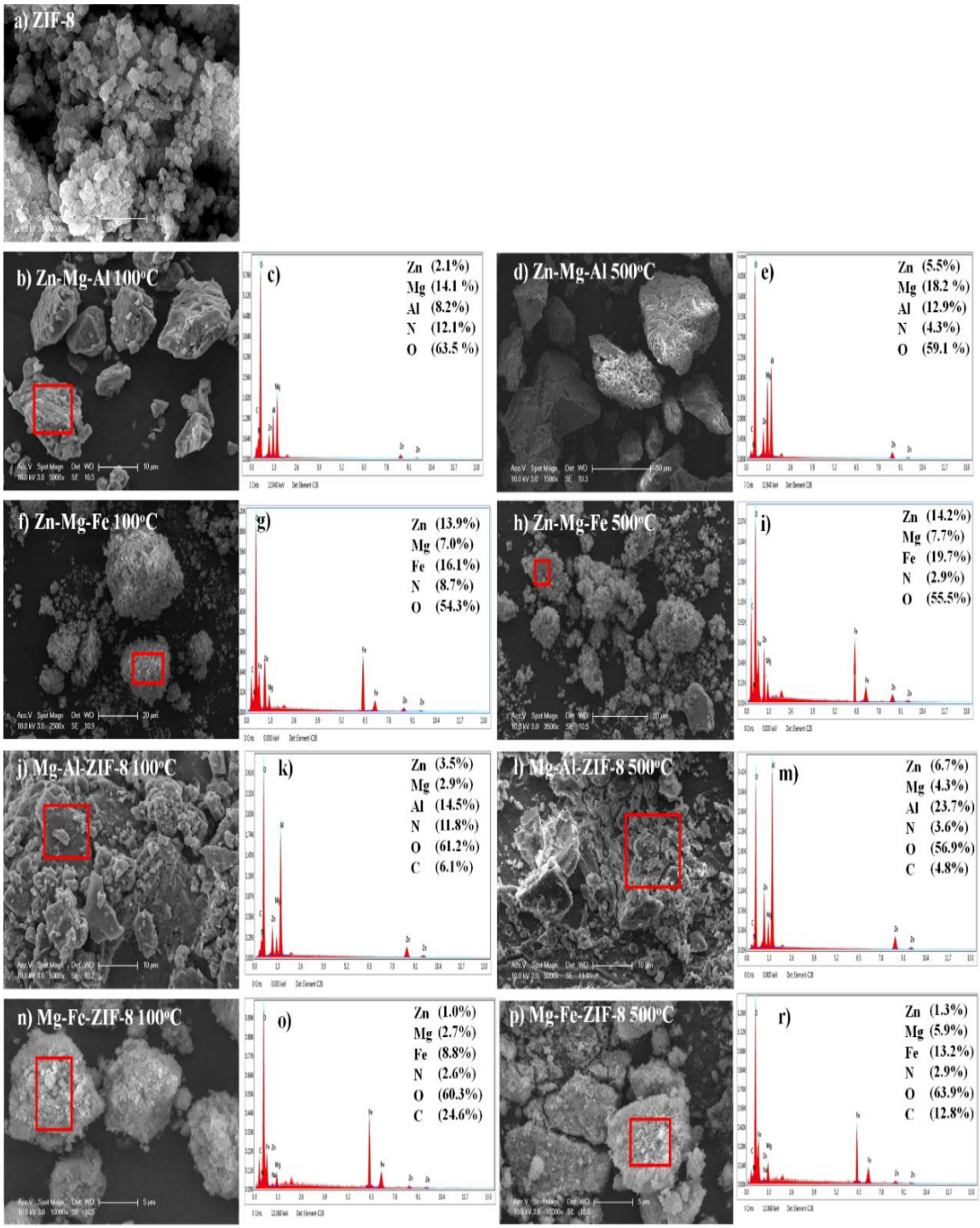

Figure 5.29. SEM images and EDX analysis of (a) ZIF-8, (b,c) Zn-Mg-Al 100°C (d,e) Zn-Mg-Al 500°C, (f,g) Zn-Mg-Fe 100°C (h,i) Zn-Mg-Fe 500°C, (j,k) Mg-Al-ZIF-8 100°C (l,m) Mg-Al-ZIF-8 500°C, (n,o) Mg-Fe-ZIF-8 100°C (p,r) Mg-Fe-ZIF-8 500°C.

5.6.4. UV-Vis DRS Analysis

The optical properties and band gap energy plots of Zn-Mg-Al 100ºC, Zn-Mg-Al 500ºC, Zn-Mg-Fe 100ºC, Zn-Mg-Fe 500ºC, ZIF-8, Mg-Al-ZIF-8 100ºC, Mg-Al-ZIF-8 500ºC, Mg-Fe-ZIF-8 100ºC and Mg-Fe-ZIF-8 500ºC are displayed in Figure 5.30. In the absorption spectrum of Zn-Mg-Al 100ºC, the minor peak detected in the region of 280-320 nm is attributed to the talcite structure's interlayer nitrate anions (Figure 5.30a). For Zn-Mg-Al 500ºC, this peak disappears while ZnO absorption edge is detected at around 390 nm. The corresponding band gap energies of Zn-Mg-Al 100ºC and Zn-Mg-Al 500ºC are calculated as 4.5 eV and 3.01 eV, respectively (Figure 5.30b). Zn-Mg-Fe 100ºC and Zn-Mg-Fe 500ºC display absorption edges at around 550 nm indicating the existence of Fe_2O_3 in the lattice (Figure 5.30c). The sharpness of the edge increases in the profile of Zn-Mg-Fe 500ºC due to the crystal growth of Fe_2O_3 upon calcination. The band gap values are determined as 2.02 eV for Zn-Mg-Fe 100ºC and 2.09 eV for Zn-Mg-Fe 500ºC (Figure 5.30d). The absorption of ZIF-8 at 230 nm is ascribable to the ligand-to-metal charge transfer mechanism in the framework (Figure 5.30e). A weaker absorption detected at 280 nm points out the pyrrolic and pyridine nitrogen atoms in the ligands of ZIF-8. In the spectrum of Mg-Al-ZIF-8 100ºC, both ZIF-8 edge at around 230 nm and talcite peak at around 300 nm are noticed. These two peaks disappear while the characteristic ZnO absorption edge is observed in the profile of Mg-Al-ZIF-8 500ºC, indicating the formation of ZnO crystals. The calculated band gap energies of ZIF-8, Mg-Al-ZIF-8 100ºC and Mg-Al-ZIF-8 500ºC are 4.92 eV, 3.53 eV and 3.02 eV, respectively (Figure 5.30f). In the profiles of Mg-Fe-ZIF-8 100ºC and Mg-Fe-ZIF-8 500ºC, the absorption edge at around 550 nm is ascribed to Fe_2O_3 existence in the matrix (Figure 5.30g). The edge of the absorption becomes sharper in the spectrum of Mg-Fe-ZIF-8 500ºC due to the improvement of the Fe_2O_3 crystallites. The band gap energy decreases from 2.2 eV in Mg-Fe-ZIF-8 100ºC to 2.15 eV in Mg-Fe-ZIF-8 500ºC due to the additional energy levels with the formation of ZnO and Fe_2O_3 after calcination (Figure 5.30h).

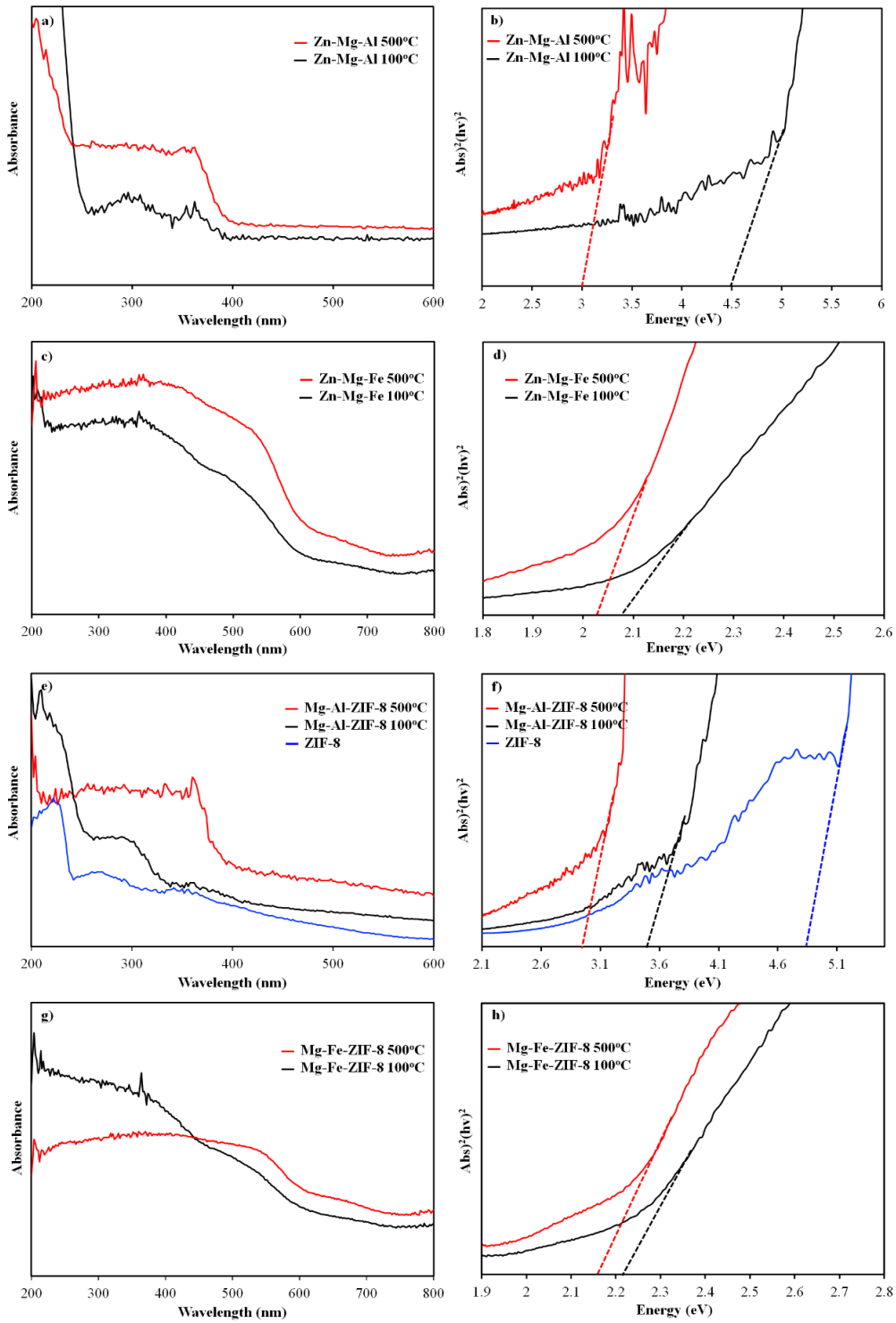

Figure 5.30. UV–vis DRS spectra and band gap absorption plots of (a,b) Zn-Mg-Al 100°C, Zn-Mg-Al 500°C, (c,d) Zn-Mg-Fe 100°C, Zn-Mg-Fe 500°C (e,f) ZIF-8, Mg-Al-ZIF-8 100°C, Mg-Al-ZIF-8 500°C (g,h) Mg-Fe-ZIF-8 100°C and Mg-Fe-ZIF-8 500°C.

5.6.5. Adsorption and Photocatalytic Tests

The dark adsorption performances of the Zn-Mg-Al 100°C, Zn-Mg-Al 500°C, Zn-Mg-Fe 100°C, Zn-Mg-Fe 500°C, ZIF-8, Mg-Al-ZIF-8 100°C, Mg-Al-ZIF-8 500°C, Mg-Fe-ZIF-8 100°C and Mg-Fe-ZIF-8 500°C for MO, MB and SA are displayed in Figure 5.31a,c and e.

In the presence of Zn-Mg-Al 100°C, the residual percentage of MO is detected as 14% at the end of the 100 min (Figure 5.31a). The adsorption process of MO on Zn-Mg-Al 100°C is mediated by ion exchange mechanisms and surface interactions. The interlayer distance in the structure of Zn-Mg-Al 100°C (0.887 nm) ensures the intercalation of MO molecules (0.555 nm width) into the layers via an ion exchange mechanism by replacing nitrate anions. The surface interactions can be established between the negatively charged sulphonic groups oxygens of MO and metal cations in the Zn-Mg-Al 100°C. Moreover, the dipole-π attraction among the benzene rings of MO and metal cations contributes the adsorption of MO. In the case of Zn-Mg-Al 500°C, the remaining MO percentage is found as 31%. The adsorption process of MO on Zn-Mg-Al 500°C can be driven by the surface interactions such as dipole-dipole attractions and dipole-π attractions. The high surface area and porosity of Zn-Mg-Al 500°C support these interactions. However, the adsorption capability of Zn-Mg-Al 500°C is found to be lower than that of the Zn-Mg-Al 100°C due to the distortion of the talcite and formation of ZnO crystallites. The remaining MB percentages are found as 65% and 40% for Zn-Mg-Al 100°C and Zn-Mg-Al 500°C, respectively (Figure 5.31c). MB molecules can interact with the interlayer nitrate anions through electrostatic forces. Also, metal cations form dipole-π interactions with the benzene rings in MB. On the other hand, surface adsorption is prohibited by the repulsive forces between metal cations on the layers of Zn-Mg-Al 100°C and cationic MB molecules. Since Zn-Mg-Al 500°C surface is negatively charged due to the generation of metal oxides, MB adsorption is viable through the C-S+=C group of MB. The percentages of SA in the remaining solutions are determined as 31% and 38%, respectively (Figure 5.31e). Adsorption of SA on Zn-Mg-Al 100°C can be achieved by intercalation process and also surface adsorption. SA molecules can be intercalated into the Zn-Mg-Al 100°C due to their smaller molecule sizes than the interlayer space of Zn-Mg-Al 100°C. Also, surface interactions can be formed between cationic metal ions on the surface of Zn-Mg-Al 100°C and the carboxyl group of SA, as well

as the dipole-π attractions. In the presence of Zn-Mg-Al 500ºC, surface adsorption can be achieved via hydrogen bonding among oxygens of ZnO nanoparticles and the hydroxyl groups of SA.

In the existence of Zn-Mg-Fe 100ºC and Zn-Mg-Fe 500ºC, the residual amounts of MO are found as 42% and 58%, respectively (Figure 5.31a). The appropriate interlayer distance of Zn-Mg-Fe 100ºC (0.633 nm) allows the anion exchange reaction between the intercalated nitrate anions and MO molecules. However, the existence of Fe_2O_3 and $Zn(OH)_2$ crystallites in the matrix induces the repulsive forces for MO molecules. On the surface of Zn-Mg-Fe 500ºC, the increment in the crystal growth of mixed metal oxides (Fe_2O_3, ZnO and MgO) leads to the lower adsorption of MO compared to Zn-Mg-Fe 100ºC. The intercalation process is not suggested for MO adsorption due to the distortion of the lamellar structure of Zn-Mg-Fe 500ºC upon thermal treatment. The remaining MB percentages are found as 54% for Zn-Mg-Fe 100ºC and 34% for Zn-Mg-Fe 500ºC (Figure 5.31c). Despite the existence of metal cations on the surface, the formation of Fe_2O_3 and $Zn(OH)_2$ induces electrostatic interactions with MB molecules. Also, hydrogen bonding can be formed between the hydroxy group of $Zn(OH)_2$ and nitrogen atoms in MB. The ZnO crystal growth in the structure of Zn-Mg-Fe 500ºC promotes the adsorption of MB through dipole-dipole interactions. The residual amounts of SA are found as 36% and 22%, in the presence of Zn-Mg-Fe 100ºC and Zn-Mg-Fe 500ºC, respectively (Figure 5.31e). The possibility of intercalation of SA molecules into the interlayer space of Zn-Mg-Fe 100ºC and also hydrogen bond formation (among the hydroxyl group of SA and $Zn(OH)_2$) promote adsorption of SA. The formation of ZnO in the Zn-Mg-Fe 500ºC matrix enhances the hydrogen bonding and leads to the higher adsorption capability of Zn-Mg-Fe 500ºC than that of the Zn-Mg-Fe 100ºC for SA.

The remaining percentages of MO in the presence of Mg-Al-ZIF-8 100ºC and Mg-Al-ZIF-8 500ºC are found as 8% and 20%, respectively (Figure 5.31a). The high adsorption ability of Mg-Al-ZIF-8 100ºC and Mg-Al-ZIF-8 500ºC than that of the ZIF-8 (34% remaining MO) is attributed to the combination of desired features of LDH and ZIF-8 structures. The interlayer distances of Mg-Al-ZIF-8 100ºC (0.907 nm) and Mg-Al-ZIF-8 500ºC (0.793 nm) are conducive for intercalation of MO molecules (with the 0.555 nm width) via anion exchange mechanism. The Mg^{2+} and Al^{3+} metal cations on the layers of

Mg-Al-ZIF-8 100°C and Mg-Al-ZIF-8 500°C are electrostatically attracted to the negatively charged sulphonic groups of MO. Moreover, the cationic metal center of ZIF-8 serves as a positively charged surface to promote the adsorption of anionic MO. However, the formation of ZnO crystallites upon calcination leads to the increment of negative charge on the surface of Mg-Al-ZIF-8 500°C, and reduces the adsorption of MO. The MB percentages are found as 54% for Mg-Al-ZIF-8 100°C and 27% for Mg-Al-ZIF-8 500°C (Figure 5.31c). The dominant positive charge on the Mg-Al-ZIF-8 100°C structure limits the adsorption of MB. On the other hand, Mg-Al-ZIF-8 100°C exhibit higher adsorption ability than that of ZIF-8 toward MB, due to the electrostatic attractions between the intercalated anions in the Mg-Al-ZIF-8 100°C structure and MB molecules. Also, dipole-π interactions among cationic metals on the layers of Mg-Al-ZIF-8 100°C and the benzene rings of MB can be suggested for the adsorption of MB. The higher adsorption ability of Mg-Al-ZIF-8 500°C than that of the Mg-Al-ZIF-8 100°C is attributed to the formation of ZnO nanoparticles in the matrix. The SA percentage in the remaining solution is found as 28% in the presence of Mg-Al-ZIF-8 100°C and as 18% in the presence of Mg-Al-ZIF-8 500°C (Figure 5.31e). The small size of SA favors the intercalation of SA molecules in Mg-Al-ZIF-8 100°C and Mg-Al-ZIF-8 500°C structures. Moreover, hydrogen bonds can be formed between the nitrogen atoms in ZIF-8 and the phenolic hydroxyl and/or carboxyl groups of SA. The formation of ZnO crystals in the Mg-Al-ZIF-8 500°C structure also improves the adsorption of SA.

The adsorption abilities of Mg-Fe-ZIF-8 100°C (14% remaining MO percentage) and Mg-Fe-ZIF-8 500°C (27% remaining MO percentage) are found to be higher than that of ZIF-8 (Figure 5.31a). The high adsorption capacity of Mg-Fe-ZIF-8 100°C is attributed to the high surface area and porosity which provide more spaces for electrostatic attractions such as dipole-dipole and dipole-π interactions. The relatively lower MO adsorption on Mg-Fe-ZIF-8 500°C compared to Mg-Fe-ZIF-8 100°C may stem from the existence of the mixed metal oxides (Fe_2O_3, ZnO and MgO) in the Mg-Fe-ZIF-8 500°C structure. The residual percentage of MB is found as 48% for Mg-Fe-ZIF-8 100°C and 29% for Mg-Fe-ZIF-8 500°C (Figure 5.31c). Despite the dominant positive charge on the surface of Mg-Fe-ZIF-8 100°C, the adsorption of MB is found to be higher in the presence of Mg-Fe-ZIF-8 100°C and Mg-Fe-ZIF-8 500°C in comparison to ZIF-8 (73% remaining MB percentage). The adsorption process of MB by Mg-Fe-ZIF-8 100°C is mainly driven by the electrostatic attractions of MB molecules toward interlayer nitrate anions, Fe_2O_3 and $Zn(OH)_2$. After calcination, the

formation of mixed metal oxide crystallites leads to the relatively higher adsorption of MB in Mg-Fe-ZIF-8 500ºC. The remaining SA percentages are determined as 20% and 12% by Mg-Fe-ZIF-8 100ºC and Mg-Fe-ZIF-8 500ºC, respectively (Figure 5.31e). In addition to the dipole-dipole and dipole-π interactions, hydrogen bonding contributes the adsorption of SA.

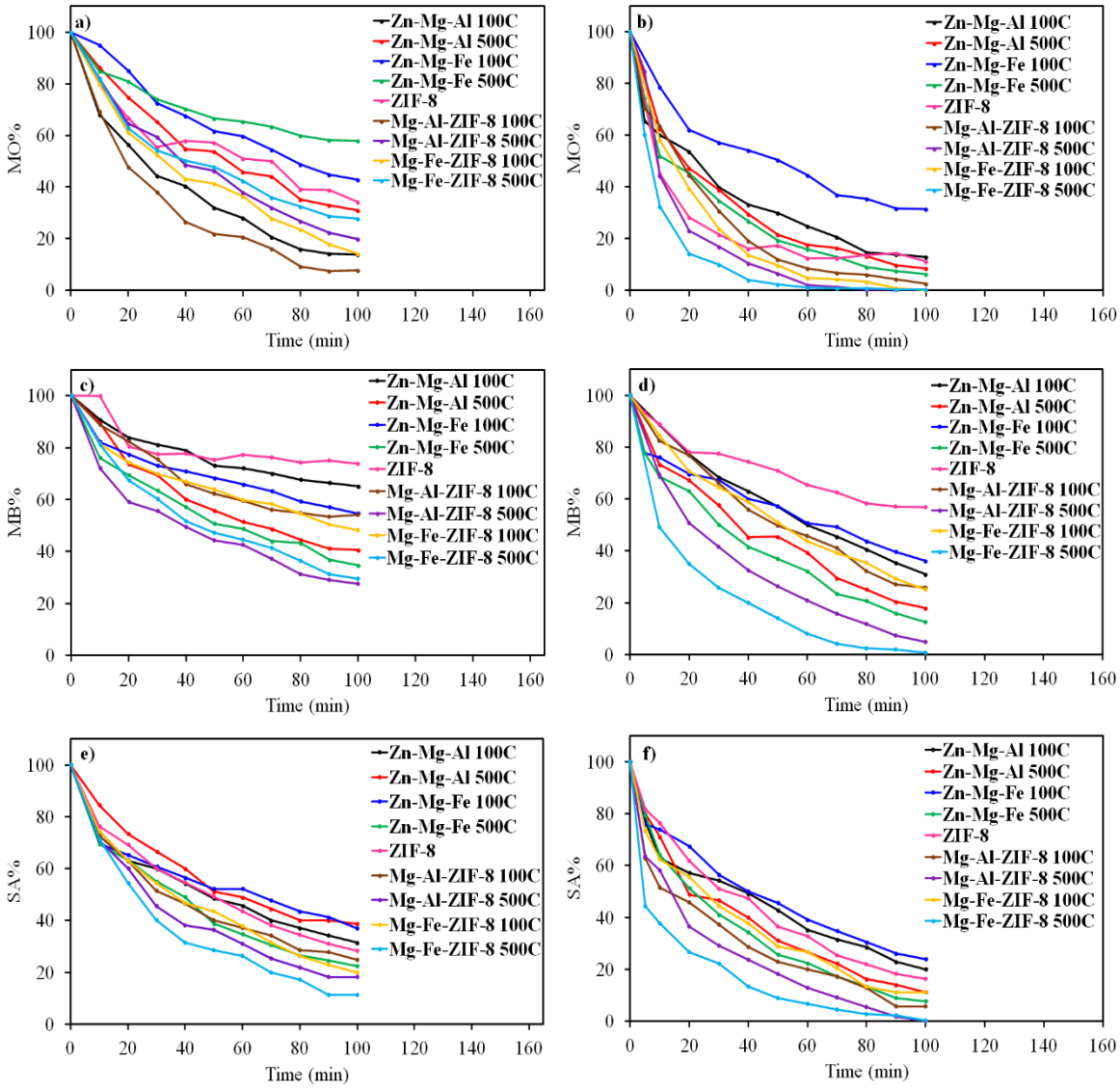

Figure 5.31. Dark adsorption and photocatalytic degradation (a,b) of MO, (c,d) of MB and (e,f) SA in the presence of Zn-Mg-Al 100ºC, Zn-Mg-Al 500ºC, Zn-Mg-Fe 100ºC, Zn-Mg-Fe 500ºC, ZIF-8, Mg-Al-ZIF-8 100ºC, Mg-Al-ZIF-8 500ºC, Mg-Fe-ZIF-8 100ºC and Mg-Al-ZIF-8 500ºC.

As a concluding remark, ZIF-8 supported LDH materials exhibit higher adsorption performances than the ternary metal-included LDH materials in the presence of all model

compounds MO, MB and SA as a result of the synergy between LDH and ZIF-8 structures. Briefly, the adsorption performances of materials are as follows: Mg-Al-ZIF-8 100ºC > Zn-Mg-Al 100ºC, Mg-Al-ZIF-8 500ºC > Zn-Mg-Al 100ºC, Mg-Fe-ZIF-8 100ºC > Zn-Mg-Fe 100ºC, Mg-Fe-ZIF-8 500ºC > Zn-Mg-Fe 500ºC.

Figure 5.31b,d and f show the photoactivities of the Zn-Mg-Al 100ºC, Zn-Mg-Al 500ºC, Zn-Mg-Fe 100ºC, Zn-Mg-Fe 500ºC, ZIF-8, Mg-Al-ZIF-8 100ºC, Mg-Al-ZIF-8 500ºC, Mg-Fe-ZIF-8 100ºC and Mg-Fe-ZIF-8 500ºC for MO, MB and SA.

After 100 min irradiation, the remaining concentration of MO, MB and SA are found as 13%, 30% and 20%, respectively in the presence of Zn-Mg-Al 100ºC (Figure 5.31b,d and f). The photoactivity of Zn-Mg-Al 100ºC is derived from the delocalized electrons in the metal deflections of the talcite structure. For Zn-Mg-Al 500ºC, the residual amounts are found as 8% for MO, 17% for MB and 11% for SA. The higher photoactivity of Zn-Mg-Al 500ºC than that of the Zn-Mg-Al 100ºC is attributed to the formation of ZnO crystallites in the structure. The band gap energy decreases upon formationof ZnO in the matrix, thus the photoexcitation of electrons in valence band is enhanced. In the presence of Zn-Mg-Fe 100ºC, the remaining percentages of MO, MB and SA are determined as 30%, 36% and 23%, respectively (Figure 5.31b,d and f). The existence of Fe_2O_3 leads to generation of electron-hole pairs and photoactivity of Zn-Mg-Fe 100ºC. The photocatalytic performance of Zn-Mg-Fe 500ºC results in 9%, 20% and 7% remaining percentages of MO, MB and SA, respectively. The higher performance of Zn-Mg-Fe 500ºC compared to Zn-Mg-Fe 100ºC can be ascribed to the growth of ZnO and Fe_2O_3 crystals upon calcination. Formation of Fe_2O_3 nanoparticles in Zn-Mg-Fe 500ºC may retard the electron-hole recombination, utilize these charge carriers effectively and hence, improve the photoactivity relative to that of the Zn-Mg-Al 500ºC.

The activity of ZIF-8 UV illumination is deduced to the ligand-to-metal charge transfer process. In the existence of Mg-Al-ZIF-8 100ºC, MO and SA degradations are completed in 100 min and the percentage of MB is found as 35% in the remaining solution (Figure 5.31b,d and f). Meanwhile, the photocatalytic degradations of MO, MB and SA are accomplished in the presence of Mg-Al-ZIF-8 500ºC. A similar trend is also observed in the case of Mg-Fe-ZIF-8 100ºC and Mg-Fe-ZIF-8 500ºC. For Mg-Fe-ZIF-8 100ºC, the

remaining MO, MB and SA are found as 0%, 33% and 11%, respectively. Meanwhile, MB and SA are completely degraded in the presence of Mg-Fe-ZIF-8 500ºC. The higher performances of calcined samples (Mg-Fe-ZIF-8 500ºC and Mg-Al-ZIF-8 500ºC) compared to the uncalcined forms (Mg-Fe-ZIF-8 100ºC and Mg-Al-ZIF-8 100ºC) is attributed to the formation of ZnO nanoparticles. Simultaneous generation of ZnO and Fe_2O_3 nanoparticles in Mg-Fe-ZIF-8 500ºC increases its photocatalytic performance compared to Mg-Al-ZIF-8 500ºC. Besides, ZIF-8 supported LDHs prepared at 100ºC show much better photoactivities than the ternary LDHs owing to the ligand-to-metal charge transfer mechanism of ZIF-8.

5.6.6. Dark Adsorption Kinetics and Isotherms

Mg-Al-ZIF-8 100ºC, Mg-Fe-ZIF-8 500ºC and Mg-Fe-ZIF-8 500ºC show the highest dark adsorption capacities for MO, MB and SA, respectively. Thus, pseudo-first order and pseudo-second order models are applied to analyze these samples. According to linearized plots and the corresponding correlation coefficients, proposed adsorptions are mainly governed by the chemisorption, following pseudo-second order model (Table 5.14, Figure 5.32). Moreover, the experimental q_e values (q_e (exp)) are found to be closer to the calculated q_e values (q_e (calc)) of the pseudo-second order model.

Table 5.14. Kinetic parameters of Mg-Al-ZIF-8 100ºC for MO, Mg-Fe-ZIF-8 500ºC for MB and Mg-Fe-ZIF-8 500ºC for SA adsorption.

		Pseudo-first order $\ln(q_e - q_t) = \ln q_e - k_1 t$			**Pseudo-second order** $\frac{t}{q_t} = \left(\frac{1}{k_2 q^2_e}\right) + \frac{t}{q_e}$		
	$q_{e\ (exp)}$	**k_1**	**$q_{e\ (calc)}$**	**R^2**	**k_2**	**$q_{e(calc)}$**	**R^2**
Mg-Al-ZIF-8 100ºC (MO)	2.84	0.0316	2.33	0.9916	0.453	2.82	0.9995
Mg-Fe-ZIF-8 500ºC (MB)	2.73	0.0201	2.21	0.9912	0.390	2.67	0.9974
Mg-Fe-ZIF-8 500ºC (SA)	2.52	0.0133	2.04	0.9909	0.382	2.54	0.9968

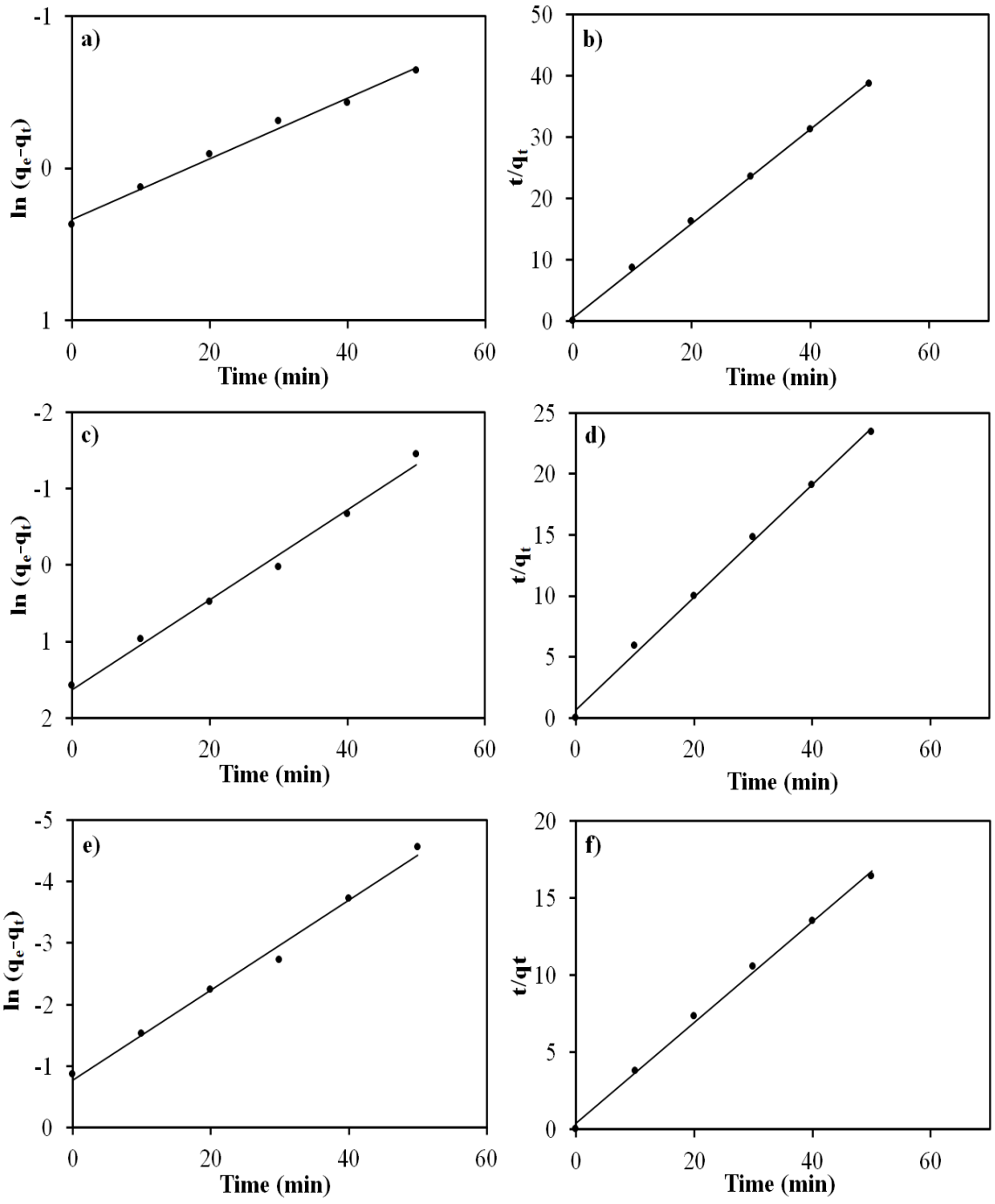

Figure 5.32. Pseudo-first order and pseudo-second order kinetics of (a,b) Mg-Al-ZIF-8 100ºC for MO (c,d) Mg-Fe-ZIF-8 500ºC for MB and (e,f) Mg-Fe-ZIF-8 500ºC for SA adsorption.

The adsorption kinetics of Mg-Al-ZIF-8 100ºC for MO, Mg-Fe-ZIF-8 500ºC for MB and Mg-Fe-ZIF-8 500ºC for SA are also evaluated based on the Langmuir and Freundlich

isotherms models. The plots and the corresponding fitting parameters demonstrate that the Langmuir model is more appropriate than the Freundlich model according to its higher R^2 values (Table 5.15, Figure 5.33). Hence, MO, MB and SA are assumed to be adsorbed on Mg-Al-ZIF-8 100ºC, Mg-Fe-ZIF-8 500ºC and Mg-Fe-ZIF-8 500ºC as monolayer coverage, respectively. Besides, the highest adsorption capacity (q_L) noticed in the presence of Mg-Al-ZIF-8 100ºC for MO adsorption is found to be consistent with the dark adsorption results. The separation factor (R_L) values of Mg-Al-ZIF-8 100ºC for MO (0.65), Mg-Fe-ZIF-8 500ºC for MB (0.59) and Mg-Fe-ZIF-8 500ºC for SA (0.55) verify that the suitability of the Langmuir model.

Table 5.15. Langmuir and Freundlich isotherm models of Mg-Al-ZIF-8 100ºC for MO, Mg-Fe-ZIF-8 500ºC for MB and Mg-Fe-ZIF-8 500ºC for SA.

	Langmuir $\frac{C_e}{q_e} = \frac{1}{K_L\, q_L} + \frac{C_e}{q_L}$			**Freundlich** $\ln q_e = \ln K_F + \frac{1}{n} \ln C_e$		
	K_L	**q_L**	**R^2**	**K_F**	**1/n**	**R^2**
Mg-Al-ZIF-8 100ºC (MO)	0.420	16.1	0.9976	0.181	0.826	0.9902
Mg-Fe-ZIF-8 500ºC (MB)	0.378	13.7	0.9952	0.171	0.817	0.9873
Mg-Fe-ZIF-8 500ºC (SA)	0.359	8.78	0.9948	0.152	0.764	0.9868

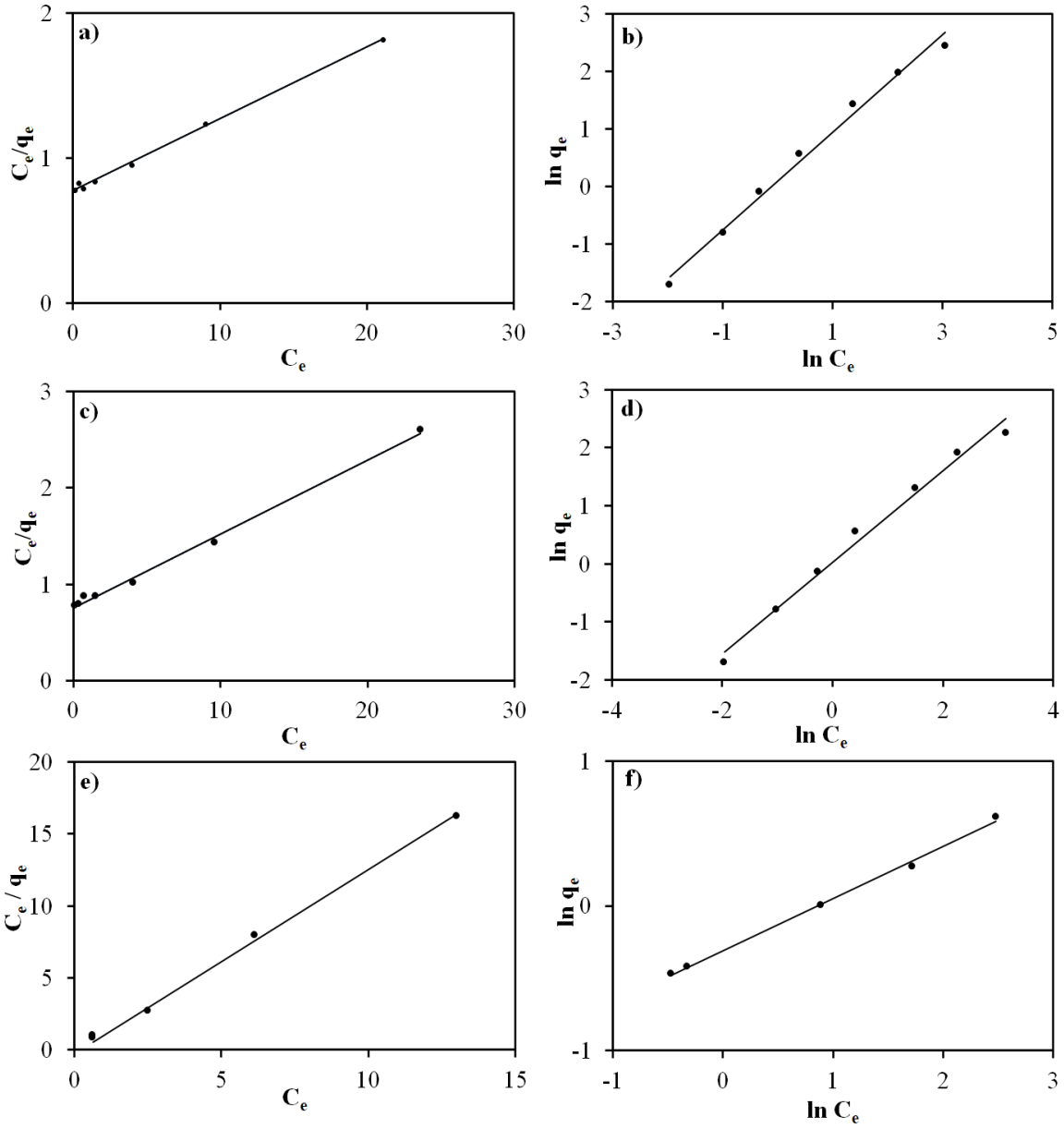

Figure 5.33. Langmuir and Freundlich isotherms of (a,b) Mg-Al-ZIF-8 100ºC for MO, (c,d) Mg-Fe-ZIF-8 500ºC for MB and (e,f) Mg-Fe-ZIF-8 500ºC for SA adsorption.

5.6.7. Kinetic analysis under irradiation

In this part, Mg-Fe-ZIF-8 500ºC is selected due to its highest photoactivity for MO, MB and SA. The influence of initial concentrations is examined in range of 32.7-0.327 mg L^{-1} for MO, in the range of 31.9-0.319 mg L^{-1} for MB and in the range of 13.8 to 0.138 mg L^{-1} for SA. The corresponding plots and their high correlation coefficients confirm the

applicability of the pseudo-first order kinetics for photocatalytic runs (Figure A.32). The rate constants k (min^{-1}) obtained from the slopes of these plots show an inverse relation to the initial concentrations of MO, MB and SA since their high concentrations may restrict the photon penetration to the active surface sites, and hence decrease the photocatalytic degradation rates (Table 5.16).

The saturation levels detected in the plots of rate (R) versus initial concentrations ($[MO]_0$, $[MB]_0$ and $[SA]_0$) indicate zero-order kinetics for the high concentrations of MO, MB and SA (Figure 5.34a,c and e). The linearized plots of reciprocal rate (1/R) versus reciprocal initial concentrations ($(1/[MO]_0)$, $(1/[MB]_0)$, $(1/[SA]_0)$) reveal adsorption coefficients (K) and the reaction rate constants (k) for the degradation reactions of MO, MB and SA (Figure 5.34b,e and f). Accordingly, the K values of Mg-Fe-ZIF-8 500ºC are determined as 0.344 L mg^{-1},0.319 L mg^{-1} and 0.313 L mg^{-1} for the degradation of MO, MB and SA, respectively. And, the k values for the degradation of MO, MB and SA are found to be 0.435 mg L^{-1} min^{-1}, 0.427 mg L^{-1} min^{-1} and 0.421 mg L^{-1} min^{-1}, respectively. The Mg-Fe-ZIF-8 500ºC has the highest rate constant for MO degradation, as corroborated with the photocatalytic results.

Table 5.16. First-order rate constants (k, min^{-1}) and linear regression values (R^2) for different initial concentrations of MO, MB and SA (mg L^{-1}) in the presence of Mg-Fe-ZIF-8 500ºC, Mg-Fe-ZIF-8 500ºC and Mg-Fe-ZIF-8 500ºC, respectively.

	Mg-Al-ZIF-8 100ºC		**Mg-Fe-ZIF-8 500ºC**			**Mg-Fe-ZIF-8 500ºC**		
$[MO]_0$	**k**	**R^2**	**$[MB]_0$**	**k**	**R^2**	**$[SA]_0$**	**k**	**R^2**
32.7	0.0254	0.9782	**31.9**	0.0232	0.9721	**13.8**	0.0230	0.9715
16.3	0.0265	0.9883	**15.9**	0.0245	0.9776	**6.90**	0.0241	0.9773
8.17	0.0267	0.9887	**7.95**	0.0278	0.9823	**3.45**	0.0274	0.9820
3.27	0.0289	0.9903	**3.19**	0.0282	0.9887	**1.38**	0.0285	0.9873
1.63	0.0376	0.9932	**1.59**	0.0321	0.9908	**0.69**	0.0325	0.9903
0.82	0.0423	0.9945	**0.79**	0.0411	0.9921	**0.34**	0.0415	0.9920
0.33	0.0551	0.9967	**0.31**	0.0533	0.9952	**0.14**	0.0521	0.9955

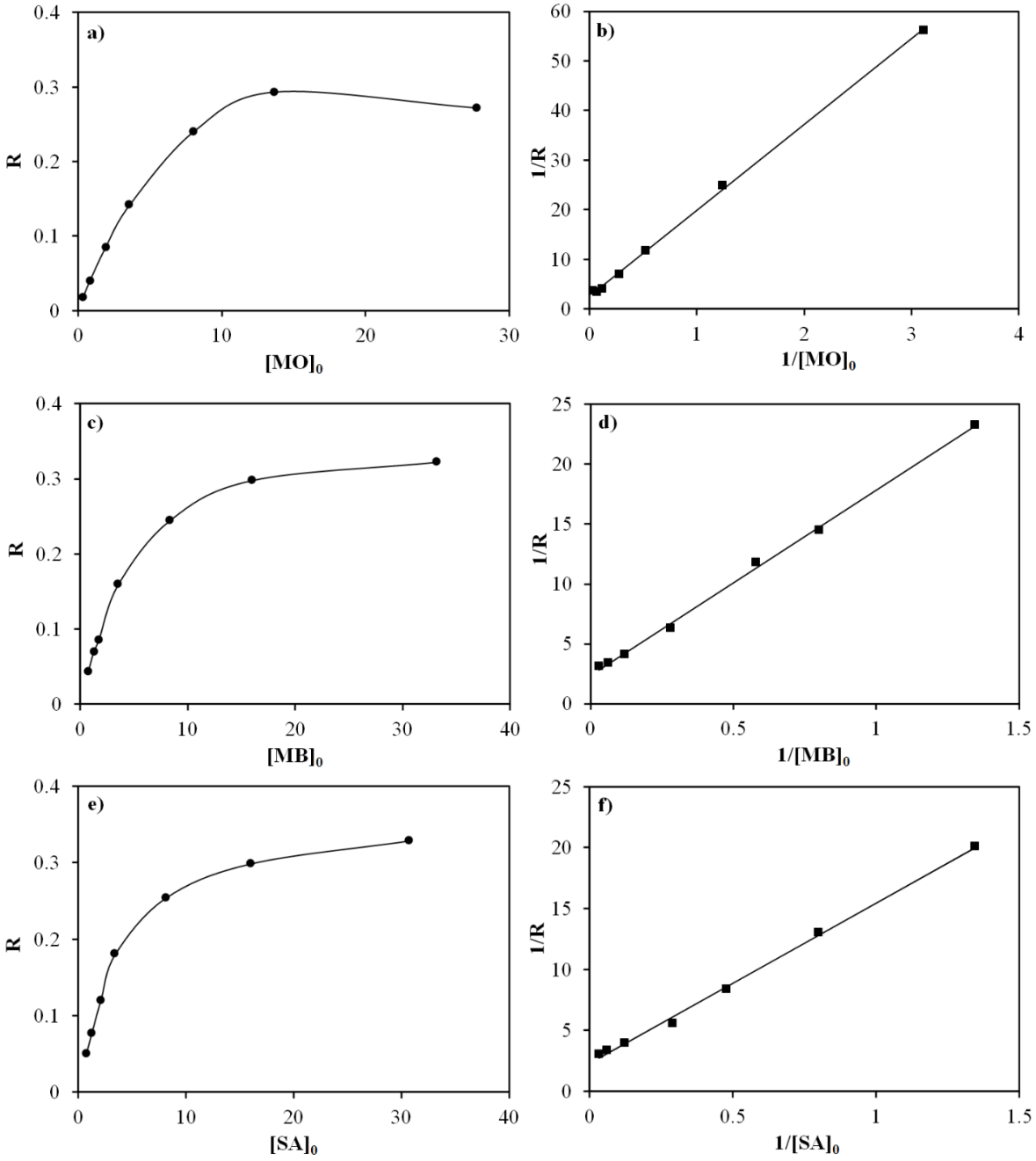

Figure 5.34. Langmuir-Hinshelwood kinetic analysis of (a,b) Mg-Fe-ZIF-8 100ºC for MO, (c,d) Mg-Fe-ZIF-8 500ºC for MB and (e,f) Mg-Fe-ZIF-8 500ºC for SA degradation.

5.7. Conclusion

The synthesized binary LDHs and LDOs exhibit typical features of hydrotalcite-like structures. In general, LDOs show lower surface areas than LDHs due to the generation of mixed metal oxides. Although the calcination process decreases the MO adsorption in the presence of LDOs, MB adsorption is enhanced due to the enhanced electrostatic attractions with the existence of mixed metal oxides. Also, LDOs show higher photocatalytic activity for MO, MB and SA. The highest photocatalytic efficiency is achieved by the Zn consisted LDOs due to the formation of ZnO photocatalyst.

The successful combination of fly ash and zeolite supports with the LDHs and LDOs leads to higher surface areas and porosities compared to the pristine LDHs and LDOs. This, eventually, improves both adsorption capacities and photoactivities of the supported LDHs and LDOs owing to the increased interactions with the active sites.

It is also noticed that ternary LDHs and LDOs have increased surface areas in comparison to that of LDHs and LDOs. Moreover, ZIF-8-supported LDHs and LDOs reveal larger surface areas than the ternary LDHs and LDOs. Thus, ZIF 8 as a support material (in LDHs) and as a ZnO generator (being Zn^{+2} ion precursor in LDOs) promote adsorption abilities as well as photocatalytic performances.

6. CONCLUDING REMARKS

In this study, different catalyst matrixes are prepared, structurally analyzed and examined in terms of adsorption capacity and photoactivity under dark and irradiation conditions. Results are presented in three chapters.

The first chapter reports recent publications of Cu-BTC-supported and ZIF-8-supported catalysts. 0.25M ZnO-Cu-BTC, 25% TiO_2-Cu-BTC, 0.25M ZnO-ZIF-8 and 25% TiO_2-ZIF-8 are successfully synthesized in the first group of these catalysts. XRD and SEM analysis verify the in-situ generation of ZnO and TiO_2 on the surface of Cu-BTC and ZIF-8. The results of adsorption and photocatalytic tests carried out in the presence of MO and MB model compounds highlight the importance of electrostatic interactions in both processes. 0.25M ZnO-ZIF-8 exhibits the highest photoactivity due to the inherited Zn^{2+} ions within the ZIF-8 framework.

The second study extends the investigations of TiO_2-hybrid porous nanocomposite (TiO_2-hybrid-PNC) formed by the coupling of TiO_2 nanoparticles with Cu-BTC. The as-synthesized nanocomposite serves as a porous network that improves the adsorption of MO. The photocatalytic activity of TiO_2-hybrid-PNC is enhanced compared to bare TiO_2 and Cu-BTC due to the inhibition of electron-hole recombination. The effect of humidity on the dark adsorption ability and photoactivity of TiO_2-hybrid-PNC is examined after its exposure to 40%, 67% and 84% RH values. In addition to the structural stability of humidified TiO_2-hybrid-PNC samples, the photocatalytic degradation rate of MO is improved with the increasing RH value owing to the formation of more hydroxyl radicals.

The third study explores the successful synthesis of ZnO@CuO nanocatalyst via CuO development from Cu-BTC support and simultaneous in-situ build of ZnO photocatalyst. XRD, SEM (EDX), XPS and UV-vis DRS analysis prove the formation of CuO and ZnO. In addition to the high surface area and porosity of ZnO@CuO, the electrostatic interactions consolidate its adsorption capacity and photoactivity for MO and MB. The enhanced photocatalytic activity of ZnO@CuO compared to ZnO is also attributed to the effective charge separation in the heterojunction. Moreover, photocatalytic degradation rates of MO

and MB are found to increase in the presence of humidified ZnO@CuO, among which ZnO@CuO (84% RH) displays the highest photoactivity for both MO and MB.

The last study of the first chapter comprises the ZnO-ZIF-8 nanocomposite synthesized at 300°C via coupling of ZnO and ZIF-8. The growth of ZnO nanoparticles with the preserved ZIF-8 structure is confirmed by XRD, SEM (EDX), BET, XPS and UV-vis DRS analysis. The adsorption capability and photocatalytic activity of ZnO-ZIF-8 300°C are compared with those of ZnO, ZIF-8 and ZIF-8 300°C in the presence of MO and MB. And, the higher adsorption ability of ZnO-ZIF-8 300°C is mainly attributed to its high surface area and porous structure inherited from ZIF-8. The improved photoactivity of ZnO-ZIF-8 300°C is due to the efficient charge separation by the co-existence of ZnO and ZIF-8 in the matrix. ZnO-ZIF-8 (84% RH) demonstrates the highest dark adsorption capacity and photoactivity.

The second chapter mainly examines two catalyst groups; eggshell-supported and HAP-supported catalysts. In the first group, ZnO, La-ZnO and ZnO and La-ZnO loaded eggshell catalysts are synthesized and calcined at 500°C. The characterization results of ZnO-Eggshell 500°C and La-ZnO-Egshell 500°C reveal the successful formation of ZnO nanoparticles and the preserved structure of the eggshell. The surface areas and porosities increase with ZnO and further La-ZnO loading on the eggshell. ZnO-Eggshell 500°C and La-ZnO-Eggshell 500°C exhibit characteristic ZnO absorption behavior in the UV region. The existence of La^{3+} in the La-ZnO Eggshell 500°C catalyst leads to a reduction in the band gap energy compared to the ZnO and ZnO-Eggshell 500°C due to the additional energy bands stemming from La^{3+} ions. The dark adsorption capacities and photocatalytic efficiencies of ZnO, La-ZnO, eggshell, ZnO-Eggshell 500°C and La-ZnO-Eggshell 500°C are explored in the presence of MO and MB. Accordingly, La-ZnO-Eggshell 500°C possesses a high adsorption capacity toward MO and MB by means of the increased surface area and porosity. Meanwhile, electrostatic attractions, H-bonding and Lewis acid-base interactions contribute to the adsorption processes. Similar to the dark adsorption results, the highest photocatalytic degradation rate is obtained in the presence of La-ZnO-Eggshell 500°C. The humidity effect is controlled under the 84% RH value. The humidified catalysts display higher adsorption and photocatalytic performances relative to their unhumidified forms owing to the contribution of the adsorbed water molecules on the catalyst surfaces.

In the second group, HAP 100ºC, HAP 500ºC, ZnO-HAP 500ºC and La-ZnO-HAP 500ºC catalysts are prepared. The successful derivation of HAP 100ºC from the eggshell as a calcium precursor is confirmed by the characterization results. HAP 100ºC exhibits higher surface area and pore volume compared to the eggshell. The calcined form of HAP at 500ºC possesses phase purity and increment in surface area with the formation of a mesoporous structure. Upon loading of ZnO and La-ZnO on the HAP, the catalysts reveal characteristics of both ZnO and HAP structures. The surface area and porosity of La-ZnO-HAP 500ºC are found to be higher than HAP 100ºC, HAP 500ºC, ZnO-HAP 500ºC owing to the voids among ZnO aggregates by dispersion of La^{3+} ions. HAP 100ºC and HAP 500ºC show activity under UV region due to the existence of oxygen vacancies in the matrix. The light absorption intensity of HAP 500ºC increases accompanied by the lower band gap energy in comparison to HAP 100ºC as a result of the high crystallinity upon calcination. ZnO-HAP 500ºC and La-ZnO-HAP 500ºC display the characteristic absorption behavior of ZnO. Moreover, the band gap energy decrement in La-ZnO HAP 500ºC than that of ZnO-HAP 500ºC is induced by the La existence in the matrix. According to the dark adsorption tests, the highest performance is achieved by La-ZnO-HAP 500ºC due to the enhancement of surface properties and also the formation of electrostatic interactions. The dark adsorption mechanisms of all samples are described as chemisorption following the pseudo-second order kinetic model. The experiments under irradiation exhibit that both HAP 100ºC and HAP 500ºC have photoactivity derived from the oxygen vacancies at PO_4^{3-} and HPO_4^{2-}. The photocatalytic efficiency of ZnO-HAP 500ºC is found to be higher than ZnO, HAP 100ºC and HAP 500ºC owing to the extended lifetimes of the photogenerated charge carriers by the cooperation of ZnO and HAP in the matrix. The highest photoactivity is attained in the existence of La-ZnO-HAP 500ºC on account of the synergy established between La-ZnO and HAP. Similar to the eggshell supported catalysts, the HAP-derived catalysts are humidified at 84% RH. In addition to the structural stabilities of the samples under humidity, the efficiencies of the humidified samples are promoted in the adsorption and photocatalytic processes in comparison to their unhumidified forms.

The third chapter explores detailed preparation, characterization and adsorption–photoactivity analysis of binary LDHs-LDOs, fly ash, zeolite and ZIF-8-supported LDHs-LDOs and ternary LDHs-LDOs. In the first part of this chapter, binary LDHs, namely as Mg-Al 100ºC, Zn-Al 100ºC, Mg-Fe 100ºC and Zn-Fe 100ºC are synthesized by the

combination of divalent metal cations with trivalent metal cations. The successful formations of LDH structures with the talcite-like features are confirmed by the characterization techniques. The higher d-spacing values are obtained in the structure of Zn-Al 100^{o}C and Zn-Fe 100^{o}C due to the higher ionic radius of the Zn^{2+} metal cation. The calcination of the binary LDHs at 500^{o}C leads to the transformation of the talcite structure into LDO forms with the formation of mixed metal oxides. The decrement in the d-spacing values and specific surface areas of all binary LDOs compared to their LDH forms is related to the distortion of the talcite structures. The dark adsorption capacities and photocatalytic activities of the binary LDHs and LDOs are studied in the presence of MO, MB and SA. The adsorption abilities of the LDHs and LDOs vary depending on the electrostatic interactions between the surface charges of the LDHs (and LDOs) and the functional groups of the model compounds. The surface areas and d-spacing values of the LDHs and LDOs also affect the surface adsorption and intercalation of the MO, MB and SA molecules. The photocatalytic activities of the LDOs are found to be higher than the LDHs owing to the generation of metal oxides such as ZnO, Fe_2O_3.

In the second and third parts of this chapter, fly ash and zeolite-supported LDHs are investigated, respectively. The LDO forms of the supported LDHs are obtained by calcination at 500^{o}C. Similar to the binary LDOs in the first part, the mixed metal oxides appear in the matrixes of the fly ash and zeolite-supported LDOs upon thermal treatment. The higher surface areas and porosities of the fly ash and zeolite-supported LDHs compared to the binary LDHs are attributed to the existence of fly ash and zeolite in the structures. Therefore, supported LDHs show higher adsorption capacities than binary LDHs. The adsorption processes of the MO, MB and SA are also contributed to the functional groups of fly ash and zeolite. The photocatalytic activities are enhanced in the presence of fly ash ad zeolite supported LDHs. The generation of mixed metal oxides in the fly ash ad zeolite-supported LDO catalysts leads to the promoted photocatalytic degradation rates in comparison to the fly ash ad zeolite-supported LDHs.

In the last part of this chapter, ternary LDH and their calcined forms (LDOs) are synthesized by the combination of co-existing divalent metal cations with a trivalent metal cation. The ternary LDHs and LDOs exhibit typical talcite peaks with higher surface area and porosity compared to the binary LDHs and LDOs. Moreover, Mg-Al and Mg-Fe LDHs

are combined with the ZIF-8 as a support material and as a Zn^{2+} precursor. In their LDO forms, ZnO formation is observed upon calcination at 500°C. ZIF-8-supported LDHs and LDOs display higher adsorption abilities in comparison to the ternary LDHs due to the increased surface area and porosity. The higher photocatalytic performance of ZIF-8-supported LDHs than the ternary LDHs is attributed to the ligand-to-metal charge transfer mechanism of ZIF-8.

In conclusion, this dissertation presents a detailed investigation of the different catalyst groups. The facile synthesis routes, desirable structural features and applicabilities of the catalysts highlight them as promising materials and also throw light on the path for their future applications.

REFERENCES

1. Ökte, A. N., D. Karamanis, and D. Tuncel, "Dual Functionality of TiO_2-Flyash Nanocomposites: Water Vapor Adsorption and Photocatalysis", *Catalysis Today*, Vol. 230, pp. 205-213, 2014.

2. Soltani, D. C. R. and M. Mashayekhi, "Decomposition of Ibuprofen in Water via an Electrochemical Process with Nano-Sized Carbon Black-Coated Carbon Cloth as Oxygen-Permeable Cathode Integrated with Ultrasound", *Chemosphere*. Vol. 194, pp. 471-480, 2018.

3. Gholami, P., A. Khataee, R. D. C. Soltani, L. Dinpazhoh, and A. Bhatnagar, "Photocatalytic Degradation of Gemifloxacin Antibiotic Using Zn-Co-LDH@Biochar Nanocomposite", *Journal of Hazardous Materials*. Vol. 382, p. 121070, 2020.

4. Feng, L., E. D. van Hullebusch, M. A. Rodrigo, G. Esposito, and M. A. Oturan, "Removal of Residual Anti-Inflammatory and Analgesic Pharmaceuticals from Aqueous Systems by Electrochemical Advanced Oxidation Processes. A Review", *Chemical Engineering Journal*, Vol. 228, pp. 944-964, 2013.

5. Lv, S., H. Wang, Y. Zhou, D. Tang, and S. Bi, "Recent Advances in Heterogeneous Single-Atom Nanomaterials: From Engineered Metal-Support Interaction to Applications in Sensors", *Coordination Chemistry Reviews*, Vol. 478, p. 214976, 2023.

6. Thongam, D. D. and H. Chaturvedi, "Advances in Nanomaterials for Heterogeneous Photocatalysis", *Nano Express*, Vol.2, p. 012005, 2021.

7. Fawell, J. and M. J. Nieuwenhuijsen, "Contaminants in Drinking Water", *British Medical Bulletin*, Vol. 68, No. 1, pp. 199-208, 2003.

8 Mahmoodi, N. M., M. Arami, N. Y. Limaee, and N. S. Tabrizi, "Kinetics of Heterogeneous Photocatalytic Degradation of Reactive Dyes in an Immobilized TiO_2 Photocatalytic Reactor", *Journal of Colloid and Interface Science*, Vol. 295, No. 1, pp. 159-164, 2006.

9. Morales-Flores, N., U. Pal, and E. Sánchez Mora, "Photocatalytic Behavior of ZnO and Pt-Incorporated ZnO Nanoparticles in Phenol Degradation", *Applied Catalysis A: General*, Vol. 394, No. 1, pp. 269-275, 2011.

10. Pascariu, P., M. Homocianu, C. Cojocaru, P. Samoila, A. Airinei, and M. Suchea, "Preparation of La Doped ZnO Ceramic Nanostructures by Electrospinning–Calcination Method: Effect of La^{3+} Doping on Optical and Photocatalytic Properties", *Applied Surface Science*, Vol. 476, pp. 16-27, 2019.

11. Ibhadon, A. O. and P. Fitzpatrick, "Heterogeneous Photocatalysis: Recent Advances and Applications", *Catalysts*, Vol. 3, No. 1, pp. 189-218, 2013.

12. Zong, Y., Z. Li, X. Wang, J. Ma, and Y. Men, "Synthesis and High Photocatalytic Activity of Eu-Doped ZnO Nanoparticles" *Ceramics International*. Vol. 40, No.7, pp. 10375-10382, 2014.

13. El Fidha, G., N. Bitri, F. Chaabouni and E. Llobet, "Physical and Photocatalytic Properties of Sprayed Dy Doped ZnO Thin Films under Sunlight Irradiation for Degrading Methylene Blue", *RSC Advances*. Vol. 11, No. 40, pp. 24917-24925, 2021.

14. Choudhary, S., M. Sharma, V. Krishnan, and S. Mohapatra, "Facile Synthesis of Ce Doped ZnO Nanowires for Efficient Photocatalytic Removal of Organic Pollutants from Water", *Materials Today Communications*. Vol. 34, p. 105361, 2023.

15. Punia, K., G. Lal, S. Dalela, S. N. Dolia, P.A. Alvi, S. K. Barbar, K. B. Modi and S. Kumar, "A Comprehensive Study on the Impact of Gd Substitution on Structural, Optical and Magnetic Properties of ZnO Nanocrystals", *Journal of Alloys and Compounds*, Vol. 868, p. 159142, 2021.

16. Khatamian, M., A. A. Khandar, B. Divband, M. Haghighi, and S. Ebrahimiasl, "Heterogeneous Photocatalytic Degradation of 4-Nitrophenol in Aqueous Suspension by Ln (La^{3+}, Nd^{3+} or Sm^{3+}) Doped ZnO Nanoparticles", *Journal of Molecular Catalysis A: Chemical*, Vol. 365, pp. 120-127, 2012.

17. Palanivel, B., R. R. Macadangdang, M. S. Hossain, F. A. Alhart and S. Gedi, "Rare Earth (Gd, La) Co-Doped ZnO Nanoflowers for Direct Sunlight Driven Photocatalytic Activity", *Journal of Rare Earths*, Vol. 41, No. 1, pp. 77-84, 2023.

18. Ökte, A. N. and Ö. Yilmaz, "La and Ce Loaded TiO_2-ZSM-5 Catalysts: Comparative Characterization and Photocatalytic Activity Investigations" *Microporous and Mesoporous Materials*, Vol. 126, No. 3, pp. 245-252, 2009.

19. Chen, D., H. Zhu, and X. Wang, "A Facile Method to Synthesize the Photocatalytic TiO_2/Montmorillonite Nanocomposites with Enhanced Photoactivity", *Applied Surface Science*, Vol. 319, No. 1, pp. 158-166, 2014.

20. Karamanis, D., A.N. Ökte, E. Vardoulakis, and T. Vaimakis, "Water Vapor Adsorption and Photocatalytic Pollutant Degradation with TiO_2-Sepiolite Nanocomposites" *Applied Clay Science*, Vol. 53, No. 2, pp. 181-187, 2011.

21. Ökte, A. N. and D. Karamanis, "A Novel Photoresponsive ZnO-Fly Ash Nanocomposite for Environmental and Energy Applications", *Applied Catalysis B: Environmental*, Vol. 142, pp. 538-552, 2013.

22. Augugliaro, V., J. Blanco Gálvez, J. Cáceres Vázquez, E. G. Lopez, V. Loddo, M. J. Lopez Munoz, S. M. Rodriguez, G. Marci, L. Palmisano, M. Schiavello and J. Soria Ruiz, "Photocatalytic Oxidation of Cyanide in Aqueous TiO_2 Suspensions Irradiated by Sunlight in Mild and Strong Oxidant Conditions", *Catalysis Today*, Vol. 54, No. 2, pp. 245-253, 1999.

23. Mai, F. D., C. S. Lu, C. W. Wu, C. H. Huang, J. Y. Chen, and C. C. Chen, "Mechanisms of Photocatalytic Degradation of Victoria Blue R Using Nano-TiO_2", *Separation and Purification Technology*, Vol. 62, No. 2, pp. 423-436, 2008.

24. Férey, G., "Hybrid Porous Solids: Past, Present, Future", *Chemical Society Reviews*, Vol. 37, No. 1, pp. 191-214, 2008.

25. Lu, W., Z. Wei, Z. Y. Gu, T. F. Liu, J. Park, J. Park, J. Tian, M. Zhang, Q. Zhang, T. Gentle, M. Bosch, H. C. Zhou, "Tuning the Structure and Function of Metal-Organic Frameworks via Linker Design", *Chemical Society Reviews*, Vol. 43, pp. 5561-5593, 2014.

26. Juan-Alcañiz, J., R. Gielisse, A. B. Lago, E. V. R. Fernandez, P. S. Crespo, T. Devic, N. Guillou, C. Serre, F. Kapteijn and J. Gascon, "Towards Acid MOFs-Catalytic Performance of Sulfonic Acid Functionalized Architectures", *Catalysis Science and Technology*, Vol. 3, No. 9, pp. 2311-2318, 2013.

27. Prestipino, C., L. Regli, J. G. Vitillo, F. Bonino, A. Damin, C. Lamberti, A. Zecchina, P. L. Solari, K. O. Kongshaug and S. Bordiga, "Local Structure of Framework Cu(II) in HKUST-1 Metallorganic Framework: Spectroscopic Characterization Upon Activation and Interaction with Adsorbates", *Chemistry of Material*, Vol. 18, No. 5, pp. 1337-1346, 2006.

28. Park, K. S., Z. Ni, A. P. Cô and O. M. Yaghi, "Exceptional Chemical and Thermal Stability of Zeolitic Imidazolate Frameworks", *PNAS*, Vol. 103, No. 27, pp. 10186-10191, 2006.

29. Tian, F., A. M. Cerro, A. M. Mosier and L. Benz, "Surface and Stability Characterization of a Nanoporous ZIF-8 Thin Film", *Journal of Physical Chemistry C*, Vol. 118, No. 26, pp. 14449-14456, 2014.

30. Lin, K. S., A. K. Adhikari, C. N. Ku, C. L. Chiang, and H. Kuo, "Synthesis and Characterization of Porous HKUST-1 Metal Organic Frameworks for Hydrogen Storage", *International Journal of Hydrogen Energy*, Vol.37, pp. 13865-13871, 2012.

31. Li, J. R., Y. Ma, M. C. McCarthy, J. Sculley, J. Yu, H. K. Jeong, P. B. Balbuena and H. C. Zhou, "Carbon Dioxide Capture-Related Gas Adsorption and Separation in Metal-Organic Frameworks", *Coordination Chemistry Reviews*, Vol. 255, pp. 1791-1823, 2011.

32. Liang, Z., M. Marshall, and A. L. Chaffee, "CO_2 Adsorption-Based Separation by Metal Organic Framework (Cu-BTC) Versus Zeolite (13X)", *Energy and Fuels*, Vol. 23, No. 5, pp. 2785-2789, 2009.

33. Wang, Q. M., D. Shen, M. Bülow, M. L. Lau, S. Deng, F. R. Fitch, N. O. Lemcoff and J. Semanscin, "Metallo-Organic Molecular Sieve for Gas Separation and Purification", *Microporous and Mesoporous Materials*, Vol. 55, pp. 217-230, 2002.

34. Blanco-Brieva, G., J. M. Campos-Martin, S. M. Al-Zahrani, and J. L.G. Fierro, "Efficient Solvent Regeneration of Basolite C300 Used in the Liquid-Phase Adsorption of Dibenzothiophene", *Fuel*, Vol. 113, pp. 216-220, 2013.

35. Jiang, J. Q., C. X. Yang, and X. P. Yan, "Zeolitic Imidazolate Framework-8 for Fast Adsorption and Removal of Benzotriazoles from Aqueous Solution", *ACS Applied Materials and Interfaces*, Vol. 5, No. 19, pp. 9837-9842, 2013.

36. Lin, S., Z. Song, G. Che and J. Zhang, "Adsorption Behavior of Metal-Organic Frameworks for Methylene Blue from Aqueous Solution", *Microporous and Mesoporous Materials*, Vol. 193, pp. 27-34, 2014.

37. Isimjan, T. T., H. Kazemian, S. Rohani, and A. K. Ray, "Photocatalytic Activities of Pt/ZIF-8 Loaded Highly Ordered TiO_2 Nanotubes", *Journal of Materials Chemistry*, Vol. 20, No. 45, pp. 10241-10245, 2010.

38. Yu, B., F. Wang, W. Dong, J. Hou, P. Lu, and J. Gong, “Self-Template Synthesis of Core-Shell ZnO@ZIF-8 Nanospheres and the Photocatalysis under UV Irradiation”, *Materials Letters*, Vol. 156, pp. 50-53, 2015.

39. Anandan, S., A. Vinu, K. L. P. Sheeja Lovely and K. Ariga, “Photocatalytic Activity of La-Doped ZnO for the Degradation of Monocrotophos in Aqueous Suspension”, *Journal of Molecular Catalysis A: Chemical*, Vol. 266, No. 1, pp. 149-157, 2007.

40. Kaneko, T., M. Fujii, T. Kodama, and Y. Kitayama, “Synthesis of Titania Pillared Mica in Aqueous Solution of Acetic Acid”, *Journal of Porous Materials*, Vol. 8, pp. 99-109, 2001.

41. L. Yanbo, L. H. Wee, A. Volodin, J. A. Martens, and I. F. J. Vankelecom, “Polymer Supported ZIF-8 Membranes Prepared via Interfacial Synthesis Method”, *Chemical Communications*, Vol. 51, p. 918, 2015.

42. Schlichte, K., T. Kratzke, and S. Kaskel, “Improved Synthesis, Thermal Stability and Catalytic Properties of the Metal-Organic Framework Compound $Cu_3(BTC)_2$”, *Microporous and Mesoporous Materials*, Vol. 73, No. 1-2, pp. 81-88, 2004.

43. Pan, Y., Y. Liu, G. Zeng, L. Zhao, and Z. Lai, “Rapid Synthesis of Zeolitic Imidazolate Framework-8 (ZIF-8) Nanocrystals in an Aqueous System”, *Chemical Communications*, Vol. 47, No. 7, pp. 2071-2073, 2011.

44. Jian, M., B. Liu, G. Zhang, R. Liu, and X. Zhang, “Adsorptive Removal of Arsenic from Aqueous Solution by Zeolitic Imidazolate Framework-8 (ZIF-8) Nanoparticles”, *Colloids and Surfaces A: Physicochemical and Engineering Aspects*, Vol. 465, pp. 67-76, 2015.

45. Nicholson, T. M. and S. K. Bhatia, “Electrostatically Mediated Specific Adsorption of Small Molecules in Metallo-Organic Frameworks”, *Journal of Physical Chemistry B*. Vol. 110, No. 49, pp. 24834-24836, 2006.

46. Wang, Z., J. Wang, M. Li, K. Sun, and C.J. Liu, “Three-Dimensional Printed Acrylonitrile Butadiene Styrene Framework Coated with Cu-BTC Metal-Organic Frameworks for the Removal of Methylene Blue”, *Scientific Reports*, Vol. 4, p. 5939, 2014.

47. Li, Y., H. Xu, S. Ouyang, and J. Ye, “Metal-Organic Frameworks for Photocatalysis”, *Physical Chemistry Chemical Physics*, Vol. 18, No. 11, pp.7563-7572, 2016.

48. Duke, A. S., E. A. Dolgopolova, R. P. Galhenage and N. B. Shustova, “Active Sites in Copper-Based Metal-Organic Frameworks: Understanding Substrate Dynamics, Redox Processes, and Valence-Band Structure”, *Journal of Physical Chemistry C*. Vol. 119, No. 49, pp. 27457-27466, 2015.

49. Khan, N. A., B. K. Jung, Z. Hasan, and S. H. Jhung, “Adsorption and Removal of Phthalic Acid and Diethyl Phthalate from Water with Zeolitic Imidazolate and Metal-Organic Frameworks”, *Journal of Hazardous Materials*, Vol. 282, pp. 194-200, 2015.

50. Jing, H. P., C. C. Wang, Y. W. Zhang, P. Wang, and R. Li, “Photocatalytic Degradation of Methylene Blue in ZIF-8”, *RSC Advances*, Vol. 4, No. 97, pp. 54454-54462, 2014.

51. Wang, X., W. Cai, Y. Lin, G. Wang, and C. Liang, “Mass Production of Micro/Nanostructured Porous ZnO Plates and Their Strong Structurally Enhanced and Selective Adsorption Performance for Environmental Remediation”, *Journal of Materials Chemistry*, Vol. 20, No. 39, pp. 8582-8590, 2010.

52. Houas, A., H. Lachheb, M. Ksibi, E. Elaloui, C. Guillard, and J.-M. Herrmann, “Photocatalytic Degradation Pathway of Methylene Blue in Water”, *Applied Catalysis B: Environmental*, Vol. 31, pp. 145-157, 2001.

53. Konstantinou, I. K. and T. A. Albanis, “TiO_2-Assisted Photocatalytic Degradation of Azo Dyes in Aqueous Solution: Kinetic and Mechanistic Investigations: A Review”, *Applied Catalysis B: Environmental*, Vol. 49, pp. 1-14, 2004.

54. Park, H., Y. Park, W. Kim, and W. Choi, "Surface Modification of TiO_2 Photocatalyst for Environmental Applications", *Journal of Phorochemistry and Photobiology C: Photochemistry Reviews*, Vol. 15, pp. 1-20, 2013.

55. Song, X. and L. Gao, "Fabrication of Hollow Hybrid Microspheres Coated with Silica/Titania via Sol-Gel Process and Enhanced Photocatalytic Activities" *Journal of Physical Chemistry C*, Vol. 111, No. 23, pp. 8180-8187, 2007.

56. Zhao, W., L. Feng, R. Yang, J. Zheng, and X. Li, "Synthesis, Characterization, and Photocatalytic Properties of Ag Modified Hollow SiO_2/TiO_2 Hybrid Microspheres" *Applied Catalysis B: Environmental*, Vol. 103, No. 1-2, pp. 181-189, 2011.

57. He, L., N. Du, C. Wang, X. Chen, and W. Zhang, "A Facile Synthesis of Graphene-Supported Mesoporous TiO_2 Hybrid Sheets with Uniform Coverage and Controllable Pore Diameters", *Microporous and Mesoporous Materials*, Vol. 206, pp. 95-101, 2015.

58. Sun, Q., X. Hu, S. Zheng, Z. Sun, S. Liu, and H. Li, "Influence of Calcination Temperature on the Structural, Adsorption and Photocatalytic Properties of TiO_2 Nanoparticles Supported on Natural Zeolite", *Powder Technology*, Vol. 274, pp. 88-97, 2015.

59. Zhang, G., A. Song, Y. Duan, and S. Zheng, "Enhanced Photocatalytic Activity of TiO_2/Zeolite Composite for Abatement of Pollutants", *Microporous and Mesoporous Materials*, Vol. 255, pp. 61-68, 2018.

60. Du, G., P. Feng, X. Cheng, J. Li, and X. Luo, "Immobilizing of ZIF-8 Derived ZnO with Controllable Morphologies on Zeolite A for Efficient Photocatalysis", *Journal of Solid State Chemistry*, Vol. 255, pp. 215-218, 2017.

61. Li, R., J. Hu, M. Deng, Y. Xiong, "Integration of an Inorganic Semiconductor with a Metal-Organic Framework: A Platform for Enhanced Gaseous Photocatalytic Reactions", *Advanced Materials*, Vol. 26, No. 28, pp. 4783-4788, 2014.

62. Wang, H., T. Yu, X. Tan, and J. Ye, "Enhanced Photocatalytic Oxidation of Isopropanol by HKUST-1@TiO_2 Core-Shell Structure with Ultrathin Anatase Porous Shell: Toxic Intermediate Control", *Industrial and Engineering Chemistry Research*, Vol. 55, No. 29, pp. 8096-8103, 2016.

63. Ökte, A. N., D. Karamanis, E. Chalkia, and D. Tuncel, "The Effect of ZnO or TiO2 Loaded Nanoparticles on the Adsorption and Photocatalytic Performance of Cu-BTC and ZIF-8 MOFs", *Materials Chemistry and Physics*, Vol. 187, pp. 5-10, 2017.

64. Kaneko, T., M. Fujii, T. Kodama, and Y. Kitayama, "Synthesis of Titania Pillared Mica in Aqueous Solution of Acetic Acid", *Journal of Porous Materials*, Vol. 8, pp. 99-109, 2001.

65. Al-Janabi, N., V. Martis, N. Servi and F.R. Siperstein, and X. Fan, "Cyclic Adsorption of Water Vapour on Cu-BTC MOF: Sustaining the Hydrothermal Stability under Non-Equilibrium Conditions", *Chemical Engineering Journal*, Vol. 333, pp. 594-602, 2018.

66. Liu, X., R. Dang, W. Dong and G. Wang, "A Sandwich-Like Heterostructure of TiO_2 Nanosheets with MIL-100(Fe): A Platform for Efficient Visible-Light-Driven Photocatalysis", *Applied Catalysis B: Environmental*, Vol. 209, pp. 506-513, 2017.

67 Senthil Kumar, R., S. Senthil Kumar, and M. Anbu Kulandainathan, "Efficient Electrosynthesis of Highly Active $Cu_3(BTC)_2$-MOF and Its Catalytic Application to Chemical Reduction", *Microporous and Mesoporous Materials*, Vol. 168, pp. 57-64, 2013.

68 Luo, Q. X., X. D. Song, M. Ji, S.E. Park, C. Hao, and Y.Q. Li, "Molecular Size- and Shape-Selective Knoevenagel Condensation over Microporous $Cu_3(BTC)_2$

Immobilized Amino-Functionalized Basic Ionic Liquid Catalyst", *Applied Catalysis A: General*, Vol. 478, pp. 81-90, 2014.

69. Chen, H., L. Wang, J. Yang, and R.T. Yang, "Investigation on Hydrogenation of Metal-Organic Frameworks HKUST-1, MIL-53, and ZIF-8 by Hydrogen Spillover", *Journal of Physical Chemistry C*, Vol. 117, No. 15, pp. 7565-7576, 2013.

70. Patrocínio, A. O. T., E. B. Paniago, R. M. Paniago, and N. Y. M. Iha, "XPS Characterization of Sensitized n-TiO_2 Thin Films for Dye-Sensitized Solar Cell Applications", *Applied Surface Science*, Vol. 254, No. 6, pp. 1874-1879, 2008.

71. Li, X., Y. Pi, Q. Xia, Z. Li, and J. Xiao, "TiO_2 Encapsulated in Salicylaldehyde-NH_2-MIL-101(Cr) for Enhanced Visible Light-Driven Photodegradation of MB", *Applied Catalysis B: Environmental*, Vol. 191, pp. 192-201, 2016.

72. Decoste, J. B., G. W. Peterson, B. J. Schindler, K. L. Killops, M. A. Browe, and J. J. Mahle, "The Effect of Water Adsorption on the Structure of the Carboxylate Containing Metal-Organic Frameworks Cu-BTC, Mg-MOF-74, and UiO-66", *Journal of Materials Chemistry A*, Vol. 1, No. 38, pp. 11922-11932, 2013.

73. Xiao, J. D. and H. L. Jiang, "Metal-Organic Frameworks for Photocatalysis and Photothermal Catalysis", *Accounts of Chemical Research*, Vol. 52, No. 2, pp. 356-366, 2019.

74. Duke, A. S., E. A. Dolgopolova, R. P. Galhenage and N. B. Shustova, "Active Sites in Copper-Based Metal-Organic Frameworks: Understanding Substrate Dynamics, Redox Processes, and Valence-Band Structure", *Journal of Physical Chemistry C*, Vol. 119, No. 49, pp. 27457-27466, 2015.

75. Alver, U., A. Tanriverdi, and O. Akgül, "Hydrothermal Preparation of ZnO Electrodes Synthesized from Different Precursors for Electrochemical Supercapacitors", *Synthetic Metals*, Vol. 211, pp. 30-34, 2016.

76. Chee, W. K., H. N. Lim, I. Harrison and N. M. Huang, "Performance of Flexible and Binderless Polypyrrole/Graphene Oxide/Zinc Oxide Supercapacitor Electrode in a Symmetrical Two-Electrode Configuration", *Electrochimica Acta*, Vol. 157, pp. 88-94, 2015.

77. Miao, Y., H. Zhang, S. Yuan, Z. Jiao, and X. Zhu, "Preparation of Flower-Like ZnO Architectures Assembled with Nanosheets for Enhanced Photocatalytic Activity", *Journal of Colloid and Interface Science*, Vol. 462, pp. 9-18, 2016.

[78] Zhu, L., Z. Liu, P. Xia, H. Li, and Y. Xie, "Synthesis of Hierarchical ZnO&Graphene Composites with Enhanced Photocatalytic Activity", *Ceramics International*, Vol. 44, No. 1, pp. 849-856, 2018.

79. Harish, S., J. Archana, M. Sabarinathan, Y. Hayakawa, "Controlled Structural and Compositional Characteristic of Visible Light Active ZnO/CuO Photocatalyst for the Degradation of Organic Pollutant", *Applied Surface Science*, Vol. 418, pp. 103-112, 2017.

80. Dijkstra, M. F. J., A. Michorius, H. Buwalda, H. J. Panneman, J. G. M. Winkelman, and A. A. C. M. Beenackers, "Comparison of the Efficiency of Immobilized and Suspended Systems in Photocatalytic Degradation", *Catalysis Today*, Vol. 66, No 2-4, pp. 487-494, 2001.

81. Sharma, R. K., D. Kumar and R. Ghose, "Synthesis of Nanocrystalline ZnO-NiO Mixed Metal Oxide Powder by Homogeneous Precipitation Method", *Ceramics International*, Vol. 42, No. 3, pp. 4090-4098, 2016.

82. Li, B. and Y. Wang, "Facile Synthesis and Photocatalytic Activity of ZnO-CuO Nanocomposite", *Superlattices and Microstructures*, Vol. 47, No. 5, pp. 615-623, 2010.

83. Lin, S., Z. Song, G. Che, and J. Zhang, "Adsorption Behavior of Metal-Organic Frameworks for Methylene Blue from Aqueous Solution", *Microporous and Mesoporous Materials*, Vol. 193, pp. 27-34, 2014.

84. Krungleviciute, V., K. Lask, L. Heroux and A. Skoulidas, "Argon Adsorption on Cu_3(benzene-1,3,5-tricarboxylate)$_2$(H_2O)$_3$ Metal-Organic Framework", *Langmuir*, Vol. 23, No. 6, pp. 3106-3109, 2007.

85. Decoste, J. B., G.W. Peterson, B. J. Schindler, K. L. Killops, M. A. Browe, and J. J. Mahle, "The Effect of Water Adsorption on the Structure of the Carboxylate Containing Metal-Organic Frameworks Cu-BTC, Mg-MOF-74, and UiO-66", *Journal of Materials Chemistry A*, Vol. 1, No. 38, pp. 11922-11932, 2013.

86. Calero, S., J. J. Gutiérrez-Sevillano, and E. García-Pérez, "Effect of the Molecular Interactions on the Separation of Nonpolar Mixtures using Cu-BTC Metal-Organic Framework", *Microporous and Mesoporous Materials*, Vol. 165, pp. 79-83, 2013.

87. Xiang, Z., D. Cao, X. Shao, W. Wang, J. Zhang, and W. Wu, "Facile Preparation of High-Capacity Hydrogen Storage Metal-Organic Frameworks: A Combination of Microwave-Assisted Solvothermal Synthesis and Supercritical Activation", *Chemical Engineering Science*, Vol. 65, No. 10, pp. 3140-3146, 2010.

88. Zheng, L., X. Li, W. Du, and Z. Hou, "Metal-organic framework derived Cu/ZnO Catalysts for Continuous Hydrogenolysis of Glycerol", *Applied Catalysis B: Environmental*, Vol. 203, pp. 146-153, 2017.

89. Niu, H., S. Liu, Y. Cai, F. Wu, and X. Zhao, "MOF Derived Porous Carbon Supported Cu/Cu_2O Composite as High Performance Non-Noble Catalyst", *Microporous and Mesoporous Materials*, Vol. 219, pp. 48-53, 2016.

90. Sathishkumar, P., R. Sweena, J. J. Wu, and S. Anandan, "Synthesis of CuO-ZnO Nanophotocatalyst for Visible Light Assisted Degradation of a Textile Dye in

Aqueous Solution", *Chemical Engineering Journal*, Vol. 171, No. 1, pp. 136–140, 2011.

91. M. Sahooli, S. Sabbaghi ad R. Saboori, "Synthesis and Characterization of Mono Sized CuO Nanoparticles", *Materials Letters*, Vol. 81, pp. 169-172, 2012.

92. Peng, B., C. Feng, S. Liu, and R. Zhang, "Synthesis of CuO Catalyst Derived from HKUST-1 Temple for the Low-Temperature NH_3-SCR Process", *Catalysis Today*, Vol. 314, pp. 122-128, 2018.

93. Abraham, N., A. Rufus, C. Unni, and D. Philip, "Dye Sensitized Solar Cells Using Catalytically Active CuO-ZnO Nanocomposite Synthesized by Single Step Method", *Spectrochimica Acta-Part A: Molecular and Biomolecular Spectroscopy*, Vol. 200, pp. 116-126, 2018.

94. Sivasubramanian, D., R. Ponnusamy, and V. Gandhiraj, "Low Power Optical Limiting and Thermal Lensing in Mn Doped ZnO Nanoparticles", *Materials Chemistry and Physics*, Vol. 159, pp. 93-100, 2015.

[95] Kuriakose, S., B. Satpati, and S. Mohapatra, "Enhanced Photocatalytic Activity of Co Doped ZnO Nanodisks and Nanorods Prepared by a Facile Wet Chemical Method", *Physical Chemistry Chemical Physics*, Vol. 16, No. 25, pp. 12741-12749, 2014.

96. Wang, J. X., X. W. Sun, Y. Yang, and H. V. Demir, "Free-Standing ZnO-CuO Composite Nanowire Array Films and Their Gas Sensing Properties", *Nanotechnology*, Vol. 22, No. 32, p. 325704, 2011.

97. Kuriakose, S., D. K. Avasthi, and S. Mohapatra, "Effects of Swift Heavy Ion Irradiation on Structural, Optical and Photocatalytic Properties of ZnO-CuO Nanocomposites Prepared by Carbothermal Evaporation Method", *Beilstein Journal of Nanotechnology*, Vol. 6, No. 1, pp. 928-937, 2015.

98. Li, C. J., X. Cao, W.H. Li, B.W. Zhang, and L.Q. Xiao, "Co-Synthesis of CuO-ZnO Nanoflowers by Low Voltage Liquid Plasma Discharge with Brass Electrode", *Journal of Alloys and Compounds*, Vol. 773, pp. 762-769, 2019.

99. Wongratanaphisan, D., K. Kaewyai, S. Choopun, A. Gardchareon, P. Ruankham, and S. Phadungdhitidhada, "CuO-Cu_2O Nanocomposite Layer for Light-Harvesting Enhancement in ZnO Dye-Sensitized Solar Cells", *Applied Surface Science*, Vol. 474, pp. 85-90, 2019.

100. Sun, Y., M. Amsler, S. Goedecker, A. Caravella, M. Yoshida and M. Kato, "Surfactant-Assisted Synthesis of Large Cu-BTC MOF Single Crystals and Their Potential Utilization as Photodetectors", *CrystEngComm*, Vol.21, pp. 3948-3953, 2019.

101. Sriram, S., L. K.C., and A. Thayumanavan, "Experimental and Theoretical Investigations of Photocatalytic Activity of Cu Doped ZnO Nanoparticles", *Optik*, Vol. 139, pp. 299-308, 2017.

102. Naseri, A., M. Samadi, N.M. Mahmoodi, A. Pourjavadi, H. Mehdipour, and A.Z. Moshfegh, "Tuning Composition of Electrospun ZnO/CuO Nanofibers: Toward Controllable and Efficient Solar Photocatalytic Degradation of Organic Pollutants", *Journal of Physical Chemistry C*, Vol. 121, No. 6, pp. 3327-3338, 2017.

103. Chen, Q., Q.W. Chen, C. Zhuang, P.P. Tang, N. Lin, and L.Q. Wei, "Controlled Release of Drug Molecules in Metal–Organic Framework Material HKUST-1", *Inorganic Chemistry Communications*, Vol. 79, pp. 78-81, 2017.

104. Deng, M. J., C.C. Wang, P. J. Ho, C. M. Lin, J. M. Chen, and K. T. Lu, "Facile Electrochemical Synthesis of 3D Nano-Architectured CuO Electrodes for High-Performance Supercapacitors", *Journal of Materials Chemistry A*, Vol. 2, No. 32, pp. 12857-12865, 2014.

105. Dubal, D. P., G. S. Gund, R. Holze, and C. D. Lokhande, "Mild Chemical Strategy to Grow Micro-Roses and Micro-Woolen Like Arranged CuO Nanosheets for High Performance Supercapacitors", *Journal of Power Sources*, Vol. 242, pp. 687-698, 2013.

106. Sadollahkhani, A., O. Nur, M. Willander and P.O. Holtz, "A Detailed Optical Investigation of ZnO@ZnS Core-Shell Nanoparticles and Their Photocatalytic Activity at Different PH Values", *Ceramics International*, Vol. 41, No. 5, pp. 7174-7184, 2015.

107. Zheng, L., Y. Zheng, C. Chen, and J. Zhu, "Network Structured SnO_2/ZnO Heterojunction Nanocatalyst with High Photocatalytic Activity", *Inorganic Chemistry*, Vol. 48, No. 5, pp. 1819-1825, 2009.

108. Navarro, R. M., F. del Valle, and J. L. G. Fierro, "Photocatalytic Hydrogen Evolution from CdS-ZnO-CdO Systems Under Visible Light Irradiation: Effect of Thermal Treatment and Presence of Pt and Ru Co-Catalysts", *International Journal of Hydrogen Energy*, Vol. 33, No. 16, pp. 4265-4273, 2008.

109. Mansournia, M. and L. Ghaderi, "CuO@ZnO Core-Shell Nanocomposites: Novel Hydrothermal Synthesis and Enhancement in Photocatalytic Property", *Journal of Alloys and Compounds*, Vol. 691, pp. 171-177, 2017.

110. Lathasree, S., A. N. Rao, B. Sivasankar, V. Sadasivam, and K. Rengaraj, "Heterogeneous Photocatalytic Mineralisation of Phenols in Aqueous Solutions", *Journal of Molecular Catalysis A: Chemical*, Vol. 223, No. 1, pp. 101-105, 2004.

111. Huang, H., K. Xiao, Y. He and Y. Zhang, "In Situ Assembly of BiOI@Bi12O17Cl2 p-n Junction: Charge Induced Unique Front-Lateral Surfaces Coupling Heterostructure with High Exposure of BiOI {001} Active Facets for Robust and Nonselective Photocatalysis", *Applied Catalysis B: Environmental*, Vol. 199, pp. 75-86, 2016.

112. Huang, H., K. Xiao, T. Zhang, F. Dong, and Y. Zhang, "Rational Design on 3D Hierarchical Bismuth Oxyiodides via In Situ Self-Template Phase Transformation and Phase-Junction Construction for Optimizing Photocatalysis Against Diverse Contaminants", *Applied Catalysis B: Environmental*, Vol. 203, pp. 879-888, 2017.

113. Huang, H., Y. He, X. Du, P. K. Chu, and Y. Zhang, "A General and Facile Approach to Heterostructured Core/Shell $BiVO_4$/BiOI p-n Junction: Room-Temperature in Situ Assembly and Highly Boosted Visible-Light Photocatalysis", *ACS Sustainable Chemistry and Engineering*, Vol. 3, No. 12, pp. 3262-3273, 2015.

114. Gul-E-Noor, F., D. Michel, H. Krautscheid, J. Haase, and M. Bertmer, "Time Dependent Water Uptake in $Cu_3(btc)_2$ MOF: Identification of Different Water Adsorption States by 1H MAS NMR", *Microporous and Mesoporous Materials*, Vol. 180, pp. 8-13, 2013.

115. Castillo, J. M., T. J. H. Vlugt, and S. Calero, "Understanding Water Adsorption in Cu - BTC Metal-Organic Frameworks", *Journal of Physical Chemistry C*, Vol. 112, No. 41, pp. 15934-15939, 2008.

116. Huang, H., X. Li, J. Wang, and Y. Zhang, "Anionic Group Self-Doping as a Promising Strategy: Band-Gap Engineering and Multi-Functional Applications of High-Performance CO_3^{2-}-Doped $Bi_2O_2CO_3$", *ACS Catalysis*, Vol. 5, No. 7, pp. 4094-4103, 2015.

117. Huang, H., A. H. Reshak, S. Auluck, and Y. Zhang, "Visible-Light-Responsive Sillén-Structured Mixed-Cationic $CdBiO_2Br$ Nanosheets: Layer Structure Design Promoting Charge Separation and Oxygen Activation Reactions", *Journal of Physical Chemistry C*, Vol. 122, No. 5, pp. 2661-2672, 2018.

118. Slamet, H. W. Nasution, E. Purnama, S. Kosela, and J. Gunlazuardi, "Photocatalytic Reduction of CO_2 on Copper-Doped Titania Catalysts Prepared by Improved-Impregnation Method", *Catalysis Communications*, Vol. 6, No. 5, pp. 313-319, 2005.

119. Janczarek, M. and E. Kowalska, “On the Origin of Enhanced Photocatalytic Activity of Copper-Modified Titania in the Oxidative Reaction Systems”, *Catalysts*, Vol 7, No. 11, p.317, 2017.

120. Grigioni, I., M. V. Dozzi, M. Bernareggi, G. L. Chiarello, and E. Selli, “Photocatalytic CO_2 Reduction vs. H_2 Production: The Effects of Surface Carbon-Containing Impurities on the Performance of TiO_2-Based Photocatalysts”, *Catalysis Today*, Vol. 281, pp. 214-220, 2017.

121. Cravillon, J., S. Münzer, S. J. Lohmeier, A. Feldhoff, K. Huber, and M. Wiebcke, “Rapid Room-Temperature Synthesis and Characterization of Nanocrystals of a Prototypical Zeolitic Imidazolate Framework”, *Chemistry of Materials*, Vol. 21, No. 8, pp. 1410-1412, 2009.

122. Huang, X. C., Y. Y. Lin, J. P. Zhang, and X. M. Chen, “Ligand-Directed Strategy for Zeolite-Type Metal-Organic Frameworks: Zinc(II) Imidazolates with Unusual Zeolitic Topologies”, *Angewandte Chemie-International Edition*, Vol. 45, No. 10, pp. 1557-1559, 2006.

123. Tian, F., A. M. Cerro, A. M. Mosier, and L. Benz, “Surface and Stability Characterization of a Nanoporous ZIF-8 Thin Film”, *Journal of Physical Chemistry C*, Vol. 118, No. 26, pp. 14449-14456, 2014.

124. Gao, H., W. Wei, L. Dong, and W. Li, “Enhanced Framework Rigidity of a Zeolitic Metal-Azolate via Ligand Substitution”, *Crystals*, Vol. 7, No. 4, p. 99, 2017.

125. Wang, X., J. Liu, S. Leong, and H. Wang, “Rapid Construction of ZnO@ZIF-8 Heterostructures with Size-Selective Photocatalysis Properties”, *ACS Applied Materials and Interfaces*, Vol. 8, No. 14, pp. 9080-9087, 2016.

126. Yu, B., F. Wang, W. Dong, J. Hou, P. Lu, and J. Gong, “Self-Template Synthesis of Core-Shell ZnO@ZIF-8 Nanospheres and the Photocatalysis Under UV Irradiation”, *Materials Letters*, Vol. 156, pp. 50-53, 2015.

127. Du, Y., R. Z. Chen, J. F. Yao, and H. T. Wang, "Facile Fabrication of Porous ZnO by Thermal Treatment of Zeolitic Imidazolate Framework-8 and Its Photocatalytic Activity", *Journal of Alloys and Compounds*, Vol. 551, pp. 125-130, 2013.

128. Anandan, S., A. Vinu, K. L. P. Sheeja Lovely and K. Ariga, "Photocatalytic Activity of La-Doped ZnO for the Degradation of Monocrotophos in Aqueous Suspension.," *Journal of Molecular Catalysis A: Chemical*, Vol. 266, No. 1–2, pp. 149-157, 2007.

129. Galindo, C., P. Jacques, and A. Kalt, Photodegradation of the Aminoazobenzene Acid Orange 52 by Three Advanced Oxidation Processes: UV/H_2O_2, UV/TiO_2 and VIS/TiO_2 Comparative Mechanistic and Kinetic Investigations, *Journal of Photochemistry and Photobiology A: Chemistry*, Vol. 130, No. 1-3, pp. 35-47, 2000.

130. Wang, H. T., Y. P. Liu, H. Zhang, and M. C. Lu, "Design and Synthesis of Porous C–ZnO/TiO_2@ZIF-8 Multi-Component Nano-System via Pyrolysis Strategy with High Adsorption Capacity and Visible Light Photocatalytic Activity", *Microporous and Mesoporous Materials*, Vol. 288, p. 109548, 2019.

131. Pan, L., T. Muhammad, L. Ma, and X. Zhang, "MOF-Derived C-Doped ZnO Prepared via a Two-Step Calcination for Efficient Photocatalysis", *Applied Catalysis B: Environmental*, Vol. 189, pp. 181-191, 2016.

132. Zhou, N., Y. Du, C. Wang, and R. Chen, "Facile Synthesis of Hierarchically Porous Carbons by Controlling the Initial Oxygen Concentration in-situ Carbonization of ZIF-8 for Efficient Water Treatment", *Chinese Journal of Chemical Engineering*, Vol. 26, No. 12, pp. 2523-2530, 2018.

133. Zhang, Y., Y. Jia, and L. Hou, "Synthesis of Zeolitic Imidazolate Framework-8 on Polyester Fiber for PM2.5 Removal", *RSC Advances*, Vol. 8, No. 55, pp. 31471-31477, 2018.

134. Zhou, J., W. Liu, and W. Cai, "The Synergistic Effect of Ag/AgCl@ZIF-8 Modified g-C_3N_4 Composite and Peroxymonosulfate for the Enhanced Visible-Light Photocatalytic Degradation of Levofloxacin", *Science of the Total Environment*, Vol. 696, p. 133962, 2019.

135. Wee, L. H., N. Janssens, S. P. Sree, and J. A. Martens, "Local Transformation of ZIF-8 Powders and Coatings into ZnO Nanorods for Photocatalytic Application", *Nanoscale*, Vol. 6, No. 4, pp. 2056-2060, 2014.

136. Silva, C. G., A. Corma, and H. García, "Metal-Organic Frameworks as Semiconductors", *Journal of Materials Chemistry*, Vol. 20, No. 16, pp. 3141-3156, 2010.

137. Ökte, A. N. and Ö. Yilmaz, "Characteristics of Lanthanum Loaded TiO_2-ZSM-5 Photocatalysts: Decolorization and Degradation Processes of Methyl Orange", *Applied Catalysis A: General*, Vol. 354, No. 1-2, pp. 132-142, 2009.

138. Chen, M., X. Wang, Y. H. Yu, L. S. Wen, "X-Ray Photoelectron Spectroscopy and Auger Electron Spectroscopy Studies of Al-Doped ZnO Films", *Applied Surface Science*, Vol. 158, No.1, pp. 134-140, 2000.

139. Hsieh, P. T., Y. C. Chen, K. S. Kao, and C. M. Wang, "Luminescence Mechanism of ZnO Thin Film Investigated by XPS Measurement", *Applied Physics A: Materials Science and Processing*, Vol. 90, No. 2, pp. 317-321, 2008.

140. Hu, C., L. Lu, Y. Zhu, R. Li, and Y. Xing, "Morphological Controlled Preparation and Photocatalytic Activity of Zinc Oxide", *Materials Chemistry and Physic*, Vol. 217, pp. 182-191, 2018.

141. Jian, M., B. Liu, G. Zhang, R. Liu, and X. Zhang, "Adsorptive Removal of Arsenic from Aqueous Solution by Zeolitic Imidazolate Framework-8 (ZIF-8) Nanoparticles", *Colloids and Surfaces A: Physicochemical and Engineering Aspects*, Vol. 465, pp. 67-76, 2015.

142. Wang, X., W. Cai, Y. Lin, G. Wang, and C. Liang, “Mass Production of Micro/Nanostructured Porous ZnO Plates and Their Strong Structurally Enhanced and Selective Adsorption Performance for Environmental Remediation”, *Journal of Materials Chemistry*, Vol. 20, No. 39, pp. 8582-8590, 2010.

143. Zeng, X., L. Huang, C. Wang, J. Wang, J. Li, and X. Luo, “Sonocrystallization of ZIF-8 on Electrostatic Spinning TiO_2 Nanofibers Surface with Enhanced Photocatalysis Property through Synergistic Effect”, *ACS Applied Materials and Interfaces*, Vol. 8, No. 31, pp. 20274-20282, 2016.

144. Jing, H. P., C. C. Wang, Y. W. Zhang, P. Wang, and R. Li, “Photocatalytic Degradation of Methylene Blue in ZIF-8”, *RSC Advances*, Vol. 4, No. 97, pp. 54454-54462, 2014.

145. Photiou, P. and I. Vyrides, “Calcined Eggshells in Anaerobic Digestion: Buffering Acidification in AD and Evaluating end Products from Phosphate Adsorption as Soil Conditioners”, *Journal of Environmental Chemical Engineering*, Vol. 10, No. 3, p. 107957, 2022.

146. Abdel-Khalek, M. A., M. K. Abdel Rahman, and A. A. Francis, “Exploring the Adsorption Behavior of Cationic and Anionic Dyes on Industrial Waste Shells of Egg”, *Journal of Environmental Chemical Engineering*, Vol. 5, No. 1, pp. 319-327, 2017.

147. Rajoriya, S., V. K. Saharan, A. S. Pundir, M. Nigam, and K. Roy, “Adsorption of Methyl Red Dye from Aqueous Solution onto Eggshell Waste Material: Kinetics, Isotherms and Thermodynamic Studies”, *Current Research in Green and Sustainable Chemistry*, Vol. 4, p. 100180, 2021.

148. Mittal, A., M. Teotia, R. K. Soni, and J. Mittal, “Applications of Egg Shell and Egg Shell Membrane as Adsorbents: A Review”, *Journal of Molecular Liquids*, Vol. 223, pp. 376-387, 2016.

149. Santos, A. F., A. L. Arim, D. V. Lopes, L. M. Gando-Ferreira, and M. J. Quina, "Recovery of Phosphate from Aqueous Solutions Using Calcined Eggshell as an Eco-Friendly Adsorbent", *Journal of Environmental Management*, Vol. 238, pp. 451-459, 2019.

150. Tsai, W. T., K. J. Hsien, H. C. Hsu, C. M. Lin, K. Y. Lin, and C. H. Chiu, "Utilization of Ground Eggshell Waste as an Adsorbent for the Removal of Dyes from Aqueous Solution", *Bioresource Technology*, Vol. 99, No. 6, pp. 1623-1629, 2008.

151. Bin Mobarak, M., M. S. Hossain, Z. Yeasmin, and S. Ahmed, "Probing the Photocatalytic Competency of Hydroxyapatite Synthesized by Solid State and Wet Chemical Precipitation Method", *Journal of Molecular Structure*, Vol. 1252, p. 132142, 2022.

152. Srilakshmi, C. and R. Saraf, "Ag-Doped Hydroxyapatite as Efficient Adsorbent for Removal of Congo Red Dye from Aqueous Solution: Synthesis, Kinetic and Equilibrium Adsorption Isotherm Analysis", *Microporous and Mesoporous Materials*, Vol. 219, pp. 134-144, 2016.

153. Hirakura, S., T. Kobayashi, S. Ono, Y. Oaki, and H. Imai, "Fibrous Nanocrystals of Hydroxyapatite Loaded with TiO_2 Nanoparticles for the Capture and Photocatalytic Decomposition of Specific Proteins", *Colloids and Surfaces B: Biointerfaces*. Vol. 79, No. 1, pp. 131-135, 2010.

154. Miyauchi, M., T. Watanabe, D. Hoshi, and T. Ohba, "Irreversible Adsorption of Acidic, Basic, and Water Gas Molecules on Calcium-Deficient Hydroxyapatite", *Dalton Transactions*, Vol. 48, No. 47, pp. 17507-17515, 2019.

155. Bensalah, H., S. A. Younssi, M. Ouammou, A. Gurlo, and M. F. Bekheet, "Azo Dye Adsorption on an Industrial Waste-Transformed Hydroxyapatite Adsorbent: Kinetics, Isotherms, Mechanism and Regeneration Studies", *Journal of Environmental Chemical Engineering*, Vol. 8, No. 3, p. 103807, 2020.

156. Liu, W., G. Qian, B. Zhang, L. Liu, and H. Liu, “Facile Synthesis of Spherical Nano Hydroxyapatite and Its Application in Photocatalytic Degradation of Methyl Orange Dye Under UV Irradiation”, *Materials Letters*, Vol. 178, pp. 15-17, 2016.

157. Edralin, E. J. M., J. L. Garcia, F. M. dela Rosa, and E. R. Punzalan, “Sonochemical Synthesis, Characterization and Photocatalytic Properties of Hydroxyapatite Nano-Rods Derived from Mussel Shells”, *Materials Letters*, Vol. 196, pp. 33-36, 2017.

158. Begum, S., V. N. Narwade, D. I. Halge, and K. A. Bogle, “Remarkable Photocatalytic Degradation of Remazol Brilliant Blue R Dye Using Bio-Photocatalyst ‘Nano-Hydroxyapatite”, *Materials Research Express*, Vol. 7, No. 2, p.025013, 2020.

159. Bystrov, V. S., C. Piccirillo, D. M. Tobaldi, and R. C. Pullar, “Oxygen Vacancies, the Optical Band Gap (Eg) and Photocatalysis of Hydroxyapatite: Comparing Modelling with Measured Data”, *Applied Catalysis B: Environmental*, Vol. 196, pp. 100-107, 2016.

160. Kanchana, P. and C. Sekar, “EDTA Assisted Synthesis of Hydroxyapatite Nanoparticles for Electrochemical Sensing of Uric Acid”, *Materials Science and Engineering C*, Vol. 42, pp. 601-607, 2014.

161. Reddy, M. P., A. Venugopal, and M. Subrahmanyam, “Hydroxyapatite Photocatalytic Degradation of Calmagite (an Azo Dye) in Aqueous Suspension”, *Applied Catalysis B: Environmental*, Vol. 69, No. 3-4, pp. 164-170, 2007.

162. Tang, M., J. Shen, X. Xia, B. Jin, K. Chen, and T. Zeng, “A Novel Microbial Induced Synthesis of Hydroxyapatite with Highly Efficient Adsorption of Uranyl (VI)”, *Colloids and Surfaces A: Physicochemical and Engineering Aspects*, Vol. 635, p. 128046, 2022.

163. Mohan, N., R. Palangadan, F. B. Fernandez, and H. Varma, “Preparation of Hydroxyapatite Porous Scaffold from a ‘Coral-Like’ Synthetic Inorganic Precursor

for Use as a Bone Substitute and a Drug Delivery Vehicle", *Materials Science and Engineering C*, Vol. 92, pp. 329-337, 2018.

164. Wang, M., H. Ye, X. Zheng and G. Lu, "Adsorption Behaviors and Mechanisms of Simultaneous Cadmium and Fluoride Removal on Waste Bovine Bone from Aqueous Solution", *Journal of Environmental Chemical Engineering*, Vol. 11, No. 1, p. 109035, 2023.

165. Anitta, S. and C. Sekar, "Voltammetric Determination of Paracetamol and Ciprofloxacin in the Presence of Vitamin C Using Cuttlefish Bone-Derived Hydroxyapatite Sub-Microparticles as Electrode Material", *Results in Chemistr,* Vol. 5, p. 100816, 2023.

166. Bramhe, S., T. N. Kim, A. Balakrishnan, and M. C. Chu, "Conversion from Biowaste Venerupis Clam Shells to Hydroxyapatite Nanowires", *Materials Letters*, Vol. 135, pp. 195-198, 2014.

167. Ayodele, O., S. J. Olusegun, O. O. Oluwasina, E. A. Okoronkwo, E. O. Olanipekun, N. D. S. Mohallem, W. G. Guimaraes, B. L. F. M. Gomes, G. O. Souza, and H. A. Duarte, "Experimental and Theoretical Studies of the Adsorption of Cu and Ni Ions from Wastewater by Hydroxyapatite Derived from Eggshells", *Environmental Nanotechnology, Monitoring and Management*, Vol. 15, p. 100439, 2021.

168. Vidhya, G., G. Suresh Kumar B, V. S. Kattimani, and E .K. Girija, *"*Comparative Study of Hydroxyapatite Prepared from Eggshells and Synthetic Precursors by Microwave Irradiation Method for Medical Applications*"*, *Materials Today: Proceedings*, Vol. 15, pp. 344-352, 2019.

169. Bystrov, V. S., C. Piccirillo, D. M. Tobaldi, and R. C. Pullar, "Oxygen Vacancies, the Optical Band Gap (Eg) and Photocatalysis of Hydroxyapatite: Comparing Modelling with Measured Data", *Applied Catalysis B: Environmental*, Vol. 196, pp. 100-107, 2016.

170. Pattanayak, D. K., R. Dash, R. C. Prasad, B. T. Rao, and T. R. Rama Mohan, "Synthesis and Sintered Properties Evaluation of Calcium Phosphate Ceramics", *Materials Science and Engineering C*, Vol. 27, No. 4, pp. 684-690, 2007.

171. Bulina, N. V., S. V. Makarova, S. G. Baev, A. A. Matvienko, K. B. Gerasimov, O. A. Logutenko and V. S. Bystrov, "A Study of Thermal Stability of Hydroxyapatite", *Minerals*, Vol. 11, No. 12, p. 1310, 2021.

172. Abidi, S. S. A. and Q. Murtaza, "Synthesis and Characterization of Nano-Hydroxyapatite Powder Using Wet Chemical Precipitation Reaction", *Journal of Materials Science and Technology*, Vol. 30, No. 4, pp. 307-310, 2014.

173. Hu, W., J. Ma, J. Wang, and S. Zhang, "Fine Structure Study on Low Concentration Zinc Substituted Hydroxyapatite Nanoparticles", *Materials Science and Engineering C*, Vol. 32, No. 8, pp. 2404-2410, 2012.

174. Ofudje, E. A., A. I. Adeogun, M. A. Idowu, and S. O. Kareem, "Synthesis and Characterization of Zn-Doped Hydroxyapatite: Scaffold Application, Antibacterial and Bioactivity Studies", *Heliyon*, Vol. 5, No. 5, p. 01716, 2019.

175. Ran, X., X. Yu, J. He, and Z. Xiao, "Molecular Mechanism of Nano-Hydroxyapatite Surface Changes from Hydrophilic to Hydrophobic", *Asian Journal of Chemistry*, Vol. 26, No. 17, pp. 5355-5359, 2014.

176. Nishikawa, H. and K. Omamiuda, "Photocatalytic Activity of Hydroxyapatite for Methyl Mercaptane", *Molecular Catalysis*, Vol. 179, No.1, pp. 193-200, 2002.

177. Huang, Z., J. Wang, M. Q. Yang, Q. Qian, X. P. Liu, L. Xiao, and H. Xue, "Construction of TiO_2-Eggshell for Efficient Degradation of Tetracycline Hydrochloride: Sunlight Induced In-Situ Formation of Carbonate Radical", *Materials*, Vol. 14, No. 7, p. 1598, 2021.

178. Korake, P. V., R. S. Dhabbe, A. N. Kadam, Y. B. Gaikwad, and K. M. Garadkar, "Highly Active Lanthanum Doped ZnO Nanorods for Photodegradation of Metasystox", *Journal of Photochemistry and Photobiology B: Biology*, Vol. 130, pp. 11-19, 2014.

179. Manikandan, A., E. Manikandan, B. Meenatchi, J. S. Aanand, "Rare Earth Element (REE) Lanthanum Doped Zinc Oxide (La: ZnO) Nanomaterials: Synthesis Structural Optical and Antibacterial Studies", *Journal of Alloys and Compounds*, Vol. 723, pp. 1155-1161, 2017.

180. Chandekar, K. v., M. Shkir, A. Khan, B. M. Al-Shehri, M. S. Hamdy, S. Alfaify, M. A. El-Toni, A. Aldalbahi, A. A. Ansari and H. Ghaithan, "A Facile One-Pot Flash Combustion Synthesis of La@ZnO Nanoparticles and Their Characterizations for Optoelectronic and Photocatalysis Applications", *Journal of Photochemistry and Photobiology A: Chemistry*, Vol. 395, p. 112465, 2020.

181. Nishikawa, H., "Thermal Behavior of Hydroxyapatite in Structural and Spectrophotometric Characteristics", *Materials Letters*, Vol. 50, No-5-6, pp. 364-370, 2001.

182. Hu, M., Z. Yao, X. Liu, L. Ma, Z. He, and X. Wang, "Enhancement Mechanism of Hydroxyapatite for Photocatalytic Degradation of Gaseous Formaldehyde Over TiO_2/Hydroxyapatite", *Journal of the Taiwan Institute of Chemical Engineers*, Vol. 85, pp. 91-97, 2018.

183. Tsukada, M., M. Wakamura, N. Yoshida, and T. Watanabe, "Band Gap and Photocatalytic Properties of Ti-Substituted Hydroxyapatite: Comparison with Anatase-TiO_2" *Journal of Molecular Catalysis A: Chemical*, Vol. 338, No. 1-2, pp. 18-23, 2011.

184. Shariffuddin, J. H., M. I. Jones, and D. A. Patterson, "Greener Photocatalysts: Hydroxyapatite Derived from Waste Mussel Shells for the Photocatalytic

Degradation of a Model Azo Dye Wastewater", *Chemical Engineering Research and Design*, Vol. 91, No. 9, pp. 1693-1704, 2013.

185. Elmi, F., B. Yousefi, M. M. Elmi, H. Alinezhad, and Z. Moulana, "Thermal Decomposition Synthesis of Zn-HAP (Extracted from Fish Scale) Nanopowder and Its Photocatalytic and Antibacterial Activities Under Visible Light", *Ceramics International*, Vol. 47, No. 15, pp. 21862-21872, 2021.

186. Mohamed, R. M. and E. Aazam, "Synthesis and Characterization of Pt-ZnO-Hydroxyapatite Nanoparticles for Photocatalytic Degradation of Benzene Under Visible Light", *Desalination and Water Treatment*, Vol. 51, No. 31, pp. 6082-6090, 2013.

187. Candido, I. C. M., J. M. D. Soares, J. de Araujo Barros Barbosa, and H. P. de Oliveira, "Adsorption and Identification of Traces of Dyes in Aqueous Solutions Using Chemically Modified Eggshell Membranes", *Bioresource Technology Reports*, Vol. 7, p. 100267, 2019.

188. Abdel-Khalek, M. A., M. K. Abdel Rahman, and A .A. Francis, "Exploring the Adsorption Behavior of Cationic and Anionic Dyes on Industrial Waste Shells of Egg", *Journal of Environmental Chemical Engineering*, Vol. 5, No. 1, pp. 319-327, 2017.

189. Flores-Cano, J. V., R. Leyva-Ramos, J. Mendoza-Barron, R. M. Guerrero-Coronado, A. Aragón-Piña, and G.J. Labrada-Delgado, "Sorption Mechanism of Cd(II) from Water Solution onto Chicken Eggshell", *Applied Surface Science*, Vol. 276, pp. 682-690, 2013.

190. Wang, J., S. Sun, L. Pan, Z. Xu, H. Ding, and W. Li, "Preparation and Properties of $CaCO_3$-Supported Nano-TiO_2 Composite with Improved Photocatalytic Performance", *Materials*, Vol. 12, No. 20, p.3369, 2019.

191. Mansri, A., H. Mahroug, and F. Dergal, “In Situ Preparation of Hydroxyapatite Composites into Hydrolyzed Polyacrylamide Solution and Methylene Blue Dye Retention”, *Turkish Journal of Chemistry*, Vol. 43, No. 2, pp. 582-593, 2019.

192. Hokkanen, S., A. Bhatnagar, E. Repo, S. Lou, and M. Sillanpää, “Calcium Hydroxyapatite Microfibrillated Cellulose Composite as a Potential Adsorbent for the Removal of Cr(VI) from Aqueous Solution”, *Chemical Engineering Journal*, Vol. 283, pp. 445-452, 2016.

193 Labrag, J., C. el Bekkali, A. Oulguidoum, D. Robert, A. Laghzizil, and J. M. Nunzi, “Porous and Bifunctional ZnO-Hydroxyapatite Nanostructure for Photocatalytic Degradation of Paracetamol and Methylene Blue in Water”, *Iranian Journal of Catalysis*, Vol. 11, No. 4, pp. 389-395, 2021.

194. Yeasmin, Z., A. Alim, S. Ahmed, M. M. Rahman, S. M. Masum, and A. K. Ghosh, “Synthesis, Characterization and Efficiency of HAp-TiO_2-ZnO Composite as a Promising Photocatalytic Material”, *Transactions of the Indian Ceramic Society*, Vol. 77, No. 3, pp. 161-168, 2018.

195. Mohamed, R. M. and E. S. Baeissa, “Preparation and Characterisation of Pd-TiO_2-Hydroxyapatite Nanoparticles for the Photocatalytic Degradation of Cyanide Under Visible Light”, *Applied Catalysis A: General*, Vol. 464-465, pp. 218-224, 2013.

196 Liu, W., G. Qian, L. Liu, and M. Gao, “The Growth Mechanism of Titania/Hydroxyapatite and Its Application in the Photodegradation of Methyl Orange Dye Under UV Irradiation”, *Results in Physics*, Vol. 11, pp. 112-117, 2018.

197. Elkady, M. F., A. M. Ibrahim, and M. M. A. El-Latif, “Assessment of the Adsorption Kinetics, Equilibrium and Thermodynamic for the Potential Removal of Reactive Red Dye Using Eggshell Biocomposite Beads”, *Desalination*, Vol. 278, No. 1-3, pp. 412-423, 2011.

198. Batool, F., J. Akbar, S. Iqbal, S. Noreen, and S. N. A. Bukhari, “Study of Isothermal, Kinetic, and Thermodynamic Parameters for Adsorption of Cadmium: An Overview of Linear and Nonlinear Approach and Error Analysis”, *Bioinorganic Chemistry and Applications*, Vol. 2018, p. 3463724, 2018.

199. Dębek, R., M. Motak, T. Grzybek, M. E. Galvez, and P. da Costa, “A Short Review on the Catalytic Activity of Hydrotalcite-Derived Materials for Dry Reforming of Methane”, *Catalysts*, Vol, 7, No.1, p.32, 2017.

200. Bukhtiyarova, M. V., “A Review on Effect of Synthesis Conditions on the Formation of Layered Double Hydroxides”, *Journal of Solid State Chemistry*, Vol. 269, pp. 494-506, 2019.

201. Chen, Y., L. Wu, W. Yao, J. Wu, Z. Xie, Y. Yuan and F. Pan, “In Situ Growth of Mg-Zn-Al LDHs by ZIF-8 Carrying Zn Source and Micro-Arc Oxidation Integrated Coating for Corrosion and Protection of Magnesium Alloys”, *Surface and Coatings Technology*, Vol. 451, p. 129032, 2022.

202. Li, S. and B. Bhushan, “Lubrication Performance and Mechanisms of Mg/Al-, Zn/Al, and Zn/Mg/Al-Layered Double Hydroxide Nanoparticles as Lubricant Additives”, *Applied Surface Science*, Vol. 378, pp. 308-319, 2016.

203. Haraketi, M., K. Hosni, and E. Srasra, “Intercalation Behavior of Salicylic Acid into Calcined Cu-Al-Layered Double Hydroxides for a Controlled Release Formulation”, *Surface Engineering and Applied Electrochemistry*, Vol. 53, No. 4, pp. 360-370, 2017.

204. Shi, Z., Y. Wang, S. Sun, C. Zhang, and H. Wang, “Removal of Methylene Blue from Aqueous Solution Using Mg-Fe, Zn-Fe, Mn-Fe Layered Double Hydroxide”, *Water Science and Technology*, Vol. 81, No. 12, pp. 2522-2532, 2020.

205. Parida, K. M. and L. Mohapatra, "Carbonate Intercalated Zn/Fe Layered Double Hydroxide: A novel Photocatalyst for the Enhanced Photo Degradation of Azo Dyes", *Chemical Engineering Journal*, Vol. 179, pp. 131-139, 2012.

206. Zhou, Y., W. Hu, J. Yu, and F. Jiao, "Effective Photocatalytic Degradation of Methylene Blue by Cu_2O/MgAl Layered Double Hydroxides", *Reaction Kinetics, Mechanisms and Catalysis*, Vol. 115, No. 2, pp. 581-596, 2015.

207. Daud, M., A. Hai, F. Banat, M. B. Wazir, M. Habib, G. Bharath and M. A. Al-Harthi, "A Review on the Recent Advances, Challenges and Future Aspect of Layered Double Hydroxides (LDH)-Containing Hybrids as Promising Adsorbents for Dyes Removal", *Journal of Molecular Lipids*, Vol. 288, p. 110989, 2019.

208. Mantilla, A., F. Tzompantzi, J.L. Fernández, J. A. I. D. Góngora, and R. Gómez, "Photodegradation of Phenol and Cresol in Aqueous Medium by Using Zn/Al+Fe Mixed Oxides Obtained from Layered Double Hydroxides Materials", *Catalysis Today*, Vol. 150, No. 3-4, pp. 353-357, 2010.

209. Morimoto, K., K. Tamura, N. Iyi, J. Ye, and H. Yamada, "Adsorption and Photodegradation Properties of Anionic Dyes by Layered Double Hydroxides", *Journal of Physics and Chemistry of Solids*, Vol. 72, No. 9, pp. 1037-1045, 2011.

210. Caporale, A. G., M. Pigna, J. J. Dynes, V. Cozzolino, J. Zhu, and A. Violante, "Effect of Inorganic and Organic Ligands on the Sorption/Desorption of Arsenate on/from Al-Mg and Fe-Mg Layered Double Hydroxides", *Journal of Hazardous Materials*, Vol. 198, pp. 291-298, 2011.

211. Gilea, D., R. G. Ciocarlan, E. M. Seftel, P. Cool, and G. Carja, "Engineering Heterostructures of Layered Double Hydroxides and Metal Nanoparticles for Plasmon-Enhanced Catalysis", *Catalysts*, Vol. 12, No. 10, p. 1210, 2022.

212. Santos, R. M. M., J. Tronto, V. Briois, and C. V. Santilli, "Thermal Decomposition and Recovery Properties of ZnAl-CO_3 Layered Double Hydroxide for Anionic Dye

Adsorption: Insight into the Aggregative Nucleation and Growth Mechanism of the LDH Memory Effect", *Journal of Materials Chemistry A*, Vol. 5, No. 20, pp. 9998-10009, 2017.

213. Zaghouane-Boudiaf, H., M. Boutahala, and L. Arab, "Removal of Methyl Orange from Aqueous Solution by Uncalcined and Calcined MgNiAl Layered Double Hydroxides (LDHs)", *Chemical Engineering Journal*, Vol. 187, pp. 142-149, 2012.

214. Lei, C., M. Pi, P. Kuang, Y. Guo, and F. Zhang, "Organic Dye Removal from Aqueous Solutions by Hierarchical Calcined Ni-Fe Layered Double Hydroxide: Isotherm, Kinetic and Mechanism Studies", *Journal of Colloid and Interface Science*, Vol. 496, pp. 158-166, 2017.

215. Gaini, L., M. Lakraimi, E. Sebbar, A. Meghea, and M. Bakasse, "Removal of Indigo Carmine Dye from Water to Mg-Al-CO_3-Calcined Layered Double Hydroxides", *Journal of Hazardous Materials*, Vol. 161, No. 2-3, pp. 627-632, 2009.

216. Santos, R. M. M., R. G. L. Gonçalves, V. R. L. Constantino, F. G. Pinto, "Adsorption of Acid Yellow 42 Dye on Calcined Layered Double Hydroxide: Effect of Time, Concentration, pH and Temperature", *Applied Clay Science*, Vol. 140, pp. 132-139, 2017.

217. Guo, Y., Z. Zhu, Y. Qiu, and J. Zhao, "Enhanced Adsorption of Acid Brown 14 Dye on Calcined Mg/Fe Layered Double Hydroxide with Memory Effect", *Chemical Engineering Journal*, Vol. 219, pp. 69-77, 2013.

218. Yang, Q., S. Wang, F. Chen, and G. Zeng, "Enhanced Visible-Light-Driven Photocatalytic Removal of Refractory Pollutants by Zn/Fe Mixed Metal Oxide Derived from Layered Double Hydroxide", *Catalysis Communications*, Vol. 99, pp. 15-19, 2017.

219. Seftel, E. M., E. Popovici, M. Mertens, and E. F. Vansant, “Zn-Al Layered Double Hydroxides: Synthesis, Characterization and Photocatalytic Application”, *Microporous and Mesoporous Materials*, Vol. 113, No. 1-3, pp. 296-304, 2008.

220. Zhao, Y., M. Wei, J. Lu, Z.L. Wang, and X. Duan, “Biotemplated Hierarchical Nanostructure of Layered Double Hydroxides with Improved Photocatalysis Performance”, *ACS Nano*, Vol. 3, No. 12, pp. 4009-4016, 2009.

221. Rashed, S. H., A. I. Abd-Elhamid, S. Y. H. Abdalkarim, and A. A. Nayl, “Preparation and Characterization of Layered-Double Hydroxides Decorated on Graphene Oxide for Dye Removal from Aqueous Solution”, *Journal of Materials Research and Technology*, Vol. 17, pp. 2782-2795, 2022.

222. Gholami, P., A. Khataee, R. D. C. Soltani, L. Dinpazhoh, and A. Bhatnagar, “Photocatalytic Degradation of Gemifloxacin Antibiotic Using Zn-Co-LDH@Biochar Nanocomposite”, *Journal of Hazardous Materials*, Vol. 382, p. 121070, 2020.

223. Yu, Z., X. Li, Y. Peng, X. Min, D. Yin, and L. Shao, “MgAl-Layered-Double-Hydroxide/Sepiolite Composite Membrane for High-Performance Water Treatment Based on Layer-by-Layer Hierarchical Architectures”, *Polymers*, Vol. 11, No. 3, p. 525, 2019.

224. Biernacki, J. J., A. K. Vazrala, and H. W. Leimer, “Sintering of a Class F Fly Ash”, *Fuel*, Vol. 87, No. 6, pp. 782-792, 2008.

225. Qin, B., Y. Lu, Y. Li, and D. Wang, “Aqueous Three-Phase Foam Supported by Fly Ash for Coal Spontaneous Combustion Prevention and Control”, *Advanced Powder Technology*, Vol. 25, No. 5, pp. 1527-1533, 2014.

226. Minmin L., L. Hou, B. Xi, Y. Zhao, and X. Xia, “Synthesis, Characterization and Mercury Adsortpion Properties of Hybrid Mesoporous Aluminosilicate Sieve Prepared with Fly Ash”, *Applied Surface Science*, Vol. 273, pp. 706-716, 2013.

227. Lei, Z., S. Hao, J. Yang, L. Zhang, B. Fang, K. Wei, Q. Lingbo and C. Wei, "Study on Denitration and Sulfur Removal Performance of Mn–Ce Supported Fly Ash Catalyst", *Chemosphere*, Vol. 270, p. 128646, 2021.

228. Yusuff, A. S., A. K. Bhonsle, J. Trivedi, D. P. Bangwal, L. P. Singh, and N. Atray, "Synthesis and Characterization of Coal Fly Ash Supported Zinc Oxide Catalyst for Biodiesel Production Using Used Cooking Oil as Feed", *Renewable Energy*, Vol. 170, pp. 302-314, 2021.

229. Usman, M., I. Anastopoulos, Y. Hamid, and A. Wakeel, "Recent Trends in the Use of Fly Ash for the Adsorption of Pollutants in Contaminated Wastewater and Soils: Effects on Soil Quality and Plant Growth", *Environmental Science and Pollution Research*, Vol. 23, p. 19192, 2022.

230. Sareen, D., R. Garg, and N. Grover, "A Study on Removal of Methylene Blue Dye From Waste Water By Adsorption Technique Using Fly Ash Briquette", *International Journal of Engineering and Technology*, Vol. 3. No. 7, pp. 610-613, 2014.

231. Sun, D., X. Zhang, Y. Wu, and X. Liu, "Adsorption of Anionic Dyes from Aqueous Solution on Fly Ash", *Journal of Hazardous Materials*, Vol. 181, No. 1-3, pp. 335-342, 2010.

232. Lei, Z., S. Hao, J. Yang, L. Zhang, B. Fang, K. Wei, Q. Lingbo, S. Jin, and C. Wei, "Study on Denitratio and Sulfur Removal Performance of Mn, Ce Supported Fly Ash Catalyst", *Chemosphere*, Vol. 270, p. 128646, 2021.

233. Katančić, Z., I. Gavran, J. Smolković, and Z. Hrnjak-Murgić, "Fly Ash Supported Photocatalytic Nanocomposite Poly(3,4-Ethylenedioxythiophene)/TiO_2 for Azo Dye Removal Under Simulated Solar Irradiation", *Journal of Applied Polymer Science*, Vol. 135, No. 22, p. 46316, 2018.

234. Wen, J., H. Dong, and G. Zeng, "Application of Zeolite in Removing Salinity/Sodicity from Wastewater: A Review of Mechanisms, Challenges and Opportunities", *Journal of Cleaner Production*, Vol. 197, No.1 pp. 1435-1446, 2018.

235. Alver, E. and A. Metin, "Anionic Dye Removal from Aqueous Solutions Using Modified Zeolite: Adsorption Kinetics and Isotherm Studies", *Chemical Engineering Journal*, Vol. 200-202, pp. 59-67, 2012.

236. Malamis, S. and E. Katsou, "A Review on Zinc and Nickel Adsorption on Natural and Modified Zeolite, Bentonite and Vermiculite: Examination of Process Parameters, Kinetics and Isotherms", *Journal of Hazardous Materials*, Vol. 252, pp. 428-461, 2013.

237. Piri, F., A. Mollahosseini, A. Khadir, and M. M. Hosseini, "Enhanced Adsorption of Dyes on Microwave-Assisted Synthesized Magnetic Zeolite-Hydroxyapatite Nanocomposite", *Journal of Environmental Chemical Engineering*, Vol. 7, No. 5, p. 103338, 2019.

238 Shaban, M., M. R. Abukhadra, M. G. Shahien, and S. S. Ibrahim, "Novel Bentonite/Zeolite-NaP Composite Efficiently Removes Methylene Blue and Congo Red Dyes", *Environmental Chemistry Letters*, Vol. 16, No. 1, pp. 275-280, 2018.

239. Ravi, M., V. L. Sushkevich, and J. A. van Bokhoven, "Towards a Better Understanding of Lewis Acidic Aluminium in Zeolites", *Nature Materials*, Vol. 19, pp. 1047-1056, 2020.

240. Alswata, A., M. B. hmad, N. M. Al-Hada, H. M. Kamari, M. Z. B. Hussein and N. A. Inrahim, "Preparation of Zeolite/Zinc Oxide Nanocomposites for Toxic Metals Removal from Water", *Results in Physics*, Vol. 7, pp. 723-731, 2017.

241. Gong, T., L. Qin, J. Lu and H. Feng, "ZnO Modified ZSM-5 and Y Zeolites Fabricated by Atomic Layer Deposition for Propane Conversion", *Physical Chemistry Chemical Physics*, Vol. 18, No.1, pp.601-614, 2016.

242. Gayatri, R., T. E. Agustina, R. Moeksin, D. Bahrin and G. Gustini, "Preparation and Characterization of ZnO-Zeolite Nanocomposite for Photocatalytic Degradation by Ultraviolet Light", *Journal of Ecological Engineering*, Vol. 22, No.2, pp. 178-186, 2021.

243. Iazdani, F. and A. Nezamzadeh-Ejhieh, "The Photocatalytic Rate of ZnO Supported Onto Natural Zeolite Nanoparticles in the Photodegradation of an Aromatic Amine", *Environmental Science and Pollution Research*, Vol. 28, No. 38, pp. 53314-53327, 2021.

244. Fukahori, S. and T. Fujiwara, "Preparation of Flexible TiO_2/Zeolite Composite Sheets for Removal of Sulfamethazine from Wastewater Using Papermaking Technique", *Journal of Water and Environment Technology*, Vol. 17, No. 6, pp. 395-406, 2019.

245. Inayat, A., M. Klumpp, and W. Schwieger, "The Urea Method for the Direct Synthesis of ZnAl Layered Double Hydroxides with Nitrate as the Interlayer Anion", *Applied Clay Science*, Vol. 51, No. 4, pp. 452-459, 2011.

246. Fang, H., F. Meng, J. Yan, Y. Zhang, "Fe_3O_4 Hard Templating to Assemble Highly Wrinkled Graphene Sheets into Hierarchical Porous Film for Compact Capacitive Energy Storage", *RSC Advances*, Vol. 9, No. 35, pp. 20107-20112, 2019.

247. Ji, H., W. Wu, F. Li, X. Yu, J. Fu, and L. Jia, "Enhanced Adsorption of Bromate from Aqueous Solutions on Ordered Mesoporous Mg-Al Layered Double Hydroxides (LDHs)", *Journal of Hazardous Materials*, Vol. 334, pp. 212-222, 2017.

248. Zhang, L., Z. Xiong, L. Li, R. Burt, and X. S. Zhao, "Uptake and Degradation of Orange II by Zinc Aluminum Layered Double Oxides", *Journal of Colloid and Interface Science*, Vol. 469, pp. 224-230, 2016.

249. Hu, M., X. Yan, X. Hu, R. Feng, and M. Zhou, "High-Capacity Adsorption of Benzotriazole from Aqueous Solution by Calcined Zn-Al Layered Double

Hydroxides", *Colloids and Surfaces A: Physicochemical and Engineering Aspects*, Vol. 540, pp. 207-214, 2018.

250. Zuo, J., Z. C. Peng, B. Dong, and Y. Wang, "In Situ Growth of Corrosion Resistant Mg-Fe Layered Double Hydroxide Film on Q235 Steel", *Journal of Colloid and Interface Science*, Vol. 610, pp. 202-212, 2022.

251. Loh, K. S., Y. H. Lee, A. Musa, A. A. Salmah, and I. Zamri, "Use of Fe_3O_4 Nanoparticles for Enhancement of Biosensor Response to the Herbicide 2,4-Dichlorophenoxyacetic Acid", *Sensors*, Vol. 8, No. 9, pp. 5775-5791, 2008.

252. Zhu, M. X., Y. P. Li, M. Xie, and H. Z. Xin, "Sorption of an Anionic Dye by Uncalcined and Calcined Layered Double Hydroxides: A Case Study", *Journal of Hazardous Materials*, Vol. 120, No. 1-3, pp. 163-171, 2005.

253. Li, F., X. Jiang, D. G. Evans, and X. Duan, "Structure and Basicity of Mesoporous Materials from Mg/Al/In Layered Double Hydroxides Prepared by Separate Nucleation and Aging Steps Method", *Journal of Porous Materials*, Vol. 12, pp. 55-63, 2005.

254. Zhao, X., L. Wang, X. Xu, X. Lei, S. Xu, and F. Zhang, "Fabrication and Photocatalytic Properties of Novel $ZnO/ZnAl_2O_4$ Nanocomposite with $ZnAl_2O_4$ Dispersed Inside ZnO Network", *AIChE Journal*, Vol. 58, No. 2, pp. 573-582, 2012.

255. Ji, H., W. Wu, F. Li, X. Yu, J. Fu, and L. Jia, "Enhanced Adsorption of Bromate from Aqueous Solutions on Ordered Mesoporous Mg-Al Layered Double Hydroxides (LDHs)", *Journal of Hazardous Materials*, Vol. 334, pp. 212-222, 2017.

256. Peng, C., J. Dai, J. Yu, and J. Yin, "Calcined Mg-Fe Layered Double Hydroxide as an Absorber for the Removal of Methyl Orange", *AIP Advances*, Vol. 5, No. 5, p. 057138, 2015.

257. Santos, R. M. M., J. Tronto, V. Briois, and C. Santilli, “Thermal Decomposition and Recovery Properties of ZnAl-CO_3 Layered Double Hydroxide for Anionic Dye Adsorption: Insight into the Aggregative Nucleation and Growth Mechanism of the LDH Memory Effect”, *Journal of Materials Chemistry A*, Vol. 5, No. 20, pp. 1-11, 2017.

258. Shan, R. Ran, L. Yan, Y. Yang, B. Du, “Highly Efficient Removal of Three Red Dyes by Adsorption onto Mg-Al-Layered Double Hydroxide”, *Journal of Industrial and Engineering Chemistry*, Vol. 21, pp. 561-568, 2015.

259. Chen, Y., Z. Shui, W. Chen, Q. Li, and G. Chen, “Effect of MgO Content of Synthetic Slag on the Formation of Mg-Al LDHs and Sulfate Resistance of Slag-Fly Ash-Clinker Binder”, *Construction and Building Materials*, Vol. 125, pp. 766-774, 2016.

260. Mantilla, A., G. Jácome-Acatitla, G. Morales-Mendoza, F. Tzompantzi, and R. Gómez, “Photoassisted Degradation of 4-Chlorophenol and P-Cresol Using MgAl Hydrotalcites”, *Industrial and Engineering Chemistry Research*, Vol. 50, No. 5, pp. 2762-2767, 2011.

261. Flores-Flores, M., E. Luévano-Hipólito, L. M. T. Martínez, G. Morales-Mendoza, and R. Gómez, “Photocatalytic CO_2 Conversion by MgAl Layered Double Hydroxides: Effect of Mg^{2+} Precursor and Microwave Irradiation Time”, *Journal of Photochemistry and Photobiology A: Chemistry*, Vol. 363, pp. 68-73, 2018.

262. Ramos-Ramírez, E., N. L. Gutiérrez-Ortega, F. Tzompantzi-Morales, G. A. del Ángel, C. Martínez-Gómez, and E. Pabón-Gelves, “Effect of the Mg/Al Ratio on Activated Sol-Gel Hydrotalcites for Photocatalytic Degradation of 2,4,6-Trichlorophenol”, *International Journal of Photoenergy*, Vol. 3-4, pp. 1-9, 2017.

263. Morimoto, K., K. Tamura, H. Yamada, T. Sato, and M. Suzuki, “Determination and Reduction of Fe(III) Incorporated into Mg-Fe Layered Double Hydroxide Structures”, *Applied Clay Science*, Vol. 121-122, pp. 71-76, 2016.

264. Kusior, A., K. Michalec, P. Jelen, and M. Radecka, "Shaped Fe_2O_3 Nanoparticles Synthesis and Enhanced Photocatalytic Degradation Towards RhB", *Applied Surface Science*, Vol. 476, pp. 342-352, 2019.

265. Liu, J., B. Wang, Z. Li, and Z. Lin, "Photo-Fenton Reaction and H_2O_2 Enhanced Photocatalytic Activity of α-Fe_2O_3 Nanoparticles Obtained by a Simple Decomposition Route", *Journal of Alloys and Compounds*, Vol. 771, pp. 398-405, 2019.

266. Al-Kuhaili, M. F., M. Saleem, and S. M. A. Durrani, "Optical Properties of Iron Oxide (α-Fe_2O_3) Thin Films Deposited by the Reactive Evaporation of Iron", *Journal of Alloys and Compounds*, Vol. 521, pp. 178-182, 2012.

267. Xia, S. J., F. X. Liu, Z. M. Ni, J. L. Xue, and P. P. Qian, "Layered Double Hydroxides as Efficient Photocatalysts for Visible-Light Degradation of Rhodamine B", *Journal of Colloid and Interface Science*, Vol. 405, pp. 195-200, 2013.

268. Ahmed, A. A. A., Z.A. Talib, M. Z. bin Hussein, and A. Zakaria, "Improvement of the Crystallinity and Photocatalytic Property of Zinc Oxide as Calcination Product of Zn-Al Layered Double Hydroxide", *Journal of Alloys and Compounds*, Vol. 539, pp. 154-160, 2012.

269. Sharma, S., G. Sharma, A. Kumar, and F. J. Stadler, "Controlled Synthesis of Porous Zn/Fe Based Layered Double Hydroxides: Synthesis Mechanism, and Ciprofloxacin Adsorption", *Separation and Purification Technology*, Vol. 278, p. 119481, 2022.

270. Huang, P., J. Liu, F. Wei, W. Song, "Size-Selective Adsorption of Anionic Dyes Induced by the Layer Space in Layered Double Hydroxide Hollow Microspheres", *Materials Chemistry Frontiers*, Vol. 1, No. 8, pp. 1550-1555, 2017.

271. Morimoto, K., K. Tamura, N. Iyi, J. Ye, and H. Yamada, "Adsorption and Photodegradation Properties of Anionic Dyes by Layered Double Hydroxides", *Journal of Physics and Chemistry of Solids*, Vol. 72, No. 9, pp. 1037-1045, 2011.

272. Fahel, J., S. Kim, P. Durand, E. André, and C. Carteret, “Enhanced Catalytic Oxidation Ability of Ternary Layered Double Hydroxides for Organic Pollutants Degradation”, *Dalton Transactions*, Vol. 45, No. 19, pp. 8224-8235, 2016.

273. Santamaría, L., M. López-Aizpún, M. García-Padial, M. A. Vicente, S. A. Korili, and A. Gil, “Zn-Ti-Al Layered Double Hydroxides Synthesized from Aluminum Saline Slag Wastes as Efficient Drug Adsorbents”, *Applied Clay Science*, Vol. 187, p. 105486, 2020.

274. Shan, Z., M. Lu, D.E. Curry, and X. Zhang, “Regenerative Nanobots Based on Magnetic Layered Double Hydroxide for Azo Dye Removal and Degradation”, *Chemical Communications*, Vol. 53, No. 75, pp. 10456-10458, 2017.

275. Mohapatra, L. and K. Parida, “A Review on the Recent Progress, Challenges and Perspective of Layered Double Hydroxides as Promising Photocatalysts”, *Journal of Materials Chemistry A*, Vol. 4, No. 28, pp. 10744-10766, 2016.

276. Parida, K. M. and L. Mohapatra, “Carbonate Intercalated Zn/Fe Layered Double Hydroxide: A Novel Photocatalyst for the Enhanced Photo Degradation of Azo Dyes”, *Chemical Engineering Journal*, Vol. 179, pp. 131-139, 2012.

277. Ahmed, A. A. A., Z. A. Talib, M. Z. bin Hussein, and A. Zakaria, “Zn-Al Layered Double Hydroxide Prepared at Different Molar Ratios: Preparation, Characterization, Optical and Dielectric Properties”, *Journal of Solid State Chemistry*, Vol. 191, pp. 271-278, 2012.

278. Song, J., M. Leng, X. Fu, and J. Liu, “Synthesis and Characterization of Nanosized Zinc Aluminate Spinel from a Novel Zn-Al Layered Double Hydroxide Precursor”, *Journal of Alloys and Compounds*, Vol. 543, pp. 142-146, 2012.

279. Morimoto, K., K. Tamura, H. Yamada, T. Sato, and M. Suzuki, “Determination and Reduction of Fe (III) Incorporated into Mg-Fe Layered Double Hydroxide Structures”, *Applied Clay Science*, Vol. 121-122, pp. 71-76, 2016.

280. Parida, K. M. and L. Mohapatra, “Carbonate Intercalated Zn/Fe Layered Double Hydroxide: A Novel Photocatalyst for the Enhanced Photo Degradation of Azo Dyes”, *Chemical Engineering Journal*, Vol. 179, pp. 131-139, 2012.

281. Ghasemian, N. and C. Falamaki, “Zn^{2+}, Fe^{2+}, Cu^{2+}, Mn^{2+}, H^{+} Ion-Exchanged and Raw Clinoptilolite Zeolite Catalytic Performance in the Propane-SCR-NOx Process: A Comparative Study”, *International Journal of Chemical Reactor Engineering*, Vol. 16, No. 1, p. 20160192, 2018.

282. Tao, X., D. Liu, W. Cong, and L. Huang, “Controllable Synthesis of Starch-Modified ZnMgAl-LDHs for Adsorption Property Improvement”, *Applied Surface Science*, Vol. 457, pp. 572-579, 2018.

APPENDIX A:

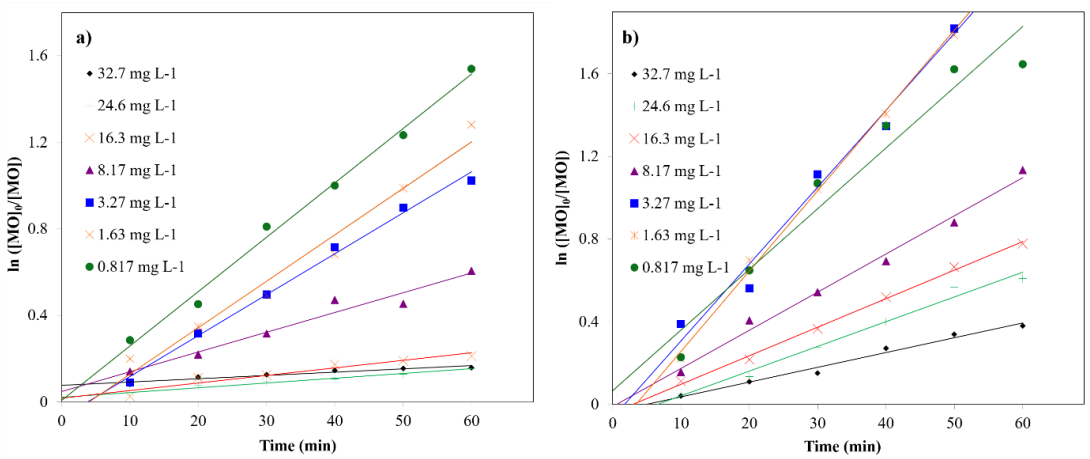

Figure A.1. Pseudo first order kinetic analysis in the presence of (a) TiO_2-hybrid PNC and (b) TiO_2-hybrid PNC (84% RH).

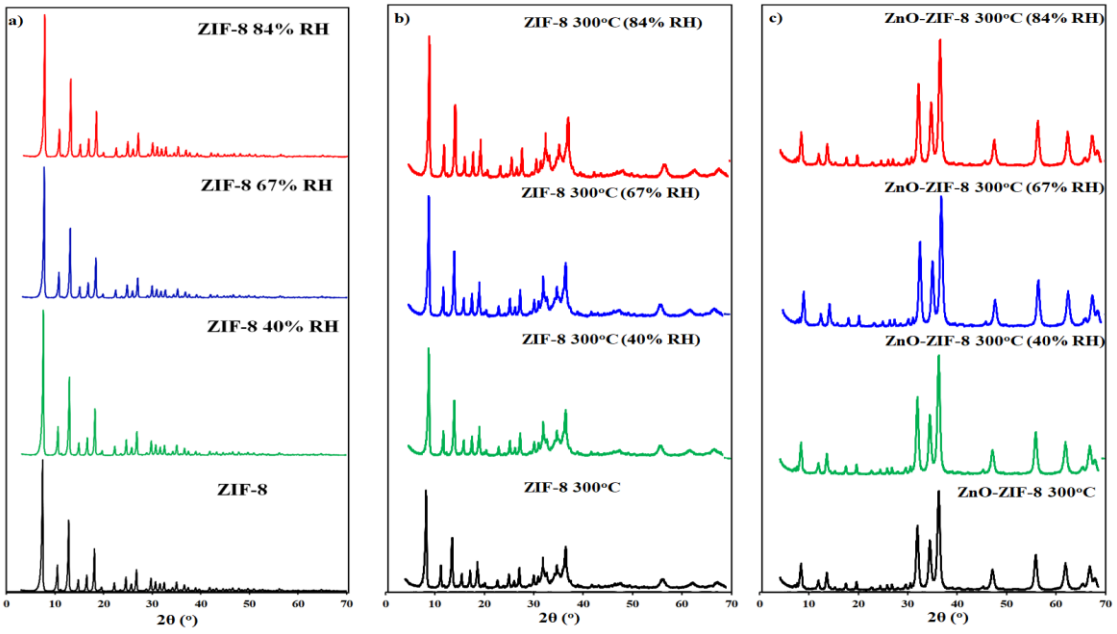

Figure A.2. (a) XRD patterns of ZIF-8, ZIF-8 (40% RH), ZIF-8 (64% RH), ZIF-8 (84%), (b) ZIF-8 300°C (40% RH), ZIF-8 300°C (67% RH), ZIF-8 300°C (84%), (c) ZnO-ZIF-8 300°C, ZnO-ZIF-8 300°C (40% RH), ZnO-ZIF-8 300°C (67% RH), ZnO-ZIF-8 300°C (84%).

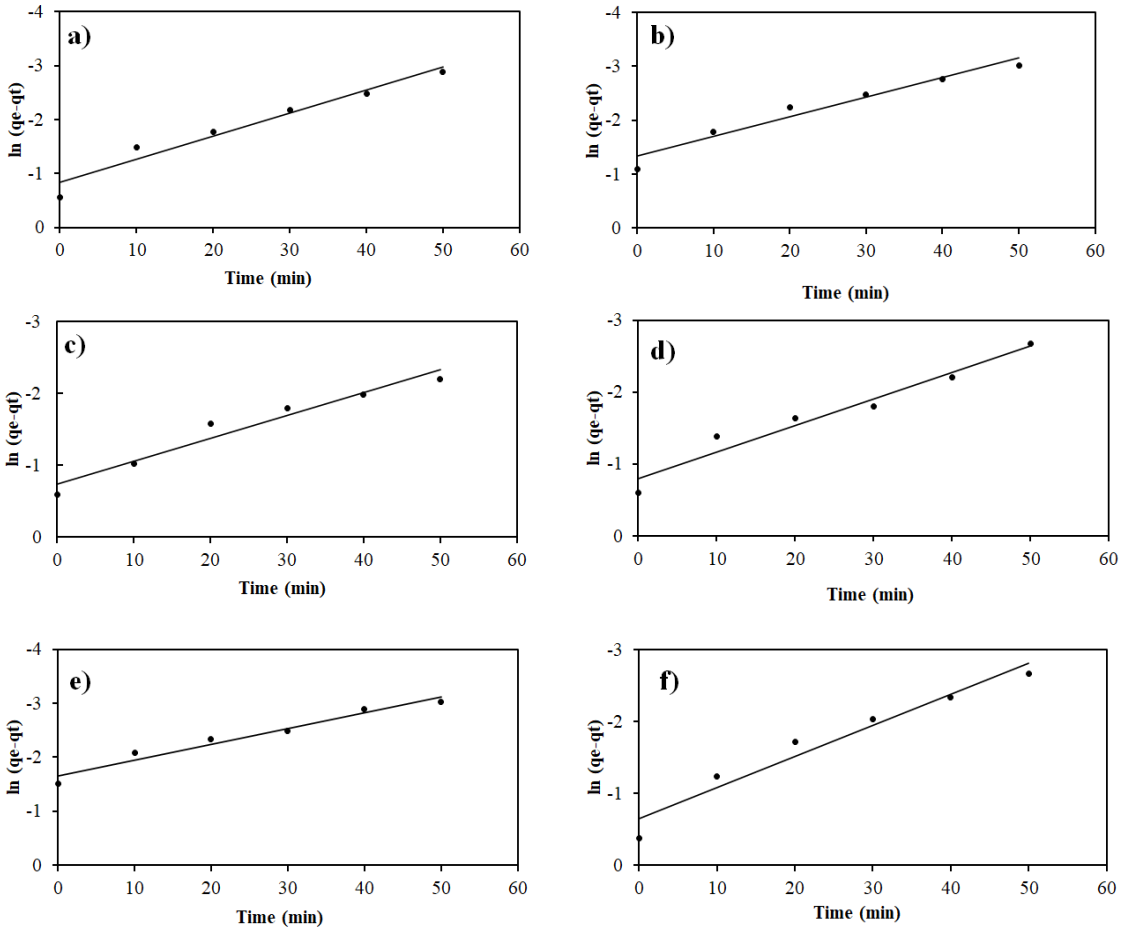

Figure A.3. Pseudo-first order kinetic analysis in the presence of a) eggshell for MO, b) eggshell for MB, c) ZnO-Eggshell 500^{o}C for MO, d) ZnO-Eggshell 500^{o}C for MB, e) La-ZnO-Eggshell 500^{o}C for MO and e) La-ZnO-Eggshell 500^{o}C for MB.

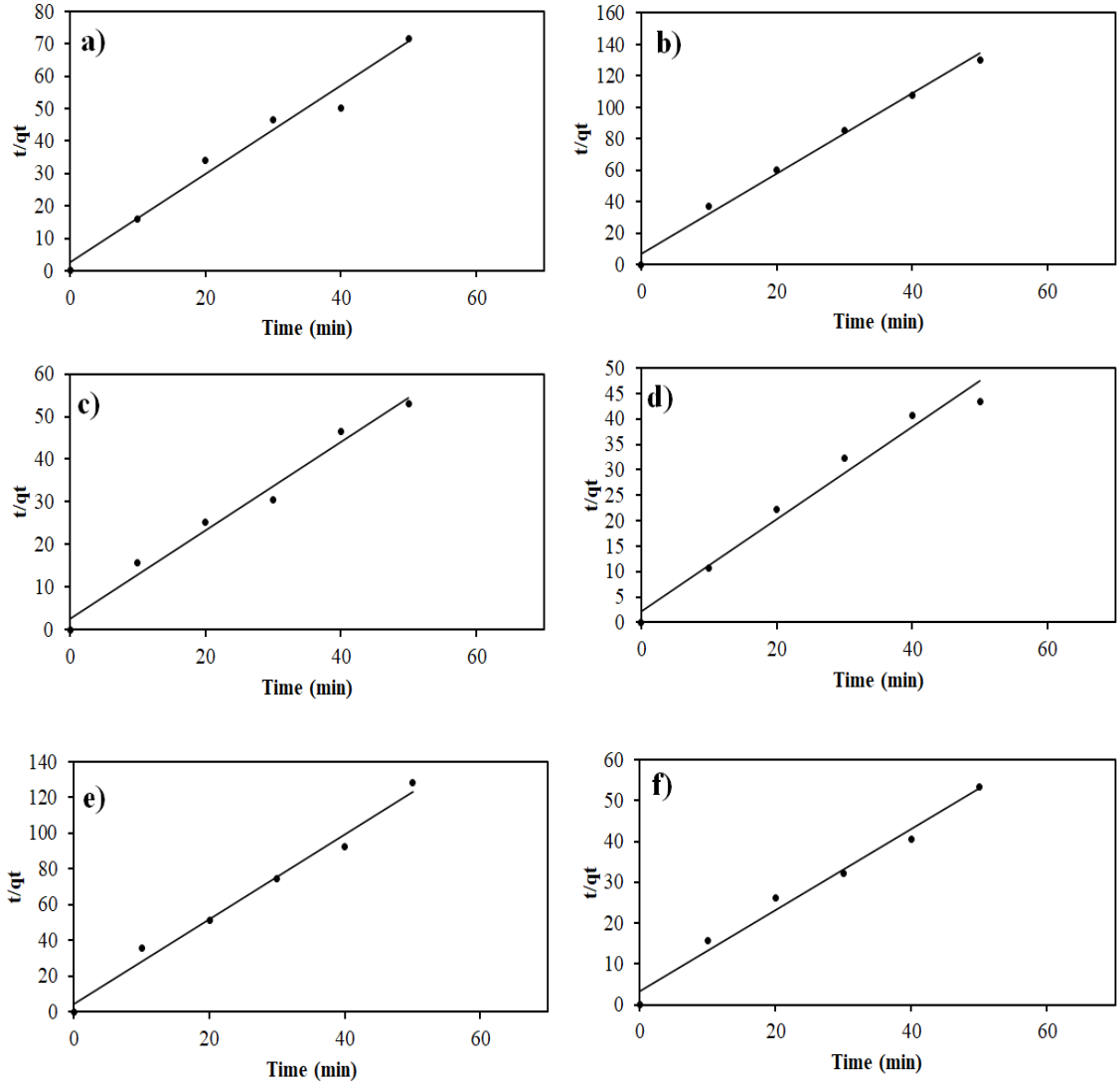

Figure A.4. Pseudo-second order kinetic analysis in the presence of a) eggshell for MO, b) eggshell for MB, c) ZnO-Eggshell 500°C for MO, d) ZnO-Eggshell 500°C for MB, e) La-ZnO-Eggshell 500°C for MO and e) La-ZnO-Eggshell 500°C for MB.

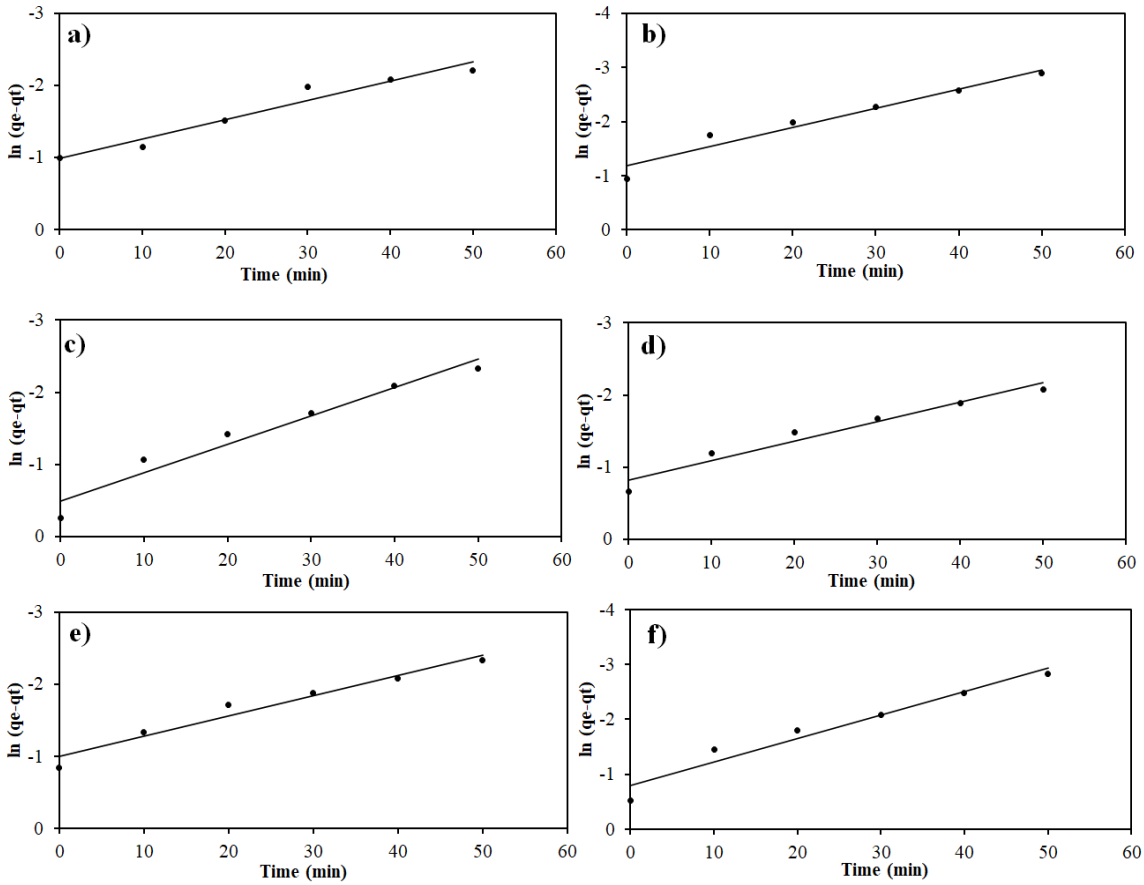

Figure A.5. Pseudo-first order kinetic analysis in the presence of a) eggshell (RH) for MO, b) eggshell (RH) for MB, c) ZnO-Eggshell 500ºC (RH) for MO, d) ZnO-Eggshell 500ºC (RH) for MB, e) La-ZnO-Eggshell 500ºC (RH) for MO and e) La-ZnO-Eggshell 500ºC (RH) for MB.

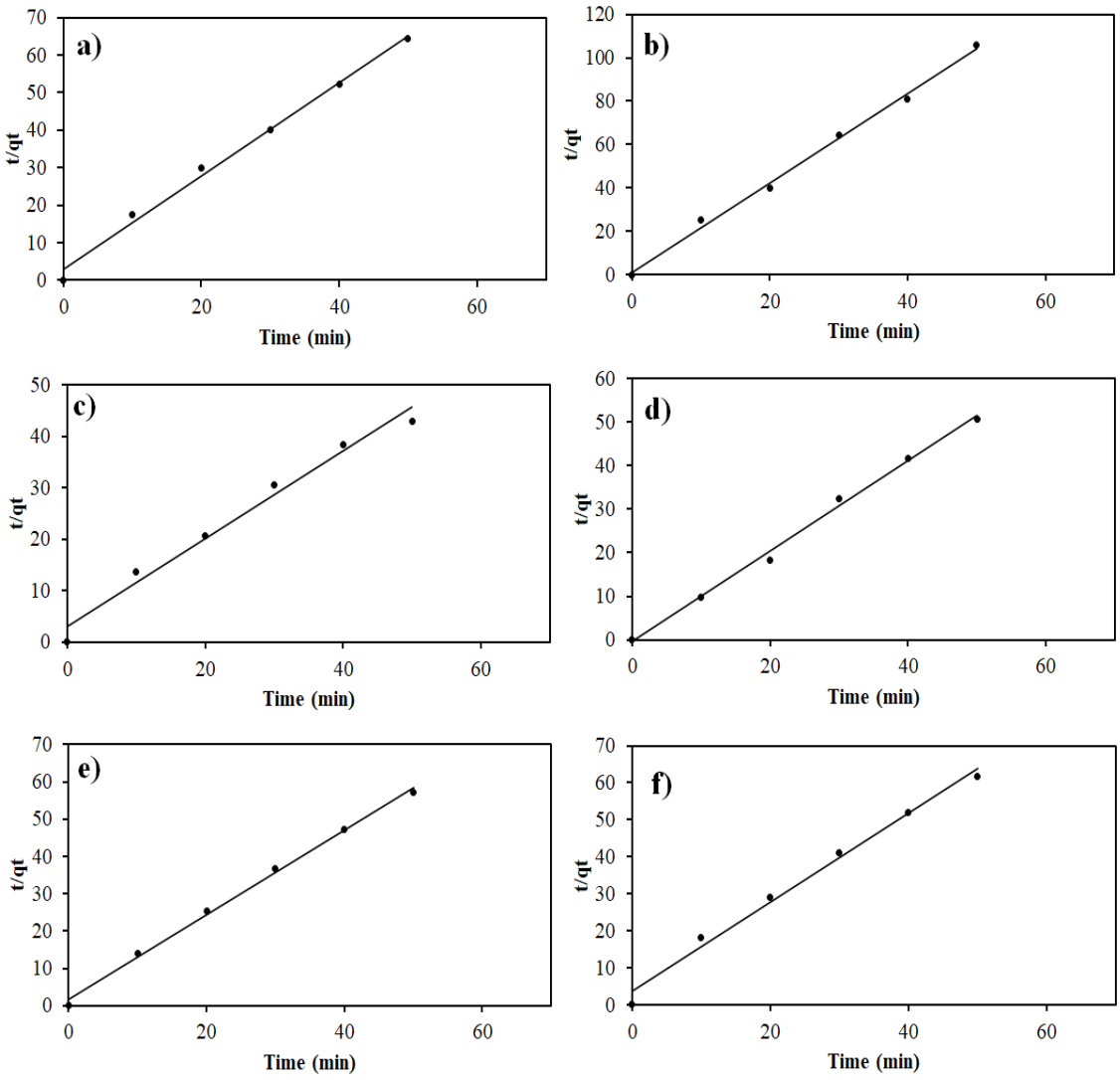

Figure A.6. Pseudo-second order kinetic analysis in the presence of a) eggshell (RH) for MO, b) eggshell (RH) for MB, c) ZnO-Eggshell 500ºC (RH) for MO, d) ZnO-Eggshell 500ºC (RH) for MB, e) La-ZnO-Eggshell 500ºC (RH) for MO and e) La-ZnO-Eggshell 500ºC (RH) for MB.

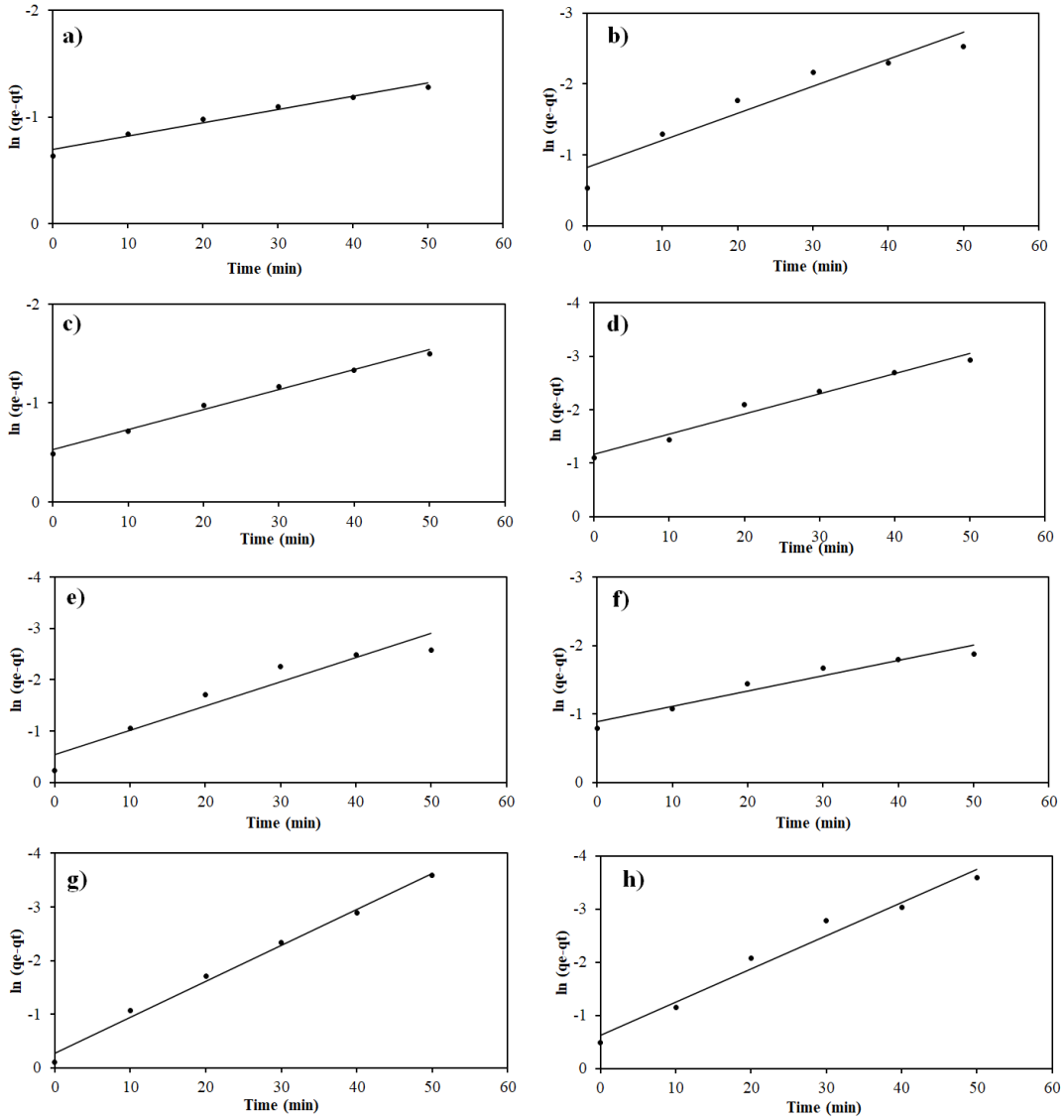

Figure A.7. Pseudo-first order kinetic analysis in the presence of a) HAP 100ºC for MO, b) HAP 500ºC for MB, c) ZnO-HAP 500ºC for MO, d) ZnO-HAP 500ºC for MB, e) La-ZnO-HAP 500ºC for MO and e) La-ZnO-HAP 500ºC for MB.

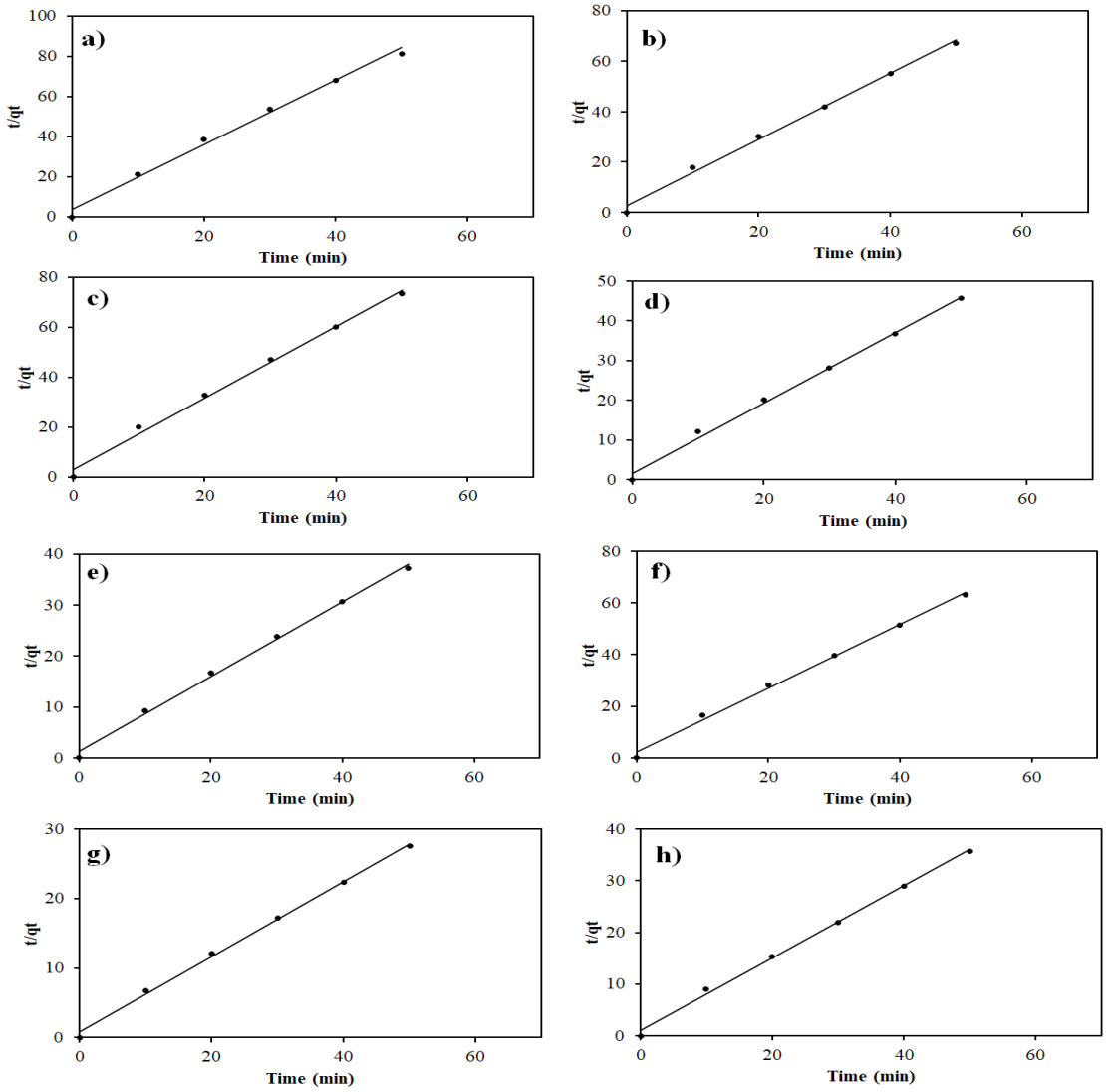

Figure A.8. Pseudo-second order kinetic analysis in the presence of a) HAP 100ºC for MO, b) HAP 500ºC for MB, c) ZnO-HAP 500ºC for MO, d) ZnO-HAP 500ºC for MB, e) LaZnO-HAP 500ºC for MO and e) La-ZnO-HAP 500ºC for MB.

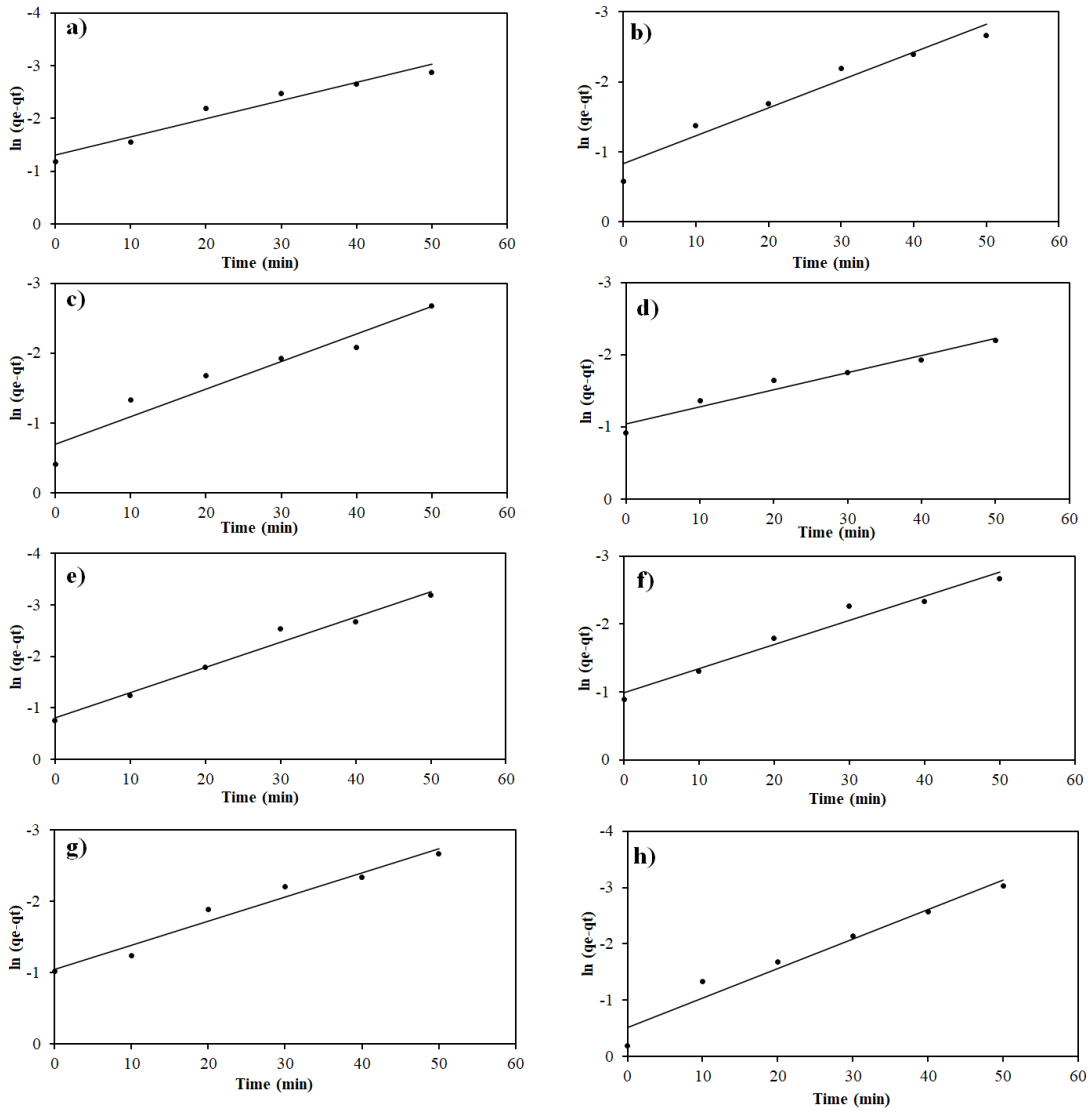

Figure A.9. Pseudo-first order kinetic analysis in the presence of a) HAP 100ºC (RH) for MO, b) HAP 500ºC (RH) for MB, c) ZnO-HAP 500ºC (RH) for MO, d) ZnO-HAP 500ºC (RH) for MB, e) La-ZnO-HAP 500ºC (RH) for MO and e) La-ZnO-HAP 500ºC (RH) for MB.

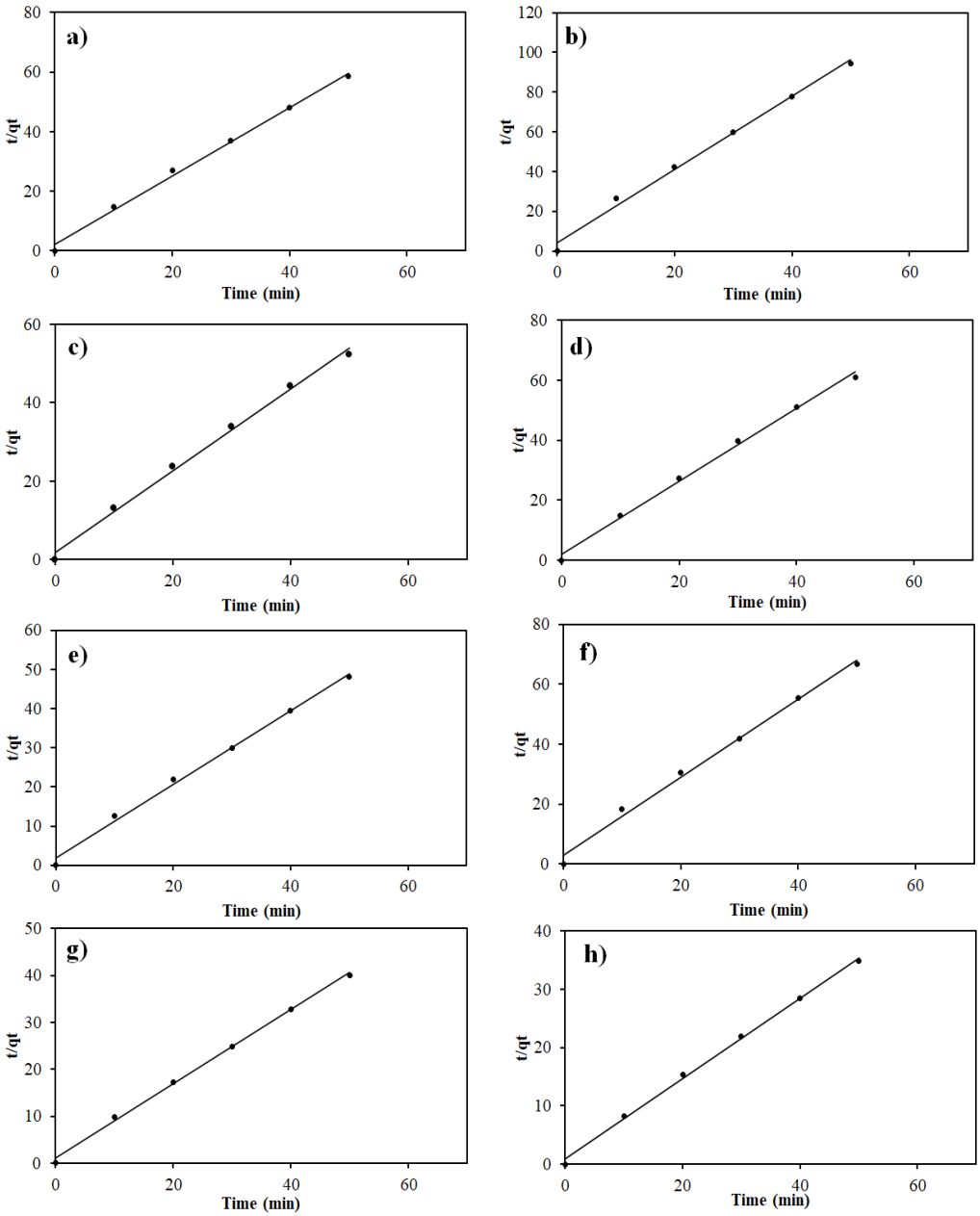

Figure A.10. Pseudo-second order kinetic analysis in the presence of a) HAP 100ºC (RH) for MO, b) HAP 500ºC (RH) for MB, c) ZnO-HAP 500ºC (RH) for MO, d) ZnO-HAP 500ºC (RH) for MB, e) La-ZnO-HAP 500ºC (RH) for MO and e) La-ZnO-HAP 500ºC (RH) for MB.

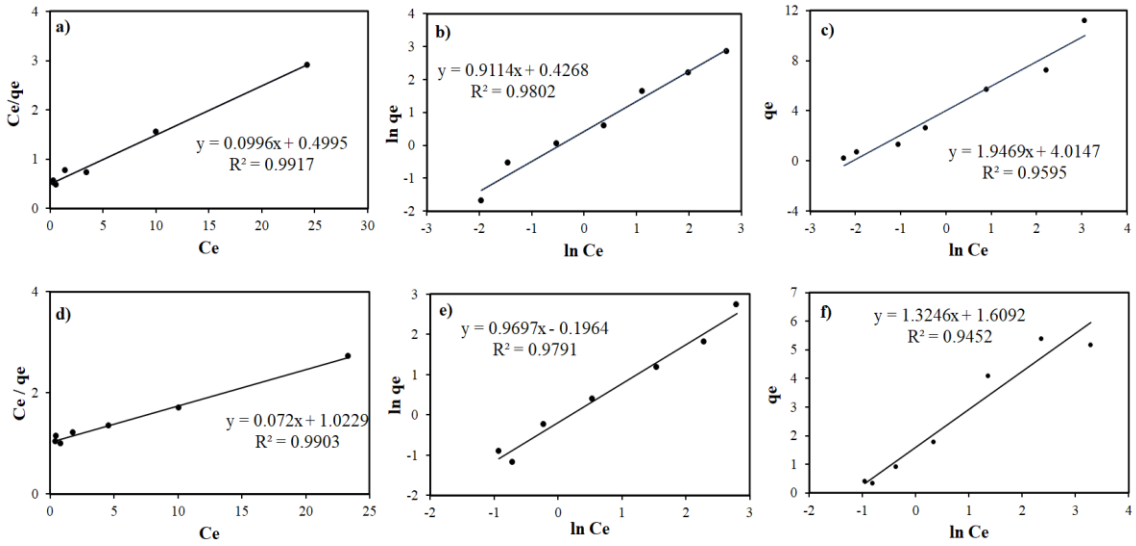

Figure A.11. Langmuir, Freundlich, Temkin isotherms for MO (a-c) and MB (d-f) in the presence of eggshell.

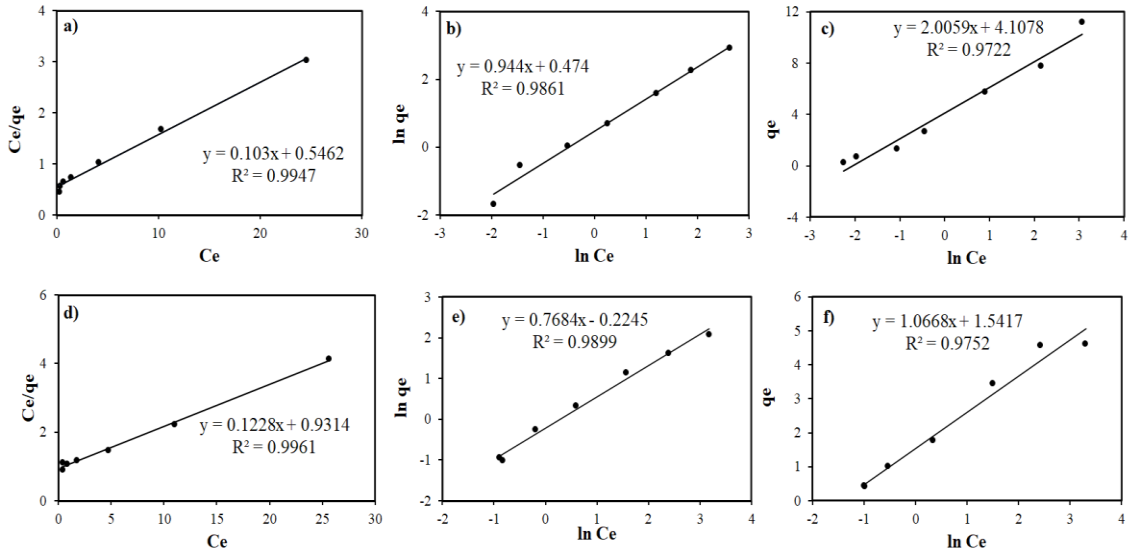

Figure A.12. Langmuir, Freundlich, Temkin isotherms for MO (a-c) and MB (d-f) in the presence of ZnO-Eggshell 500ºC.

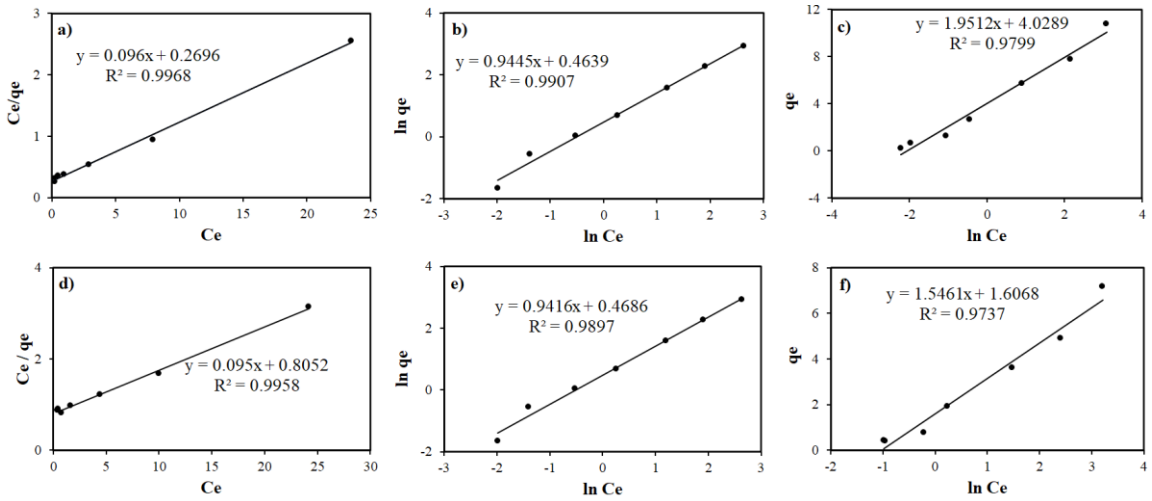

Figure A.13. Langmuir, Freundlich, Temkin isotherms for MO (a-c) and MB (d-f) in the presence of La-ZnO-Eggshell 500^{o}C.

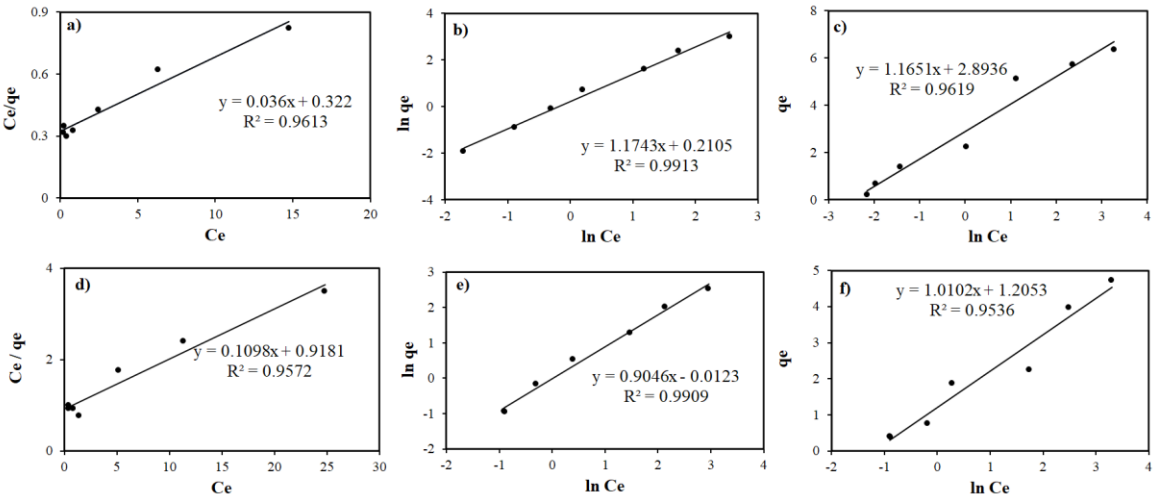

Figure A.14. Langmuir, Freundlich, Temkin isotherms for MO (a-c) and MB (d-f) in the presence of eggshell (RH).

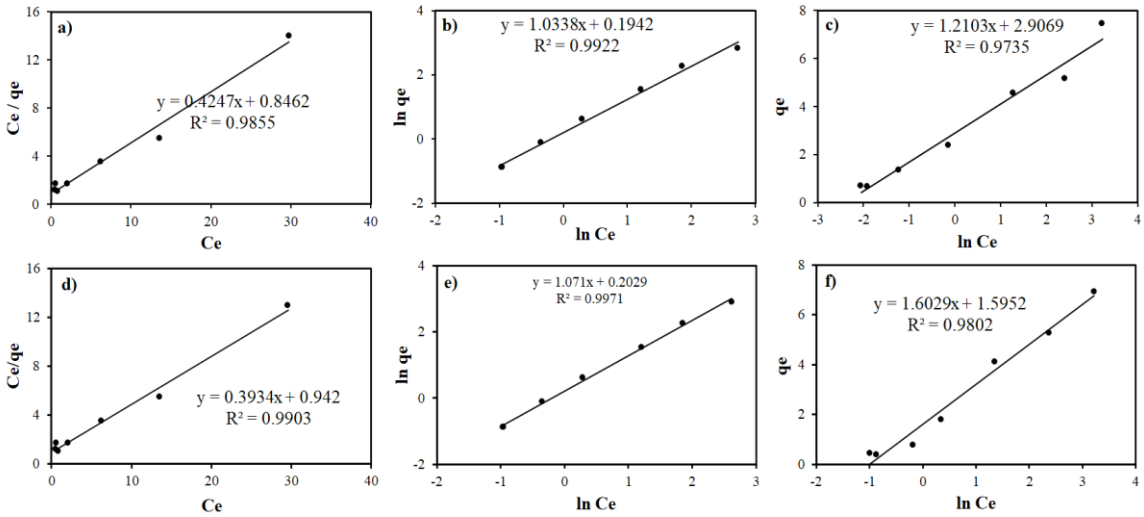

Figure A.15. Langmuir, Freundlich, Temkin isotherms for MO (a-c) and MB (d-f) in the presence of ZnO-Eggshell (RH) 500ºC.

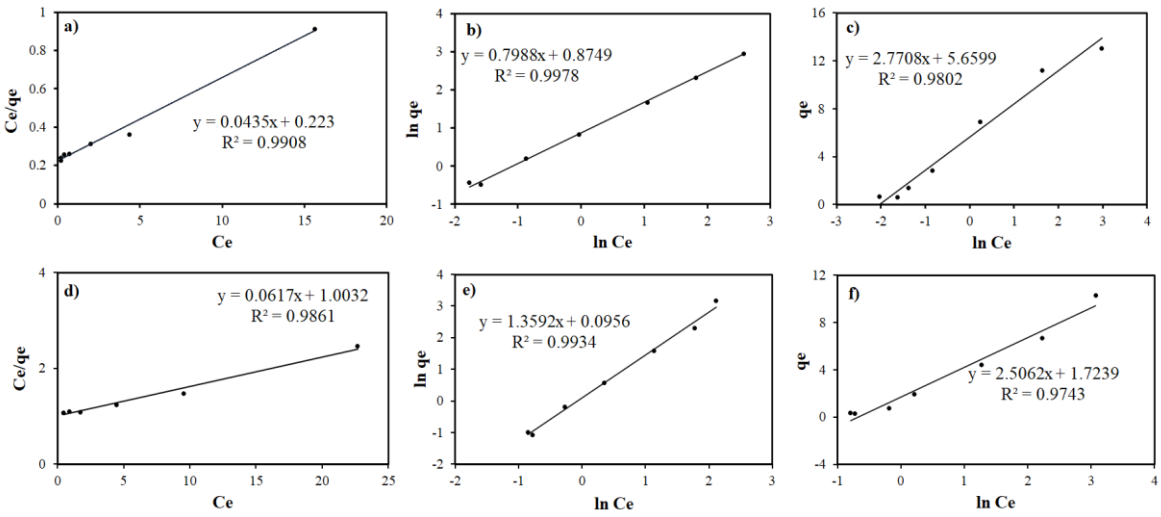

Figure A.16. Langmuir, Freundlich, Temkin isotherms for MO (a-c) and MB (d-f) in the presence of La-ZnO-Eggshell (RH) 500ºC.

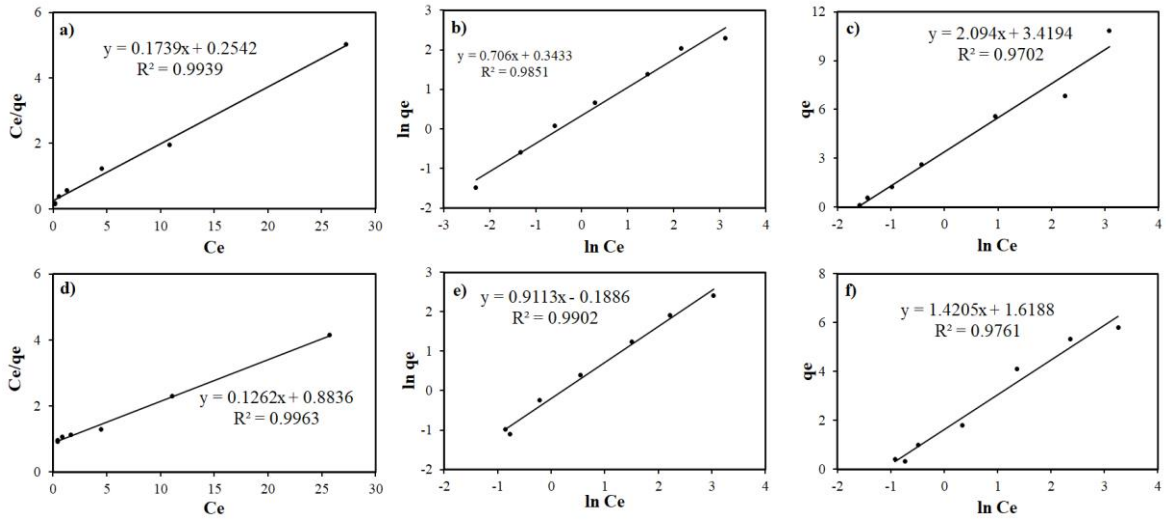

Figure A.17. Langmuir, Freundlich, Temkin isotherms for MO (a-c) and MB (d-f) in the presence of HAP 100ºC.

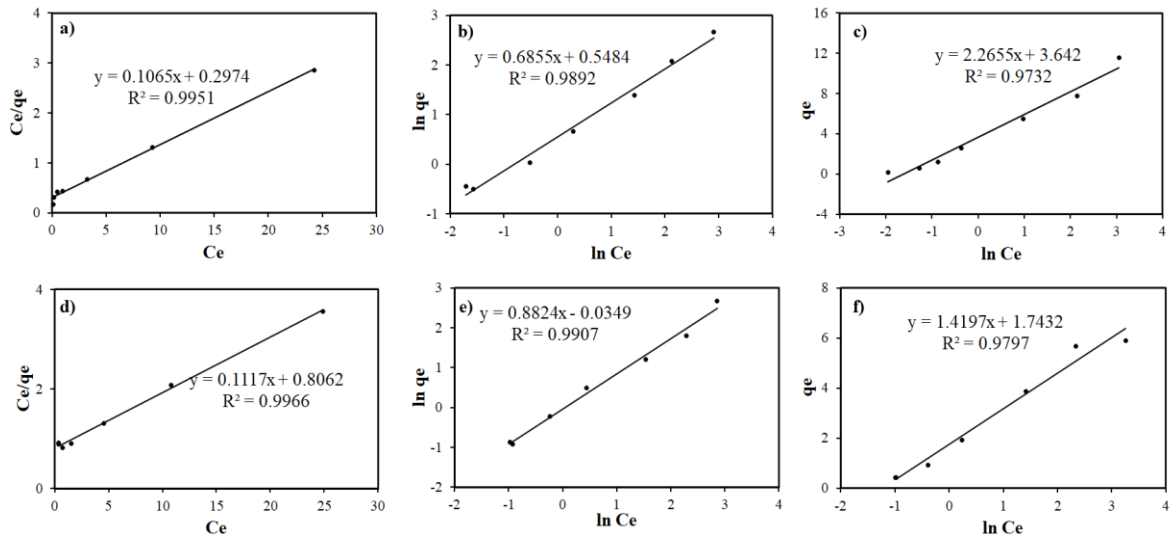

Figure A.18. Langmuir, Freundlich, Temkin isotherms for MO (a-c) and MB (d-f) in the presence of HAP 500ºC.

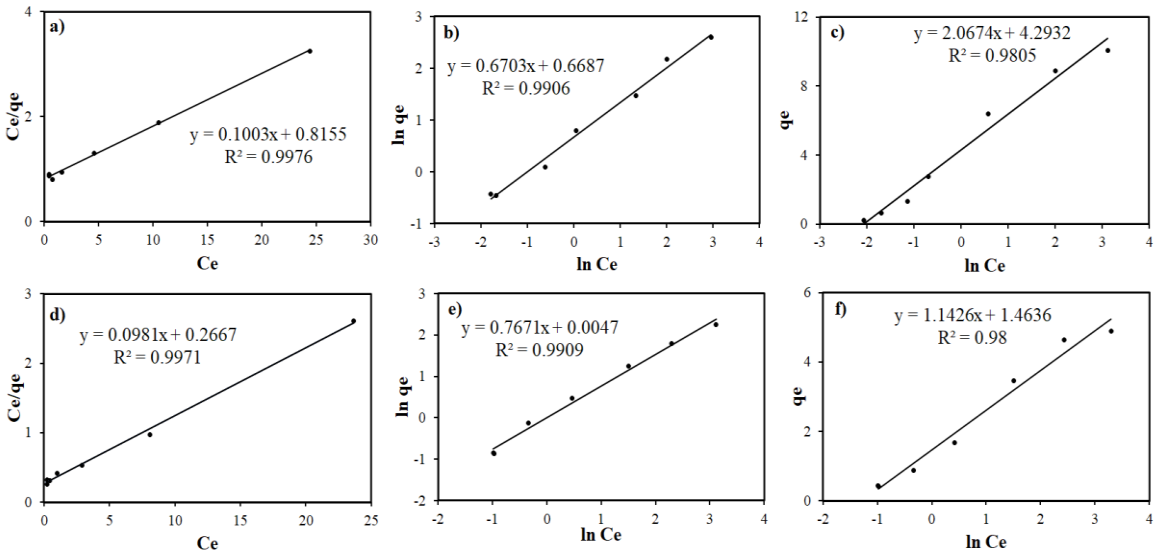

Figure A.19. Langmuir, Freundlich, Temkin isotherms for MO (a-c) and MB (d-f) in the presence of ZnO-HAP 500ºC.

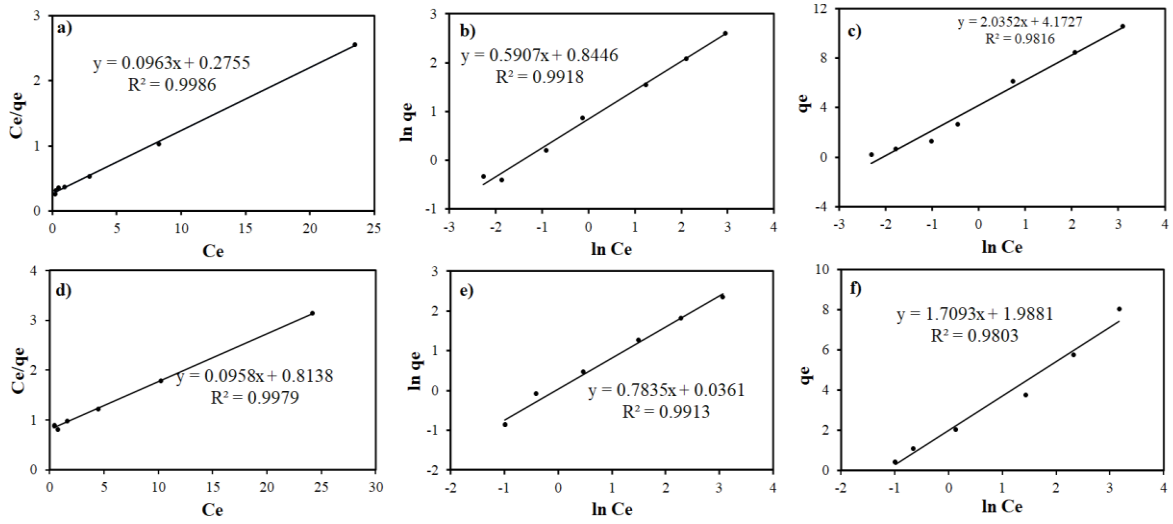

Figure A.20. Langmuir, Freundlich, Temkin isotherms for MO (a-c) and MB (d-f) in the presence of La-ZnO-HAP 500ºC.

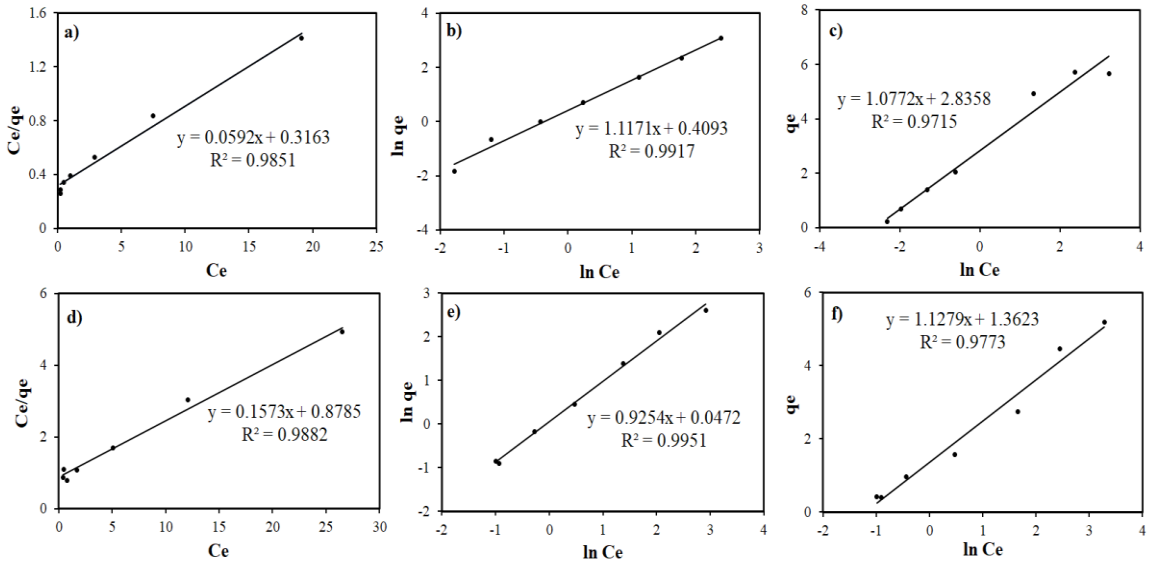

Figure A.21. Langmuir, Freundlich, Temkin isotherms for MO (a-c) and MB (d-f) in the presence of HAP 100ºC (RH).

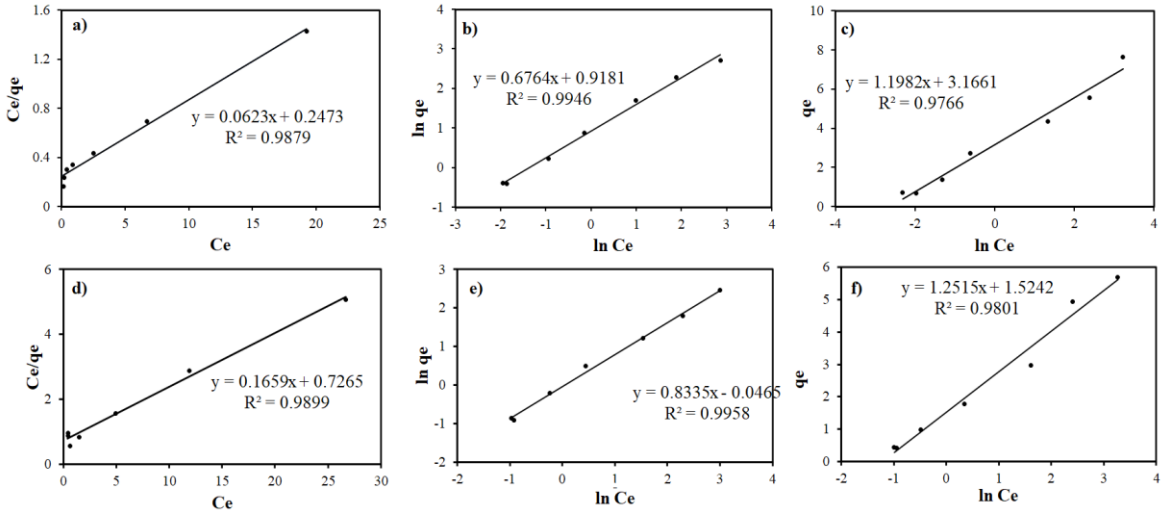

Figure A.22. Langmuir, Freundlich, Temkin isotherms for MO (a-c) and MB (d-f) in the presence of HAP 500ºC (RH).

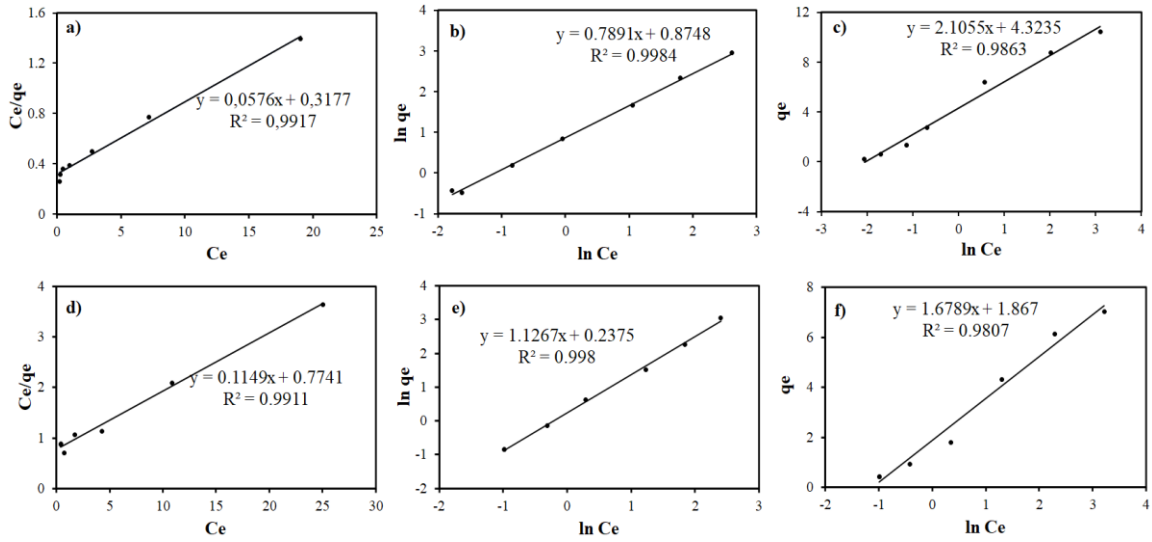

Figure A.23. Langmuir, Freundlich, Temkin isotherms for MO (a-c) and MB (d-f) in the presence of ZnO-HAP 500ºC (RH).

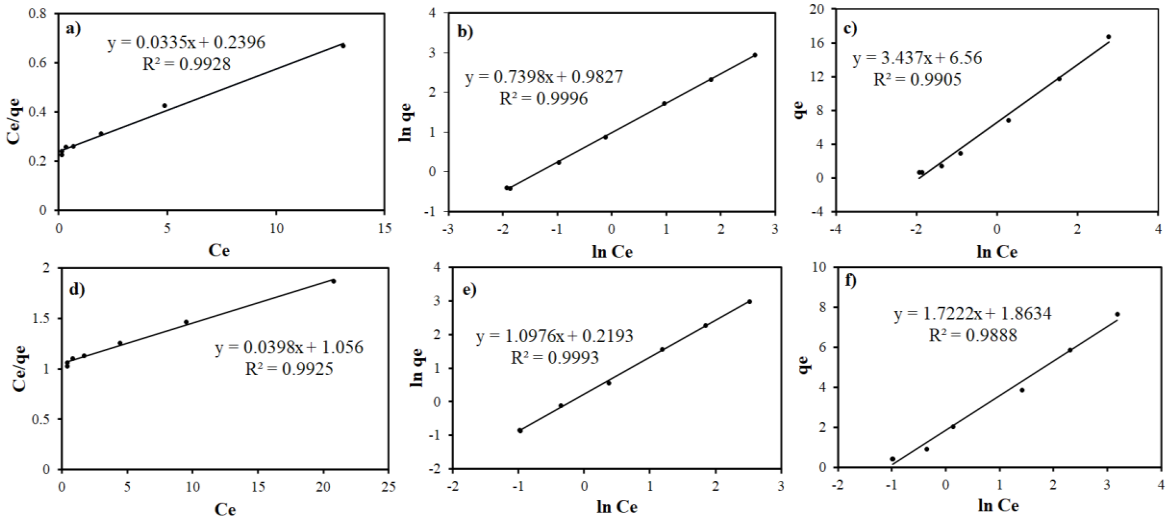

Figure A.24. Langmuir, Freundlich, Temkin isotherms for MO (a-c) and MB (d-f) in the presence of La-ZnO-HAP 500ºC (RH).

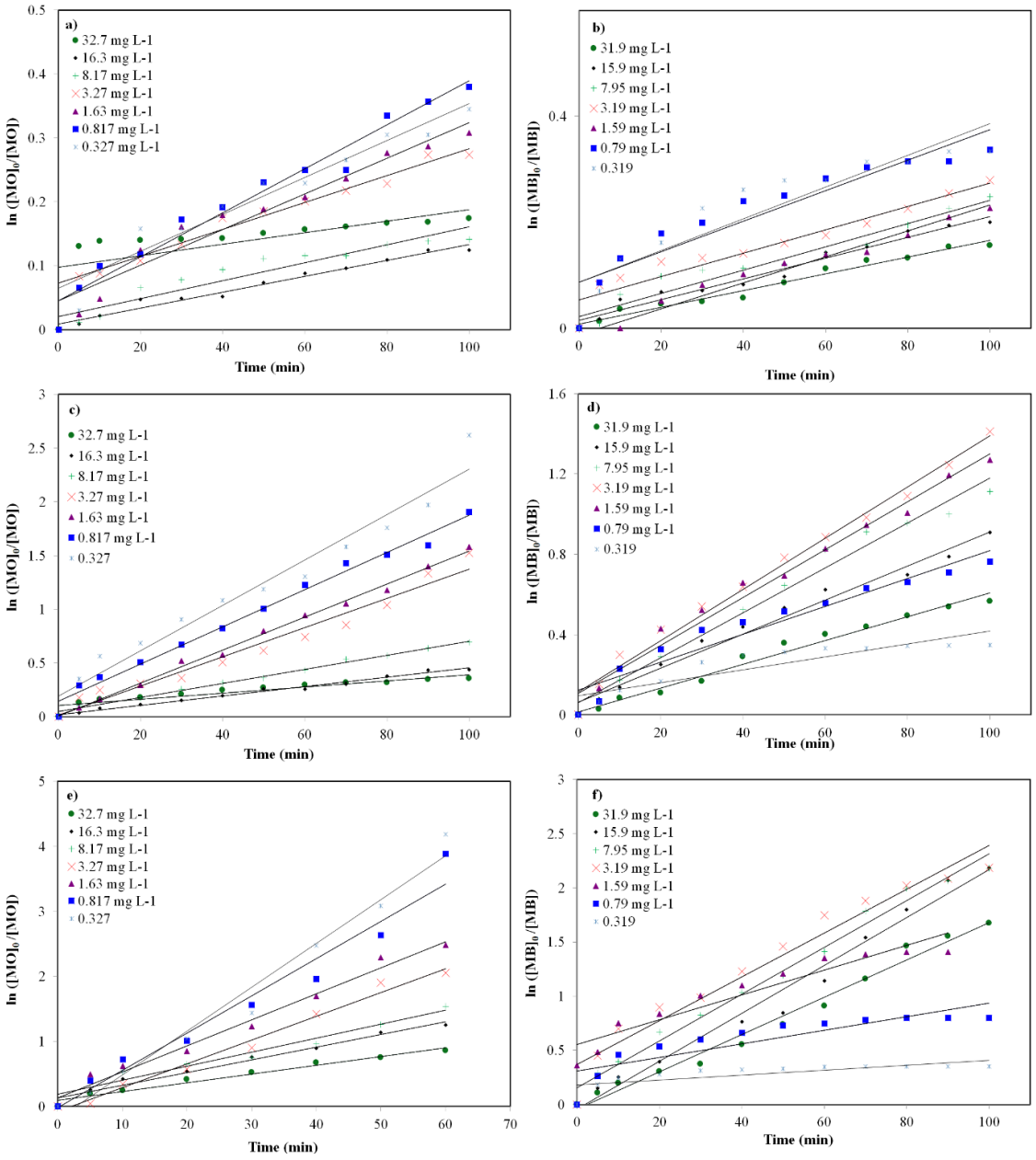

Figure A.25. Pseudo-first order degradation of MO and MB in the presence of (a,b) eggshell, (c,d) ZnO-Eggshell 500ºC, (e,f) La-ZnO-Eggshell 500ºC.

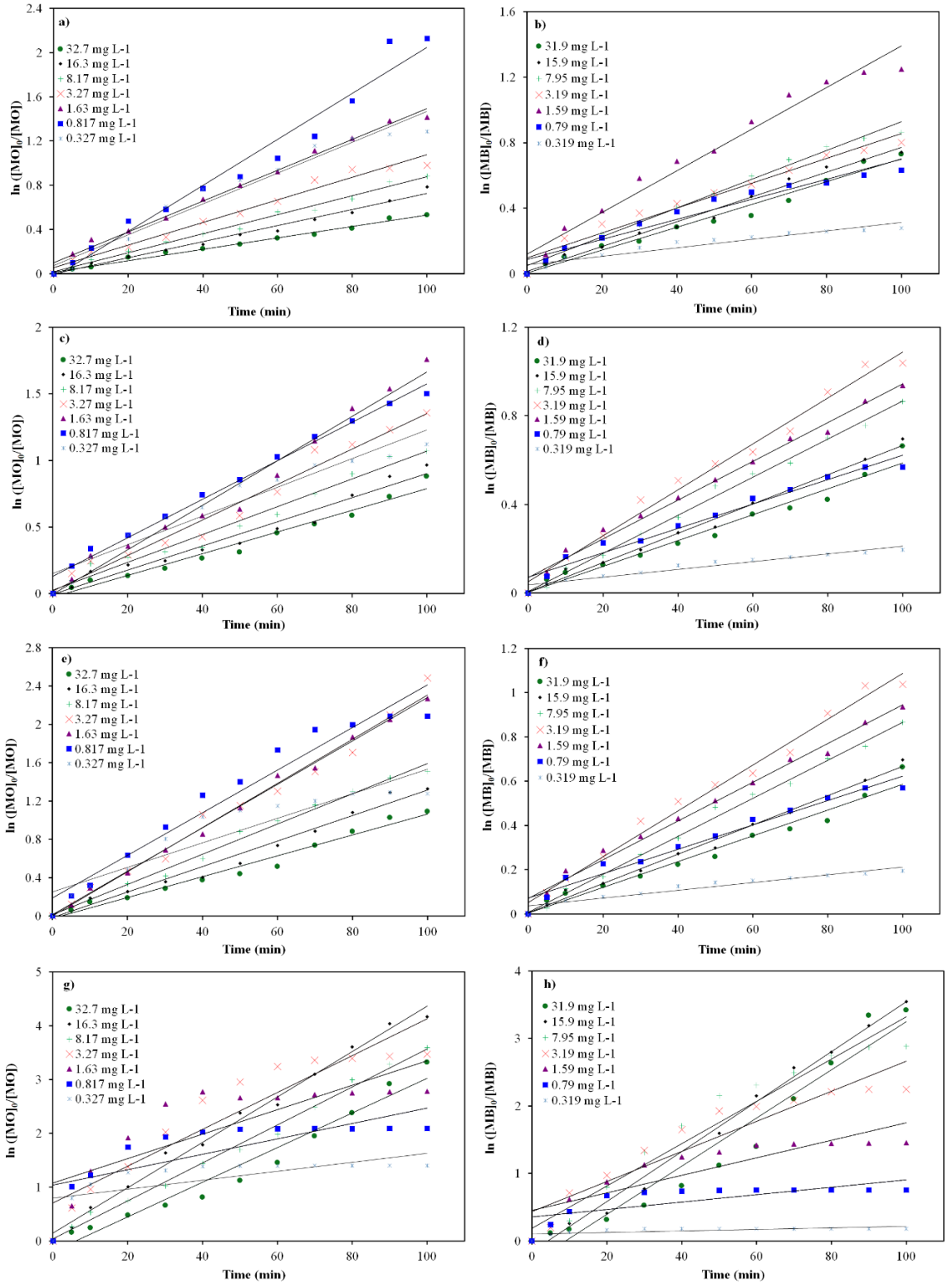

Figure A.26. Pseudo-first order degradation of MO and MB in the presence of (a,b) HAP 100ºC, (c,d) HAP 100ºC (e,f) ZnO-HAP 500ºC, (g,h) La-ZnO-HAP 500ºC.

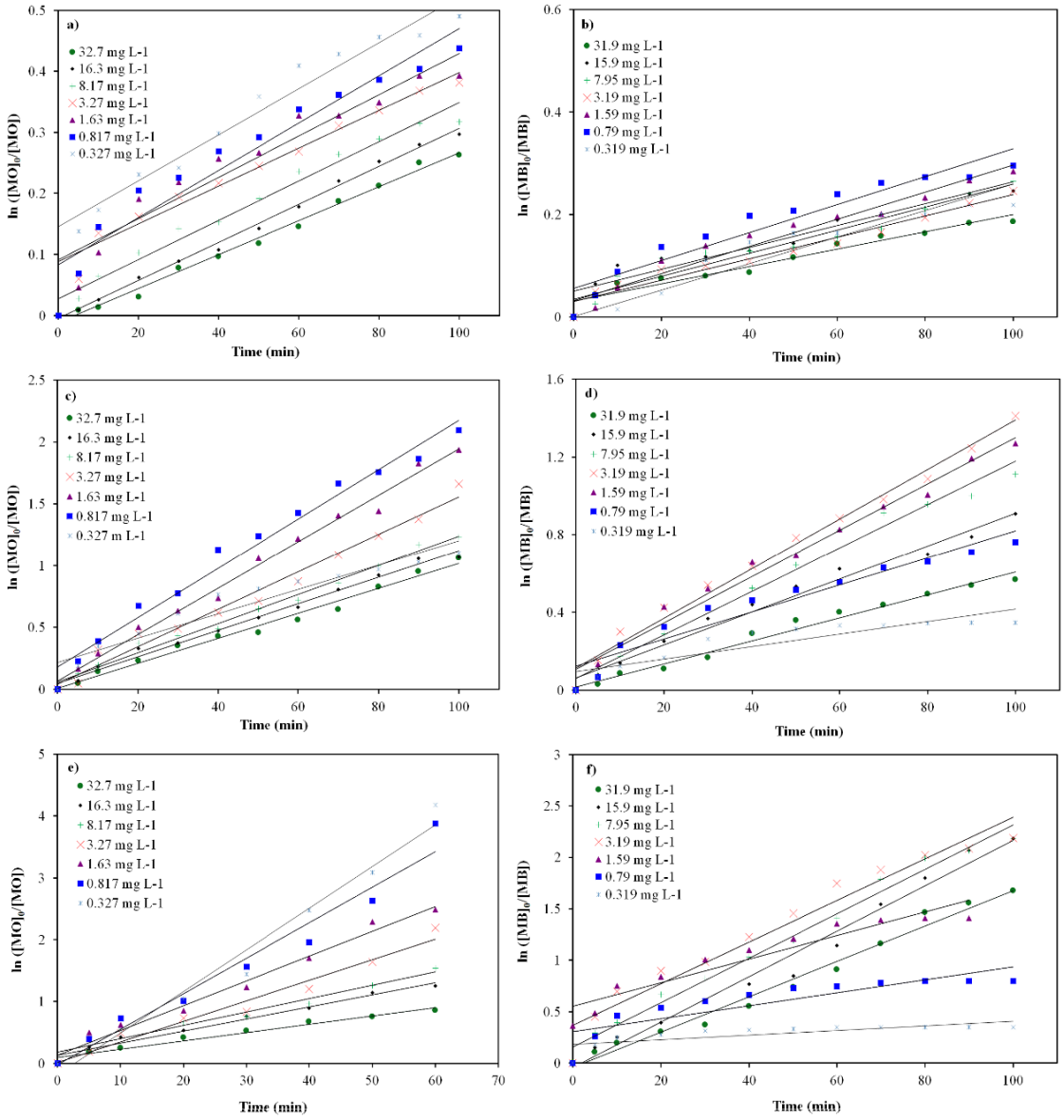

Figure A 27. Pseudo-first order degradation of MO and MB in the presence of (a,b) eggshell (RH), (c,d) ZnO-Eggshell 500^{o}C (RH), (e,f) La-ZnO-Eggshell 500^{o}C (RH).

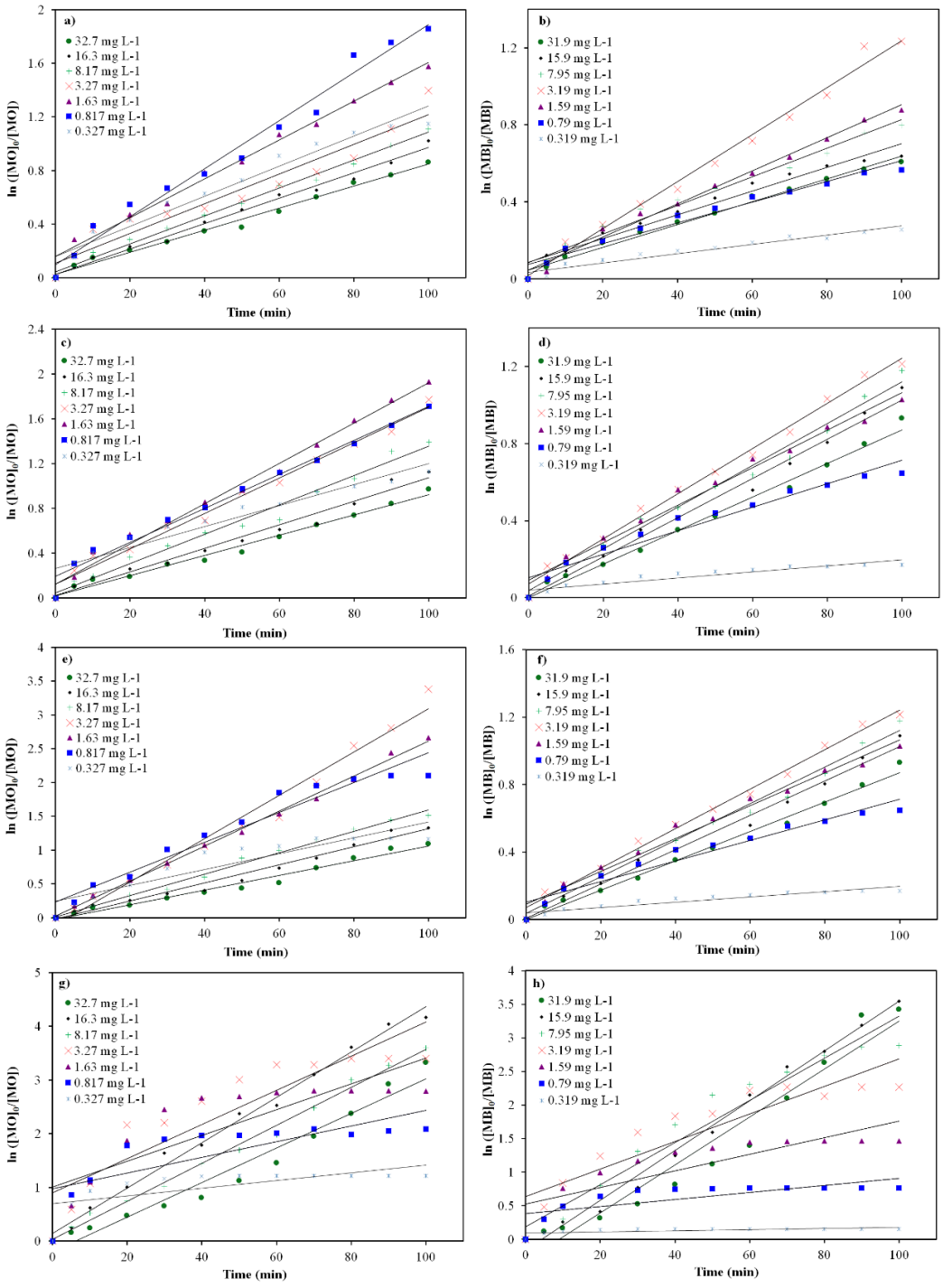

Figure A.28. Pseudo-first order degradation of MO and MB in the presence of (a,b) HAP 100ºC (RH) , (c,d) HAP 100ºC (RH) (e,f) ZnO-HAP 500ºC (RH), (g,h) La-ZnO-HAP 500ºC (RH).

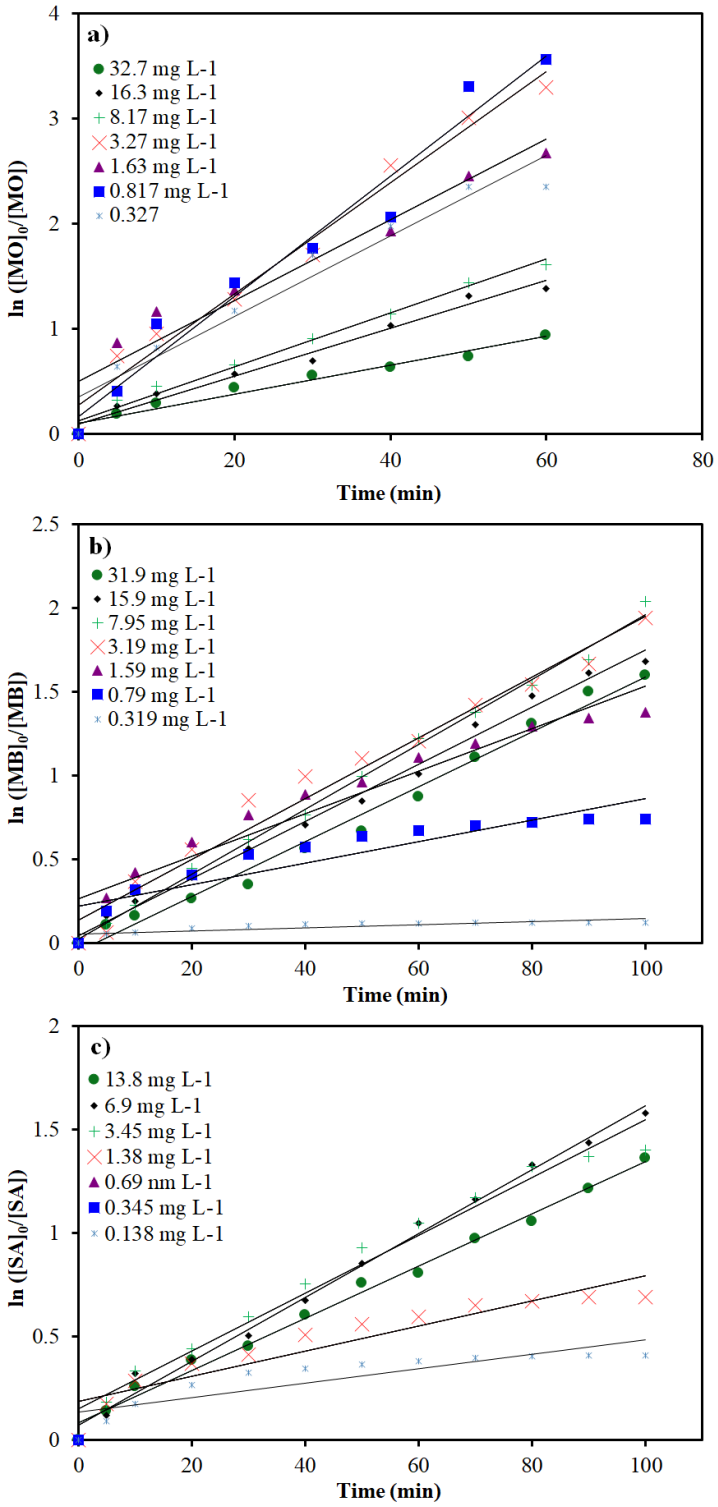

Figure A.29. Pseudo-first order degradation of (a) MO in the presence of Zn-Al 500ºC, (b) MB in the presence of Zn-Fe 500ºC and (c) SA in the presence of Zn-Fe 500ºC.

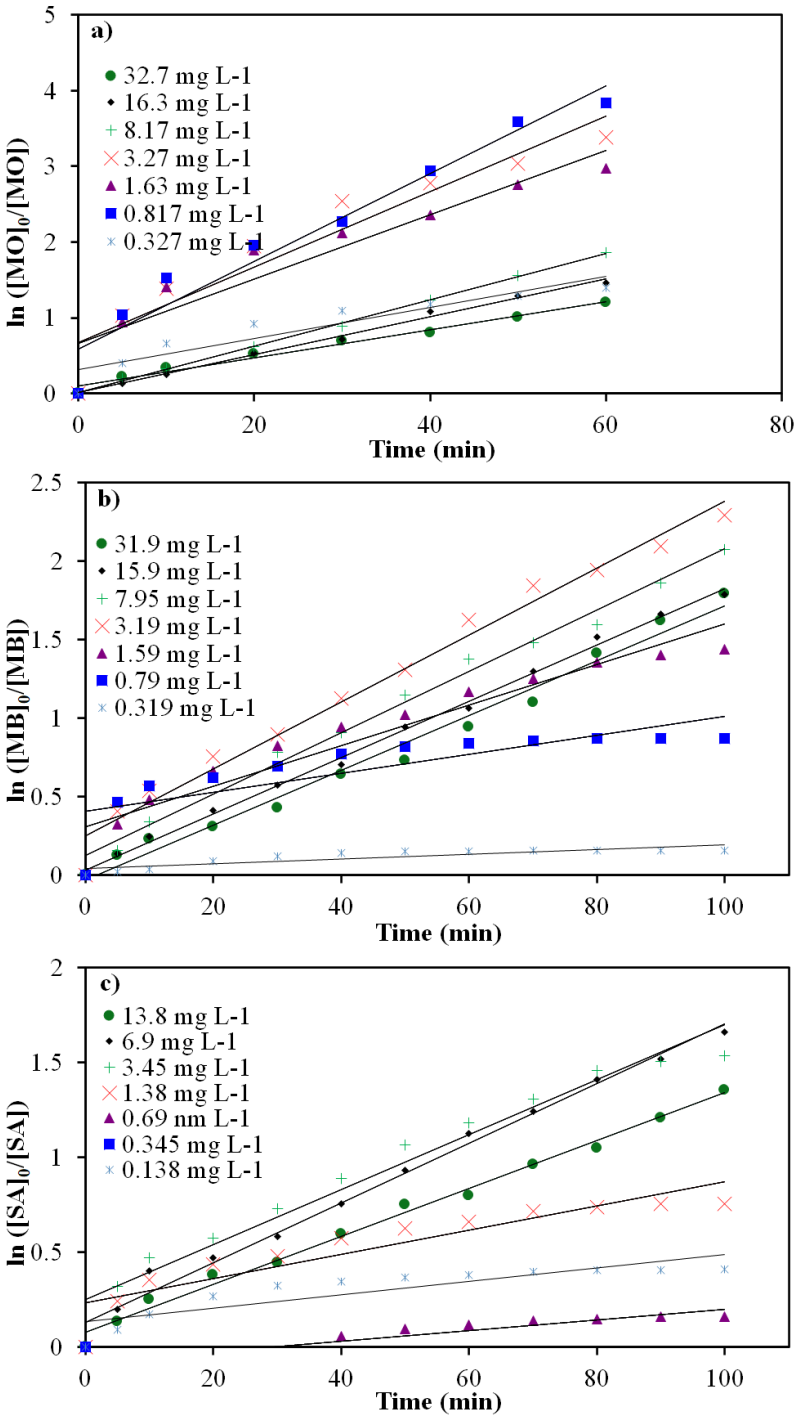

Figure A.30. Pseudo-first order degradation of (a) MO in the presence of Zn-Al-Fly Ash 500ºC, (b) MB in the presence of Zn-Fe-Fly Ash 500ºC and (c) SA in the presence of Zn-Fe-Fly Ash 500ºC.

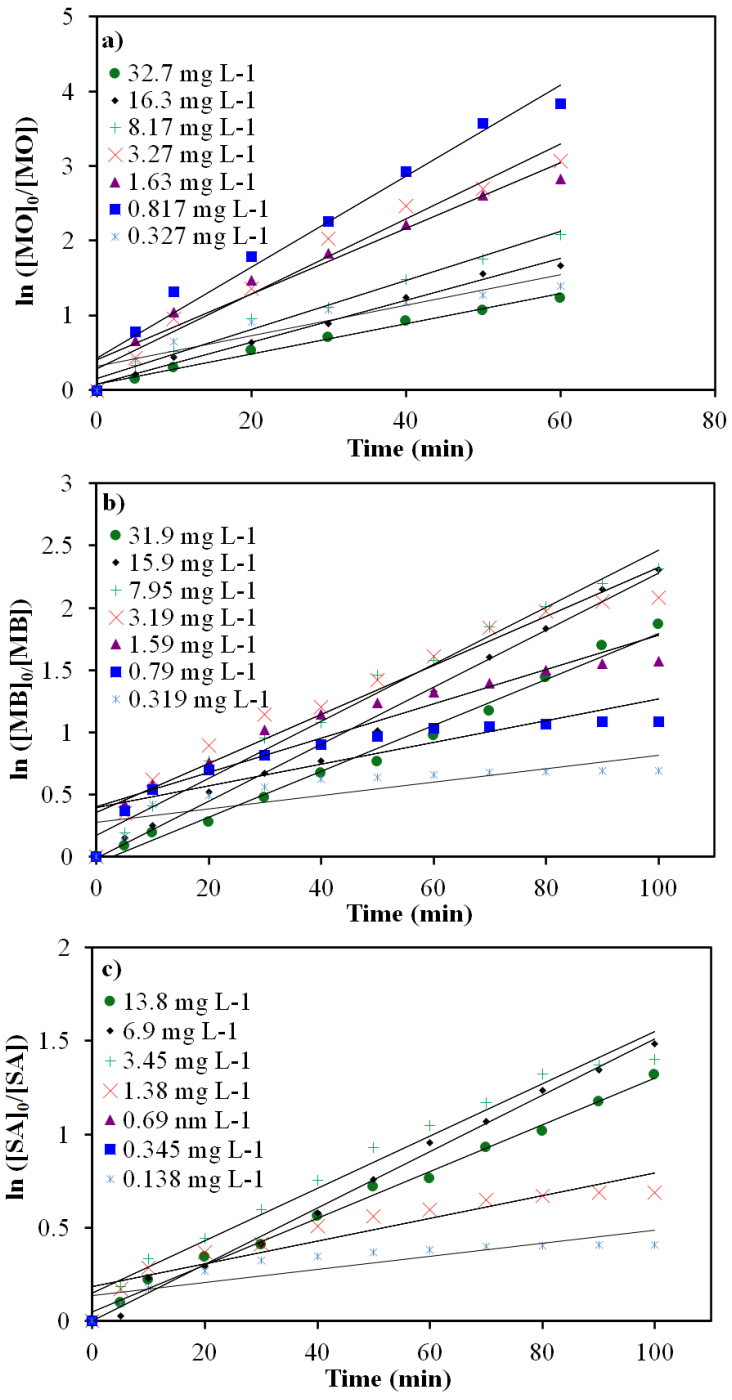

Figure A.31. Pseudo-first order degradation of (a) MO in the presence of Zn-Al-Zeolite 500ºC, (b) MB in the presence of Zn-Fe-Zeolite 500ºC and (c) SA in the presence of Zn-Fe-Zeolite 500ºC.

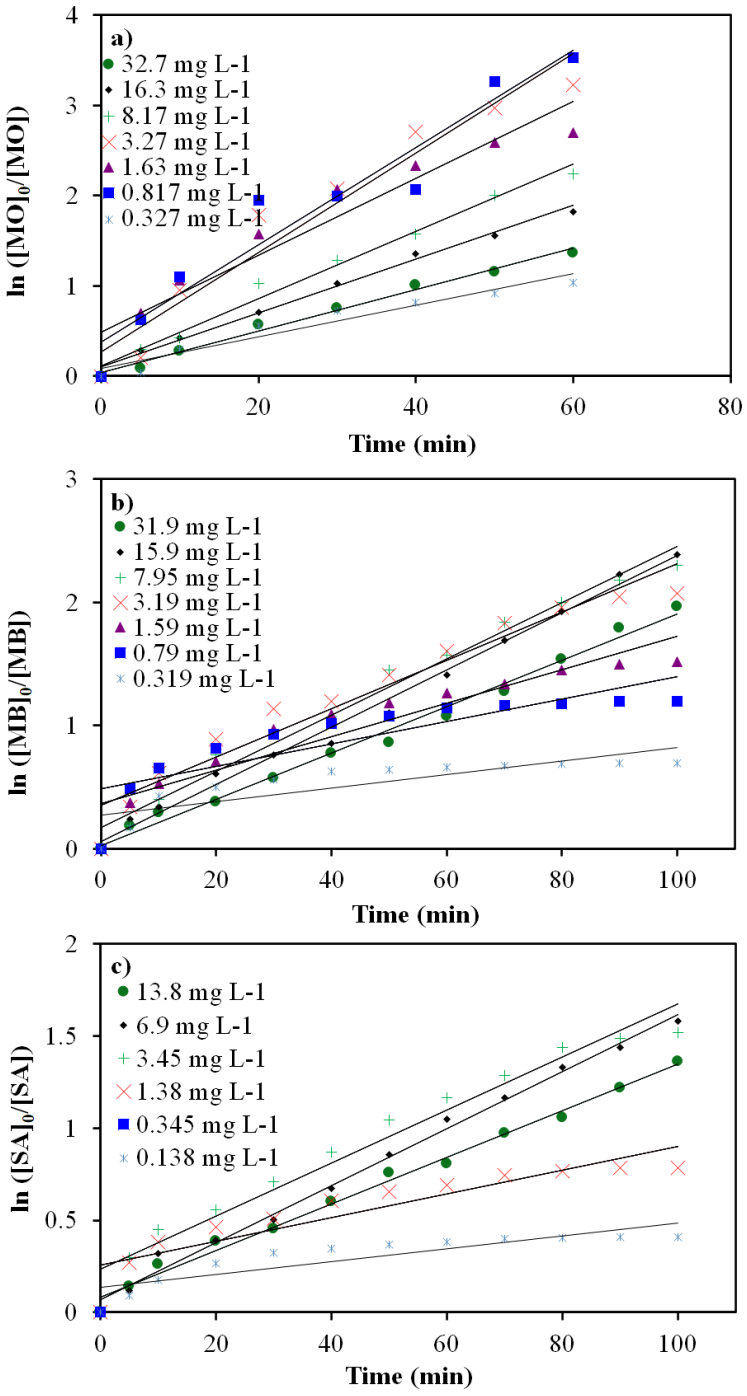

Figure A.32. Pseudo-first order degradation of (a) MO, (b) MB and (c) SA in the presence of Mg-Fe-ZIF-8 500ºC.

APPENDIX B: COPYRIGHT LICENCES

The effect of ZnO or TiO2 loaded nanoparticles on the adsorption and photocatalytic performance of Cu-BTC and ZIF-8 MOFs

Author: A.N. Ökte,D. Karamanis,E. Chalkia,D. Tuncel

Publication: Materials Chemistry and Physics

Publisher: Elsevier

Date: 1 February 2017

Figure B.1. Permission for Section 3.1, Elsevier, Copyright (2017).

Efficient photoactivity of TiO2-hybrid-porous nanocomposite: Effect of humidity

Author: D. Tuncel,A.N. Ökte

Publication: Applied Surface Science

Publisher: Elsevier

Date: 15 November 2018

Figure B.2. Permission for Section 3.2, Elsevier, Copyright (2018).

ZnO@CuO derived from Cu-BTC for efficient UV-induced photocatalytic applications

Author: D. Tuncel,A.N. Ökte
Publication: Catalysis Today
Publisher: Elsevier
Date: 15 May 2019

Figure B.3. Permission for Section 3.3, Elsevier, Copyright (2019).

Improved Adsorption Capacity and Photoactivity of ZnO-ZIF-8 Nanocomposites

Author: D. Tuncel,A.N. Ökte
Publication: Catalysis Today
Publisher: Elsevier
Date: 1 February 2021

Figure B.4. Permission for Section 3.4, Elsevier, Copyright (2021).